

**THEORETICAL STUDIES ON NOVEL
MOLECULAR SYSTEMS
AND NANOMATERIALS FOR HYDROGEN
ENERGY APPLICATIONS**

By

K. SRINIVASU

(CHEM01200804003)

BHABHA ATOMIC RESEARCH CENTRE, MUMBAI

A thesis submitted to the

Board of Studies in Chemical Sciences

In partial fulfillment of requirements

For the Degree of

DOCTOR OF PHILOSOPHY

of


HOMI BHABHA NATIONAL INSTITUTE



November, 2013

Homi Bhabha National Institute
Recommendations of the Viva Voce Board

As members of the Viva Voce Board, we certify that we have read the dissertation prepared by **K. Srinivasu** entitled "**Theoretical studies on novel molecular systems and nanomaterials for hydrogen energy applications**" and recommend that it may be accepted as fulfilling the dissertation requirement for the Degree of Doctor of Philosophy.

25.07.2014

Chairman- Prof. Tulsi Mukherjee Date:

25-7-2014

Guide / Convener- Prof. Swapan K. Ghosh Date:



External Examiner - Prof. M. Durga Prasad Date: 25/7/14

25/7/14

Member-1 Dr. T. K. Ghanty Date:



Member-2 Dr. A. K. Samanta Date: 25/07/14



Member-3 Dr. D. K. Maity Date: 25/07/14

Final approval and acceptance of this dissertation is contingent upon the candidate's submission of the final copies of the dissertation to HBNI.

I hereby certify that I have read this dissertation prepared under my direction and recommend that it may be accepted as fulfilling the dissertation requirement

Date: 25-7-2014

Place: Mumbai


Guide

STATEMENT BY AUTHOR

This dissertation has been submitted in partial fulfillment of requirements for an advanced degree at Homi Bhabha National Institute (HBNI) and is deposited in the Library to be made available to borrowers under rules of the HBNI.

Brief quotations from this dissertation are allowable without special permission, provided that accurate acknowledgement of source is made. Requests for permission for extended quotation from or reproduction of this manuscript in whole or in part may be granted by the Competent Authority of HBNI when in his or her judgment the proposed use of the material is in the interests of scholarship. In all other instances, however, permission must be obtained from the author

K. Srinivasu

DECLARATION

I, hereby declare that the investigation presented in the thesis has been carried out by me. The work is original and has not been submitted earlier as a whole or in part for a degree / diploma at this or any other Institution / University.

K. Srinivasu

List of Publications arising from the thesis

Journals

1. Quantum chemical studies on hydrogen adsorption in carbon-based model systems: role of charged surface and the electronic induction effect, **Srinivasu, K.**; Chandrakumar, K. R. S.; Ghosh, S. K. *Phys. Chem. Chem. Phys.*, **2008**, *10*, 5832–5839.
2. Nanoscale curvature-induced hydrogen adsorption in alkali metal doped carbon nanomaterials, Chandrakumar, K. R. S.; **Srinivasu, K.**; Ghosh, S. K. *J. Phys. Chem. C* **2008**, *112*, 15670–15679.
3. Computational investigation on hydrogen adsorption by alkali metal doped organic molecules: Role of aromaticity, **Srinivasu, K.**; Chandrakumar, K. R. S.; Ghosh, S. K. *ChemPhysChem* **2009**, *10*, 427–435.
4. Ab initio studies on the electronic structure and properties of aluminum hydrides that are analogues of boron hydrides, **Srinivasu, K.**; Chandrakumar, K. R. S.; Ghosh, S. K. *J. Phys. Chem. A* **2010**, *114*, 12244–12250.
5. An ab initio investigation of hydrogen adsorption in Li-doped closo-boranes, **Srinivasu, K.**; Ghosh, S. K. *J. Phys. Chem. C* **2011**, *115*, 1450–1456.
6. Tuning the metal binding energy and hydrogen storage in alkali metal decorated MOF-5 through boron doping: a theoretical investigation, **Srinivasu, K.**; Ghosh, S. K. *J. Phys. Chem. C* **2011**, *115*, 16984–16991.
7. Theoretical studies on hydrogen adsorption properties of lithium decorated diborene ($B_2H_4Li_2$) and diboryne ($B_2H_2Li_2$), **Srinivasu, K.**; Ghosh, S. K. *Int J Hydrogen Energy* **2011**, *36*, 15681–15688.
8. Graphyne and graphdiyne: Promising materials for nanoelectronics and energy storage applications, **Srinivasu, K.**; Ghosh, S. K. *J. Phys. Chem. C* **2012**, *116*, 5951–5956.

9. Transition metal decorated porphyrin like porous fullerene: Promising materials for molecular hydrogen adsorption, **Srinivasu, K.;** Ghosh, S. K. *J. Phys. Chem. C* **2012**, *116*, 25184–25189.
10. Electronic structure, optical properties and hydrogen adsorption characteristics of supercubane based three-dimensional porous carbon, **Srinivasu, K.;** Ghosh, S. K. *J. Phys. Chem. C* **2012**, *116*, 25015–25021.
11. Hydrogen adsorption in lithium decorated conjugated microporous polymers: A DFT investigation, **Srinivasu, K.;** Ghosh, S. K. *RSC Advances* **2014**, *4*, 4170–4176.
12. Transition metal decorated graphyne: an efficient catalyst for oxygen reduction reaction. **Srinivasu, K.;** Ghosh, S. K. *J. Phys. Chem. C*. **2013**, *117*, 26021–26028
13. Photocatalytic activity of hexagonal porous carbon nitride: An ab initio investigation. **Srinivasu, K.;** Modak, B.; Ghosh, S. K. *J. Phys. Chem. C* (Communicated)
14. Silicene: A metal free electro-catalyst for oxygen reduction reaction. **Srinivasu, K.;** Ghosh, S. K. (To be communicated)

K. Srinivasu

Dedicated

To

My Family

Acknowledgements

I owe my deepest gratitude and sincere thanks to my Ph. D supervisor Prof. Swapan K. Ghosh for his invaluable inspiration and guidance throughout my Ph. D tenure. He has been highly supportive and encouraging at all the times. His valuable suggestions and scientific discussions are highly stimulating and encouraging throughout my research. My experience of working with Prof. S. K. Ghosh has been a cherished experience, which will definitely benefit my entire career. It gives me immense pleasure to acknowledge Dr. K. R. S. Chandrakumar for his valuable guidance and suggestions throughout the years. It is my pleasure to thank Dr. B. N. Jagatap, Director Chemistry Group, Dr. T. Mukherjee, Chairman, and all the member of Doctoral Committee for their encouragement and support.

I would also like to acknowledge my divisional colleagues, Dr. A. K. Samanta, Dr. T. K. Ghanty, Dr. C. N. Patra, Dr. D. K. Maity, Dr. T. Bandopadhyay, Dr. N. Choudhury, Dr. A. K. Pathak, Dr. M. K. Nayak, Dr. M. Sundararajan, Dr. Y. Sajeew, B. Modak and D. Manna for sharing their knowledge and experiences with me. I also like to thank Dr. C. Majumder and Dr. S. Nigam of chemistry division for their valuable discussions. The list of friends can be huge, however, I would like to name few of them, Satyanarayana, Nagaraju, Ramakrishna, Rambabu, Vasu, Murthy, Kiran, Suresh, Rajesh, Suman, Naidu, Dinesh, Sagar, Manoj, Visu, Jagan, Ravikanth, Babu and Manik for their help and wishes.

I wish to express my sincere gratitude to my parents, parents-in-laws, all other family members and all the well wishers for their support and blessings on me. Finally I would like to thank my wife Deepa and my son Haricharan for their support and help.

....Srinivasu

CONTENTS

	Page No
SYNOPSIS	i
LIST OF FIGURES	xii
LIST OF TABLES	xviii
Chapter 1 Introduction	1
1.1 Current energy scenario	2
1.2 Hydrogen: The fuel of the future	4
1.3 Hydrogen generation	6
1.3.1 From fossil resources	6
1.3.2 From renewable resources	7
1.4 Hydrogen storage	12
1.4.1 Metal hydrides	14
1.4.2 Hydrogen storage through physisorption	18
1.5 Hydrogen as a fuel	23
1.6 Computational methods	26
1.6.1 The Schrödinger equation	26
1.6.2 Born-Oppenheimer approximation	27
1.6.3 The variational principle	28
1.6.4 The Hartree-Fock method	29
1.6.5 Density Functional Theory (DFT)	31
1.6.6 The Bloch electrons and plane wave basis set	35
1.7 Scope of the present thesis	37
Chapter 2 Designing g-CN Based Photocatalyst for Hydrogen Generation Through Solar Water Splitting	43
2.1 Introduction	44
2.2 Computational details	45

	2.3 Results and discussion	46
	2.4 Conclusions	58
Chapter 3	Hydrogen Adsorption Properties of Alkali Metal Decorated Cyclic Hydrocarbons (C_nH_n-M)	59
	3.1 Introduction	60
	3.2 Computational details	62
	3.3 Results and discussion	63
	3.3.1 Role of charged surface and the electronic induction effect	63
	3.3.2 Role of aromaticity	73
	3.4 Conclusions	86
Chapter 4	Hydrogen Adsorption Properties of Alkali Metal Decorated Boron Hydrides (B_mH_n-M)	87
	4.1 Introduction	88
	4.2 Computational details	90
	4.3 Results and discussion	91
	4.3.1 Hydrogen adsorption properties of lithium decorated diborene ($B_2H_4Li_2$) and diboryne ($B_2H_2Li_2$)	91
	4.3.2 Hydrogen adsorption in Li-doped <i>closo</i> -boranes	99
	4.4 Conclusions	106
Chapter 5	Electronic Structure and Properties of Boron Hydrides Analogues of Aluminum Hydrides	107
	5.1 Introduction	108
	5.2 Computational details	110
	5.3 Results and discussion	111
	5.3.1 The <i>closo</i> -alanes (Al_nH_{n+2})	111

	5.3.2 The <i>nido</i> -alanes ($\text{Al}_n\text{H}_{n+4}$)	114
	5.3.3 The <i>arachno</i> -alanes ($\text{Al}_n\text{H}_{n+6}$)	118
	5.3.4 The tetra-alanes (Al_4H_m) ($m=6, 8$ and 10)	121
	5.4 Conclusions	124
Chapter 6	Hydrogen Adsorption in Light Metal Decorated Fullerenes Clusters	125
	6.1 Introduction	126
	6.2 Computational details	128
	6.3 Results and discussion	129
	6.3.1 Nanoscale curvature-induced hydrogen adsorption in alkali metal doped carbon nanomaterials	129
	6.3.2 Transition metal decorated porphyrin like porous fullerene: Promising materials for molecular hydrogen adsorption	139
	6.4 Conclusions	146
Chapter 7	Alkali Metal Decorated Two-dimensional Materials as Promising Hydrogen Storage Materials	147
	7.1 Introduction	148
	7.2 Computational details	149
	7.3 Results and discussion	150
	7.3.1 Graphyne and graphdiyne: Promising materials for nanoelectronics and energy storage applications	150
	7.3.2 Hydrogen adsorption in lithium decorated conjugated microporous polymers	158
	7.4 Conclusions	164

Chapter 8	Hydrogen Adsorption in Three-dimensional Porous Materials	165
	8.1 Introduction	166
	8.2 Computational details	168
	8.3 Results and discussion	169
	8.3.1 Tuning the metal binding energy and hydrogen storage in alkali metal decorated MOF-5 through boron doping	169
	8.3.2 Electronic structure and hydrogen adsorption characteristics of supercubane based three- dimensional porous carbon	179
	8.4 Conclusions	187
Chapter 9	First Principles Modelling of New Catalyst for Oxygen Reduction Reaction	188
	9.1 Introduction	189
	9.2 Computational details	191
	9.3 Results and discussion	191
	9.3.1 Transition metal decorated graphyne: An efficient catalyst for oxygen reduction reaction	191
	9.3.2 Silicene: a metal-free catalyst for ORR	197
	9.4 Conclusions	202
Chapter 10	Outlook and Future Explorations	203
	References	209

SYNOPSIS

Supplying safe and uninterrupted energy to the society has always been a challenging issue and has been of major concern particularly in recent times. Worldwide energy demands are drastically increasing day by day due to improved standard of living along with industrial revolutions. At present, nearly 80% of the energy used comes from the fossil fuels like coal, oil and gas which are expected to get depleted with time.¹⁻² If this same trend of fossil fuel usage continues, all the available reserves will be depleted soon and future generations may not have the chance of using fossil fuels for energy applications. Renewable energy is the energy obtained from inexhaustible sources like solar power, wind power, tidal power, etc. The main feature of this renewable energy is that it will not release any polluting gases to the atmosphere.³⁻⁴ At present nearly 75% of the carbon dioxide emissions are fossil fuel-related, and if there is no proper action taken for changing the energy policy, it may become worse in future, thereby ruining the atmosphere.⁵

All these above mentioned facts clearly indicate that new alternative energy sources are required to supplement and eventually replace the fossil fuels. Hydrogen is considered to be a potential alternative to the existing fossil fuels and expected to play a major role in future energy scenario. As nearly 70% of earth's surface is covered with water, we have unlimited source of hydrogen if it can be generated from water. As a fuel, hydrogen has the highest gravimetric energy density of 142 MJ/kg which is at least three times more than that of gasoline (~47 MJ/kg). Another attractive feature of hydrogen energy is its environmental advantages over fossil fuels. With water as the final product of this energy conversion, hydrogen energy can be considered as clean and sustainable energy. However, as it is mentioned, hydrogen is only an energy carrier, but not a source and its cleanness depends on

the technologies used to produce it. One of the important and well explored concepts is the utilization of solar energy to produce hydrogen and use this hydrogen as an energy source.⁵⁻⁶

The so called hydrogen economy covers three functional areas: production, storage, and usage and each of the area have lots of scientific and technological challenges. Nearly 95% of the today's hydrogen is produced from steam reforming technique which is proven to be the cheapest commercial technology for hydrogen production on a large scale.⁷⁻⁸ Another technique used in the initial times to generate hydrogen from fossil resources is the gasification of coal. However, both these methods are not green as they emit the carbon dioxide. An ideal way is to generate hydrogen through water splitting using the sunlight.⁹⁻¹⁰ Hydrogen being very light in weight, the energy density per unit volume is rather less. The two ways of physical storage commonly practised are the storage at high pressure as a gas and liquid hydrogen storage which requires cryogenic temperatures. In gaseous form, even at a pressure of 700 bar, the energy density is just 4.4 MJ/L. On liquefying, the energy density can go to a maximum of 8.0 MJ/L and in both the ways the volumetric energy density is very less as compared to that of gasoline (~36 MJ/L). Apart from energy density, these two methods are neither safe nor cost effective. Another important way is through the adsorption of hydrogen on some solid material with high gravimetric and volumetric densities.¹¹⁻¹⁵ Hydrogen can be directly used as a fuel in cars through a combustion engine. Another more efficient way is through fuel cells which combine hydrogen and oxygen to produce electricity and water.¹⁶⁻¹⁷ The main obstacle to a better performance of the fuel cells is the slow kinetics of the oxygen reduction reaction (ORR) at the cathode. Although platinum (Pt) based catalysts are the best know catalyst for ORR, limited availability and high cost of Pt make the fuel cell very expensive and there is a need to find an alternate non-platinum based catalyst for large scale commercialization of fuel cells.¹⁸⁻¹⁹

In the present study, we have focussed on these three important aspects of the hydrogen economy as discussed above. Using the first principles based electronic structure calculations, we have designed a photo-catalyst based on porous carbon nitride for hydrogen generation through water splitting. For hydrogen storage, we have designed different molecules and materials especially the light metal decorated materials which can adsorb hydrogen in molecular form. We have also designed new catalyst materials for the oxygen reduction reaction. The overall thesis is composed of ten chapters and the brief discussion of each chapter is given below.

Chapter 1: This chapter deals with a general introduction about the current energy scenario, need of alternate energy source, hydrogen economy, hydrogen generation, hydrogen storage and fuel cells. It also includes discussion on the theoretical background and the computational methods used throughout the thesis.

Chapter 2: This chapter deals with the studies on designing a photo-catalyst for hydrogen generation by water splitting using the sunlight. Graphitic carbon nitride ($g\text{-C}_3\text{N}_4$) is proposed to be one of the possible metal-free catalysts for visible light driven water splitting.²⁰ However, this material is reported to have a very poor quantum yield of $\sim 0.1\%$ which is attributed to the high recombination rate of electron-hole pairs. In this study, we have explored another carbon nitride, hexagonal carbon nitride with 1:1 stoichiometry ($h\text{-CN}$) as a new photo-catalyst for solar water splitting. The calculated band structure results have shown that though the hydrogen oxidation and oxygen reduction potentials are within the band gap, the band gap is large and not useful for adsorption of the visible portion of the solar spectra. We have tried to tune the band gap of this material through doping of foreign elements. We have carried out two different kinds of doping viz. (1) substitutional doping

with non-metal elements like oxygen, sulphur and phosphorus and (2) doping with different metal atoms which can induce some intermediate energy levels thereby decreasing the band gap.

Chapter 3: This chapter is concerned with studies on the hydrogen adsorption properties of small organic molecules decorated with alkali metal atoms, C_nH_n-M .²¹⁻²² We found that the simple van der Waals surfaces are not capable of holding the molecular hydrogen. However, the presence of an ionic site is found to enhance the hydrogen adsorption energy by many folds. We have taken C_6H_6 as the model system since it is the main building unit in all the carbon nanomaterials and decorated with alkali metal ions. We have demonstrated that creating a charged surface on the model system by doping the alkali metal cations can improve the hydrogen adsorption energy significantly. We have also shown that, introduction of a functional group in the model system affects the hydrogen adsorption and the binding of the alkali metal cations to the organic system significantly, due to the electronic induction effects. Further, we have extended the present single hexagonal ring model study to the planar as well as curved coronene carbon surface and it was observed that the ionic surface with a significant degree of curvature enhances the hydrogen adsorption significantly. Apart from C_6H_6 , we have also studied other systems like C_4H_4 , C_5H_5 and C_8H_8 . Being electron deficient with respect to the corresponding Hückel aromatic systems, these molecules are found to bind the alkali metal atoms more strongly and the metal site becomes cationic in nature indicating an electron transfer from metal to the carbon surface. These metal sites are found to adsorb hydrogen more efficiently.

Chapter 4: This chapter includes the results of studies on hydrogen adsorption properties on alkali metal decorated boron hydrides.²³⁻²⁴ For achieving high gravimetric densities of

adsorbed hydrogen, materials made up of low molecular weight systems like carbon, boron, etc. are more suitable. Chemistry of boron hydrides is relatively new in comparison to hydrocarbon chemistry. B_2H_6 is the boron analogue of ethane which is a well known electron deficient molecule. Lithium complexes of dihydrodiborate dianion ($B_2H_2Li_2$) and tetrahydrodiborate dianion ($B_2H_4Li_2$) have been considered and it was found that in both these complexes, the Li sites are cationic in nature, and thus can bind molecular hydrogen through ion-quadrupole and ion-induced dipole interactions. We have also modelled a one-dimensional nanowire with $C_6H_4B_2Li_2$ as the repeating unit, which was found to adsorb three hydrogen molecules resulting into a gravimetric density of 9.68 wt% of hydrogen. In another study, We have shown that the hexaborane (6) dianion ($B_6H_6^{2-}$) can form a stable complex (salts) with a highly electropositive alkali metal cation (Li^+). Each Li is found to adsorb a maximum of three hydrogen molecules which corresponds to a gravimetric density of 12 wt %. We have also designed a model three-dimensional material with lithium-doped borane as the building block and $-C\equiv C-$ as a linking agent. The molecular hydrogen adsorption in this designed material corresponds to a gravimetric density of around 7.3 wt %.

Chapter 5: This chapter deals with the interpretation of new aluminium hydrides that are analogues of boron hydrides.²⁵ Alkali metal alanates are found to be attractive for hydrogen storage which undergo dehydrogenation in the temperature range of 200-300°C to give aluminium metal and the corresponding alkali metal hydrides along with hydrogen. Although aluminum and boron belong to the same group in the periodic table, there is a large difference in the chemistry of their hydrides. Aluminum hydride chemistry is limited to very few systems such as AlH_3 , its dimer Al_2H_6 , its polymeric form $(AlH_3)_n$, AlH_4^- , and its alkali alanates like $LiAlH_4$, whereas boron has a great history of its hydride chemistry. AlH_3 can be a potential hydrogen storage material as it contains 10% hydrogen and has a theoretical

hydrogen density of 148 g/L. We have carried out a systematic study on the electronic structure and properties of these aluminum hydrides. Here, we have studied different classes of hydrides, viz., *closo* ($\text{Al}_n\text{H}_{n+2}$), *nido* ($\text{Al}_n\text{H}_{n+4}$), and *arachno* ($\text{Al}_n\text{H}_{n+6}$), similar to the boranes. All these clusters have considerably large HOMO-LUMO gaps, low electron affinities, large ionization potentials, and also large enthalpy and free energy of atomization. These exceptional properties can be indicative of their pronounced stability, and hence it can be expected that these complexes can indeed be observed experimentally.

Chapter 6: In this chapter, we have discussed our results on the hydrogen adsorption on metal decorated fullerenes. In one of the studies, we have demonstrated the effect of curvature present in the carbon fullerenes on the reactivity towards the alkali metals and hydrogen adsorption in these metal decorated fullerenes.²⁶ For this study, we have considered fullerenes of different sizes, viz. C_{20} , C_{28} , C_{32} , C_{36} , C_{60} , and C_{70} and the results reveal that the metal binding energy is high in the fullerenes with high curvature. The higher reactivity of the surface, associated with the maximum curvature, has been attributed to the weakening of the π -conjugation due to bending of the carbon surface which forces the system to have a quasi- sp^2 - sp^3 hybridization. In another study, we have considered the transition metal decorated porphyrin-like porous fullerene, $\text{C}_{24}\text{N}_{24}$ for hydrogen adsorption. Transition metal decorated carbon materials like fullerenes and nanotubes have been studied extensively for hydrogen adsorption applications. However, the weaker metal binding energy in these materials makes them unsuitable for making a stable hydrogen storage material. Here, we have designed a new porous fullerene generated through truncated substitutional doping of 24 carbon atoms in C_{60} by 24 nitrogen atoms, and the resulting fullerene contains six N_4 cavities.²⁷ This fullerene is found to bind with transition metal atoms (Sc, Ti, and V) very strongly, and the binding energies are found to be considerably larger than (nearly double)

the corresponding metal cohesive energies. These transition metal sites are found to adsorb molecular hydrogen through well-known Kubas-type interactions. The calculated adsorption energies of molecular hydrogen around the different metal sites are found to be in the range of -9.0 to -3.0 kcal/mol, which is considered to be the enthalpy range required for hydrogen storage under ambient condition.

Chapter 7: This chapter deals with the studies on two-dimensional carbon materials and their energy storage properties. We have carried out detailed studies on the newly emerging 2D carbon allotropes, viz. Graphyne and graphdiyne.²⁸ Our results reveal that the band gap in these conjugated carbon materials can be tuned by changing the length of the acetylenic linking chain. We could show that both graphyne and graphdiyne can host a large amount of lithium with considerably higher lithiation potentials and specific capacities, which indicates that these materials can be used to design efficient anode materials for lithium batteries. Each lithium atom in these metal-dispersed materials is found to carry nearly one unit positive charge and bind molecular hydrogen with considerably improved adsorption energies. We have also investigated expanded porous two-dimensional conjugated microporous polymers (CMPs) based on benzene, 1,3,5-triethynyl (CMP-1) and benzene, 1,3,5-tributadiyne (HCMP-1) decorated with lithium metal for efficient hydrogen adsorption.

Chapter 8: In this chapter we have elaborated the studies on three-dimensional (3D) porous materials as efficient hydrogen storage materials. Among the many materials investigated, porous materials like MOFs and COFs are found to be promising materials for hydrogen storage because of their porous and robust nature and also exceptionally high specific surface areas as well as pore volumes. In these materials, hydrogen binds through van der Waals interaction and the adsorption enthalpies are typically in the range of 1.0 to 1.5 kcal/mol.

Various approaches have been pursued for improving the hydrogen adsorption characteristics in these materials. One such strategy that has been of recent interest is the metal ion decoration and in fact Li-decorated MOF-5 has been shown to have significant improvement in hydrogen adsorption. The Li atom is positioned on top of the six-membered carbon rings and because of the aromatic nature of the ring, the binding energy of the metal atom is poor. We have proposed that the binding energy of metal with MOF-5 can be improved by disturbing the aromatic nature of the linker group through the substitution of its two carbon atoms with two boron atoms, thus making it electron-deficient.²⁹ In another study, we have modelled super-cubane based three-dimensional carbon allotropes with different pore sizes and densities.³⁰ The basic supercubane structure is expanded through the insertion of acetylinic and diacetylinic units between both inter- and intra-cubane C–C bonds leading to more variety of porous carbon materials. As these designed structures are associated with high porosity and reactive carbon sites, we have investigated their hydrogen adsorption properties and it is observed that the expanded supercubanes can adsorb hydrogen with a gravimetric density of ~2.0 wt %.

Chapter 9: This chapter deals with the design of a new catalyst for the oxygen reduction reaction (ORR). The ORR at the cathode of the fuel cell is known to be the main limiting factor in the fuel cells especially at low temperature. Though the platinum (Pt) based catalysts are the best known catalyst for ORR, limited availability and high cost of Pt make the fuel cell very expensive and there is a need to find an alternate non-platinum based catalyst for large scale commercialization of fuel cells. We have studied the catalytic activity of the transition metal (Fe, Co and Ni) decorated graphyne towards the ORR. The calculated results reveal that the Fe and Co complexes are active whereas the Ni decorated system is almost inert. Between the Fe and Co decorated systems, Fe decorated system is more reactive. In

acid medium, both Iron and Cobalt decorated systems are observed to follow a more efficient four electron path. In alkaline medium, the reduction on Iron decorated system is through a four electron path while in Cobalt system it is through a two electron path with the formation of hydroperoxide anion. In another study, we have shown that the silicene, silicon analogue of graphene can be a metal free catalyst for ORR. We have studied the step by step mechanism of ORR on both the single layer and bi-layer silicene. The calculated results show that silicene can be an effective metal free catalyst for ORR.

Chapter 10: This chapter consists of conclusions and discussion on future directions. This gives a brief outline about the possible outcomes and future directions that can be charted out from the present studies on designing new materials for hydrogen energy applications which have been discussed in the present work.

References

- (1) Lewis, N. S.; Nocera, D. G. *Proc. Natl. Acad. Sci.*, **2006**, *103*, 15729.
- (2) <http://www.iea.org/publications/freepublications/publication/kwes.pdf>
- (3) Bajpai, P.; Dash, V. *Renewable Sustainable Energy Rev.* **2012**, *16*, 2926.
- (4) Dillon, A. C. *Chem. Rev.* **2010**, *110*, 6856.
- (5) Armaroli, N.; Balzani, V. *Chem. Asian J.* **2011**, *6*, 768.
- (6) Mazloomi, K.; Gomes, C. *Renewable Sustainable Energy Rev.* **2012**, *16*, 3024.
- (7) Christopher, K.; Dimitrios, R. *Energy Environ. Sci.*, **2012**, *5*, 6640.
- (8) www.cleanenergystates.org
- (9) Bard, A. J.; Fox, M. A. *Acc. Chem. Res.*, **1995**, *28*, 141.
- (10) Bak, T.; Nowotny, J.; Rekas, M.; Sorrell, C.C. *Int. J. hydrogen energy.* **2002**, *27*, 991.
- (11) Schlapbach, L.; Züttel, A. *Nature* **2001**, *414*, 353.
- (12) Züttel, A.; Remhof, A.; Borgschulte, A.; Friedrichs, O. *Phil. Trans. R. Soc. A* **2010**, *368*, 3329.
- (13) Patchkovskii, S.; Tse, J. S.; Yurchenko, S. N.; Zhechkov, L.; Heine, T.; Seifert, G. *Proc. Natl. Acad. Sci.* **2005**, *102*, 10439.
- (14) Lubitz, W.; Tumas, W. *Chem. Rev.* **2007**, *107*, 3900.
- (15) Coontz, R.; Hanson, B. *Science* **2004**, *305*, 957.
- (16) Winter, M.; Brodd, R. J. *Chem Rev.* **2004**, *104*, 4245.
- (17) Carrette, L.; Friedrich, K. A.; Stimming, U. *Fuel cells* **2001**, *1*, 5.
- (18) Steele, B. C. H.; Heinzel, A. *Nature* **2001**, *414*, 345.
- (19) Debe, M. K. *Nature* **2012**, *486*, 43-51.
- (20) Wang, X.; Maeda, K.; Thomas, A.; Takanabe, K.; Xin, G.; Carlsson, J. M.; Domen, K.; Antonietti, M. *Nat. Mater.* **2008**, *8*, 76.

- (21) Srinivasu, K.; Chandrakumar, K. R. S.; Ghosh, S. K. *Phys. Chem. Chem. Phys.*, **2008**, *10*, 5832.
- (22) Srinivasu, K.; Chandrakumar, K. R. S.; Ghosh, S. K. *ChemPhysChem* **2009**, *10*, 427.
- (23) Srinivasu, K.; Ghosh, S. K. *Int J Hydrogen Energy* **2011**, *36*, 15681.
- (24) Srinivasu, K.; Ghosh, S. K. *J. Phys. Chem. C* **2011**, *115*, 1450.
- (25) Srinivasu, K.; Chandrakumar, K. R. S.; Ghosh, S. K. *J. Phys. Chem. A* **2010**, *114*, 12244.
- (26) Chandrakumar, K. R. S.; Srinivasu, K.; Ghosh, S. K. *J. Phys. Chem. C* **2008**, *112*, 15670.
- (27) Srinivasu, K.; Ghosh, S. K. *J. Phys. Chem. C* **2012**, *116*, 25184.
- (28) Srinivasu, K.; Ghosh, S. K. *J. Phys. Chem. C* **2012**, *116*, 5951.
- (29) Srinivasu, K.; Ghosh, S. K. *J. Phys. Chem. C* **2011**, *115*, 16984.
- (30) Srinivasu, K.; Ghosh, S. K. *J. Phys. Chem. C* **2012**, *116*, 25015.

Figure number	Figure Caption	Page number
Figure 1.1.	Projected world energy consumption, 1990-2035 (quadrillion Btu)	2
Figure 1.2	Projected world energy consumption by fuel, 1990-2035	3
Figure 1.3	World energy-related carbon dioxide emissions by fuel, 1990-2035	3
Figure 1.4	Working principle of the Photo electrochemical cell	10
Figure 1.5	Comparison of the size of hydrogen tank with different way of storage	13
Figure 1.6	Schematic representation of PEMFC and AFC.	24
Figure 2.1	Optimized geometries of the (a) unit cell and (b) 3 x 3 x 1 super cell of g-CN along with its band structure plot using (c) PBE and (d) HSE06 methods and the band decomposed charge density plot of (e) highest valance and (f) lowest conduction states	47
Figure 2.2	Optimized unit cell and super cell structures of different g-CN nanotubes	50
Figure 2.3	Optimized unit cell, supercell and band dispersion plots of three different CNRs	51
Figure 2.4	Optimized supercell structures of double layer g-CN with (a) AA stacking and (b) AB stacking along with the band structure of AB double layer from (c) PBE and (d) HSE06 functionals	53
Figure 2.5	Optimized supercell structures of tri-layer g-CN with (a) ABA and (b) ABC stacking along with the band structure of ABC g-CN from (c) PBE and (d) HSE06 methods	54
Figure 2.6	Optimized unit cell geometries of the boron substituted g-CN with boron replacing the (a) nitrogen atom and (b) carbon atom	56
Figure 2.7	Optimized unit cell structures of g-CN doped with (a) Oxygen, (b) Sulphur and (c) Phosphorous and along with their (d) optical spectra and the (e) band structure (HSE06 functional) of phosphorous doped g-CN	57

Figure 2.8	(a) Optimized supercell structure of transition metal decorated g-CN and (b) band structure of Fe decorated g-CN.	58
Figure 3.1	Interaction of molecular hydrogen with (a) Li^+ -doped $[\text{C}_6\text{H}_6\text{Li}^+(\text{H}_2)_n, n=1-4]$ and (b) Na^+ -doped $[\text{C}_6\text{H}_6\text{Na}^+(\text{H}_2)_n, n = 1-6]$ model system	66
Figure 3.2	Variation of binding energy with increase in the number of hydrogen molecules adsorbed at the cationic site in (a) $\text{C}_6\text{H}_6\text{Li}^+$ and (b) $\text{C}_6\text{H}_6\text{Na}^+$.	67
Figure 3.3	Interaction of H_2 with the alkali-metal-cation-doped benzene ring and its derivatives.	71
Figure 3.4	Modeling the hydrogen adsorption in the cation-encapsulated (endohedral) model system	72
Figure 3.5	Equilibrium geometries of C_nH_n ($n=4, 5, 6$, and 8) molecular systems. b) Interaction of molecular hydrogen with the C_nH_n molecular systems. I.E.=interaction energy	73
Figure 3.6	Charge density plots of the sodium-doped C_nH_n molecular complexes. b) ELF plots of the C_nH_n molecular system (contour value=0.7). c) ELF plots of the $\text{C}_n\text{H}_n\text{-Na}$ molecular system	76
Figure 3.7	Equilibrium geometries of $\text{C}_4\text{H}_4\text{-Na}(\text{H}_2)_m$ ($m=0-6$)	80
Figure 3.8	Equilibrium geometries of $\text{C}_5\text{H}_5\text{-Na}(\text{H}_2)_m$ ($m=0-6$).	81
Figure 3.9	Equilibrium geometries of $\text{C}_8\text{H}_8\text{-Na}(\text{H}_2)_m$ ($m=0-5$).	81
Figure 3.10	Variation of binding energy with increase in number of hydrogen molecules in a) $\text{C}_4\text{H}_4\text{-Na}$, b) $\text{C}_5\text{H}_5\text{-Na}$, and c) $\text{C}_8\text{H}_8\text{-Na}$ complexes	83
Figure 3.11	Optimized geometry of the (b) model oligomeric structure and (b) its hydrogenated one	85
Figure 4.1	(a) Optimized geometries of $\text{B}_2\text{H}_4^{2-}$ and $\text{B}_2\text{H}_4\text{Li}_2$. (b).HOMO and HOMO-3 orbital pictures of $\text{B}_2\text{H}_4\text{Li}_2$	92

Figure 4.2	(a) Optimized geometries of $B_2H_2^{2-}$ and $B_2H_2Li_2$ (b). HOMO and HOMO-1 orbital pictures of $B_2H_2Li_2$	94
Figure 4.3	Optimized geometries of $B_2H_4Li_2(H_2)_{2n}$ (n=1-4)	95
Figure 4.4	Optimized geometries of $B_2H_2Li_2(H_2)_{2n}$ (n=1-4)	97
Figure 4.5	1 x 1 x 3 supercell structures of optimized one dimensional nanowire with (a) $C_6H_4B_2Li_2$ as monomer and (b) its hydrogen adsorbed counterpart	98
Figure 4.6	Equilibrium geometry of $B_6H_6^{2-}$	99
Figure 4.7	Equilibrium geometries for two different isomers of $B_6H_6Li_2$	100
Figure 4.8	Equilibrium geometries of $B_6H_6Li_2(H_2)_n$ (n=1-3)	102
Figure 4.9	Variation of (a) HOMO-LUMO gap and (b) charge on lithium atom with number of hydrogen molecules in $B_6H_6Li_2(H_2)_n$ (n=1-3)	103
Figure 4.10	Three dimensional solid constructed by using B_6Li_2 units as building blocks and $C\equiv C$ as linker.	104
Figure 4.11	Three dimensional solid constructed by using $B_6Li_2(H_2)_3$ units as building blocks and $-C\equiv C-$ as linker	105
Figure 5.1	Optimized structures of <i>closo</i> -alanes, Al_nH_{n+2} (n=5, 6, 8, 10 and 12) as obtained by MP2 method. The symmetries are given in parenthesis.	112
Figure 5.2	Optimized structures of <i>nido</i> -alanes, Al_nH_{n+4} (n=5, 6, 8, 10 and 11) as obtained by MP2 method. The symmetries are given in parenthesis	115
Figure 5.3	Optimized structures of <i>arachno</i> -alanes, Al_nH_{n+6} (n= 6, 8 and 10) as obtained by MP2 method. The symmetries are given in parenthesis	118
Figure 5.4	Optimized structures of <i>tetra</i> -alanes, Al_4H_n (n= 6, 8 and 10) as obtained by MP2 method. The symmetries are given in parenthesis	122
Figure 6.1	Effect of curvature on the (A) charge and (B) binding energy of a sodium atom interacting with intradeformed concave and convex benzene models	130
Figure 6.2	Electron Charge density distribution in Na- C_6H_6 with the bending angle: (A)10° (B)35°	130

Figure 6.3	Molecular hydrogen adsorption in alkali metal atom doped fullerenes (only at the 6m-ring). X refers to the Na and K atoms	138
Figure 6.4	Schematic presentation of truncation substitutional doping of C_{60} to generate $C_{24}N_{24}$	140
Figure 6.5	Band decomposed charge density iso-surfaces of (a) highest valence band and (b) lowest conduction band of $C_{24}N_{24}$	140
Figure 6.6	Optimized geometries of $C_{24}N_{24}TM_6$ (TM=Sc, Ti and V)	141
Figure 6.7	Calculated total density of states (Total) and projected density of states on nitrogen (N), carbon (C) and titanium (Ti) atoms of $C_{24}N_{24}Ti_6$	142
Figure 6.8	Optimized geometries of $C_{24}N_{24}Sc_6(H_2)_{6n}$ (n=1-4)	143
Figure 6.9	Calculated total density of states (Total) and projected density of states on titanium (Ti) and hydrogen (H) atoms of $C_{24}N_{24}Ti_6(H_2)_6$	144
Figure 7.1	3x3x1 super cell of the optimized geometries of (a) graphyne (b) graphdiyne and the calculated band structure of (c) graphyne and (d) graphdiyne	151
Figure 7.2	The optimized 3x3x1 super cell geometries of (a) graphyne-Li (b) graphyne-Li ₂ (c) graphdiyne-Li and (d) graphdiyne-Li ₂	154
Figure 7.3	Optimized (a) primitive cell and (b) 3x3x1 super cell structures of graphdiyne-Li ₈	155
Figure 7.4	Optimized primitive cell structures of hydrogenated lithium decorated graphyne	156
Figure 7.5	Optimized structures of the unit cell and the 2 x 2 x 1 super cell of (i & ii) CMP-1 and (iii & iv) HCMP-1 respectively	159
Figure 7.6	Band structure plots along with the partial density of states of (a) CMP-1 and (b) HCMP-1 as calculated from the DFT-PBE method	160
Figure 7.7	Optimized unit cell structures of CMP-1-Li ₄ and its hydrogenated species CMP-1-Li ₄ (H ₂) _{4n} (n=1-3)	161
Figure 7.8	Optimized unit cell structures of HCMP-1-Li ₄ and its hydrogenated species HCMP-1-Li ₄ (H ₂) _{4n} (n=1-3)	163

Figure 8.1	Optimized structure of $C_4B_2H_6$ (b) Optimized structure of $C_4B_2H_6^{2-}$ and (c) Variation of NICS value along the perpendicular direction from the centre of the rings of $C_4B_2H_6$, $C_4B_2H_6^{2-}$ and C_6H_6	169
Figure 8.2	Optimized structures of $C_4B_2H_6M_2$ (M=Li, Na and Mg) and $C_4B_2H_6$ -Mg	170
Figure 8.3	Optimized structures of $C_4B_2H_6Li_2(H_2)_{2n}$ (n=1-4)	172
Figure 8.4	Optimized structures of $C_4B_2H_6Na_2(H_2)_{2n}$ (n=1-6)	175
Figure 8.5	Optimized structures of two isomers of $C_4B_2H_6(COOH)_2$	176
Figure 8.6	Optimized primitive cell structure of lithium decorated boron substituted MOF-5 with the formula unit $Zn_4O(C_4B_2H_4Li_2(COO)_2)_3$	177
Figure 8.7	Conventional cell structure of lithium decorated boron substituted MOF-5.	177
Figure 8.8	Conventional cell structure of hydrogen adsorbed lithium decorated modified MOF-5.	178
Figure 8.9	Optimized unit cell structures of (a) C_{12} , (b) C_{32} , (c) C_{48} , (d) C_{80} , (e) C_{96} , (f) C_{128} , and (g) C_{144}	180
Figure 8.10	Calculated band structure along with the density of states (DOS) through PBE functional (a) C_{16} , (b) C_{32} and (c) C_{48} respectively	182
Figure 8.11	Phonon dispersion plot along the high symmetry k -path of the first Brillouin zone of the unit cell (a) C_{16} (b) C_{32} , (c) C_{48} , (d) C_{80} , (e) C_{96} and (f) C_{128}	184
Figure 8.12	Variation of free energy of different carbon allotropes as a function of temperature	185
Figure 8.13	Optimized 2 x 2 x 2 super cell structures of hydrogenated C_{32} with four and six molecular hydrogens per unit cell	186
Figure 8.14	Optimized unit cell structures of C_{144} with (a) 18 and (b) 24 hydrogen molecules per unit cell	186
Figure 9.1	Optimized geometries of 3 x 3 x 1 super cell structures of (a) GY-Fe (b) GY-Co and (c) GY-Ni	192
Figure 9.2	Optimized unit cell structures of oxygen adsorbed on (a) GY-Fe (b) GY-Co and (c) GY-Ni	193

Figure 9.3	Optimized unit cell structures of (a) GY-Co-OOH (b) GY-Co-O-OH ₂ (c) GY-Co-OH-OH ₂ and (d) GY-Co-OH ₂ -OH ₂	194
Figure 9.4	Optimized unit cell structures of (a) GY-Fe-OOH ⁻ and (b) GY-Co-OOH ⁻	196
Figure 9.5	Optimized geometries of the 3x3x1 super cell in (a) top view and (b) side view along with the band dispersion plot of the silicene	197
Figure 9.6	Optimized super cell structures of silicene double layer in AA and AB stacking mode.	198
Figure 9.7	Optimized cell structures of O ₂ adsorbed on single layer and bilayer silicene	199
Figure 9.8	Possible intermediate in ORR on silicene single layer	200
Figure 9.9	Possible intermediates in ORR on double layer silicene	201

Table number	Table caption	Page number
Table 1.1	Physical and chemical properties of hydrogen, methane and petrol	5
Table 2.1	The calculated band structure results of different g-CN nanostructures from PBE and HSE06 methods.	48
Table 3.1	Interaction of molecular hydrogen with the model system and its derivatives	65
Table 3.2	Interaction of hydrogen molecules with the alkali metal cation (Li^+ and Na^+) doped model systems	67
Table 3.3	Effect of substituents on the metal and hydrogen interaction	70
Table 3.4	Binding energy of molecular hydrogen interacting with the cation encapsulated (endohedral) model system	72
Table 3.5	Interaction of sodium metal with the organic molecular systems, C_nH_n	75
Table 3.6	The nucleus-independent chemical shifts (NICS) and the harmonic oscillator model of aromaticity (HOMA) values of the sodium metal atom doped and undoped molecular systems, calculated by B3LYP/6-31+G(d,p) method	78
Table 3.7	Interaction of molecular hydrogen with $\text{C}_4\text{H}_4\text{-Na}$ complex	82
Table 3.8	Interaction of molecular hydrogen with $\text{C}_5\text{H}_5\text{-Na}$ complex	82
Table 3.9	Interaction of molecular hydrogen with $\text{C}_8\text{H}_8\text{-Na}$ complex	83
Table 4.1	Interaction energies, charge on lithium atoms and HOMO-LUMO gaps of lithiated B_2H_2 , B_2H_4 and their hydrogen adsorbed complexes	96
Table 4.2	Calculated parameters for Interaction of Li^+ ions with $\text{B}_6\text{H}_6^{2-}$ and molecular hydrogen with $\text{B}_6\text{H}_6\text{Li}_2$	101
Table 5.1	Vertical ionization potential (IP_{vert}), adiabatic ionization potential (IP), vertical electron affinity (EA_{vert}) and adiabatic electron affinity (EA) (in eV) of <i>closo</i> , <i>nido</i> , <i>arachno</i> and <i>tetra</i> alanes.	116

Table 5.2	Enthalpy of atomization (ΔH_a), free energy of atomization (ΔG_a) calculated at 298 K, and the HOMO-LUMO gap of <i>closo</i> , <i>nido</i> , <i>arachno</i> and <i>tetra</i> alanes	119
Table 6.1	Effect of Intrabending on the Binding of a Sodium Atom with a Benzene Ring	129
Table 6.2	Effect of intra-bending on the binding of hydrogen molecule with Benzene ring	131
Table 6.3	Approximate diameter (\AA units) and curvature (in degree) of the fullerenes	132
Table 6.4	HOMO-LUMO gap of the pristine and alkali metal doped fullerenes C_nX ($n=20, 28, 32, 36, 60, 70$ and $X=Li, Na$ and K) (in atomic units)	133
Table 6.5	Geometrical parameters (\AA), binding energy (kcal/mol) and Mulliken charge (atomic units) of the alkali atoms with different fullerene molecules	136
Table 6.6	Binding energy (in kcal/mol) of the hydrogen molecules interacting with alkali metal doped fullerene molecules C_nX ($n=20, 28, 32, 36, 60, 70$ and $X=Li, Na$ and K)	137
Table 6.7	Calculated metal binding energies (per metal atom) in kcal/mol, bond lengths in \AA and charge on metal atoms in a.u	141
Table 6.8	Calculated hydrogen interaction energies (per hydrogen molecule) in kcal/mol and metal-hydrogen bond lengths in \AA	144
Table 7.1	Calculated cell parameter and lithium interaction energy with graphyne (C_{12}) and graphdiyne (C_{18})	153
Table 7.2	Calculated lithiation potential vs. Li/Li^+ for lithium dispersed graphyne and graphdiyne in Volts	155
Table 7.3	Calculated cell parameters, different C-C bond lengths and the band gaps of CMP-1 and HCMP-1 using DFT with both PBE and B3LYP functionals	158

Table 7.4	The calculated hydrogen adsorption energies per H ₂ , shortest Li-H and H-H bond lengths of the hydrogenated species of lithiated CMP-1 and HCMP-1	162
Table 8.1	The calculated interaction energy, charge on metal, HOMO-LUMO gap and NICS(0) values in C ₄ B ₂ H ₆ -M _n (M=Li, Na and Mg)	171
Table 8.2	The calculated interaction energy, charge on metal and HOMO-LUMO gap of C ₄ B ₂ H ₆ M ₂ (H ₂) _n (M=Li and Na)	173
Table 8.3	Calculated formation energies per atom, cell parameters, densities and CCC cubane corner bond angles of the different supercubane based carbon materials	181
Table 8.4	Energy of valence band maxima (VBM), conduction band minima (CBM) and the band gap values calculated using PBE and B3LYP functionals for all the modeled 3D-carbon materials. All energy values are reported in eV	183
Table 9.1	Graphyne-TM binding energy, O ₂ adsorption energy, metal-carbon distance, metal-oxygen distance and O-O bond length calculated through the PBE method	192
Table 9.2	Calculated free energy changes (in eV) for different intermediate steps of ORR on GY-Fe and GY-Co in both acid and alkaline medium	196

CHAPTER 1

Introduction

&

Theoretical background

1.1 Current energy scenario:

Energy is considered to be the key factor in deciding the social and economic development of any country. Worldwide, especially in the developing countries, energy sector has been given prime importance in view of the rapidly increasing energy demands due to the day by day improved standards of living along with the industrial revolutions.¹ According to the International Energy Outlook 2013 (IEO2013)² published by U.S. Energy Information Administration, the world energy consumption is expected to grow by 56% from 2010 to 2040 and much of the growth is expected from the countries outside the Organization for Economic Cooperation and Development (non-OECD nations) as shown in Figure 1.1.

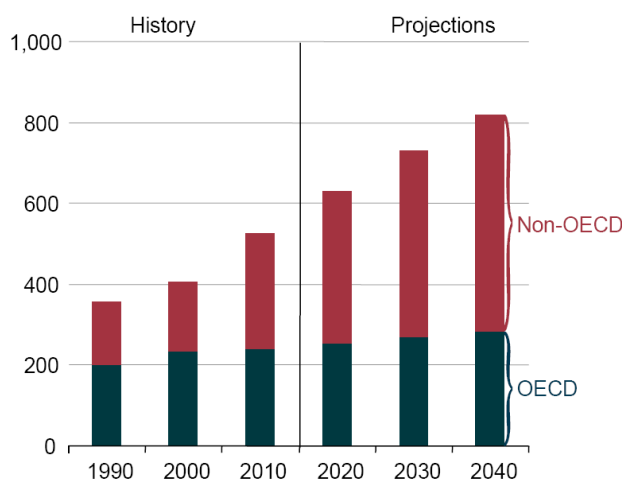


Figure 1.1. Projected world energy consumption, 1990-2035 (quadrillion Btu)

All the different forms of primary energy can be classified into two main schemes, viz. renewable and non-renewable forms of energy. Renewable energy is the energy obtained from a source which is inexhaustible like solar power, wind power, tidal power etc. The main feature of this renewable energy is that it will not release any polluting gases to the atmosphere. Non-renewable energy includes all kinds of fossil fuels like oil, coal, natural gas etc., which are expected to get depleted with time. According to the IEO report,² majority of the world energy consumption is from non-renewable forms of energy as shown in Figure 1.2. If this same trend of fossil fuel usage continues, all the available reserves will be

depleted soon and future generations may not have the chance of using fossil fuels for their energy applications. Though the exact estimation of the presently existing reserves of fossil energy resources is difficult as it is always possible to exploit new reserves, the fact is that fossil fuel reserves are limited.

Fossil fuels are claimed to be the major contributor to the worldwide rise in the global temperatures. The concentrations of carbon dioxide are steadily growing due to the industrial revolution.³⁻⁵ Carbon dioxide is known to absorb the thermal radiation emitted from earth's surface and re-radiate in all directions through the famously known greenhouse effect which leads to a higher temperature of the atmosphere. It is a well known fact that the major source for the carbon dioxide emission is the combustion of fossil fuels which ultimately leads to the adverse changes in climate. If we observe the world wide carbon dioxide emissions from different fossil fuels, coal is contributing the maximum followed by natural gas and liquids as shown in Figure 1.3. CO₂ is found to contribute about 61% to the greenhouse effect and is the major greenhouse gas. Though the change from coal to oil and then to natural gas has resulted in less CO₂ release per unit of energy consumption, it is desirable to go for a complete carbon free energy system. At present nearly 75% of the carbon dioxide emissions are fossil fuel-related, and if no proper action is taken in changing the energy policy, it may still get accelerated in future thereby ruining the atmosphere.

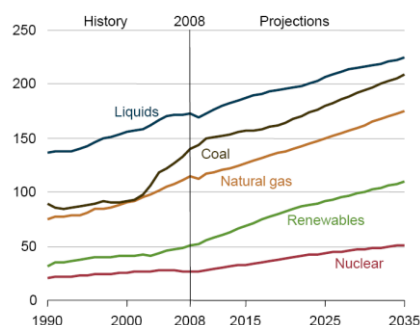


Figure 1.2. Projected world energy consumption by fuel, 1990-2035 (quadrillion Btu)

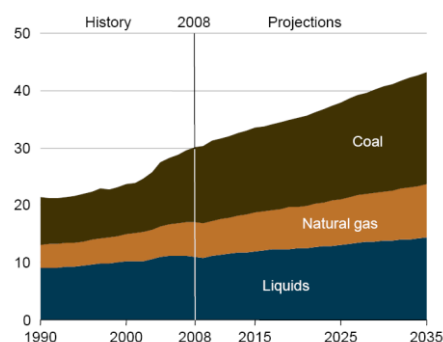


Figure 1.3. World energy-related carbon dioxide emissions by fuel, 1990-2035 (billion metric tons)

1.2 Hydrogen: The fuel of the future

Keeping attention on all the above mentioned facts, it becomes necessary to look for an alternate energy system which is sustainable and environmental friendly. Hydrogen is accepted as a potential alternative to the existing fossil fuels and is expected to play a major role in future energy scenario.⁶⁻¹² Hydrogen is the lightest and simplest element with one electron and one proton and is the first element in the periodic table. Hydrogen was first discovered by Henry Cavendish in 1766, and named in 1783 by Antoine Lavoisier. The origin of the name "Hydrogen" came from the Greek words "hydro" and "genes" having the meaning of "water" and "generator", since water is the produced when hydrogen burns. Since hydrogen does not exist in natural state on earth's surface and has to be manufactured from hydrogen rich compounds, it is a carrier of energy, and not the source. An ideal way for achieving sustainable energy is through the use of solar energy to convert water into hydrogen and oxygen. As nearly 70% of earth's surface is covered with water, we have unlimited source of hydrogen if it can be generated from water. As a fuel, hydrogen has its advantages as well as drawbacks. Hydrogen has the highest gravimetric energy density of 142 MJ/kg which is at least three times that of gasoline (~47 MJ/kg) and some of the importance properties of hydrogen are compared with that of methane and petrol in Table 1.1.¹³ Another attraction of hydrogen energy is its environmental advantages over fossil fuels.

With water as the final product of the energy conversion, hydrogen energy can be considered to be clean and sustainable energy. However, as already mentioned, hydrogen is an energy carrier, and not a source and hence its cleanness depends on the technologies used to produce it. The so called hydrogen economy has mainly three important steps viz. (1) Hydrogen generation, (2) storage and (3) end-usage. Another important hurdle in developing the hydrogen economy is its safe and economic storage. Hydrogen being very light in weight,

the energy density per unit volume is very less. The two ways of physical storage being practised are the storage at high pressure as a gas and liquid hydrogen storage which requires cryogenic temperatures.

Table 1.1. Physical and chemical properties of hydrogen, methane and petrol

Property	Hydrogen	Methane	Petrol
Lower heating value (kWh kg ⁻¹)	33.33	13.9	12.4
Self-ignition temperature (°C)	585	540	228-501
Flame temperature (°C)	2045	1875	2200
Ignition limits in air (Vol%)	4-75	5.3-15	1.0-7.6
Minimal ignition energy (mW s)	0.02	0.29	0.24
Flame propagation in air (m s ⁻¹)	2.65	0.4	0.4
Diffusion coefficient in air (cm ² s ⁻¹)	0.61	0.16	0.05
Toxicity	No	No	High

In gaseous form, even at a pressure of 700 bar, the energy density is just 4.4 MJ/L. On liquefying, the energy density can go up to a maximum of 8 MJ/L and in both cases the volumetric energy density is very less as compared to that of gasoline (~36 MJ/L). Apart from the energy density, these two methods are neither safe nor cost effective.

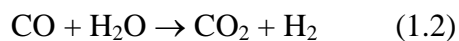
1.3. Hydrogen generation:

Though hydrogen is the most abundant element on the earth, less than 1% of it is present as molecular hydrogen and majority of it is in chemically bonded state such as in water and hydrocarbons. Hence the generation of molecular hydrogen from the other form requires breaking those molecules which is energy intensive. As has been discussed, hydrogen energy can be treated as clean and environmental friendly only when it is generated in a clean way without the emission of greenhouse gases. Though there are many industrial methods available for hydrogen production, they are quite expensive when it is compared to the cost for same amount of energy from conventional sources of energy. Hydrogen can be generated from variety of resources, which can be either fossil fuel like natural gas and coal, or natural resources like water and biomass through different techniques, viz. chemical, biological, electrolytic, photolytic, thermo-chemical etc.¹⁴ Currently, major amount of hydrogen produced worldwide is through steam reforming of fossil fuels. Some of the hydrogen generation techniques are discussed below.

1.3.1. From fossil resources:

As has been said, nearly 95% of the today's hydrogen is produced from steam reforming technique which is proven to be the cheapest commercial technology for hydrogen production on a large scale.¹⁵ Steam reforming process involves the reaction of natural gas (methane) and steam in presence of a catalyst like nickel. As this is an endothermic process, it typically occurs at temperatures of 700 to 850 °C and pressures of 3 to 25 bar. The methane gas first reacts with steam to produce carbon monoxide and hydrogen, as shown below. The product obtained contains approximately 12 % CO, which is passed over hot iron oxide or cobalt oxide catalyst, for reaction with the steam to produce carbon dioxide and additional amounts of hydrogen through the well known water-gas shift reaction.





Another method used to produce hydrogen from natural gas is by partial oxidation of methane. In this process, methane is allowed to react with limited amount of oxygen to produce hydrogen and carbon monoxide and the produced CO is further converted to hydrogen through the water-gas shift reaction, as given in equation (1.2).



Partial oxidation is an exothermic process and hence it is faster than steam reforming and requires a smaller reactor vessel. As shown in the chemical reactions of partial oxidation (1.3), the amount of hydrogen produced per unit of the input fuel in the initial step of this process is less than that obtained by steam reforming of the same fuel. The combination of both steam reforming and partial oxidation is known as autothermal reforming which is exothermic in nature.

Another technique used to generate hydrogen from fossil resources is the gasification of coal. This is the oldest technique used for hydrogen production before natural gas became available. In this process, coal is heated at high temperatures to a gaseous state, which on reaction with steam and oxygen in the presence of a catalyst produces a mixture of hydrogen, carbon monoxide, carbon dioxide and other oxides of sulphur and nitrogen, known as synthesis gas. On removing the impurities from the synthesis gas, the carbon monoxide in the mixture is reacted with steam through water-gas shift reaction to produce further hydrogen and carbon dioxide.

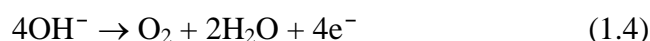
1.3.2. From renewable resources

Hydrogen can be produced from water and biomass using the renewable energy resources like wind, solar and thermal energy, etc. The major renewable and clean way of hydrogen generation is through water splitting.¹⁶⁻¹⁷ The overall water splitting reaction is

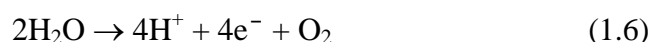
thermodynamically an uphill reaction with a positive free energy change of $\Delta G = +237.12$ kJ/mol. The hydrogen production from water can be carried out through different means such as thermal, electrical, photonic and biochemical methods. The primary energy needed for different methods to produce hydrogen can be obtained from different green energy sources like thermal and electrical energy from solar, wind, geothermal, tidal, wave, ocean thermal, hydro, biomass, nuclear energy, etc. The photonic energy can be obtained from the unique source, solar radiation and the biochemical energy from organic matter which can be manipulated by certain micro-organisms. The details of each process are discussed below.

Water electrolysis

Water electrolysis is the process of generating hydrogen through the decomposition of water into oxygen and hydrogen by passing electric current through water. Electrolysis is one of the most basic methods which can produce ultra-pure ($> 99.999\%$) hydrogen.¹⁸ In general, there are two different processes for water electrolysis namely, the alkaline process and the proton exchange membrane (PEM) process. Typical alkaline electrolyser consists of an aqueous solution of water and 25–30 wt% potassium hydroxide (KOH) as an electrolyte and the electrode reactions at anode and cathode are shown respectively as.



In PEM electrolyser, the membrane works as a gas separation device as well as an electrolyte and the anode and cathode reactions are described respectively as



As the free energy change (ΔG) of the reaction, $H_2O \rightarrow H_2 + 0.5 O_2$, is $237.12 \text{ kJ/mol} = 2.46 \text{ eV}$ and as it requires two electrons for the formation of one molecule of hydrogen, the minimum potential that should be applied is $V_{\min} = 2.46/2 = 1.23 \text{ V}$.

Thermo-chemical water splitting

Thermolysis of water is the decomposition of water into oxygen and hydrogen on heating and it requires extremely high temperature.¹⁹⁻²⁰ However, a large number of thermo-chemical cycles are proposed to decrease this operating temperature. The thermo-chemical process proceeds through multiple steps where water and heat are the main inputs with hydrogen and oxygen as outputs and other reagents are recycled in a closed loop.²¹ Though there are large number of such cycles like ZnO/Zn , Fe_3O_4/FeO , CdO/Cd , $Cu-Cl$ etc., the Sulphur-Iodine (S-I) cycle is reported to be the best with a theoretical efficiency of 52% which requires a temperature of about 900°C .²²⁻²³

The main rate limiting reaction step in S-I cycle is the sulphuric acid decomposition which is highly endothermic and it consists of two steps which can be written as



The first step of the reaction requires a temperature of 400°C - 500°C whereas the second step occurs at a temperature of around 800°C in presence of a catalyst. This reaction temperature can be reduced through the use of a proper catalyst and developing new catalyst is thus important. The main problem with this process is that it requires very high temperature and there are relatively less number of possible thermal energy sources available to drive this process. One of the few such possible sources is the nuclear heat from the high temperature gas-cooled reactors.

Photo-catalytic water splitting

Harvesting the available solar energy and storing in chemical bonds which is observed in the natural photosynthesis is an ideal approach to resolve the energy challenge.²⁴⁻²⁵ Solar water splitting using semiconductor photocatalyst has attracted immense research interest after the original work by Honda and Fujishima²⁶ using a semiconductor anode such as TiO_2 and a metal cathode like platinum. In this experiment, electron-hole pairs are produced on irradiating TiO_2 with light. The holes oxidize water at the TiO_2 surface to evolve oxygen and the electrons migrate to the counter electrode to reduce water to form hydrogen as it is shown in Figure 1.4. To be a good photocatalyst for water splitting, the materials should satisfy several requirements, viz. (i) suitable bandgap for efficient absorption of solar visible-light (ii) appropriate band edge potentials for overall water splitting (iii) ability to separate photo generated electron-hole pairs (iv) stability towards chemical and photo corrosion in aqueous environments etc.²⁷ For a photocatalyst to complete the overall water splitting, its conduction band bottom should be more negative than the proton reduction potential (0 V vs. NHE) and the top of the valence band should be more positive than the oxidation potential of water (+1.23 V vs. NHE). Though the theoretical band gap required for the overall water-splitting reaction is 1.23 eV, because of the unavoidable energy losses, the practical required bandgap is more than the theoretical value.

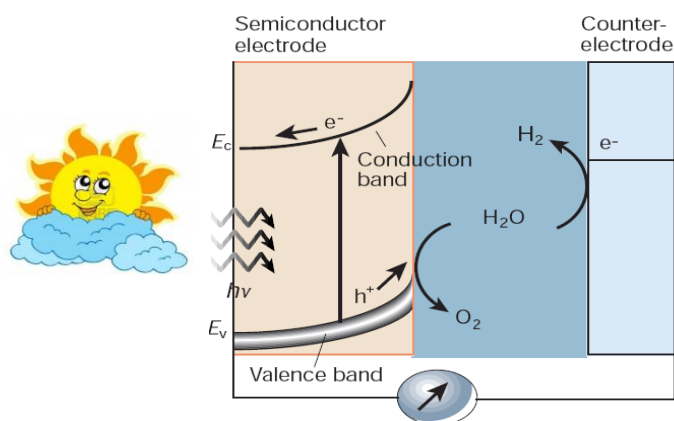
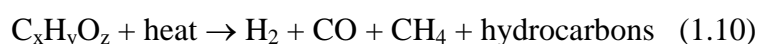


Figure 1.4: Working principle of the Photo electrochemical cell

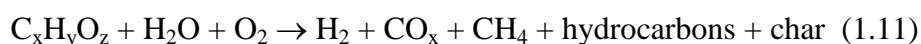
Though TiO_2 is the semiconductor that is extensively studied for photocatalysis, because of its large band gap of 3.0–3.2 eV, it absorbs only the ultraviolet component of the solar spectrum giving poor conversion efficiencies. Several attempts have been made to enhance the visible light absorption efficiency of TiO_2 through different kind of doping techniques and by creating varieties of defects. Many alternative transitional metal oxides, sulphides, selenides viz. ZnO , SrTiO_3 , NaTiO_3 , ZnS , CdS , CdSe , etc. have also been explored to implement the water cleavage by visible light.²⁸ Apart from the transition metal oxides, nitrides, oxinitrides etc, polymeric semiconductor materials like graphitic carbon nitride ($\text{g-C}_3\text{N}_4$) materials are found to have great potential as photocatalyst.²⁹ In spite of the large number of studies on different kinds of materials, none of them is successful photocatalyst so far.

Biological hydrogen generation

Hydrogen can be generated from biomass like wood chips and agricultural wastes through several thermo-chemical methods, such as pyrolysis and gasification. In pyrolysis, solid biomass is decomposed into liquid oils, solid charcoal and gaseous compounds at high temperature in the absence of air which can be represented as



and the hydrocarbons obtained can be further converted to hydrogen through steam reformation technique as discussed in the earlier section. In gasification, biomass is gasified in the presence of oxygen and water at temperatures above 1000 K, where, the biomass undergoes partial oxidation and steam reforming reactions generating gas and char product which can be expressed as.



However, all technologies based on biomass have low yields because of the low content of hydrogen in biomass (~ 6%) which lowers the overall available energy. Another way is to

use algae to decompose complex biological molecules to produce hydrogen as a by-product. Microalgae and cyanobacteria along with higher plants are capable of oxygenic photosynthesis according to the following reaction³⁰



These technologies are however limited by high capital costs and low production rates.

1.4. Hydrogen Storage:

As has been discussed in the beginning, though hydrogen is having very high energy density per unit mass, its energy density per unit volume is very less. At ambient conditions of 25 °C temperature and 1 bar pressure, 1 kg of hydrogen requires a volume of ~11 m³. For commercialization of average modern car, a driving range of at least 500 Km is considered to be crucial and a combustion engine needs approximately 30-35 liters of petrol or diesel. For a car running on a fuel cell engine, it requires 5 Kg of hydrogen to travel the same distance of 500 Km and this 5 kg of hydrogen at ambient conditions occupies a volume of ~56,000 liters. The volume of the container or material required for different means of storage of 4 kg of hydrogen is shown in Figure 1.5.¹³ Hence, the main aspect of hydrogen storage is to reduce the volume of the hydrogen gas storing material. Developing effective hydrogen storage technology for transportation applications is highly challenging and one of the key factors in moving towards the hydrogen economy.³¹⁻³⁶ A good hydrogen storage material should satisfy certain operating requirements³⁷ such as: (i) hydrogen absorption and desorption enthalpies should be in-between that of chemisorption and physisorption, (ii) fast kinetics at ambient conditions for quick uptake and release of hydrogen, (iii) high gravimetric and volumetric densities for effective hydrogen storage, (iv) effective heat transfer, (v) Long recyclable lifetime of the material for hydrogen absorption/desorption, (vi) high mechanical strength and durability, and (vii) safety at operational conditions.



Figure 1.5: Comparison of the size of hydrogen tank with different ways of storage.

Currently, hydrogen is usually stored through two technically well-understood technologies, high pressure compression of the gas and cryogenic storage of liquid hydrogen.¹³ For storing hydrogen as a gas in tanks, gas storage tanks, made of lightweight materials, such as carbon-fiber-reinforced composites that can be operated at a pressure of 5,000 psi, are already available. In gaseous form, even at a pressure of 10,000 psi, the energy density is just 4.4 MJ/L which is significantly less as compared to the same volume of gasoline (31.6 MJ/L).

Another important issue is the energy required to compress the gas, which depends on both the initial and final pressures of the tank. However, it may be possible to improve the compressed gas storage technology through the development of novel materials such as fiber-reinforced composites that are strong enough to withstand the high pressures and impermeable to hydrogen.

Another well understood method of hydrogen storage is in the form of liquid hydrogen at cryogenic temperatures where larger amount of hydrogen can be stored in a given volume as compared to the gaseous form. At standard temperature and pressure, the density of liquid hydrogen is 70.8 kg/m³. Though the maximum energy density predicted for liquid hydrogen is 8.4 MJ/L which is very high as compared to compressed gas even at 10,000 psi pressure (4.4 MJ/L), still it is very less as compared to that of gasoline (~36

MJ/L). The main drawback of this process lies in the large energy input required to cool and condense hydrogen at about 20 K temperature which is approximately one third of the amount of energy stored in hydrogen. Another problem with this system comes from the energy loss associated with the boil-off loss of hydrogen.

Apart from the energy density, both these methods are neither safe nor cost effective. The third way of storing hydrogen is by absorbing it either physically or chemically in the form of metal or chemical hydrides or adsorbing it on the surfaces and inside the pores of a porous solid matrix.

1.4.1 Metal Hydrides

Metal hydrides are one of the well explored solid state hydrogen storage materials that can be used for transportation application.³⁸⁻⁴⁴ Metal hydrides can be defined as the single phase compounds formed between the host metal and hydrogen. Hydrogen forms metal hydrides on reacting with some metals or alloys which can be released reversibly by varying the parameters like temperature or pressure. As the hydrogen release from metal hydrides is highly endothermic, it has the safety advantages over the gas and liquid state hydrogen storage technology. Hydrogen forms different kinds of metal hydrides with different metals. It forms ionic hydrides with alkali and alkaline earth metals which are also known as saline hydrides such as LiH, MgH₂, BeH₂, etc and in these hydrides, hydrogen exists as a negatively charged ion. With transition metals, lanthanides and actinides, hydrogen forms either metallic or semiconductor metal hydrides where hydrogen acts as a metal through the formation of metallic bond. Hydrogen is also known to form another class of hydrides, the complex light metal hydrides, which are extensively studied for hydrogen storage materials. These hydrides include the complexes of group IA, IIA and IIIA light metals such as AlH₄⁻, AlH₆³⁻, BH₄⁻, NH₂⁻ and NH₂²⁻, which are ionically bonded to alkali and alkaline earth metals resulting into stable hydrides, viz. NaAlH₄, Na₃AlH₆, NaBH₄, LiNH₂ and Li₂NH.

Among the light metal hydrides, MgH_2 is one of the well explored materials for hydrogen storage because of its high hydrogen content of 7.6 wt% along with the low cost and more abundance of magnesium. The main limitation of this material for practical use is due to the sluggish kinetics of adsorption/desorption along with the high desorption temperature ($\sim 300^\circ C$). Large number of studies have been reported to overcome these limitations which include decreasing the particle size and alloying with other metals.⁴⁵⁻⁴⁶ Ball-milling is found to be very effective in improving the hydrogen adsorption kinetics and thermodynamics through increased surface area and creation of defects.⁴⁷ Alloying with transition metals is found to help in the activation of molecular hydrogen and increase in the adsorption kinetics.

Though many elements can form hydrides, their dissociation pressures and temperatures are not appropriate for practical applications at ambient conditions. Vanadium hydride is found to have proper desorption conditions. However, its hydrogen storage capacity is found to be very low. To enhance the adsorption properties, another important class of metal hydrides, the intermetallic hydrides have been developed which can exist in different forms like AB_2 , A_2B , AB , and AB_5 . Generally, the intermetallic hydrides are made by alloying a metal (A) which can form stable metal hydrides and another metal (B) that does not form stable metal hydrides so that the overall dehydrogenation enthalpy is lowered. If $\Delta H(AH_n)$, $\Delta H(B_xH_n)$ are the enthalpies of metal hydride formation for AH_n , B_xH_n and $\Delta H(AB_x)$ is the enthalpy of alloying, then the enthalpy of intermetallic hydride formation can be calculated as

$$\Delta H(AB_xH_{2n}) = \Delta H(AH_n) + \Delta H(B_xH_n) - \Delta H(AB_x) \quad (1.13)$$

As $\Delta H(AB_x)$ is highly negative as compared to $\Delta H(B_xH_n)$, the overall $\Delta H(AB_xH_{2n})$ will be more positive as compared to $\Delta H(AH_n)$, indicating that the intermetallic hydride is more

unstable and can be formed at lower temperatures. One of the intermetallic hydrides that is extensively studied is LaNi_5 . Although LaNi_5 hydride ($\text{LaNi}_5\text{H}_{6.7}$) is found to have good volumetric H_2 densities ($\sim 130 \text{ kg H}_2/\text{m}^3$), its gravimetric density is found to be just 1–2 wt%. Apart from LaNi_5 , large number of intermetallics of 3d-transition metals like Ti-Fe, Ti-V based alloys or even with multiple metal containing alloys are under study to enhance the hydrogen storage properties of these materials.

Complex metal hydrides are found to be potential candidates for hydrogen storage because of their high hydrogen storage capacities.⁴⁸ These materials include the complex salts of alanates, amides, borohydrides, etc. Though the hydrogen gravimetric densities are high in these hydrides, once it is dehydrogenated, it is highly irreversible which cannot be used for rechargeable hydrogen storage. Though they are thermodynamically quite stable and decomposition requires high temperature in their pure form, the decomposition temperatures can be reduced through doping and also by reducing the particle size.

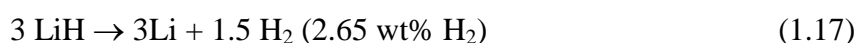
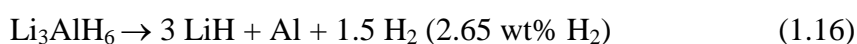
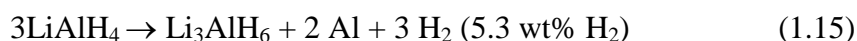
Metal borohydrides are found to be promising candidates for hydrogen storage with high gravimetric hydrogen densities because of the light weight of boron and the large amount hydrogen present in the system.⁴⁹⁻⁵⁰ The main disadvantages associated with these materials are the high decomposition temperatures and poor recyclability. Lithium borohydride (LiBH_4) can store hydrogen with a gravimetric density of 18.4 wt% and its decomposition requires a temperature of around $\sim 320\text{--}380^\circ\text{C}$. Sodium borohydride (NaBH_4) is another candidate which contains 10.8 wt% of hydrogen. Though the hydrogen evolution in NaBH_4 is found to start at about 240°C , only ~ 1.0 wt% is released at lower temperatures and most of the remaining hydrogen is found to be liberated at around 450°C . Beryllium borohydride with the formula $\text{Be}(\text{BH}_4)_2$ is found to contain highest hydrogen wt% among the complex borohydrides with 20 wt% H_2 . However, the high toxicity associated with Be metal prohibits its use for hydrogen storage applications. $\text{Mg}(\text{BH}_4)_2$ also seems to be interesting

candidate for hydrogen storage with a hydrogen density of 14.8 wt%. The high decomposition temperature (300 °C) of $\text{Mg}(\text{BH}_4)_2$ makes it less suitable for storing hydrogen reversibly, although presence of TiCl_3 is found to decrease the decomposition temperature to 100 °C.

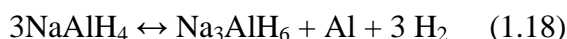
Though boron and aluminium belong to the same group in the periodic table, they differ a lot in their hydride chemistry. Boron is known to form a large number of hydrides with the common name of boranes, while aluminium forms only a limited number of hydrides. Alkali metal aluminates are found to be attractive for hydrogen storage as they are readily available and also can be readily prepared. Alkali metal aluminates undergo dehydrogenation in the temperature range of 200-300 °C to give aluminium metal and the corresponding alkali metal hydrides along with hydrogen.



Lithium aluminium hydride (LiAlH_4), well known as the reducing agent in organic chemistry, is found to contain 10.5 wt% of hydrogen. LiAlH_4 is found to decompose in multiple steps as shown below



The first step of the decomposition, LiAlH_4 to Li_3AlH_6 is found to be exothermic which hinders the rehydrogenation of Li_3AlH_6 to LiAlH_4 making it unsuitable for reversible hydrogen storage. Sodium aluminium hydride is another complex hydride extensively studied for hydrogen storage. Sodium aluminates are found to decompose in two steps as shown below.



In the first step, 3.7 wt% of hydrogen is released which is found to be endothermic with an enthalpy change of 37 kJ/mol. In the second step, Na_3AlH_6 decomposes to give NaH, Al metal and H_2 with 1.8 wt% of hydrogen evolution and an associated enthalpy change of 47 kJ/mol. Apart from the thermodynamic aspects, the slow kinetics of hydrogen release and the difficulty in rehydrogenation under ambient conditions are found to be main difficulties with this material. However, many catalysts are under study for improvement of the kinetics of hydrogen release.

1.4.2 Hydrogen storage through physisorption

As discussed in the previous section, in most of the materials where hydrogen is stored through chemisorption, the hydrogenation enthalpies are quite higher than the predicted enthalpies for ambient temperature hydrogen storage. Though the hydrogen molecule does not have a permanent dipole moment (non-polar), it possesses quadrupole moment and polarizability and can get adsorbed on surfaces by means of weak van der Waals interactions.⁵¹ In view of this, recent attention has been shifting towards the molecular hydrogen storage where the hydrogen is mainly adsorbed through physical adsorption. In physical adsorption, hydrogen is bound to the substrate through weak van der Waals forces of interaction between the hydrogen and the substrate. These weak and long-range interactions arise because of the fluctuations in the charge distribution in both the gas molecule as well as the adsorbing surface. The typical enthalpy of physical adsorption is in the range of 1 to 10 kJ/mol which is not sufficient to break the chemical bond between the two hydrogen atoms and hence the hydrogen will be adsorbed in molecular form. As the binding interactions between hydrogen molecules and the substrate are very weak, physisorption typically takes place at low temperature. In the case of physisorption, in general, there is no energy barrier for adsorption and therefore the process is associated with fast kinetics. The amount of

hydrogen that can be absorbed is expected to increase with increase in the surface area of the adsorbing host material and hence making highly porous materials having large surface area can enhance the adsorption capacity of the material.

Large number of materials has been explored for physisorption of hydrogen and they are light, porous and robust.⁵² Although hydrogen can be stored reversibly through physisorption in porous materials by changing pressure and/or temperature, the hydrogen binding energies are too low and hence cryogenic temperatures are need to achieve reasonable hydrogen uptake capacities. In materials such as metal organic frameworks, porous carbons, zeolites, clathrates and organic polymers etc., hydrogen is physisorbed on the surface of the pores. Hydrogen storage through physisorption in carbon-based nanomaterials have received special attention because of their low densities, broad range of bulk and pore structures, good recycling characteristics, reasonably good chemical stability etc. Large number of carbon materials such as carbon nanotubes (CNTs), graphite, carbon nanofibers, activated carbon and ordered porous carbons have been proposed for hydrogen storage.⁵³⁻⁵⁷ In 1997, Dillon et al.⁵⁸ have measured the H₂ adsorption in freshly prepared soot containing only about 0.1 to 0.2 weight % SWNTs at 133 K and proposed H₂ adsorption capacity of 5 to 10 wt % for pure SWNTs. In 1999, Liu et al.⁵⁹ synthesised the single walled carbon nanotubes with a diameter of 1.85 nm by semi-continuous hydrogen arc discharge method, and reported a H₂ storage capacity of 4.2 wt%. Heine and co-workers⁶⁰ have proposed the graphene (or graphitic platelets) and polycyclic aromatic hydrocarbon based nanostructures as tunable storage media for molecular hydrogen.

Among the other porous materials developed, metal organic frameworks (MOFs) and covalent organic frameworks (COFs) materials are found to be attractive because of the huge surface areas associated with these structures, their robust nature and well developed synthesis methods.⁶¹⁻⁶⁷ Metal organic frameworks have attracted a great deal of interest

because of their promising applications in a number of areas, including gas storage, heterogeneous catalysis, nonlinear optics, host-guest induced separation, drug delivery etc. MOFs are crystalline materials which contain the metal ions linked through organic ligands as linkers generating micropores and channels. The framework topology, pore size, and surface area of these frameworks can be tuned through the proper selection of the metal and organic ligand to achieve desirable properties. Though Zn(II) and Cu(II) are the most common metal ions used in the synthesis of MOFs, other transition metal ions may also be used as metal building blocks. As the organic ligand, large number of carboxylic acids and heterocyclic compounds containing nitrogen donors is used for the design of MOFs. Unlike metal-organic frameworks, covalent organic frameworks by definition doesn't contain any metal and are constructed entirely from strong covalent bonds. Yaghi and co-workers have designed numerous number of framework materials like MOFs, COFs, ZIFs etc. using the so called iso-reticular synthesis. In these classes of materials, the H₂ storage capacity mainly depends on the surface area and pore volume.

In most of these materials where the hydrogen is stored through physisorption, the main disadvantage is the low hydrogen adsorption enthalpies because of the simple van der Waals forces of interaction associated. As a result, though they show considerable hydrogen densities at 77 K, they have very low storage capacities observed at ambient conditions. Lochan and Head-Gordon⁶⁸ have made the rough estimate of the ideal hydrogen binding energy range given as 5.0-7.6 kcal/mol at -20 °C, 5.7-8.1 kcal/mol at 0 °C, 6.6-9.6 kcal/mol at room temperature, and 7.2-10 kcal/mol at 50 °C.

Many methods have been proposed to enhance the adsorption enthalpies in these framework materials and also carbon nanomaterials. Doping with light metal atoms like alkali and alkaline earth metals is found to be effective.⁶⁹⁻⁷² On decorating the carbon surfaces with alkali metal atoms, the metal sites are found to get partially ionized because of

the charge transfer from metal to surface. The cationic sites can adsorb hydrogen through the ion-induced dipole and ion-quadrupole interactions. Chen et al.⁷³ have reported that the Li- and K-doped carbon nanotubes can adsorb hydrogen with a gravimetric density of 20 and 14 wt%, respectively. This has, however, later been contradicted by other reports which explained that the apparently observed excessive hydrogen adsorption is in fact due to the presence of water. Yang et al.⁷⁴ were able to achieve an adsorption of only 2 wt% in dry hydrogen atmosphere, by alkali metal doped carbon nanotubes.

Transition metal decorated carbon nanomaterials are found to have hydrogen adsorption energies that are suitable for ambient temperature hydrogen storage through the well established Kubas-type of interactions. Zhao et al.⁷⁵ and Yildirim et al.⁷⁶ studied the hydrogen storage in transition metal-doped fullerenes and single-walled carbon nanotubes, respectively, and have shown that the decorated metal atoms such as Sc and Ti can bind hydrogen in molecular forms with a binding energy of the order of 0.5 eV/H₂ and with gravimetric density of around 8-9 wt%. Phillips et al.⁷⁷ have experimentally studied the hydrogen storage in transition metal-ethylene complexes and reported 12 wt% uptake of H₂. Although the hydrogen adsorption in transition metal-doped carbon materials has been found to be better than in other materials, because of their huge cohesive energies and relatively low binding energies to the carbon host materials, transition metals are found to aggregate and form metal clusters which not only lowers the hydrogen adsorption capacities but also lets the material change to another form which is not suitable for recyclable hydrogen storage applications.⁷⁸ Sun et al.⁷⁹ have shown that the clustering problem can be avoided through the grafting of the transition metal-C₅H₅ complex on silsesquioxanes. Doping of the carbon surface with boron has been proposed to be effective in preventing the clustering of metal atoms. A. K. Singh et al.⁸⁰ Proposed that the metallocarboranes can store hydrogen with a gravimetric density of 8 wt% and the transition metal binding is quite strong in these systems.

Even in MOFs and COFs, various approaches have been pursued for improving the hydrogen adsorption characteristics. One such strategy that has been of recent interest is the metal ion decoration approach which had already been followed in the case of fullerenes to improve the hydrogen storage capacity. Kaye and Long⁸¹ experimentally studied MOF-5 with Cr metal decoration to its benzene ring. However, the extent of hydrogen adsorption was found to be very low at 298 K. A possible reason for this is the clustering of the metal atoms. Alkali metal atoms have been found to be good candidates to be used for decoration because of their low cohesive energies which can avoid the clustering problem. Much of the recent work has thus focused on Li-doped MOFs and COFs for hydrogen storage.⁸²⁻⁸⁶ Using an *ab initio* based GCMC simulation, Han and Goddard III⁸⁷ have predicted gravimetric hydrogen adsorption isotherms for several pure and Li-doped MOFs at 300 K. Interesting results have been reported based on their calculation of a high H₂ uptake of 6.47 wt % for MOF-C30 at 300 K and 100 bar pressure. Blomqvist et al.⁸⁸ have carried out *ab initio* periodic DFT calculations on molecular hydrogen adsorption properties of Li-decorated MOF-5, which showed significant improvement. Their results showed that each Li over the benzene ring can adsorb up to three H₂ molecules with a binding energy of 2.8-4.3 kcal/mol per H₂ and *ab initio* molecular dynamics simulations revealed that a hydrogen uptake of 2.9 wt % and 2.0 wt % could be achieved even at higher temperatures of 200 K and 300 K, respectively. Lan *et al.*⁸⁹ studied hydrogen adsorption in Li-doped and nondoped covalent organic borosilicate frameworks using GCMC simulations and have predicted that the total gravimetric and volumetric uptakes of hydrogen in the Li-doped COF-202 reach 4.39 wt % and 25.86 g/L at $T=298$ K and $P=100$ bar, respectively. Cao *et al.*⁹⁰ have carried out a GCMC simulation study and shown that COF materials are superior to MOF materials for hydrogen storage and the gravimetric adsorption capacities for hydrogen in Li-doped COF-105 and COF-108 can reach up to 6.84 and 6.73 wt% at $T=298$ K and $P=100$ bar respectively. Mulfort et al.⁹¹ showed experimentally that chemical reductive doping of MOF with alkali metal ions can substantially enhance both nitrogen and hydrogen gas uptake.

1.5. Hydrogen as a fuel

When hydrogen reacts with oxygen in presence of air, the only product delivered is water along with energy, and therefore hydrogen offers the advantage of carbon-free energy. Hydrogen can be used as fuel in two different ways in vehicles viz. (1) hydrogen-fuelled internal combustion engines (H_2 ICEs) and (2) the fuel cells (FCs). The ICE converts the chemical energy to mechanical energy which can then be transformed to electrical energy.⁹² The existing gasoline ICEs can be modified and can be used for H_2 ICEs. In the case of normal ICEs, the only undesirable emissions are the nitrogen oxides (NO_x) formed by the thermal dissociation and oxidation of N_2 in atmospheric air during combustion. Since the ICE includes an intermediate heat phase, its efficiency is restricted according to the Carnot's cycle. However, the hydrogen internal combustion engines offer the advantage of lower weight and low cost as compared to fuel cells and can be run on impure fuels.

Fuel cells are the electro chemical devices which can convert the chemical energy to electrical energy through electrochemical reaction which are found to be important component in transition to hydrogen economy.⁹³⁻⁹⁴ The first fuel cell application was achieved with the space technology and NASA has used the alkaline fuel cell system in Apollo space craft. The overall chemical reaction in a hydrogen/oxygen fuel cell can be written as:



with an equilibrium cell voltage of 1.23 V under standard conditions, which is the difference of the equilibrium electrode potentials arising from cathode and anode reactions. However, because of the associated losses at both the half cell reactions, the practical cell voltage achievable is always less than the theoretical value predicted and also it decreases with increasing current density. The basic structure of any fuel cell consists of two electrodes that are separated by the electrolyte and are connected in an external circuit. The electrodes are

exposed to fuel or oxidant and the electrodes have to be permeable for the passage of fuel or oxidant and therefore need to possess a porous structure.

There are different types of fuel cells based on the electrolyte, viz. polymer electrolyte membrane fuel cells, alkaline fuel cells, solid oxide fuel cells, phosphoric acid fuel cells, direct methanol fuel cells and molten carbonate fuel cells etc.⁹⁵ Based on the operational temperature, again these fuel cells can be categorised into two groups, viz. (1) low-temperature fuel cells such as alkaline fuel cell, the polymer electrolyte fuel cell, the direct methanol fuel cell, the phosphoric acid fuel cell and (2) high temperature fuel cells such as molten carbonate fuel cell and the solid oxide fuel cell. The two main reactions at the electrodes are the hydrogen oxidation reaction at the anode and the oxygen reduction reaction (ORR) at the cathode of the fuel cell. In the case of fuel cells that are operating at low temperatures, the kinetics of the electrode reactions are very slow and requires a good catalyst like platinum, while for the high temperature fuel cells as the reaction temperatures are high, catalysts like transition metals and their alloys are generally used.

Among the many other fuel cells, the polymer electrolyte membrane fuel cells (PEMFC) and the alkaline fuel cells (AFC) are found to be more advantageous as they can be operated at ambient temperatures. The schematic representation of both the PEMFC and AFC are shown in Figure 1.6.

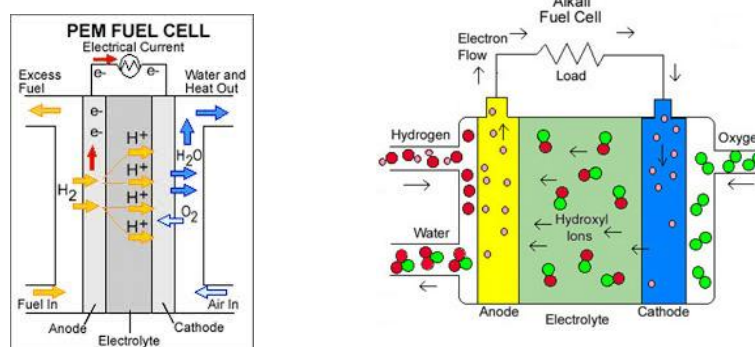


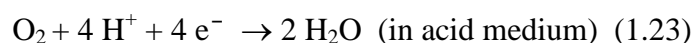
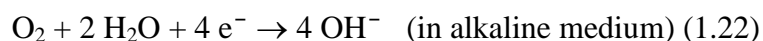
Figure 1.6: Schematic representation of PEMFC and AFC.

The hydrogen oxidation at the anode generally occurs readily on the platinum based catalysts with fast kinetics, mainly controlled by mass transfer limitation. The overall anodic reaction can be written as

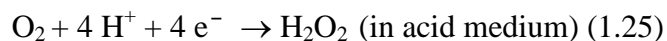


This reaction is found to be very fast with a rate constant of $10^{-5} \text{ mol sce}^{-1}\text{cm}^{-2}$ when pure hydrogen is used, although use of impure hydrogen may lead to some problems.

The main rate limiting step in a fuel cell is found to be its cathode reaction, the ORR, which is found to be around 6-fold slower as compared to the anode reaction.⁹⁶⁻⁹⁷ The ORR is shown to follow two different paths depending on the environment. It can be either a direct four electron path as shown below:



or it can follow a two electron path through the formation of hydrogen peroxide like



The four electron reduction path is more desirable as compared to the two electron path.

Platinum is known to be the best conventional catalyst so far reported in the literature. But, limited abundance of Pt and its cost make the fuel cell very expensive and there is a need to find alternatives.⁹⁸⁻¹⁰⁰ Large number of studies have been carried out to minimize the amount of Pt amount by using shape and size controlled nanostructures and by making Pt-based alloys in order to get high activity for ORR. Another way of reducing the amount of Pt is by anchoring Pt nanostructures onto active supports such as carbon that improves the performance of the fuel cell reactions. Apart from the metal based catalysts, many metal free catalysts are also under consideration for making an effective catalyst.

1.6. Computational methods

In the present thesis, we have employed different quantum mechanical methods, viz. wave function based Hartre-Fock and MP2 methods and also the density functional theory (DFT) based methods for all the studies carried out. In principle, the molecular level calculations are carried out by using the localised Gaussian basis sets, while the plane-wave basis sets were used for the periodic solid state calculations. Within the framework of DFT, we have used several exchange-correlation energy functionals, such as the local density approximation (LDA)¹⁰¹, generalized gradient approximation (GGA)¹⁰²⁻¹⁰³, Becke's three-parameter exchange functional and Lee-Yang-Parr correlation functional (B3LYP)¹⁰⁴⁻¹⁰⁶, and also the recently developed Minnesota functionals.¹⁰⁷⁻¹¹⁰ The individual computational methods used will be discussed in respective chapters under the subsection computational details. The theoretical basis for all the methods used throughout the thesis is outlined here.

1.6.1. The Schrödinger Equation

In the history of quantum mechanics, the Schrödinger equation, introduced by the Austrian physicist Erwin Schrödinger is considered as a breakthrough. Schrödinger equation is a partial differential equation, which describes how the quantum state of a system changes with time. The time-independent Schrödinger equation of a system of M nuclei with N electrons can be written as

$$\hat{H}\psi_i(r_1, r_2, r_3, \dots, r_N, R_1, R_2, R_3, \dots, R_M) = E_i\psi_i(r_1, r_2, r_3, \dots, r_N, R_1, R_2, R_3, \dots, R_M) \quad (1.26)$$

where, \hat{H} is the Hamiltonian operator, ψ_i is the wave function which depends on both the electronic and nuclear coordinates and E_i is the eigenvalue of the i^{th} state. The Hamiltonian operator for this system can be written, in atomic units, as

$$\hat{H} = -\frac{1}{2} \sum_{i=1}^N \nabla_i^2 - \frac{1}{2} \sum_{A=1}^M \frac{1}{M_A} \nabla_A^2 - \sum_{i=1}^N \sum_{A=1}^M \frac{Z_A}{r_{iA}} + \sum_{i=1}^N \sum_{j>i}^N \frac{1}{r_{ij}} + \sum_{A=1}^M \sum_{B>A}^M \frac{Z_A Z_B}{R_{AB}} \quad (1.27)$$

Here, A and B run over the M nuclei whereas i and j run over the N electrons of the system. Z_A and M_A represent the charge and mass of the A^{th} nuclei in atomic units. The first two terms of the expression represent the kinetic energy of the electrons and nuclei respectively. Out of the last three terms, which represent the potential energy part of the Hamiltonian, the first term represents the attractive interaction between the nuclei and the electrons, whereas the last two terms represent the electron-electron and nucleus-nucleus repulsive interactions respectively. In principle, the Schrödinger equation can be applied to any system of interest and can be solved exactly. However, in practice, it is not computationally affordable due to the huge number of variables involved for large systems. Hence, it is important to impose certain approximations, which can make it possible to handle such many body systems.

1.6.2. Born-Oppenheimer Approximation

The Born-Oppenheimer approximation, proposed in 1927 by Max Born and J. Robert Oppenheimer, makes it possible to split the wavefunction into nuclear and electronic components.

$$\psi_{\text{total}}(r, R) = \psi_{\text{electronic}}(r; R) \times \psi_{\text{nuclear}}(R) \quad (1.28)$$

This approximation is based on the fact that the nuclei are much heavier as compared to the electrons. Because of the large difference in their mass, the electrons can be approximated as if they are moving in the field of fixed nuclei. The electronic Hamiltonian for fixed nuclear coordinates can be written as

$$\hat{H}_{\text{elec}} = -\frac{1}{2} \sum_{i=1}^N \nabla_i^2 - \sum_{i=1}^N \sum_{A=1}^M \frac{Z_A}{r_{iA}} + \sum_{i=1}^N \sum_{j>i}^N \frac{1}{r_{ij}} = \hat{T}_{\text{elec}} + \hat{V}_{\text{Ne}} + \hat{V}_{\text{ee}} \quad (1.29)$$

This indicates that the electronic wavefunction depends only on the electronic coordinates and does not explicitly depend on nuclear coordinates. The electronic Schrödinger equation then solved as

$$\hat{H}_{elec} \psi_{elec} = E_{elec} \psi_{elec} \quad . \quad (1.30)$$

However, it should be noted that the simple electronic energy E_{ele} represents only one component of the total energy of the system which is given by sum of electronic energy, nuclear repulsion energy and the nuclear kinetic energy, viz.

$$E_{tot} = E_{elec} + E_{nucl} \quad . \quad (1.31)$$

1.6.3. The Variational Principle

In principle, one can get the eigenfunction ψ_i for the i^{th} state by solving equation (1.30). Once the wavefunction is determined, all the observable properties of the system can be obtained by calculating the expectation values of the corresponding operators. However, in practice, the electronic Schrödinger equation cannot be solved exactly for the many-electron atomic and molecular systems of practical importance. One of the important approximations is the variational principle, which can be useful to approach the ground state eigenfunction ψ_0 . According to the variational principle, the expectation value (E) of the Hamiltonian operator (\hat{H}) using any trial wave function (ψ_{trial}) is always greater than or equal to the true ground state energy (E_0)

$$E \geq E_0$$

where,

$$E = \frac{\langle \psi_{trial} | \hat{H} | \psi_{trial} \rangle}{\langle \psi_{trial} | \psi_{trial} \rangle} \quad (1.32)$$

1.6.4. The Hartree-Fock Method

Solving the Schrödinger equation for an N electrons system is a computationally formidable task because of the electron-electron repulsion terms. Hartree developed the so called self-consistent field (SCF) procedure which was further improved by incorporating the electron exchange by Fock and Slater.¹¹¹⁻¹¹² The Hartree or the Hartree-Fock method introduces one-electron orbitals in terms of which the wavefunction is expressed as a simple product or a determinant respectively. The SCF approach assumes that each electron moves in the field of the nuclei as well as the average (mean field) potential due to the other electrons. The one-electron Schrödinger equation corresponding to this average potential is then solved for each electrons of the system. Now, since the SCF potential depends on the wavefunction, the same has to be evaluated using the set of improved wave functions (orbitals) and the solution procedure is to be repeated using the new potential. This procedure is iteratively carried out and each time the new set of orbitals is compared to the same from the previous iteration till the values differ only insignificantly, leading to what is known as self-consistency and the computation is complete and the wavefunctions and energy values are said to be self-consistent.

According to Hartree, the many electron wavefunction can be represented by the product of one electron wavefunctions, known as the Hartree product.

$$\psi = \psi_1(r)\psi_2(r)\psi_3(r).....\psi_N(r) \quad (1.33)$$

However, this product is not anti-symmetric and does not obey the Pauli Exclusion Principle. This electron exchange is incorporated by Fock and Slater by approximating the N-electron wavefunction as an anti-symmetrised product of N-one electron wave functions, the Slater determinant, given by

$$\psi_{HF}(\mathbf{r}_1, \mathbf{r}_2, \dots, \mathbf{r}_N) = \frac{1}{\sqrt{N!}} \begin{vmatrix} \phi_1(\mathbf{r}_1) & \phi_2(\mathbf{r}_1) & \dots & \phi_N(\mathbf{r}_1) \\ \phi_1(\mathbf{r}_2) & \phi_2(\mathbf{r}_2) & & \phi_N(\mathbf{r}_2) \\ \vdots & \vdots & & \vdots \\ \phi_1(\mathbf{r}_N) & \phi_2(\mathbf{r}_N) & & \phi_N(\mathbf{r}_N) \end{vmatrix} \quad (1.34)$$

Here, the $1/\sqrt{N!}$ is the normalization factor and the one-electron wave functions are called spin-orbitals which are composed of both spatial orbitals and the spin functions. As it can be seen from the above equations, exchanging the coordinates of i^{th} and j^{th} particles is equivalent to interchanging i^{th} and j^{th} columns of the determinant. As the sign of the determinant changes on exchange of any two rows or columns of the matrix, exchange of any two particle coordinates changes the sign of the wavefunction making it antisymmetric. The Hartree-Fock energy (E_{HF}) can be evaluated by operating the Hamiltonian operator on the Slater determinant as

$$E_{HF} = \langle \psi_{HF} | \hat{H} | \psi_{HF} \rangle = \sum_{i=1}^N H_i + \frac{1}{2} \sum_{i,j=1}^N (J_{ij} - K_{ij}) \quad (1.35)$$

where

$$H_i = \int \phi_i^*(r) \left\{ -\frac{1}{2} \nabla^2 - \sum_{A=1}^M \frac{Z_A}{r_{iA}} \right\} \phi_i(r) dr \quad (1.36)$$

$$J_{ij} = \iint \phi_i(\mathbf{r}_1) \phi_i^*(\mathbf{r}_1) \frac{1}{r_{12}} \phi_j^*(\mathbf{r}_2) \phi_j(\mathbf{r}_2) d\mathbf{r}_1 d\mathbf{r}_2 \quad (1.37)$$

$$K_{ij} = \iint \phi_i^*(\mathbf{r}_1) \phi_j(\mathbf{r}_1) \frac{1}{r_{12}} \phi_i(\mathbf{r}_2) \phi_j^*(\mathbf{r}_2) d\mathbf{r}_1 d\mathbf{r}_2 \quad (1.38)$$

All these integral are real and $J_{ij} \geq K_{ij} \geq 0$. Hence, J_{ij} is known as the coulomb integral which is present even in the Hartree theory where the wavefunction is just the product of one electron wavefunctions rather than the Slater determinant, whereas K_{ij} , the exchange integral, arises as a result of the anti-symmetric nature of the wavefunction. The Hartree-Fock equations can be solved numerically and Roothaan proposed that by introducing a set of

known basis functions, these differential equations can be converted to a set of algebraic equations which can be solved by using the matrix techniques. By introducing the set of known basis functions $\{\chi_\mu(\mathbf{r}) | \mu = 1, 2, 3, \dots, K\}$, the unknown orbitals can be expressed as a linear combination of the basis functions as

$$\phi_i = \sum_{\mu=1}^K C_{\mu i} \chi_\mu \quad (1.39)$$

The total energies calculated from the HF method are found to be associated with an error of 0.5-1.0%. Though it is not very high in terms of total energy, it is in the range of the chemical bond energies and hence it is important to consider the electron correlation effect which is not accounted for in the HF method. From the definition of variational principle, it is clear that the HF energy (E_{HF}) is always greater than the true ground state non-relativistic energy and the difference between the two is the correlation energy.

$$E_{\text{corr}} = E_0 - E_{\text{HF}} \quad (1.40)$$

To take care of the electron correlation energy, several wavefunction based methods have been developed, viz. the Møller-Plesset perturbation, Configuration interaction, Coupled Cluster, etc. However, all these post Hartree-Fock methods are found to be highly expensive computationally and it may not be possible to deal with large systems of practical importance.

1.6.5. Density Functional Theory (DFT)

The main idea of DFT is to replace the much complicated N-electron wavefunction and the associated Schrödinger equation with the simple electron density $\rho(\mathbf{r})$.¹¹³ DFT has quite a long history and the pioneering work came from Thomas and Fermi in 1927. The Thomas-Fermi model is a quantum statistical model which assumes that the electrons are

uniformly distributed over the six-dimensional phase space. The relation between the total kinetic energy and the electron density in this model is given as (atomic units are used)

$$T_{TF}[\rho] = C_F \int \rho^{5/3}(\mathbf{r}) d\mathbf{r}, \quad (1.41)$$

$$C_F = \frac{3}{10} (3\pi^2)^{2/3} \quad (1.42)$$

The electron-electron and electron-nucleus interactions are treated through the simple classical electrostatics and the overall energy formula in terms of electron density is given as

$$E_{TF}[\rho(\mathbf{r})] = C_F \int \rho^{5/3}(\mathbf{r}) d\mathbf{r} - Z \int \frac{\rho(\mathbf{r})}{r} d\mathbf{r} + \frac{1}{2} \iint \frac{\rho(\mathbf{r}_1)\rho(\mathbf{r}_2)}{|\mathbf{r}_1 - \mathbf{r}_2|} d\mathbf{r}_1 d\mathbf{r}_2 \quad (1.43)$$

A large number of modifications have been proposed to improve the Thomas-Fermi model. However, none of them could predict the bonding in molecules and also the accuracy in the atomic systems is very poor and thus the methods are of not much practical importance. Important breakthrough in density based theory came after the work of Hohenberg and Kohn (H-K) in 1964.¹¹⁴

For an N-electron system, all the ground state properties are determined from the total number of electron (N) and the external potential $v(\mathbf{r})$. The first H-K theorem states that the ground state energy of an N-electron system in an external potential $v(\mathbf{r})$ is a unique functional of its ground state electron density $\rho(\mathbf{r})$. For a non degenerate ground state of an N-electron system, $\rho(\mathbf{r})$ determines the N as

$$\int \rho(\mathbf{r}) d\mathbf{r} = N \quad (1.44)$$

and also determines the $v(\mathbf{r})$ and hence it can determine all the properties. The total energy can be written as

$$E[\rho] = T[\rho] + V_{ne}[\rho] + V_{ee}[\rho] \quad (1.45)$$

$$= \int \rho(\mathbf{r}) v(\mathbf{r}) d\mathbf{r} + F_{HK}[\rho] \quad (1.46)$$

$$F_{HK}[\rho] = T[\rho] + V_{ee}[\rho] \quad (1.47)$$

The second H-K theorem establishes the variational principle and states that for a positive trial density $\rho(\mathbf{r})$ satisfying the condition $\int \rho(\mathbf{r}) d\mathbf{r} = N$, the energy functional $E[\rho]$ is an upper bound to the true ground state energy.

$$E[\rho] \geq E_0$$

The Kohn-Sham Method

In 1965, Kohn and Sham invented an indirect way of calculating the kinetic energy functional $T_s[\rho]$ thereby making the DFT method as an efficient tool for carrying out rigorous calculations.¹¹⁵ Kohn and Sham, for the first time introduced the concept of orbitals in DFT and showed that the kinetic energy can be computed to reasonable accuracy and the remaining part can be handled in the exchange-correlation energy functional. For a non-interacting system of N-electrons, the Hamiltonian can be written as

$$\hat{H} = \sum_{i=1}^N \left(-\frac{1}{2} \nabla_i^2 \right) + \sum_{i=1}^N v(\mathbf{r}_i) \quad (1.48)$$

where no electron-electron interaction is considered and its ground state electron density will be exactly $\rho(\mathbf{r})$. The exact ground state wavefunction for such a non-interacting system will be the Slater determinant of the one electron wavefunctions

$$\psi_{KS}(\mathbf{r}_1, \mathbf{r}_2, \dots, \mathbf{r}_N) = \frac{1}{\sqrt{N!}} \begin{vmatrix} \phi_1(\mathbf{r}_1) & \phi_2(\mathbf{r}_1) & \dots & \phi_N(\mathbf{r}_1) \\ \phi_1(\mathbf{r}_2) & \phi_2(\mathbf{r}_2) & & \phi_N(\mathbf{r}_2) \\ \vdots & \vdots & & \vdots \\ \phi_1(\mathbf{r}_N) & \phi_2(\mathbf{r}_N) & & \phi_N(\mathbf{r}_N) \end{vmatrix} \quad (1.49)$$

and the kinetic energy functional can be calculated as

$$T_s[\rho] = \left\langle \psi_{KS} \left| \sum_{i=1}^N \left(-\frac{1}{2} \nabla_i^2 \right) \right| \psi_{KS} \right\rangle. \quad (1.50)$$

The overall energy functional can be written as

$$E[\rho] = \int \rho(\mathbf{r})v(\mathbf{r})d\mathbf{r} + T_s[\rho] + J[\rho] + E_{xc}[\rho] \quad (1.51)$$

where

$$E_{xc}[\rho] = T[\rho] - T_s[\rho] + V_{ee}[\rho] - J[\rho] \quad (1.52)$$

is known as the exchange correlation energy which does not have any exact form and hence has to be approximated. The main challenging aspect in implementing DFT is to find a good approximation to the exchange-correlation energy functional $E_{xc}[\rho]$. There are various approximations to calculate $E_{xc}[\rho]$, such as Local Density Approximation (LDA), Local Spin density Approximation (LSDA), Generalised Gradient Approximation (GGA) and many other hybrid functionals like B3LYP, HSE, M06 etc.

Local Density Approximation (LDA)

Local Density Approximation is the simplest approximation to the $E_{xc}[\rho]$ using the uniform electron gas formula, viz.

$$E_{xc}^{LDA}[\rho] = \int \rho(\mathbf{r})\varepsilon_{xc}(\rho)d\mathbf{r} \quad (1.53)$$

where, $\varepsilon_{xc}(\rho)$ is the exchange-correlation energy per electron in a homogeneous electron gas with density ρ . The functional $\varepsilon_{xc}(\rho)$ can be separated into exchange and correlation contributions as $\varepsilon_{xc}(\rho) = \varepsilon_x(\rho) + \varepsilon_c(\rho)$, so that the exchange part can be obtained from the Dirac exchange-energy functional as

$$\varepsilon_x(\rho) = -\frac{3}{4} \left(\frac{3}{\pi} \rho(\mathbf{r}) \right)^{1/3}. \quad (1.54)$$

The correlation part $\varepsilon_c(\rho)$ is unknown and for homogeneous electron gas it has been simulated through the quantum Monte Carlo approach.

Generalized gradient approximation

Though the LDA approximation is successful for many systems where the electron density is varying slowly, it fails for highly inhomogeneous systems. One way to improve the LDA method is by considering that the exchange-correlation energy depends not only on the density $\rho(\mathbf{r})$ but also on its gradient $\nabla\rho(\mathbf{r})$ and the typical GGA functional can be written as

$$E_{xc}^{GGA}[\rho] = \int \rho(\mathbf{r}) \varepsilon_{xc}(\rho, \nabla\rho) d\mathbf{r} \quad (1.55)$$

There are many GGA functionals developed to handle the $E_{xc}[\rho]$ more exactly and some of the widely used GGA functionals are Perdew, Burke and Ernzerhof (PBE), Perdew and Wang (PW91), Becke (B88) etc. Besides these pure DFT functionals, large number of hybrid DFT functionals are developed by incorporating the exact HF exchange into the $E_{xc}[\rho]$ like B3LYP, PBE0, Heyd-Scuseria-Ernzerhof (HSE) etc. As a next step to the GGA methods and hybrid methods, the meta-GGA functionals are developed in recent years where in addition to density and gradient the Laplacian (second derivative of electron density) is also incorporated, as is done in TPSS and the Minnesota Functionals.

1.6.6. The Bloch electrons and plane wave basis set

In the case of the periodic solid state systems, the effective potential will also have the periodicity of the crystal lattice i.e, $v(\mathbf{r} + \mathbf{R}) = v(\mathbf{r})$, where \mathbf{R} is Bravais lattice vector. Independent electrons obeying the Schrödinger equation with a periodic potential are known as the Bloch electrons.¹¹⁶ According to the Bloch theorem, the K-S orbitals can be written as a plane wave times a function that is having the same periodicity as the Bravais lattice.

$$\psi_{nk}(\mathbf{r}) = e^{ik \cdot \mathbf{r}} v_{nk}(\mathbf{r}) \quad (1.56)$$

where n is the band index. As $v(\mathbf{r} + \mathbf{R}) = v(\mathbf{r})$, it implies that

$$\psi_{nk}(\mathbf{r} + \mathbf{R}) = e^{i\mathbf{k} \cdot \mathbf{R}} \psi_{nk}(\mathbf{r}) \quad (1.57)$$

As any periodic function that obeys the Born-von Karman boundary condition can be expanded using a set of all plane-waves that satisfy the boundary condition, the periodic potential can be expanded as

$$V(\mathbf{r}) = \sum_{\mathbf{K}} V_{\mathbf{K}} e^{i\mathbf{K} \cdot \mathbf{r}} \quad (1.58)$$

where \mathbf{K} are set of plane waves vectors that have the same periodicity as the lattice which will be the set of reciprocal lattice vectors.

And hence the wave function can be expanded using the plane wave basis sets as

$$\psi_{nk}(\mathbf{r}) = \sum_{\mathbf{K}} V_{\mathbf{K}} e^{i(\mathbf{K} + \mathbf{k}) \cdot \mathbf{r}} \quad (1.59)$$

1.7 Scope of the present thesis

As has been discussed, there are number of scientific and technological challenges in moving towards the hydrogen economy. Developing new materials with desired applications towards generation, storage, transportation and usage of hydrogen is one of the important issues. Theoretical modelling is an important tool in designing new materials which can provide valuable inputs for the experiments, thereby saving time as well as the chemicals. Therefore, the present thesis aims at the modelling of new molecular systems and materials that are desirable for hydrogen energy applications. Using different computational techniques, we have designed isolated molecular systems as well as periodic solids mainly for hydrogen energy applications such as, hydrogen generation through photocatalytic water splitting, hydrogen storage and catalytic oxygen reduction reaction in fuel cells. All these studies have been elaborated in eight chapters (chapter 2-chapter 9) and the final chapter (chapter 10) deals with concluding remarks and possible future directions as envisaged from the results reported in the present thesis. A brief objective of each chapter is discussed below.

Chapter 2 deals with the design of a graphitic carbon nitride (g-CN) based photocatalyst for hydrogen generation through solar water splitting. We have considered different morphologies of g-CN, viz. two-dimensional infinite sheets, one-dimensional nanotubes and nanoribbons. The calculated band structure results show that although the band edge potentials of all the morphologies are suitable for overall water splitting, the band gaps of these materials are found to be around 3.2 eV which is beyond the visible region. We have attempted to engineer the band gap through different ways such as formation of multiple layers, substitutional doping with foreign elements, like boron, oxygen, sulphur, phosphorous and decorating with metals atoms like alkali metals and transition metals. The calculated results have shown that on forming multi layers, the band gap decreases to have the value ~ 3.10 eV in bi-layer and 3.03 eV in tri-layers. In the case of non-metal doping,

except for phosphorous, the band gap becomes nearly zero, while phosphorous doping is found to be effective leading to a band gap of 2.51 eV. In all the cases of metal decoration considered, the calculated band gaps are near to zero and hence metal decoration is not suitable for this application. In summary, the formation of multilayer and phosphorous doping are found to be effective in bringing down the band gap with appropriate band edge potentials that are suitable for overall water splitting.

In chapter 3, we have elaborated the results on hydrogen adsorption properties of alkali metal decorated small cyclic hydrocarbons (C_nH_n-M). Molecular hydrogen, being a non-polar molecule, does not bind to simple van der Waals surfaces very strongly. However, it has been shown that the presence of an ionic site can enhance the hydrogen adsorption energy considerably. In the first part of the chapter, we have considered C_6H_6 as the model system, since it is the main building unit in most of the carbon nanomaterials, and it has been decorated with alkali metal ions. The calculated results have demonstrated that creating a charged surface by doping the alkali metal cations can improve the hydrogen adsorption energy significantly. It has also been shown that, the introduction of a functional group in the model system can alter the hydrogen adsorption energy as well as the binding of the alkali metal cations to the organic system through the well known electronic induction effects. In the second part of the chapter, we have studied the hydrogen adsorption in alkali metal atom decorated cyclic systems like C_4H_4 , C_5H_5 and C_8H_8 . Being electron deficient with respect to the corresponding Hückel aromatic systems, these molecules are found to bind the alkali metal atoms more strongly and the metal site becomes cationic in nature indicating an electron transfer from metal to the carbon surface. These metal sites are found to adsorb hydrogen more efficiently. We have also modelled a cyclic oligomer consisting of alkali metal atom decorated five membered ring as the building unit and $-C\equiv C-$ as the linking group. All these studies indicate that the presence of ionic sites can improve the hydrogen

adsorption properties and the basic principles like electron induction effect and aromaticity can be used to design the stable systems with ionic sites.

In chapter 4, we have discussed the hydrogen adsorption properties of small boron hydride systems decorated with alkali metal atoms. In the first part of the chapter, we have reported results on the hydrogen adsorption in lithium complexes of dihydrodiborate dianion ($\text{B}_2\text{H}_2\text{Li}_2$) and tetrahydrodiborate dianion ($\text{B}_2\text{H}_4\text{Li}_2$). It has been shown that in both these complexes, the Li sites are cationic in nature, and thus bind molecular hydrogen through ion-quadrupole and ion-induced dipole interactions. We have also modelled a one-dimensional nanowire with $\text{C}_6\text{H}_4\text{B}_2\text{Li}_2$ as the repeating unit, which was found to adsorb three hydrogen molecules resulting into a gravimetric density of 9.68 wt% of hydrogen. In the second part of the chapter, we have shown that the hexaborane (6) dianion ($\text{B}_6\text{H}_6^{2-}$) can form a stable complex (salt) with a highly electropositive alkali metal cation (Li^+). Each Li is found to adsorb a maximum of three hydrogen molecules which corresponds to a gravimetric density of 12 wt % of hydrogen. We have also designed a model three-dimensional material with lithium-doped borane as the building block and $-\text{C}\equiv\text{C}-$ as a linking agent. The molecular hydrogen adsorption in this newly designed material corresponds to a gravimetric density of around 7.3 wt%.

Chapter 5 deals with studies on the electronic structure and properties of borane like analogues of aluminium hydrides. Alanes and the complex metal hydrides, alkali metal alانات are found to be promising materials for hydrogen storage. Though boron and aluminium belong to the same group, the hydride chemistry of aluminium is not much explored like boron hydrides. In this study, we have systematically explored the electronic structure and properties of these aluminum hydrides. Here, we have studied different classes of aluminium hydrides, viz., *closo* ($\text{Al}_n\text{H}_{n+2}$), *nido* ($\text{Al}_n\text{H}_{n+4}$), and *arachno* ($\text{Al}_n\text{H}_{n+6}$) alanes, similar to the boranes. All these clusters are found to have large HOMO-LUMO gaps, low

electron affinities, large ionization potentials, and also large enthalpy and free energy of atomization. These exceptional properties can be indicative of their pronounced stability, and hence it can be expected that these complexes can indeed be observed experimentally.

In chapter 6, we discuss the hydrogen adsorption properties of metal atom decorated fullerenes. Light metal atom decorated carbon nanomaterials and hetero atom substituted carbon nanomaterials are found to form important class of hydrogen storage materials. In the first part of the chapter, we have discussed results of study on hydrogen adsorption in alkali metal decorated carbon fullerenes and the effect of the curvature present in fullerene on the metal binding energy as well as the hydrogen adsorption energy. We have considered a range of fullerenes with varying curvature starting from C_{20} to C_{70} and the calculated results indicate that the metal binding energy is higher for the carbon surface with large curvature. In the second part of this chapter, we have modelled a carbon nitride porous fullerene ($C_{24}N_{24}$) through the truncated substitutional doping of carbons with nitrogen atoms. This porous fullerene is found to have six N_4 cavities which can bind with the transition metal atoms strong enough to avoid metal clustering problem observed in transition metals. As the transition metal decorated systems are more suitable for hydrogen adsorption, we have studied these transition metal decorated fullerenes for hydrogen adsorption and the results show that the hydrogen adsorption energies are in the range suitable for hydrogen storage at ambient conditions and they can store hydrogen with a gravimetric density of ~5.0 wt %.

In chapter 7, we present the results on energy storage applications of two-dimensional (2D) carbon materials. Following the synthesis of the 2D carbon allotrope, graphene, large number of 2D carbon nanomaterials and hetero atom containing nanomaterials have been explored. Graphyne and graphdiyne are the new 2D carbon allotropes with a one atom thick layer of carbon sheet having two different types of carbon atoms of sp - and sp^2 -hybridized nature, both having the same symmetry as graphene. Our calculated band structure results

reveal that both these are semiconductors and the band gap in these materials can be tuned by varying the length of the linking chain. More interestingly, the band gap of graphdiyne is found to be 1.18 eV which is very close to silicon band gap and hence can have applications in nano-electronics. Due to the presence of more reactive sp-carbons, these materials are found to bind with alkali metal atoms with improved binding energies and hence stabilize the metal decorated materials. These materials are also found to adsorb sufficiently large amounts of lithium, thus making them suitable for being used as anode materials for lithium batteries. The metal sites in the metal decorated materials are found to be positively charged and adsorb hydrogen with interaction energies in the range of -3.5 to -2.5 kcal/mol. Another class of 2D materials studied are the conjugated micro-porous polymers. Under this category, we considered two different structures based on benzene, 1,3,5-triethynyl (CMP-1) and benzene, 1,3,5-tributadiyne (HCMP-1). In these materials, all the lithium metal atoms adsorbed are above the C₆ rings and can be used for hydrogen adsorption.

Chapter 8 discusses results of our studies on the hydrogen adsorption in three-dimensional porous materials. Porous materials with high surface area are one of the interesting classes of materials particularly for the gas storage applications. Metal organic frameworks (MOFs) are the new class of ordered organic-inorganic hybrid solids composed of metal or metal oxide clusters as building blocks and organic bridges as linkers. Light metal decorated MOFs are shown to have better hydrogen adsorption characteristics as compared to their pristine counterparts. However, in most of the cases, the metal binding energies to the frameworks are less than the corresponding metal cohesive energies leading to the metal clustering problem. Here, we have proposed that the substitutional doping of carbon atoms in C₆ ring with boron can increase the metal binding strength thereby improving the stability of the material. The hydrogen adsorption properties of these modified MOF decorated with Li and Na have been studied and the results reveal that Li decorated

ones can adsorb hydrogen with a gravimetric density of 4.3 wt% whereas the corresponding density in Na decorated system is found to be 7.4 wt%. In another study, we have modelled varieties of super-cubane 3D porous carbon materials with different porosity through the insertion of $\text{-C}\equiv\text{C-}$ groups between the inter- as well as intra-cubane C-C bonds. These porous carbon materials are found to adsorb hydrogen with a gravimetric density of ~ 2.0 wt%.

Chapter 9 deals with the studies on designing new catalyst materials for the oxygen reduction reaction (ORR). The ORR at the cathode of the fuel cell is known to be the main limiting factor in the fuel cells especially at low temperature. The conventional platinum (Pt) based catalysts have the limitations of low availability and high cost which make the fuel cell very expensive. Hence, there is a need to find an alternate non-platinum based catalyst for large scale commercialization of fuel cells. We have studied the catalytic activity of the transition metal (Fe, Co and Ni) decorated graphyne materials towards the ORR. The calculated results reveal that the Fe and Co complexes are active whereas the Ni decorated system is almost inert towards oxygen adsorption. Between the Fe and Co decorated systems, Fe decorated system is more reactive. In acid medium, both Iron and Cobalt decorated systems are observed to follow a more efficient four electron path. In alkaline medium, the reduction on Iron decorated system is through a four electron path while in Cobalt system it is through a two electron path with the formation of hydroperoxide anion. In another study, we have shown that the silicene, silicon analogue of graphene, can be a metal free catalyst for ORR. We have studied the step by step mechanism of ORR on both the single layer and bi-layer silicene. The calculated results reveal that silicene can be a metal free catalyst for ORR.

Finally, the final chapter 10 presents few concluding remarks including discussion on possible further directions in this area of research.

CHAPTER-2

Designing g-CN Based Photocatalyst for Hydrogen Generation Through Solar Water Splitting

2.1 Introduction

As it is discussed in chapter-1, one of the main challenges in developing hydrogen economy is its generation. At present, nearly 95% of the today's hydrogen is produced from steam reforming technique which is found to be the cheapest for hydrogen production on a large scale. However, hydrogen generated from this technique is not clean as it is associated with the CO₂ emission and hydrogen energy can be treated as clean and environmental friendly only when it is generated in a clean way without the emission of greenhouse gases. Hydrogen generation from water through photocatalytic water splitting using the solar energy is an ideal way which does not evolve any harmful byproducts.

Following the development of photo electrochemical cell (PEC) by Fujishima and Honda²⁶ using a semiconductor anode and a metal cathode, varieties of inorganic semiconductors and molecular assemblies have been studied for making an efficient catalyst to generate hydrogen from water with the aid of visible light. Apart from TiO₂, many other transition metal oxides, sulphides, selenides viz. ZnO, SrTiO₃, NaTiO₃, ZnS, CdS, CdSe, etc. have been studied for visible light driven water splitting. Apart from the conventional transition metal containing materials, polymeric semiconductor materials like graphitic carbon nitride are found to have great potential as photocatalyst. In a recent study, Wang et al.²⁹ have reported the melem-based polymeric graphitic carbon nitrides (g-C₃N₄) as a metal-free photocatalyst for visible-light driven hydrogen production through water splitting. g-C₃N₄, with appropriate band structure for overall water splitting along with its high thermal and chemical stability gained lot of interest in designing a metal-free catalyst. However, this material is reported to have a very poor quantum yield of ~0.1% which is attributed to the high recombination rate of electron-hole pairs generated. To overcome this problem, many methods are proposed to tune the properties viz. doping, metal decoration, introducing porosity, making graphene/C₃N₄ composites etc.¹¹⁷⁻¹²⁵ Pan et al.¹²⁶ have shown that the

g-C₃N₄ nanotubes have a delocalised valence top states unlike sheet which is having strongly localized valence top states indicating the larger mobilities in nanotubes. They have also shown that functionalization of these tubes with metals like Pt and Pd can enhance the photocatalytic properties of these nanostructure materials.

In the present study, we studied another polymeric form of graphitic carbon nitride with CN stoichiometry (g-CN) for its photocatalytic activity towards water splitting. Though the g-C₃N₄ form of carbon nitride is studied extensively, the studies on g-CN are very few. Cao et al.¹²⁷⁻¹²⁸ synthesized the g-CN nanotubes through the reaction of cyanuric chloride (C₃N₃Cl₃) with sodium at a temperature of 230 °C with NiCl₂ as a catalyst. The different form of g-CN viz. nanotubes, nanoribbons and microspheres have been synthesized and their room temperature photoluminescence spectra have shown peaks centered around 430-450 nm, due to the band gap emission. These experimental observations indicate that g-CN could be a metal free photocatalyst for solar energy driven water splitting to generate hydrogen. Hence, we have considered different morphologies of g-CN viz. Two-dimensional sheets, one dimensional nanotubes and nanoribbons to study their photocatalytic activity.

2.2 Computational Details

All our spin-polarized periodic density functional theory (DFT) based electronic structure calculations have been carried out using the projector augmented wave (PAW)¹²⁹⁻¹³⁰ potentials as implemented in the first principles based *Vienna ab initio Simulation Package* (VASP).¹³¹⁻¹³² Plane-wave basis sets with an energy cut off of 550 eV have been used for all the elements. The exchange-correlation energy density functional, E_{xc} [ρ] has been treated through the spin-polarized Generalized Gradient Approximation (GGA) of Perdew-Burke-Ernzerhof (PBE).¹⁰³ An energy cut off of 1 x 10⁻⁶ eV is set as the convergence criteria for the electronic self-consistent field iterations. The atomic positions are optimized through the conjugate gradient optimization at constant volume without any symmetry constraints until

the maximum Hellmann–Feynman force on each atom is less than 0.01 eV Å⁻¹. Sufficiently large vacuum of 20 Å has been taken along the z-axis so that the image interactions can be avoided. Automatically generated Gamma centered $9 \times 9 \times 1$ Monkhorst–Pack set of k points were used to sample the Brillouin zone.¹³³ As it is known that the band gaps from PBE functional are underestimated, we have used the more accurate hybrid functional, developed by Heyd, Scuseria, and Ernzerhof (HSE06),¹³⁴ to improve the accuracy of band structure calculations. All the initial geometries and the reported figures are generated using the graphical software Molden.¹³⁵

2.3 Results and Discussion

In the present study we have mainly studied the electronic band structure of (a) single layer two dimensional g-CN sheets, (b) one dimensional nanoribbons and nanotubes, (c) bilayer and multi layer g-CN, (d) effect of non-metal doping on the band structure of g-CN, and (e) metal doping to engineer the band gap.

At first, we will look into the electronic structure of the single layer two-dimensional g-CN. The optimized unit cell and super cell structures of the g-CN using the PBE method are shown in Figure 2.1(a) and 2.1(b) respectively. The optimized cell parameter from PBE method is found to be 7.127 Å with the C-C and C-N bond distances of 1.510 Å and 1.341 Å respectively. The band structure plot of g-CN calculated from the PBE method is shown in Figure 2.1(c) and the corresponding results are reported in Table 2.1. From the PBE calculations, g-CN is found to have a direct band gap of 1.54 eV along the k-point K with conduction band minimum (CB_{min}) and valence band maximum (VB_{max}) located at -5.28 eV and -3.74 eV respectively. However, as it is well known that the band gaps calculated from pure DFT functionals like PBE are underestimated and the hybrid functionals like HSE06 can deliver

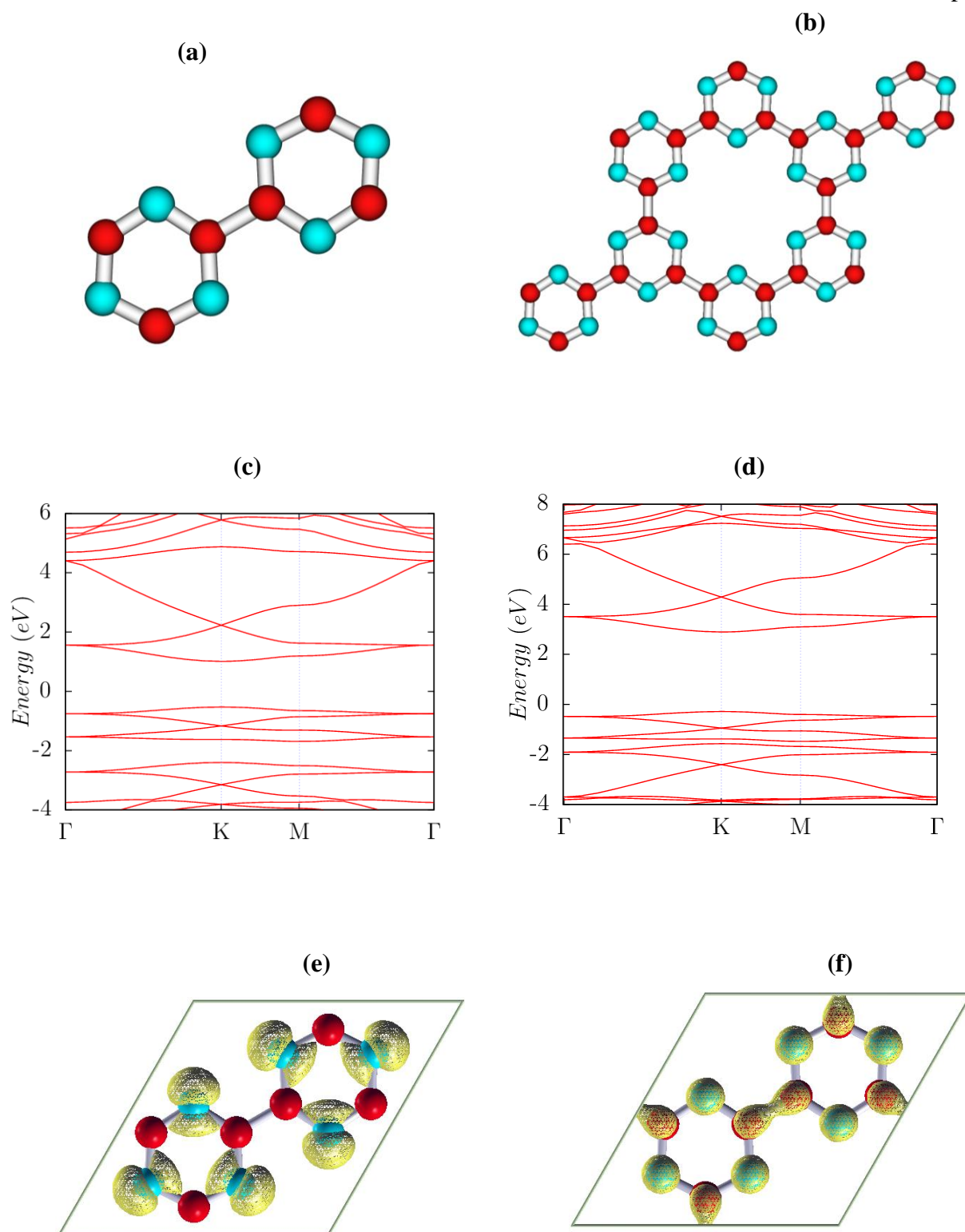


Figure 2. 1. Optimized geometries of the (a) unit cell and (b) 3 x 3 x 1 super cell of g-CN along with its band structure plot using (c) PBE and (d) HSE06 methods and the band decomposed charge density plot of (e) highest valance and (f) lowest conduction states.

Table 2.1. The calculated band structure results of different g-CN nanostructures from PBE and HSE06 methods.

Method	PBE			HSE06		
	E (CB _{min})	E (VB _{max})	BG	E (CB _{min})	E (VB _{max})	BG
Single layer	-3.74	-5.28	1.54	-3.37	-6.55	3.18
Double layer	-3.24	-4.73	1.49	-2.89	-5.99	3.10
Triple layer	-2.60	-4.06	1.45	-2.27	-5.30	3.03
g-CN-P	-3.63	-4.78	1.15	-3.33	-5.84	2.51
g-CN nanoribbons						
g-CNNR-I	-3.99	-5.71	1.72	-3.58	-6.94	3.36
g-CNNR-II	-4.09	-5.74	1.65			
g-CNNR-III	-4.05	-5.66	1.61			
g-CN nanotubes						
(3, 3)	-4.50	-6.31	1.81			
(6, 6)	-3.81	-5.78	1.97			
(9, 9)	-3.73	-5.67	1.93			
(6, 0)	-4.34	-5.99	1.65			
(9, 0)	-3.86	-5.78	1.92			

reasonably good results, we have also calculated the band structure of g-CN using HSE06 method. The band structure g-CN from HSE06 method is shown in Figure 2.1(d) and it can be seen that the band gap from this method is 3.18 eV which is more than double the corresponding value from PBE functional. The CB_{min} calculated from HSE06 method is found to be -3.37 eV which is above the water reduction potential and the VB_{max} is found to be -6.55 eV which is below the water oxidation potential. As the band edge potentials are suitable for the overall water splitting to generate hydrogen, the g-CN can be expected to be a good photocatalyst material for hydrogen generation. Figures 2.1(e) and 2.1(f) shows the band decomposed charge density isosurfaces of the highest valence band (HVB) and lowest conduction band (LCB) respectively. It is clear from the pictures that the HVB mostly originates from the nitrogen 2p states whereas the LCB is originating from the C=C anti-bonding π states. However, as the band gap from HSE06 method is high, it cannot use major

part of the visible region from the solar spectrum and hence it is required to engineer the band gap to enhance the visible light absorption efficiency.

Apart from the single layer 2D g-CN we have also studied the electronic structure of one dimensional (1D) nanotubes (CNNT) and nanowires (CNNR) of g-CN. The optimized cell structures of different nanotubes with varying diameter are reported in Figure 2.2. We have considered two different kinds of CNNT namely the zig-zag and armchair nanotubes. The armchair CNNT are the structures with the chiral index of (n, n) and we have considered three such nanotubes with the index $(3, 3)$, $(6, 6)$ and $(9, 9)$. The $(3, 3)$ and $(9, 9)$ structures look like hexagonal whereas the $(6, 6)$ looks like square from the top view as shown in Figure 2.2. In the case of zig-zag nanotubes with the chiral index $(n, 0)$, we have considered two structures with the index $(6, 0)$ and $(9, 0)$. The $(6, 0)$ structure is like an octagon where as the $(9, 0)$ structure is almost like a circular from the top view. Unlike in 2D g-CN sheet, the C-C and C-N bond distances in these CNNTs are different. The $(3, 3)$ CNNT is found to have two different C-C bond distances of 1.523 Å and 1.536 Å and three different C-N bond distances of 1.335 Å, 1.340 Å and 1.346 Å. The $(6, 6)$ and $(9, 9)$ tubes are found to have almost same C-C bond lengths of around 1.51 Å whereas the corresponding C-N distances are around 1.34 Å. The C-C bond distances are found to be increasing on increasing the diameter of the tube which is in agreement with the previous study. The calculated band structure results using the PBE method are reported in Table 2.1 and we could not perform the HSE06 calculations as the number of atoms in these unit cells is high. The band gaps in $(3, 3)$, $(6, 6)$ and $(9, 9)$ CNNTs calculated through PBE method are found to be 1.81 eV, 1.97 eV and 1.93 eV which indicate that the band gap is initially increasing on increasing the diameter (from $(3, 3)$ to $(6, 6)$) and later it is decreasing with diameter. In the case of the zig-zag CNNTs with band gaps of 1.65 eV and 1.92 eV for $(6, 0)$ and $(9, 0)$ systems respectively, it shows that the band gap is increasing on increasing the diameter. On comparing the PBE band gaps of CNNTs with

2D g-CN, one can understand that the band gaps are larger in CNNTs and visible absorption efficiency is expected to be poor as compared to the 2D g-CN. This band structure results indicate that it requires to modify the band structure so that it can absorb the visible region of the solar spectrum.

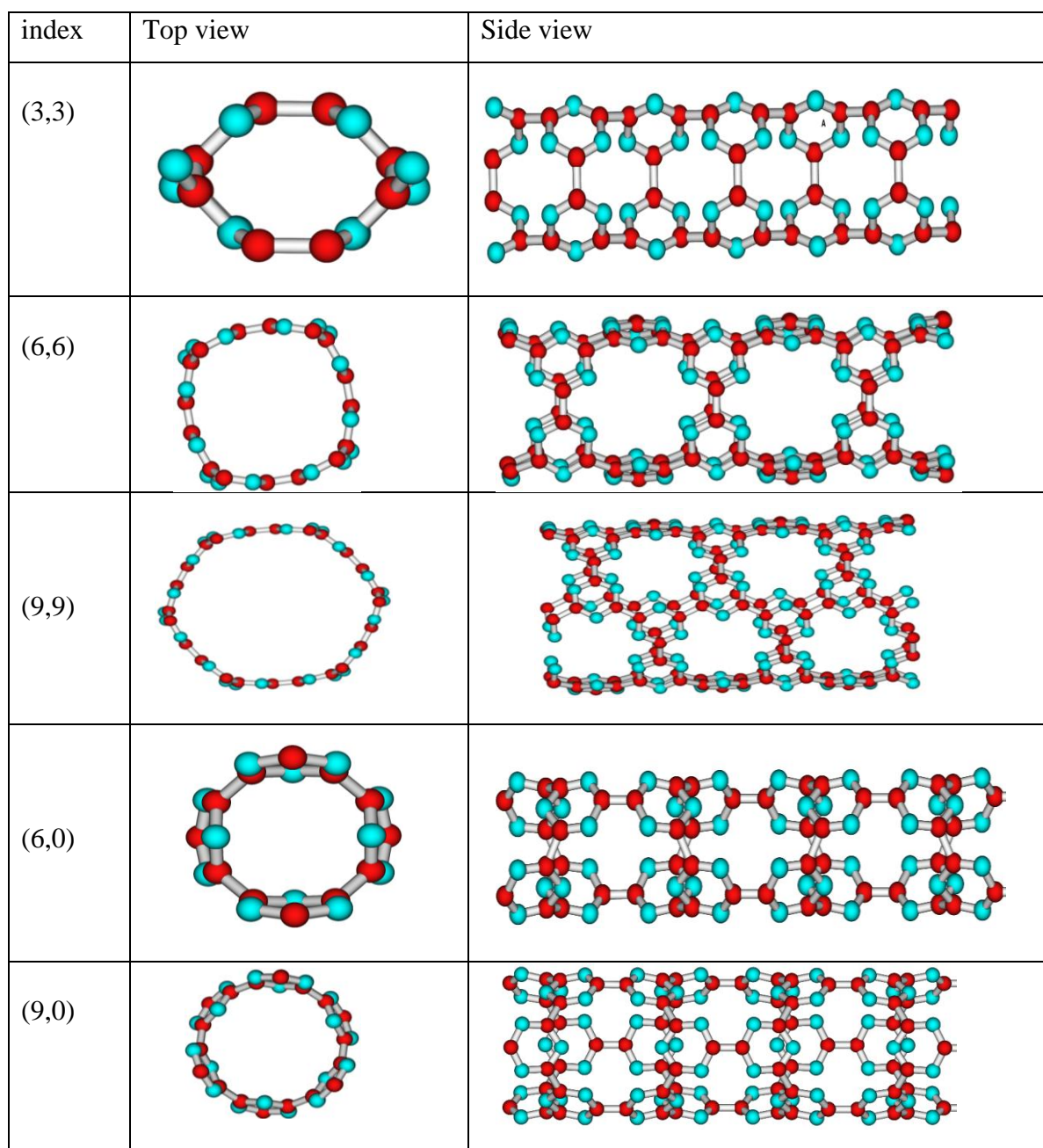


Figure 2.2. Optimized unit cell and super cell structures of different g-CN nanotubes.

In the case of g-CN nanoribbons (CNNR), we have considered three different CNNRs with varying sizes as shown in the Figure 2.3 where all the dangling bonds are saturated with hydrogen atoms. The optimized cell parameter along the periodic direction of the smallest CNNR (CNNR-I) is found to 7.127 Å with two sets of C-C bonds, 1.513 Å and 1.524 Å whereas the C-N bond distances are in the range of 1.341 Å to 1.357 Å. The next larger CNNR (CNNR-II) considered is found to have a width of around 19.15 Å and the periodic

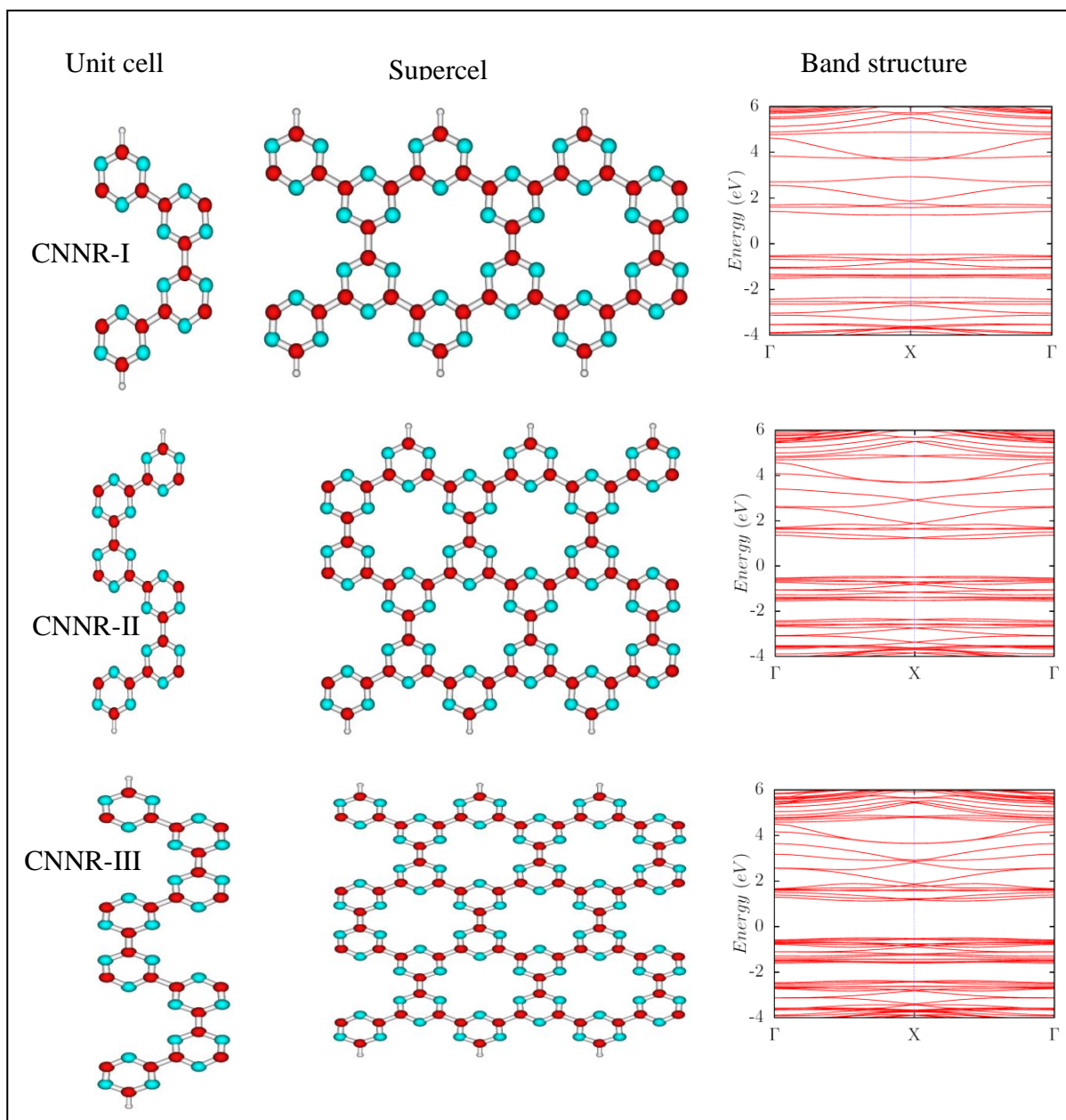


Figure 2.3. Optimized unit cell, supercell and band dispersion plots of three different CNNRs.

cell parameter is calculated to be 7.129 Å. In this CNNR-II, all the C-C bond distances are found to be nearly same (1.51 Å). The largest CNNR considered here (CNNR-III) is found have a width of 25.354 Å and cell parameter is found to be 7.129 Å similar to the CNNR-II and all the C-C bond distances are found to be 1.511 Å. The calculated band structure results for different CNNRs are reported in Table 2.1 and corresponding band dispersion plots are shown in Figure 2.3. It can be observed from the reported results that the band gap in CNNR-I from PBE method is just 1.72 eV whereas it is 3.36 from the HSE06 method which is nearly double to the PBE band gap. It is observed that the band gap in CNNR decreases with increasing the width of the CNNR, with CNNR-II and CNNR-III having band gaps (from PBE) of 1.65 eV and 1.61 eV respectively.

From the above results on both 2D and 1D nanostructures of g-CN it is understood that though the band edge potentials are appropriate for overall water splitting to generate hydrogen and oxygen, the calculated band gaps from HSE06 method are not falling in the visible region and it is required to engineer the band gap to enhance the visible absorption efficiency. Here we have tried different ways to manipulate the band structure of g-CN viz. Effect of multi layers, doping with non-metal elements and doping with metal atoms.

In one of the recent study on g-C₃N₄, through the first principle calculations, Wu et al.¹³⁶ have shown that the bilayer has much better visible light adsorption efficiency as compared to the single layer which is attribute to the interlayer coupling. To study this effect on the g-CN, we have also studied the electronic structure of bilayer as well as the trilayer of g-CN. For the bilayer, we have considered two different stacking modes, AA and AB as it is shown in Figure 2.4. From the PBE calculations, the AB stacking mode is found to be energetically more favourable as compared to the AA mode and the optimized cell parameter of the AB structure is found to be 7.120 Å which is slightly (0.007 Å) less as compared to the single layer g-CN. The inter layer separation from the PBE method is found to be 3.578 Å.

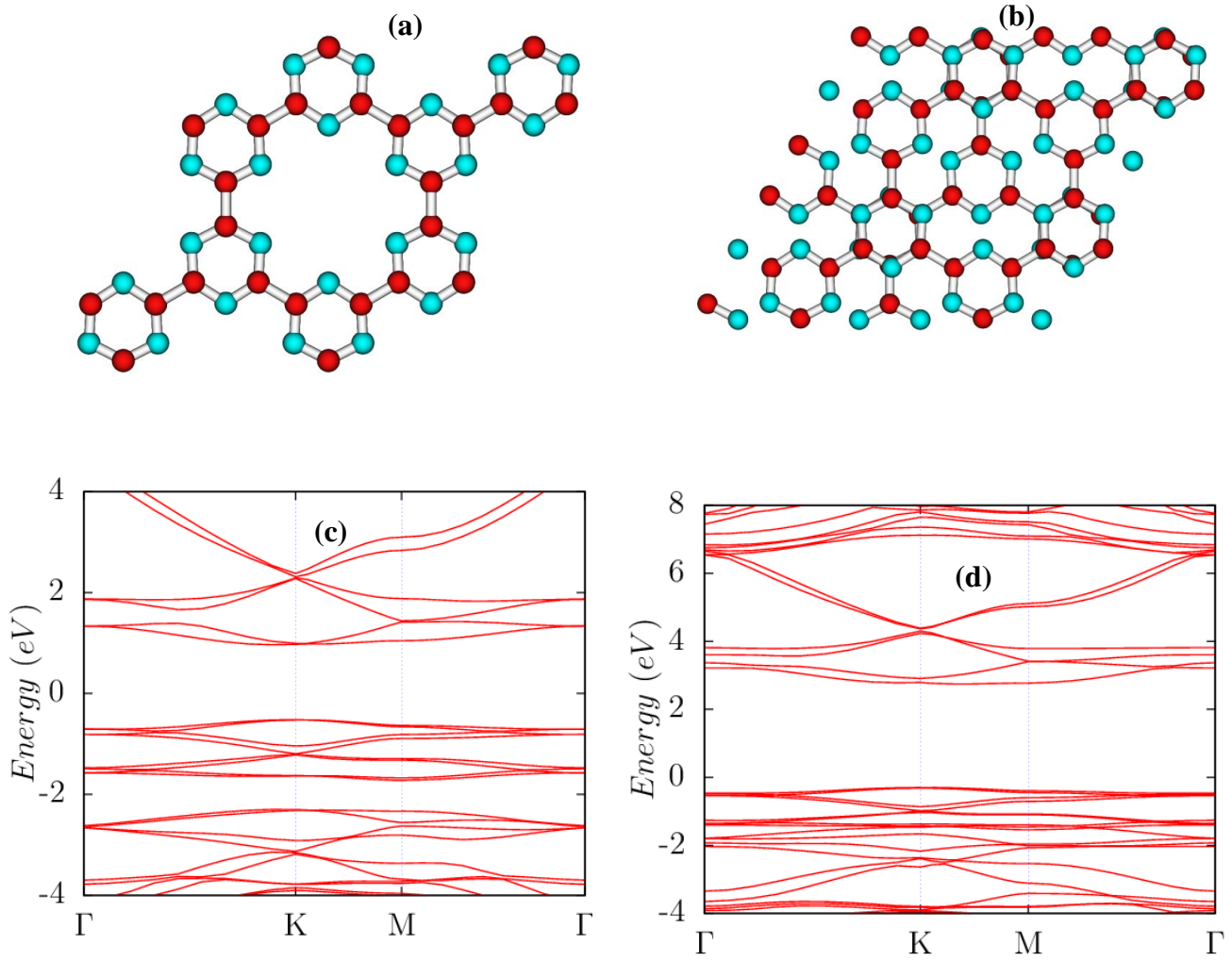


Figure 2.4. Optimized supercell structures of double layer g-CN with (a) AA stacking and (b) AB stacking along with the band structure of AB double layer from (c) PBE and (d) HSE06 functionals.

However, as it is known that the van der Waals interactions are important in this kind of systems, we have also reoptimized the structure using the dispersion corrected PBE (PBE-D) method and the interlayer separation observed to be 3.088 Å. The interlayer interaction energy per unit cell from the PBE-D method is found to be -0.57 eV. This smaller separation as compared to the graphene bilayer separation indicates the strong coupling between the two g-CN layers. The calculated band structure plots from both PBE and HSE06 methods are given in Figure 2.4 and the corresponding results are reported in Table 2.1. From the PBE

calculations, the band gap of bilayer is measured to be 1.49 eV which is 0.05 eV less than the single layer g-CN. However, from the HSE06 calculations, the band gap is measured to be 3.10 eV which is 0.08 eV less as compared to the single layer result from the same method. This indicated that the band gap get reduced by ~ 0.1 eV due to the interlayer coupling in g-CN.

To see the further effect on forming a trilayer, we have also studied the electronic structure of trilayer g-CN. For trilayer, we have added one more g-CN sheet above the bilayer in two different ways, ABA and ABC as it is shown in the Figure 2.5. From the PBE calculations, it has been found that the ABC mode of stacking is energetically more

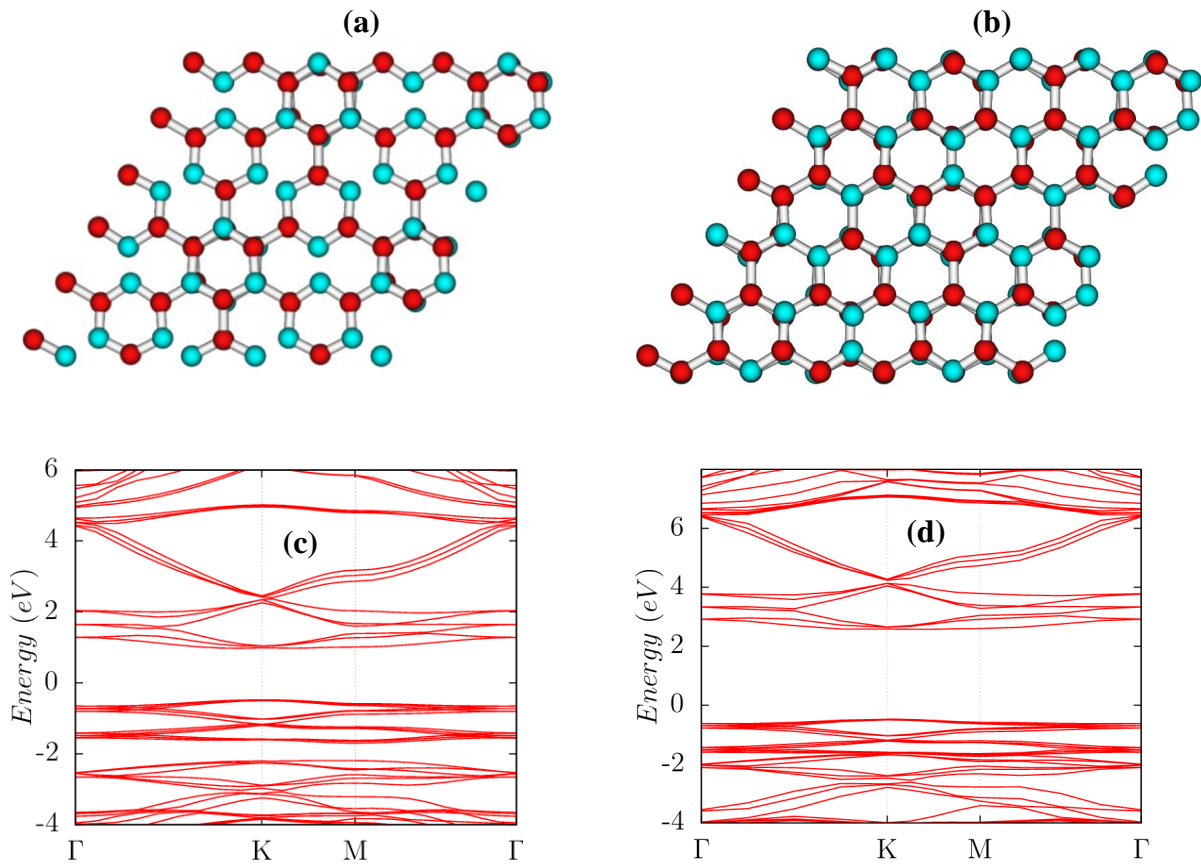


Figure 2.5. Optimized supercell structures of tri-layer g-CN with (a) ABA and (b) ABC stacking along with the band structure of ABC g-CN from (c) PBE and (d) HSE06 methods.

favourable and the optimized cell parameter for the ABC trimer is found to be 7.118 Å slightly less than the dimer cell parameter. The interlayer separation from the PBE-D method is calculated to be around 3.029 Å. The calculated band dispersion plots from both PBE and HSE06 methods are reported in Figures 2.5(c) and 2.5(d) respectively. From the PBE calculations, the band gap is calculated to be 1.45 eV which is 0.04 eV less as compared to the bilayer and 0.09 eV less than that of the single layer. The HSE06 calculations indicate a band gap of 3.03 eV which is 0.07 eV less as compared to the bilayer band gap.

These band structure results on bilayer and trilayer g-CN indicates that the band gap is getting lowered on forming multiple layer of g-CN. Though the theoretical minimum bandgap required for water splitting is 1.23 eV, due to the associated thermodynamic losses and over potentials the photocatalyst should have a bandgap in the range of 2.0 eV to 3.1 eV. From the results discussed above, the band gap of all the systems is at the higher end or above the required band gap.

To further tune the band gap of g-CN, so that the material can absorb the major part of the solar spectrum, we have tried to dope the material with non-metal elements like boron, oxygen, sulphur, and phosphorous. In the case of boron doping, we have considered two structures as shown in Figure 2.6 such that in one of the structure boron is substituted in place of nitrogen and in other the boron is replacing the carbon atom. From the optimized structures, the structure in which boron is replacing the carbon is found to be the minimum energy isomer where the boron is coordinated with once carbon and two nitrogen atoms. However, the band gap of the boron doped system calculated from PBE method is found to be 1.75 eV which is larger as compared to the undoped system and hence the boron doping is not suitable to reduce the band gap. We have also verified the effect of oxygen, sulphur and phosphorous doping on the electronic band structure of g-CN. In these cases, substitution of

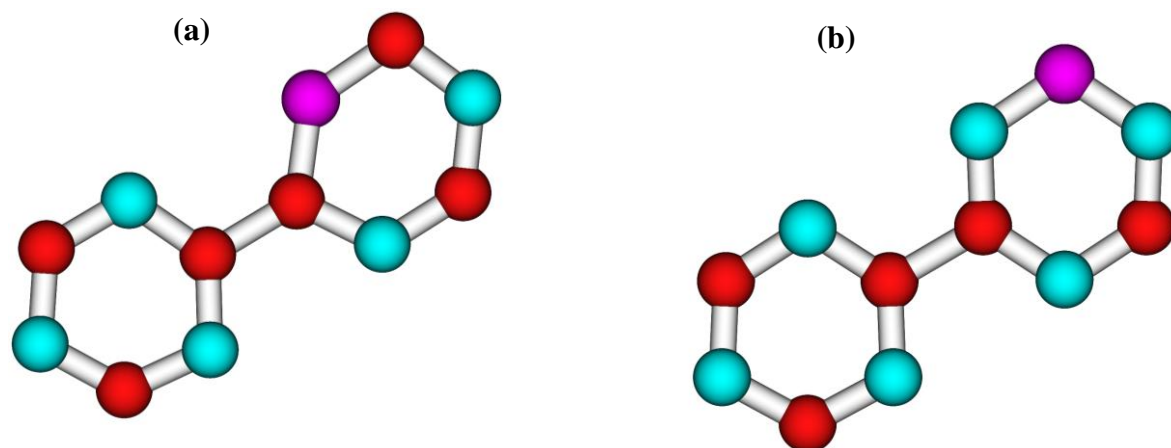


Figure 2.6. Optimized unit cell geometries of the boron substituted g-CN with boron replacing the (a) nitrogen atom and (b) carbon atom.

nitrogen is more preferred as compared to replacing the carbon and the optimized structures of the supercells of doped g-CN are shown in Figure 2.7. In both the cases of oxygen and sulphur doping, donor states very close to the conduction band are created and the band gaps from both PBE and HSE methods are close to zero. The calculated optical spectra also show strong peak at low energies apart from the original g-CN absorption peak around 4.0 eV. These results reveal that both oxygen and sulphur doping are not useful for making a photocatalyst. However, in the phosphorous doped system, the band gap is found to get decreased with appropriate band edge potentials for water splitting. The Band gap obtained from PBE method is observed to be 1.15 eV whereas it is 2.51 eV from the HSE06 method and the details of the band edge potentials are reported in Table 1 whereas the band dispersion plot from the HSE06 method is shown in Figure 2.7(e). The optical absorption also shows the broadening of the g-CN absorption peak towards the low energy region showing the possible improved visible absorption efficiency. These results on non-metal doping reveal that the phosphorous doping will be more suitable to bring down the band gap of g-CN with appropriate band edge potential positions for water splitting.

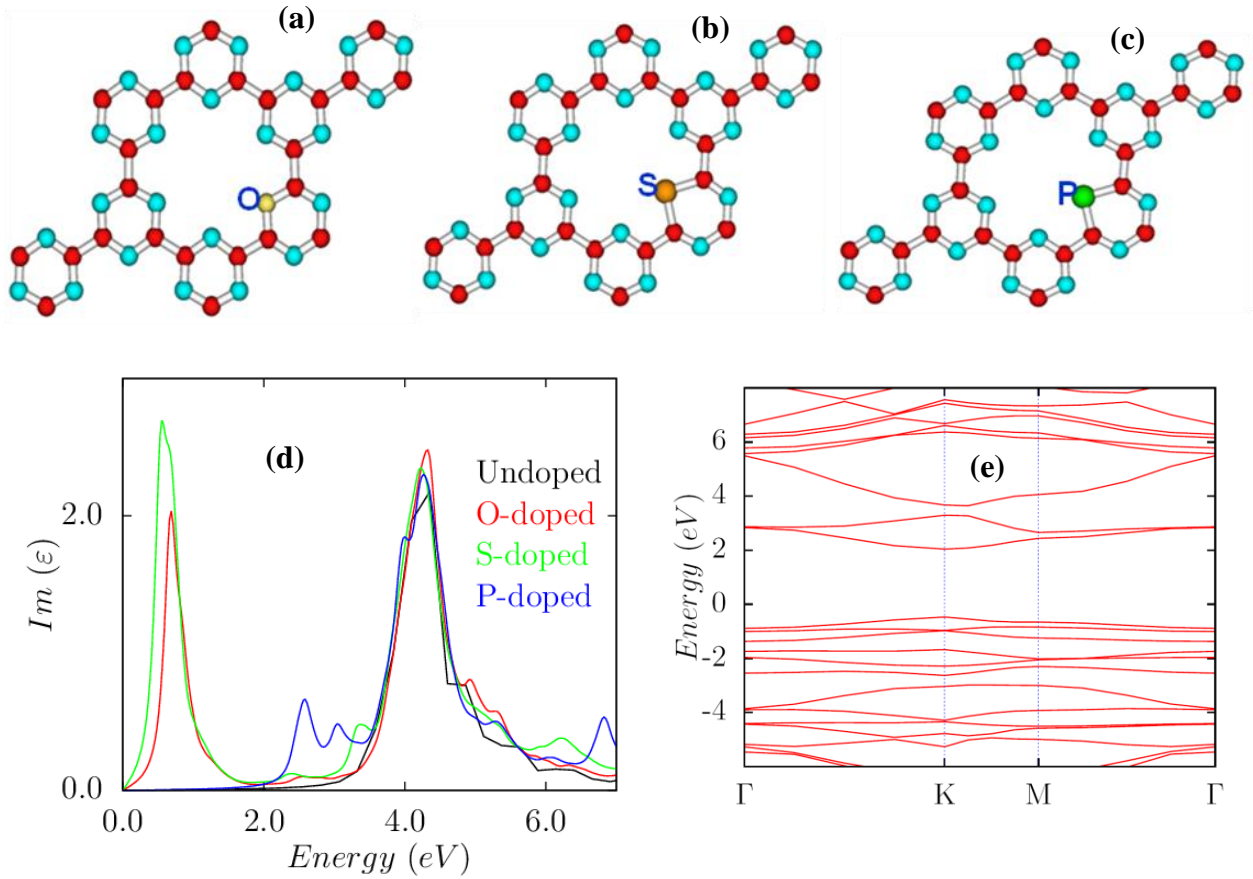


Figure 2.7. Optimized unit cell structures of g-CN doped with (a) Oxygen, (b) Sulphur and (c) Phosphorous and along with their (d) optical spectra and the (e) band structure (HSE06 functional) of phosphorous doped g-CN.

In the case of $g-C_3N_4$, doping with metals like Zn, Pt, Pd etc. is shown to be effective for tuning the bandgap and makes the material more efficient towards the visible light absorption. To verify this effect in the g-CN, we have studied the different metals doping in g-CN viz. Li, Na, Mg, Fe, Co, Ni, Zn, Pt and Pd. In all the cases, the most preferred site for metal binding is found to be the cavity with metal bonding to two or three nitrogen atoms as shown in Figure 2.8(a). The band structure calculations have shown that in all the systems, the Fermi level is located in the conduction band and the band gaps are almost zero making the material a conductor. These results reveal that the metal doping in g-CN is not suitable for making a photocatalyst.

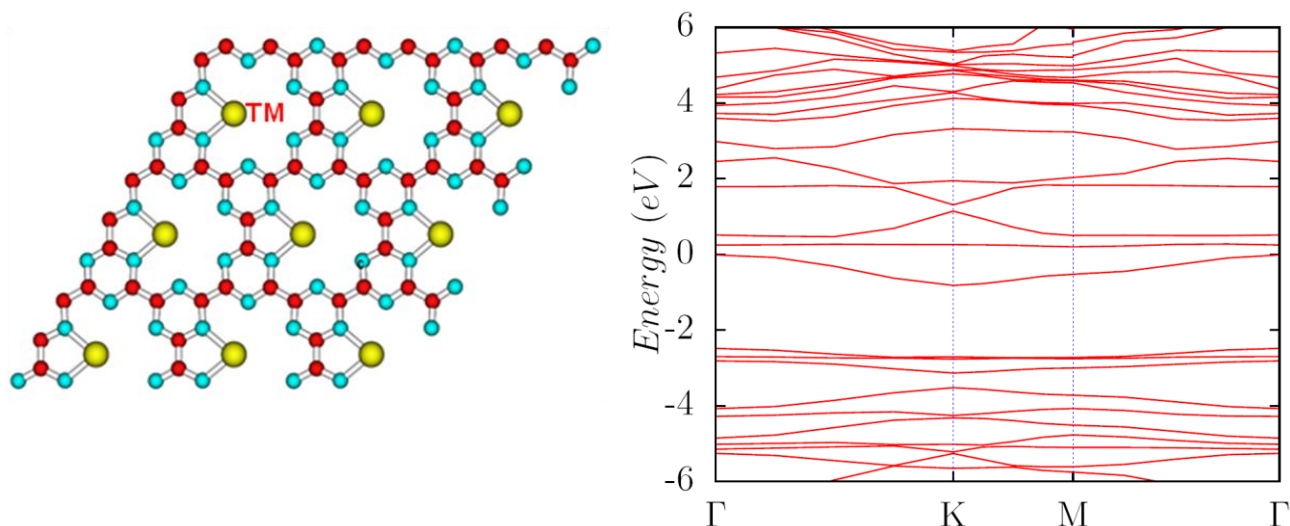


Figure 2.8. (a) Optimized supercell structure of transition metal decorated g-CN and (b) band structure of Fe decorated g-CN.

2.4 Conclusions:

In summary, we have studied the electronic structure of different g-CN nanostructures ranging from 1D nanotubes and nanoribbons to 2D nanosheets and their multiple layers. The band gaps calculated from PBE functional are found to be highly underestimated and hence we have also calculated the band structures using the screened hybrid DFT functional HSE06 which is known to give reasonably good results. All the 1D and single layer 2D g-CN systems are found to have proper band edge potentials for overall water splitting. However, in all the systems the band gap is found to be very large, hence cannot absorb the visible part of the solar spectrum. Formation of double and triple layers is found to bring down the band gap of g-CN sheets. We have also studied the effect of doping with foreign element to modulate the band structure and the phosphorous doping is found to be more efficient.

CHAPTER 3

Hydrogen Adsorption Properties of Alkali Metal Decorated Cyclic Hydrocarbons (C_nH_n -M)

3.1 Introduction

This chapter deals with the studies on hydrogen adsorption properties of different alkali metal decorated cyclic hydrocarbon systems, C_nH_n-M ($n=4, 5, 6$ and 8 and $M=Li$ and Na) and the chapter has been organised as two parts. In the first part, we discuss the effect of charged surface and electron induction effect on hydrogen adsorption properties of alkali metal ion decorated benzene model system. In the second part, we have considered different cyclic hydrocarbons for metal atom decoration and the role of aromaticity in stabilising the metal complex is discussed.

As has been discussed in the introduction chapter, out of many other materials studied for hydrogen storage, carbon nanomaterials are found to be one of the promising materials because of their low molecular weight and high surface area.⁵³⁻⁵⁷ Since the first experiment on hydrogen adsorption in carbon nanotubes reported by Dillon *et al.*,⁵⁸ different people have reported different hydrogen storage capacities of carbon nanotubes. Recently Kiran *et al.*¹³⁷ and Weck *et al.*¹³⁸ reported a hydrogen storage capacity of about 8-9 wt% using transition metal doped organometallic systems.

The important issue in the first part of our study is how to model the hydrogen adsorption properties in carbon nanomaterials. In order to address this issue, we have considered a six membered unsaturated carbon ring, which is the main building block in all carbon nanomaterials and metal organic frameworks, as our model system to mimic the hydrogen adsorption in CNT, MOF etc. In the actual carbon nanomaterials, the surrounding environment of the six membered carbon rings may deplete or enhance the electron density around the ring. The effect of such electronic induction or perturbation on the hydrogen adsorption has been studied by introducing several electron donating and withdrawing groups in the model system of 6-membered carbon ring. In addition, we have also made an attempt to study the effect of ionic surface on the hydrogen adsorption. The model system doped

with the alkali metal ion (sodium or lithium ions) has been chosen as an example for the charged surface to achieve better hydrogen storage as compared to the bare carbon materials. Since alkali metal cations are found to bind with maximum number of hydrogen molecules,¹³⁹ sodium and lithium ions have been chosen for doping in the model benzene system. We have also studied the effect of substituent by varying the different functional groups from electron donating as well as electron withdrawing groups covering the alkali metal cation doped benzene ring.

In the second part, our approach is to use the concept of aromaticity¹⁴⁰⁻¹⁴² of organic molecular systems for developing a new stable material for hydrogen storage. The concept of aromaticity was first introduced by Kekule¹⁴³ for explaining the extraordinary stability of benzene, with the corresponding quantum mechanical explanation given by Pauling¹⁴⁴⁻¹⁴⁶ later, and by Huckel through his renowned $(4n+2)$ π -electron rule.¹⁴⁷ Aromaticity is a manifestation of electron delocalization in closed circuits, either in two or in three dimensions. It is often defined by referring to a series of characteristics, such as, 1) highly symmetric delocalized structures, 2) enhanced thermodynamic stability and 3) reduced reactivity relative to non-aromatic conjugated hydrocarbons etc.¹⁴⁰⁻¹⁴² Recently, Pierrefixe and Bickelhaupt¹⁴⁸⁻¹⁴⁹ have given a quantitative Kohn-Sham molecular orbital (MO) based explanation for the aromaticity of simple organic molecular systems. Initially, the concept of aromaticity was restricted to cyclic organic molecules with an occasional mention of inorganic molecules such as borazine, which is also known as inorganic benzene. In recent times, this concept has been applied in many fields like metal clusters to explain their extraordinary stability.¹⁵⁰⁻¹⁵² Zhang *et al.*¹⁵³ have shown that the charged fullerene surface can act as high-capacity hydrogen storage media.

Keeping all these requirements in mind, in what follows, we will investigate the following organic molecular systems, such as, C_nH_n , ($n=4-8$, cyclo-butadiene (C_4H_4), cyclo-

pentadienyl radical (C_5H_5), benzene (C_6H_6) and cyclo-octatetraene (C_8H_8)) and their alkali metal-doped complexes for hydrogen adsorption. The interaction of H_2 with an alkali metal atom is through the charge-induced electrostatic interaction rather than Dewar-Chatt-Duncanson type of interactions¹⁵⁴ (where electrons from H_2 σ -orbital are partially transferred to the vacant d-orbitals of the transition metal atoms). Such interactions are especially favourable for the easy desorption of hydrogen molecules.

3.2 Computational details

In the present study, all the energy calculations and geometry optimization have been performed by using the electronic structure theory based GAMESS¹⁵⁵ suite of programs. We have employed different density functional theory (DFT) based exchange-correlation energy functionals like, pure Hartree-Fock exchange functional and Lee-Yang-Parr correlation functional (HLYP), Becke's three-parameter exchange functional and Lee-Yang-Parr correlation functional (B3LYP) as well as One-parameter Progressive (HOP) correlation functionals.^{104-106, 156-158} Although the performance of the DFT based exchange-correlation functionals is satisfactory in most of the cases, most of the existing functionals are not good enough for the description of weak interactions. Hence, we have also employed the second order Møller-Plesset (MP2) perturbation method for all the systems. In addition, we have also employed in the present study, a new exchange-correlation energy density functional, M06, proposed by Zhao and Truhlar.¹⁰⁷⁻¹¹⁰ We have used the extensive split-valence basis sets with diffuse and polarization functions, 6-31++G(2d,2p), and also the Dunning type correlation-consistent basis set, aug-cc-pVTZ. In order to characterize the aromatic nature of all the complexes considered in the present study, we have followed two important criteria, which are based on the magnetic as well as the geometric property, namely the nucleus-independent chemical shifts (NICS)^{141, 159} and the harmonic oscillator model of

aromaticity (HOMA)¹⁶⁰⁻¹⁶² respectively. The HOMA aromaticity index is calculated by the following formula, as shown in Eq. (3.1)

$$HOMA = 1 - \frac{\alpha}{n} \sum_n \left(R_{opt} - R_i \right)^2 \quad (3.1)$$

where, n is the number of bonds taken into the summation, α is a normalization constant (for C-C bonds $\alpha = 257.7$). For C-C bonds R_{opt} is equal to 1.388 Å and R_i is the running bond length. The NICS, as proposed by Schleyer and co-workers, is based on the π -electron ring current that is induced when the system is exposed to external magnetic fields.¹⁵⁹ It is defined as the negative value of the absolute shielding, computed as the ring center or at some other interesting point of the system. In addition, electron localization function (ELF)¹⁶³ along with charge density analysis has also been performed to characterize the bonding as well as the charge localization feature in the alkali metal atom doped organic molecular systems. The initial geometries, all the structures, ELF, and the charge density have been obtained from the graphical software Gabedit.¹⁶⁴

3.3 Results and discussion

3.3.1 Role of charged surface and the electronic induction effect

3.3.1.1 Interaction of molecular hydrogen with the model system and its substituted derivatives

After the initial geometry optimization of the model system (C_6H_6), the interaction of molecular hydrogen with the model system has been investigated through electronic structure calculations. Molecular hydrogen is allowed to interact with the benzene molecule along all possible directions and the minimum energy structure is found to be the structure in which H_2 molecule is perpendicular to the carbon ring. The interaction energy of molecular hydrogen with benzene calculated by MP2/6-31++G(2d,2p) method is found to be less (-1.664 kcal/mole) and the minimum carbon-hydrogen distance is 2.97 Å. This can be attributed to

the low reactivity of the benzene ring towards molecular hydrogen due to its high aromatic stability. In order to modulate or tune the binding energy of molecular hydrogen with the π electron cloud of the model system, we have perturbed the electron density distribution on the benzene ring by introducing different functional groups. The extent of perturbation can be quantified by Hammett's constant of the substituting group, depending on the nature of the substituents.¹⁶⁵⁻¹⁶⁶

The electron donating or withdrawing functional group in the benzene ring can cause its π electron cloud to be enhanced or depleted and affect its interaction energy with the hydrogen molecule. Evidently, from the results shown in Table 3.1 we find that the interaction of molecular hydrogen with the substituted model system is always found to be stronger than that of the benzene irrespective of the nature of the substituents. It clearly reveals that the molecular hydrogen can interact favorably with electron deficient as well as electron rich centre. It should be mentioned that the interaction energy calculated by B3LYP method is always found to be positive indicating the unbound nature of the hydrogen molecule to the model system. These results indicate that an accurate treatment of electron correlation is very essential to study the hydrogen adsorption.¹⁶⁷⁻¹⁶⁸ The results presented here also show that the MP2 results are more reliable than the B3LYP results. In this connection, it is worthwhile to mention about the work by Grimme and co-workers¹⁶⁹⁻¹⁷⁰ who proposed that the double-hybrid density exchange-correlation functionals can treat the electron correlation effect for such weakly interacting systems with a reasonable accuracy.

The present results suggest that modifying the carbon surface by introducing different substituents will not lead to considerable improvement in the hydrogen adsorption. We have carried out a detailed study on the effect of creating a charged surface on the benzene ring for an efficient molecular hydrogen adsorption by doping alkali metal cation into the organic system. Weber *et al.*¹⁷¹ have recently studied the interaction of anions with the fluorinated

benzene systems and shown that all anions (Cl^- , I^- and SF_6) prefer hydrogen bonding to the hydrogen atoms of the fluorine substituted benzene ring despite the positive charges of the carbon atoms.

Table 3.1: Interaction of molecular hydrogen with the model system and its derivatives

System	MP2 Binding energy(kcal/mol)	Charge on H_2 (a.u)
$\text{C}_6\text{H}_6\cdots\text{H}_2$	-1.67 (-1.66) ^a	-0.007
$\text{NH}_2\text{-C}_6\text{H}_5\cdots\text{H}_2$	-1.91 (-1.91)	-0.018
$\text{CH}_3\text{-C}_6\text{H}_5\cdots\text{H}_2$	-1.93 (-1.93)	-0.002
$\text{COOH-C}_6\text{H}_5\cdots\text{H}_2$	-1.78 (-1.76)	0.0039
$\text{CN-C}_6\text{H}_5\cdots\text{H}_2$	-1.82 (-1.81)	-0.005
$\text{NO}_2\text{-C}_6\text{H}_5\cdots\text{H}_2$	-1.76 (-1.75)	-0.021

^aThe interaction energies given in parenthesis are BSSE corrected values

3.3.1.2 Hydrogen adsorption on alkali metal cation doped model system: Effect of charged surface

The optimized structures of the alkali metal cation doped benzene ring and the geometry during interaction with molecular hydrogen are shown in Figures 3.1(a) and 3.1(b). The interaction energy of the lithium and sodium cations with benzene, calculated by MP2/6-31++ G(2d,2p) method is found to be -42.38 and -28.87 kcal/mol, respectively. The corresponding experimental binding energy of the Li^+ and Na^+ are -38.5 ± 3.1 and -22.1 ± 1.5 kcal/mol, respectively.¹⁷²⁻¹⁷³ The large difference in these two interaction energy values can be attributed to the ionic radii of Na and Li cations which play an important role in such electrostatics induced cation- π electron cloud interactions.

In Na^+ doped system, the first molecular hydrogen binding energy is found to be -3.07 kcal/mol and the charge on the cation calculated by the Mulliken population analysis method is reduced from 0.671 to 0.542 a.u. Similarly, we have also calculated the adsorption energy of subsequent hydrogen molecules and the corresponding interaction energy is found to be gradually decreasing in the range of -2.80 to -0.89 kcal/mol. Interestingly, the decrease in the

binding energy of hydrogen molecules is found to show good correlation with the residual charge on the sodium cation in $C_6H_6Na^+(H_2)_n$, as shown in Table 3.2. In the case of Li^+ doped systems, the hydrogen molecule interaction energy is found to be higher (~43%) than that of Na^+ case. For instance, the first hydrogen molecule is associated with a binding

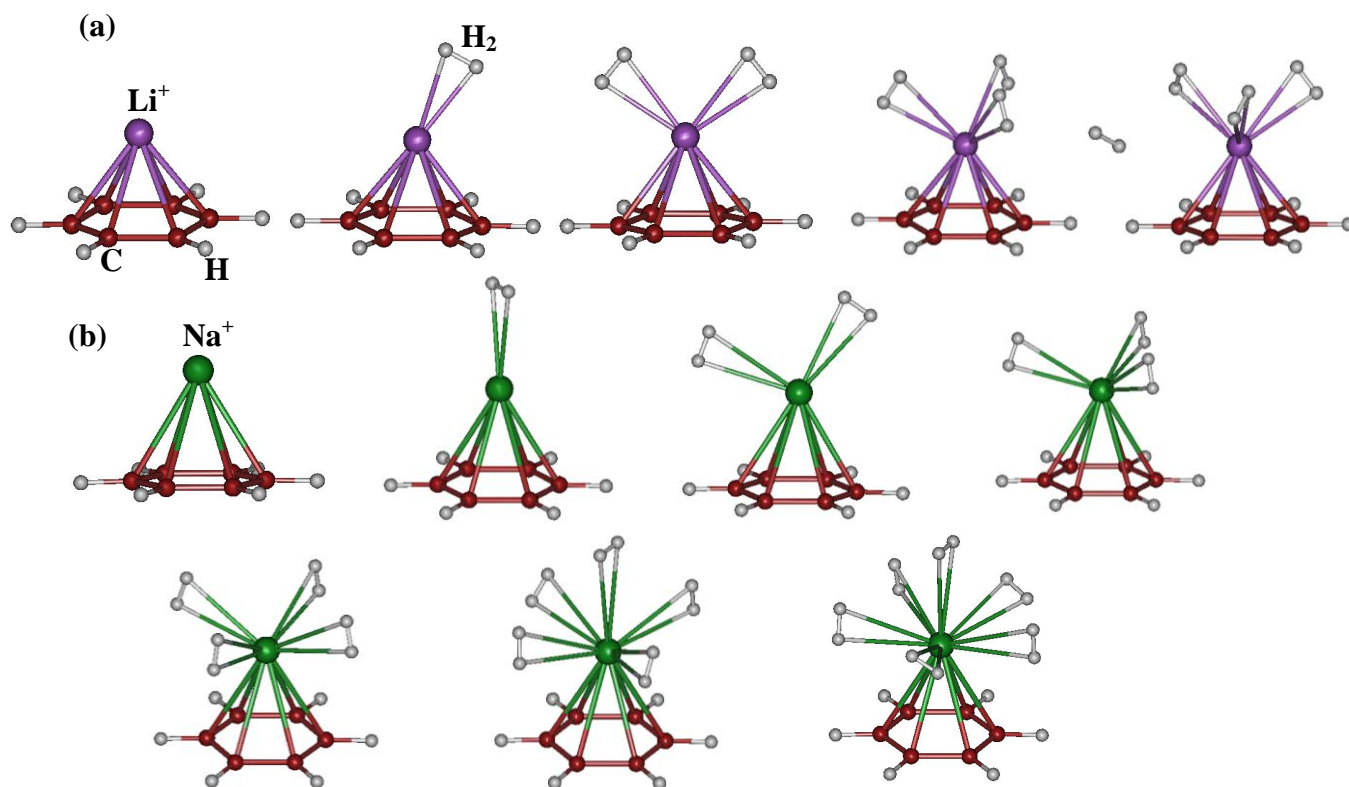


Figure 3.1 Interaction of molecular hydrogen with (a) Li^+ -doped $[C_6H_6Li^+(H_2)_n, n=1-4]$ and (b) Na^+ -doped $[C_6H_6Na^+(H_2)_n, n = 1-6]$ model system.

energy of -5.3 kcal/mol and the interaction energy of the subsequent hydrogen molecules also follows a similar trend as that of sodium doped system. It is important to note that although the adsorption energy is higher in Li^+ doped system, the maximum number of hydrogen molecules that can be adsorbed per Li^+ cationic site is found to be only three and the additional hydrogen molecules are found to move away as shown in Figure 3.1(a). The variation of BSSE corrected binding energy values with increase in the number of hydrogen molecules adsorbed at the cationic site in $C_6H_6Li^+$ and $C_6H_6Na^+$ is schematically represented

in Figure 3.2. It can be seen from Figure 3.2 that the effect of electron correlation is very significant for the case of hydrogen adsorption energy. Due to the smaller ionic radius as

Table 3.2: Interaction of hydrogen molecules with the alkali metal cation (Li^+ and Na^+) doped model systems

	Binding energy (kcal/mol)		Charge on Na (a.u)	
	B3LYP	MP2	B3LYP	HF
$\text{C}_6\text{H}_6\text{-Na}^+(\text{H}_2)_1$	-2.62 (-1.82) ^a	-3.08 (-3.07)	0.542	0.604
$\text{C}_6\text{H}_6\text{-Na}^+(\text{H}_2)_2$	-4.50 (-4.16)	-5.91 (-5.87)	0.492	0.525
$\text{C}_6\text{H}_6\text{-Na}^+(\text{H}_2)_3$	-5.97 (-4.99)	-8.69 (-8.67)	0.410	0.481
$\text{C}_6\text{H}_6\text{-Na}^+(\text{H}_2)_4$	-6.78 (-5.86)	-11.65 (-11.37)	0.235	0.341
$\text{C}_6\text{H}_6\text{-Na}^+(\text{H}_2)_5$	-7.17 (-4.72)	-13.37 (-12.87)	0.204	0.358
$\text{C}_6\text{H}_6\text{-Na}^+(\text{H}_2)_6$	-6.89 (-3.53)	-14.90 (-13.76)	0.215	0.307
$\text{C}_6\text{H}_6\text{-Li}^+(\text{H}_2)_1$	-4.11 (-3.65)	-5.38 (-5.35)	0.333	0.384
$\text{C}_6\text{H}_6\text{-Li}^+(\text{H}_2)_2$	-5.94 (-5.25)	-9.28 (-9.03)	0.255	0.267
$\text{C}_6\text{H}_6\text{-Li}^+(\text{H}_2)_3$	-6.79 (-5.86)	-12.48 (-11.74)	0.194	0.237
$\text{C}_6\text{H}_6\text{-Li}^+(\text{H}_2)_4$	-7.01 (-5.63)	-13.76 (-13.30)	0.157	0.292

^aThe interaction energies given in parenthesis are BSSE corrected values

well as the high effective charge density of the lithium ion, the steric hindrance between the hydrogen molecules around the lithium ion is expected to be more than that for a sodium ion. In addition, the ion-hydrogen molecule bond distance is also observed to be shorter in case of lithium ion than the sodium case. This might be one of the reasons why Li^+ ion cannot accommodate more than three hydrogen molecules.

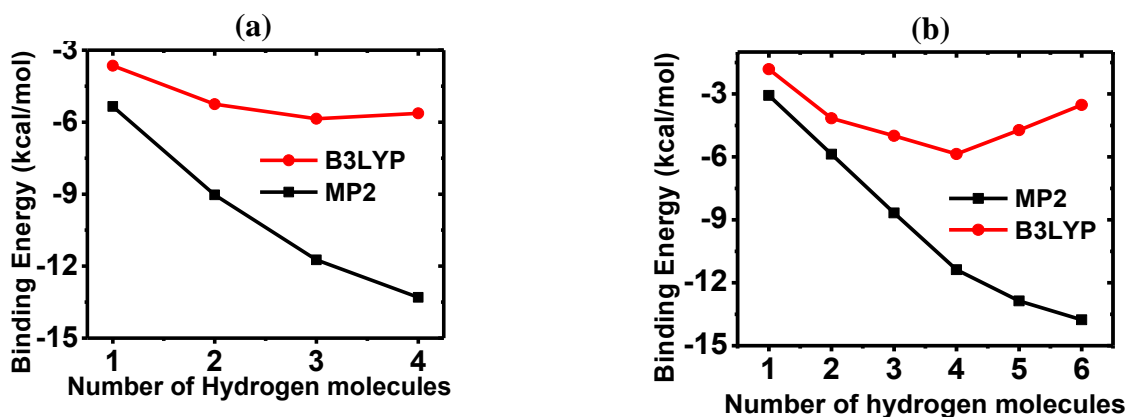


Figure 3.2 Variation of binding energy with increase in the number of hydrogen molecules adsorbed at the cationic site in (a) $\text{C}_6\text{H}_6\text{Li}^+$ and (b) $\text{C}_6\text{H}_6\text{Na}^+$.

3.3.1.3 Tuning the hydrogen adsorption energy in doped model system: Role of electron induction effect

We have used the concept of electronic induction and mesomeric effect by substituting different functional groups in the benzene ring to tune the binding energy of metal cations with the carbon surface as well as the hydrogen adsorption energy in alkali metal cation doped benzene derivatives. Let us first discuss the substitution effect on the binding of alkali metal cations with the benzene ring and the corresponding results are reported in Table 3.3(a). The interaction energy calculated by MP2/6-31++G(2d,2p), between sodium cation and benzene is -28.87 kcal/mol. However, when the substituents are varied from aniline to nitrobenzene, the interaction energy of the alkali metal cation with the aromatic ring is found to decrease by about 50%. Interestingly, the difference in the charge of the sodium cation present in these two systems is found to be rather less (5%). The variation in the binding energy of the cation is attributed to the balancing act of inductive effect due to the difference in the electronegativity of the substituents and the mesomeric effect (resonance effect) arising from the delocalization of the π electrons within the system. Similarly, one can correlate the effect of different substituents on the charge located at the cationic site from the results reported in Table 3.3(a). In general, the electron withdrawing groups will increase the charge on the cations while the reverse is true for the case of electron donating groups. For instance, the charges evaluated by the HF/6-31++G(2d,2p) reveal that the $-\text{COOH}$, $-\text{CN}$ and $-\text{NO}_2$ groups can cause more ionic character at the cationic site than that of the unsubstituted benzene-cation complex, indicating their electron withdrawing nature. Similarly, the $-\text{NH}_2$ and $-\text{CH}_3$ groups reduces the cationic charge of the cation revealing their electron donating nature. Although $-\text{NH}_2$ is an electron withdrawing group in terms of inductive effect, its mesomeric effect is dominating and makes it an electron donating group. Amino and methyl groups present in aniline and toluene, respectively, being

electron donating groups (+ve inductive groups), the π electron density can be enriched around the benzene ring, thus making the system more interactive towards the cation as compared to the unsubstituted benzene ring. In the case of nitrile, carboxylic and nitro group substituents, which act as electron withdrawing groups (-ve inductive group), the π -electron density is depleted and thereby, the interaction between the cation and the aromatic system is decreased. The order of the interaction energy of the cation with the model system is found to follow the order of inductive effect due to the different functional groups, viz., $\text{NO}_2 > \text{CN} > \text{COOH} > \text{H} > \text{CH}_3 > \text{NH}_2$. The higher binding energy of the cations is also one of the prerequisite conditions while considering the stability of the materials towards recycling or desorbing the molecular hydrogen.

Let us now turn to the discussion on the nature of the hydrogen adsorption energies. From the interaction energy values reported in Table 3.3(b), it is clearly evident that when the substituent is varied from more electron donating in nature ($-\text{NH}_2$) to electron withdrawing ($-\text{NO}_2$) or from +ve inductive to -ve inductive effect, the hydrogen adsorption energy increases gradually. The range of variation in the adsorption energy is found to be significant which is nearly 30% of the total adsorption energy. The adsorption energy as well as the maximum number of hydrogen molecules that can be adsorbed per cation is governed by the charge present on the alkali metal cation and cation-molecular hydrogen distance. As we discussed above, the charge on the alkali metal cation increases when the nature of the functional groups is varied from electron donating to electron withdrawing which in turn affects the interaction energy of hydrogen molecules significantly (in the range of -9.56 to -13.94 kcal/mol). Thus, our results demonstrate that it is possible to tune the hydrogen adsorption energy by changing the functional groups judiciously. Similar results can also be expected in different carbon based materials and metal-organic frameworks.

Table 3.3 Effect of substituents on the metal and hydrogen interaction

System	Binding energy(kcal/mol)		Charge on the cation (a.u)	
	B3LYP	MP2	B3LYP	HF
(a) on the interaction of the alkali metal cation with model system				
$\text{C}_6\text{H}_6\text{--Na}^+$	-25.53 (-25.30) ^a	-28.89 (-28.87)	0.671	0.730
$\text{NH}_2\text{--C}_6\text{H}_5\text{--Na}^+$	-31.44 (-30.85)	-34.38 (-33.60)	0.676	0.723
$\text{CH}_3\text{--C}_6\text{H}_5\text{--Na}^+$	-27.39 (-27.13)	-30.99 (-30.69)	0.665	0.718
$\text{COOH--C}_6\text{H}_5\text{--Na}^+$	-20.23 (-19.43)	-25.28 (-24.57)	0.695	0.752
$\text{CN--C}_6\text{H}_5\text{--Na}^+$	-15.24 (-14.99)	-19.75 (-19.41)	0.711	0.763
$\text{NO}_2\text{--C}_6\text{H}_5\text{--Na}^+$	-12.87 (-12.41)	-17.78 (-17.24)	0.712	0.766
$\text{C}_6\text{H}_6\text{--Li}^+$	-39.03 (-38.78)	-42.39 (-42.38)	0.579	0.579
$\text{NH}_2\text{--C}_6\text{H}_5\text{--Li}^+$	-46.28 (-44.80)	-48.82 (-46.89)	0.598	0.606
$\text{CH}_3\text{--C}_6\text{H}_5\text{--Li}^+$	-42.07 (-41.73)	-45.75 (-45.35)	0.584	0.586
$\text{COOH--C}_6\text{H}_5\text{--Li}^+$	-33.20 (-32.24)	-38.08 (-37.25)	0.585	0.588
$\text{CN--C}_6\text{H}_5\text{--Li}^+$	-26.11 (-25.86)	-31.24 (-30.89)	0.597	0.600
$\text{NO}_2\text{--C}_6\text{H}_5\text{--Li}^+$	-24.06 (-23.36)	-29.12 (-28.28)	0.602	0.606
(b) on the interaction of molecular hydrogen with alkali-metal-cationdoped model system				
$\text{C}_6\text{H}_6\text{--Na}^+(\text{H}_2)_6$	-6.89 (-3.53) ^a	-13.22 (-11.53)	0.215	0.619
$\text{NH}_2\text{--C}_6\text{H}_5\text{--Na}^+(\text{H}_2)_6$	-5.98 (-2.38)	-12.66 (-9.56)	0.249	0.635
$\text{CH}_3\text{--C}_6\text{H}_5\text{--Na}^+(\text{H}_2)_6$	-6.43 (-3.01)	-13.52 (-11.99)	0.207	0.649
$\text{COOH--C}_6\text{H}_5\text{--Na}^+(\text{H}_2)_6$	-8.24 (-5.91)	-14.69 (-13.18)	0.184	0.627
$\text{CN--C}_6\text{H}_5\text{--Na}^+(\text{H}_2)_6$	-8.51 (-5.68)	-15.42 (-13.94)	0.210	0.603
$\text{NO}_2\text{--C}_6\text{H}_5\text{--Na}^+(\text{H}_2)_6$	-8.95 (-6.09)	-14.53 (-11.86)	0.202	0.588
$\text{C}_6\text{H}_6\text{--Li}^+(\text{H}_2)_6$	-7.92 (-6.53)	-13.09 (-12.13)	0.138	0.570
$\text{NH}_2\text{--C}_6\text{H}_5\text{--Li}^+(\text{H}_2)_6$	-7.57 (-6.08)	-13.76 (-13.03)	0.168	0.623
$\text{CH}_3\text{--C}_6\text{H}_5\text{--Li}^+(\text{H}_2)_6$	-7.02 (-5.83)	-12.40 ^b	0.235	0.605
$\text{COOH--C}_6\text{H}_5\text{--Li}^+(\text{H}_2)_6$	-8.72 (-7.15)	-14.59 (-13.84)	0.229	0.713
$\text{CN--C}_6\text{H}_5\text{--Li}^+(\text{H}_2)_6$	-9.24 (-7.51)	-15.35 ^b	0.197	0.682
$\text{NO}_2\text{--C}_6\text{H}_5\text{--Li}^+(\text{H}_2)_6$	-9.95 (-8.37)	-16.24 (-15.04)	0.191	0.658

^a The interaction energies given in parenthesis are BSSE-corrected values. ^b The SCF energy of the monomers not converged.

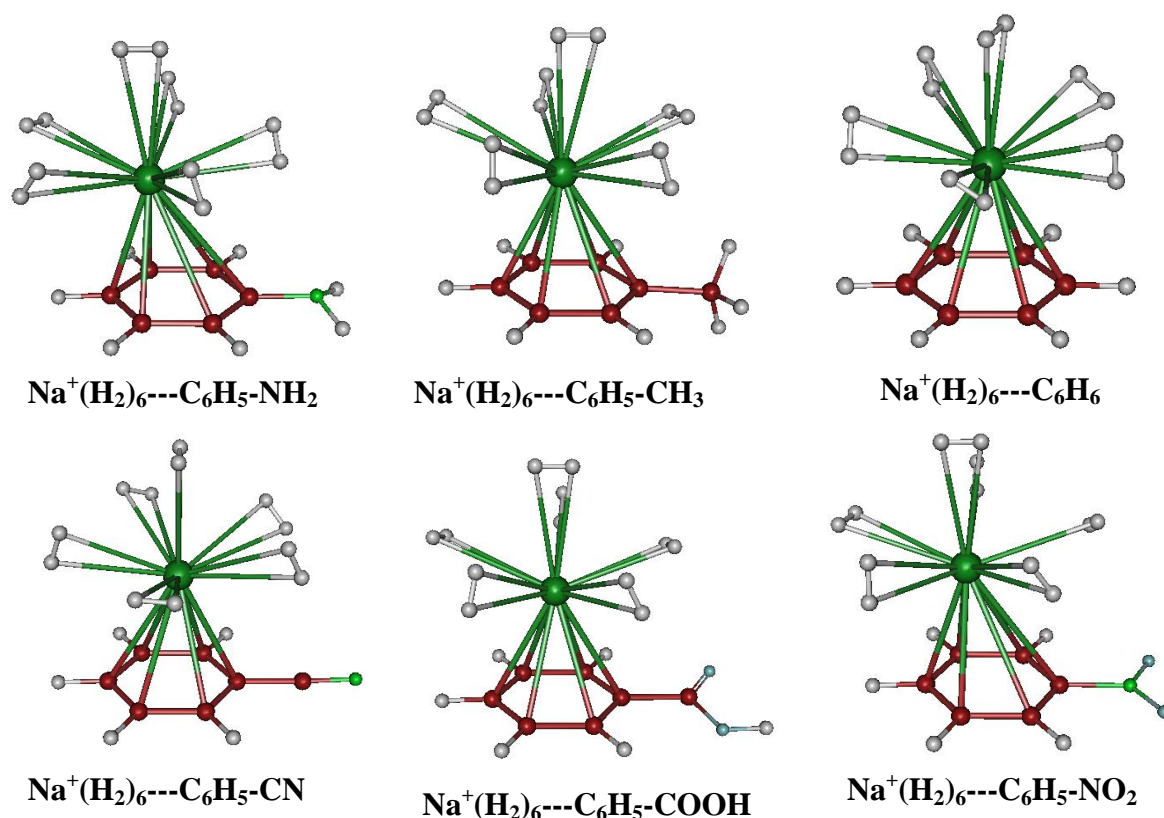


Figure 3.3 Interaction of H_2 with the alkali-metal-cation-doped benzene ring and its derivatives.

3.3.1.4 Effect of endohedral/exohedral metal cation doping on the hydrogen adsorption energy

In carbon nanotubes or fullerenes, the cation can be doped at the exohedral (outside the cage or interstitial sites) or endohedral sites (inside the cage or tube)¹⁷⁴ and hence, it may be interesting to study the interaction of hydrogen molecules in such conditions also. Accordingly, we have allowed the hydrogen molecule to interact from the opposite side of the benzene-cation system (as shown in Figure 3.4) to simulate the effect of endohedral metal complexes of carbon nanomaterials. We observe that there is only a little improvement in the hydrogen interaction with the π electron system as compared to the undoped system. It is also important to note that the effect of the electron withdrawing or donating nature of the

functional groups becomes less important in the presence of sodium cation. This effect is observed to be pronounced in the case of $-\text{NH}_2$, $-\text{NO}_2$, $-\text{COOH}$ and $-\text{CN}$ groups. The interaction energy of hydrogen molecules in such systems is increased by 20% as compared to that in unsubstituted systems (See Table 3.4).

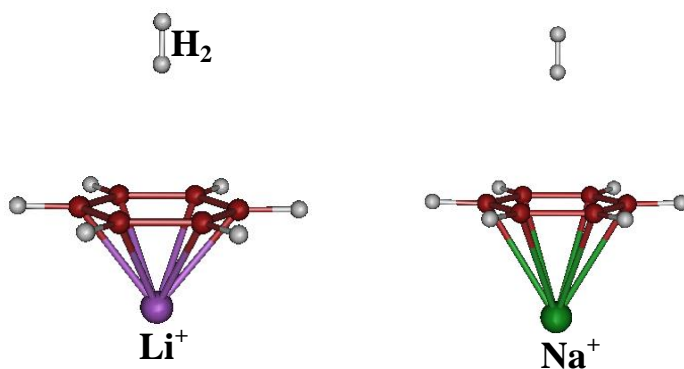


Figure 3.4 Modeling the hydrogen adsorption in the cation-encapsulated (endohedral) model system

Table 3.4: Binding energy of molecular hydrogen interacting with the cation encapsulated (endohedral) model system

System	Binding energy (kcal/mol)	Charge on H_2 (a.u)
$\text{H}_2\text{--C}_6\text{H}_6\text{--Na}$	-2.00 (-2.0) ^a	-0.018
$\text{H}_2\text{--C}_6\text{H}_5\text{--CH}_3\text{--Na}$	-2.47 (-2.46)	-0.014
$\text{H}_2\text{--C}_6\text{H}_5\text{--NH}_2\text{--Na}$	-2.14 (-2.13)	-0.016
$\text{H}_2\text{--C}_6\text{H}_5\text{--COOH--Na}$	-2.41 (-2.41)	-0.011
$\text{H}_2\text{--C}_6\text{H}_5\text{--CN--Na}$	-2.48 (-2.48)	-0.011
$\text{H}_2\text{--C}_6\text{H}_5\text{--NO}_2\text{--Na}$	-2.19 (-2.19)	-0.016

^aThe interaction energies given in parenthesis are BSSE corrected values

3.3.2 Role of aromaticity

3.3.2.1 Interaction of molecular hydrogen with the simple organic molecular systems

The optimized structures obtained by HLYP/6-31++G(2d,2p) method for the C_nH_n ($n=4, 5, 6$ and 8) molecular systems are shown in Figure 3.5(a). It is found that C_4H_4 , C_5H_5 and C_6H_6 have the planar structures with D_{2h} , C_{2v} and D_{6h} symmetry respectively, while for C_8H_8 , the minimum energy structure is the one with S_4 symmetry (non-planar tub like structure) which is found to be more stable than the planar structure with D_{4h} symmetry by an

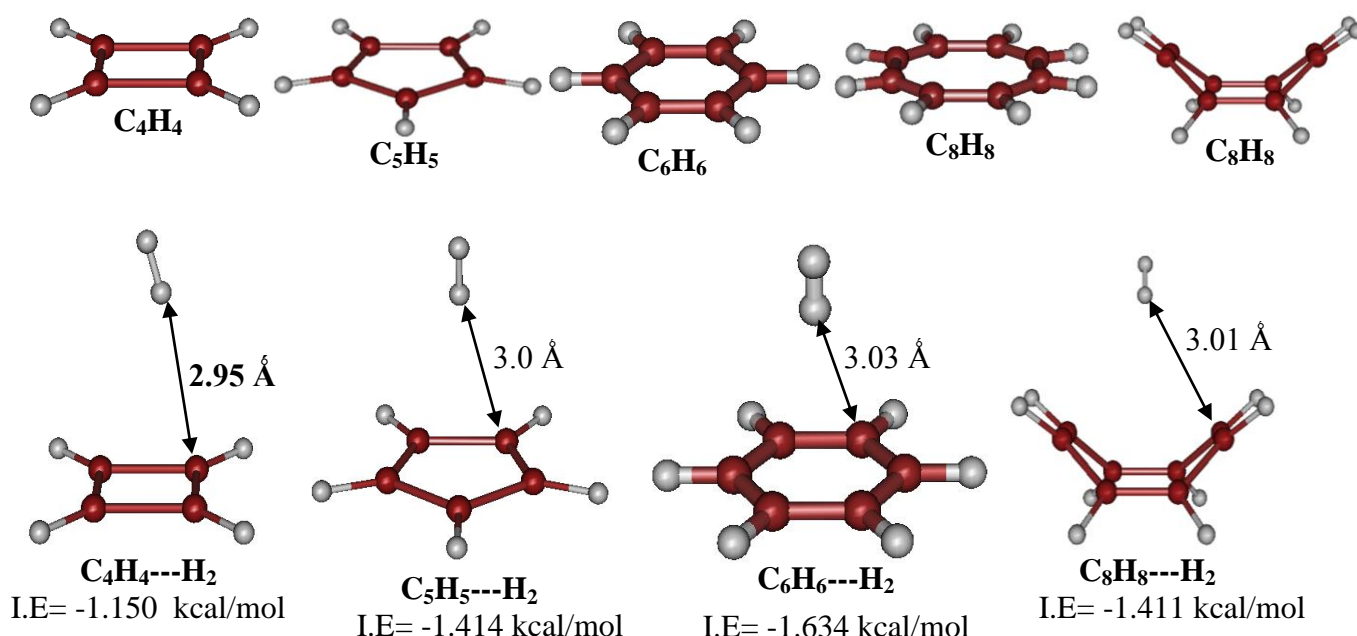


Figure 3.5 a) Equilibrium geometries of C_nH_n ($n=4, 5, 6$, and 8) molecular systems. b) Interaction of molecular hydrogen with the C_nH_n molecular systems. I.E.=interaction energy.

amount of -15.02 kcal/mol. This non-planar structure does not allow the delocalization of the π electrons. In addition, all the C-C bond lengths are found to be equal (1.396 \AA) in C_6H_6 whereas the C-C bond lengths are unequal in the rest of the molecular systems. For instance, C_4H_4 and C_8H_8 are having two sets of bond lengths ($1.307, 1.544 \text{ \AA}$ and $1.310, 1.457 \text{ \AA}$ respectively) while C_5H_5 is having three different bond lengths ($1.337, 1.418$ and 1.452 \AA).

The extent of electron localization in these molecular systems has been discussed in the next section.

Let us now turn to the discussion on the hydrogen adsorption with these organic molecular systems. The interaction energy of molecular hydrogen with all these systems is calculated using HLYP/6-31++G(2d,2p) as well as MP2/6-31++G(2d,2p) methods and the corresponding optimized geometries as well as binding energies are shown in Figure 3.5(b). In all the cases, the interaction is found to be very weak and the interaction energies calculated through MP2/6-31++G(2d,2p) are -1.15, -1.41, -1.63 and -1.41 kcal/mol for the organic molecular systems, C_nH_n , $n=4, 5, 6$ and 8 , respectively. This trend shows good correlation between the number of π electrons and interaction energy of the hydrogen molecule with the molecular system except in case of C_8H_8 wherein the actual number of π electrons exposed to the hydrogen molecules is only four. Here, the interaction of H_2 with the organic systems is mostly driven by the long-range dispersion interactions due to the π electrons.⁶⁸

3.3.2.2 Interaction of alkali metal atom with the organic molecular systems

In the present case, we have chosen alkali metal atoms, particularly, sodium atom as the dopant atom. Since benzene is aromatic in nature, it is expected that the reactivity of benzene molecule towards alkali metal atoms will be extremely weak. On the other hand, the systems, C_4H_4 , C_5H_5 and C_8H_8 are not aromatic in nature and hence, their reactivity can be different from that of the benzene molecule. For instance, these molecular systems show a dramatic difference in the values of the electron affinity. Among the selected molecular systems considered here, C_5H_5 is found to have the highest value of electron affinity while the benzene is found to have the lowest electron affinity value.¹⁷⁵ Hence, it is expected that

Table 3.5 Interaction of sodium metal with the organic molecular systems, C_nH_n

System	Interaction energy (kcal/mol)						Charge on Na (a.u) (SV6) ^[a]			
	HLYP		HOP		M06	MP2	HLYP	HOP	M06	MP2
	ACCT ^[a]	SV6 ^[a]	ACCT ^[a]	SV6 ^[a]	SV6 ^[b]	SV6 ^[a]				
Na-C ₆ H ₆	-----	-0.86	-----	-0.20	-1.40	-3.36	-0.02	0.0	0.02	-0.03
Na-C ₄ H ₄	-13.26	-14.46	-11.43	-12.29	-24.43	-23.30	0.57	0.60	0.70	0.59
Na-C ₅ H ₅	-59.83	-60.08	-58.62	-58.86	-66.18	-71.15	0.60	0.64	0.72	0.61
Na-C ₈ H ₈	-34.71	-34.95	-18.58	-18.15	-36.72	-51.84	0.59	0.65	0.57	0.63

[a]SV6 and ACCT refer to 6-31++G(2d,2p) and aug-cc-pVTZ basis sets, respectively

[b]SV6 refer to 6-31++G(d, p)

the organic molecular system, C₅H₅ should be more reactive than C₆H₆ towards the systems, which are less electronegative in nature, e.g. electropositive metal atoms like alkali or alkaline earth metal atoms.

Accordingly, we have made a detailed study on the interaction of sodium atom with C_nH_n molecules, with $n=4, 5, 6$ and 8 . It can be seen from the results reported in Table 3.5, that there is marked variation in the interaction strength of the sodium atom with these molecular systems. For instance, the interaction energy of sodium metal atom with the benzene ring is only -3.36 kcal/mol and the charge on the sodium atom is observed to be very less. This less reactivity of benzene towards sodium atom can be attributed to the high aromatic stability of the C₆H₆ system, which has $(4n+2)$ π electrons. The other systems being π electron deficient can interact rather strongly with the metal atoms as compared to C₆H₆ to attain more stable electronic configurations. Evidently, our results also show that all the other molecular systems, except benzene molecule, interact with the sodium atom very strongly and the corresponding interaction energies, as calculated by MP2/6-31++G(2d,2p) method, are -23.30, -71.15 and -51.84 kcal/mol for Na-C₄H₄, Na-C₅H₅ and Na-C₈H₈, respectively. It is pertinent to note that the corresponding energy values calculated by the M06 method is considerably higher than those using HOP and HLYP method and they are

close to the values derived from MP2 method. The charge density has been calculated for all these organic systems interacting with sodium atom and is graphically represented in Figure 3.6(a). It can indeed be observed from the charge density iso-surface of Na-C₆H₆ that there is no overlap of electron densities of the metal atom and the benzene ring. However, there is a significant overlap of the electron densities of the metal and organic moiety in the case of C₄H₄, C₅H₅ and C₈H₈, showing the chemical bond formed between the sodium atom and the organic molecules.

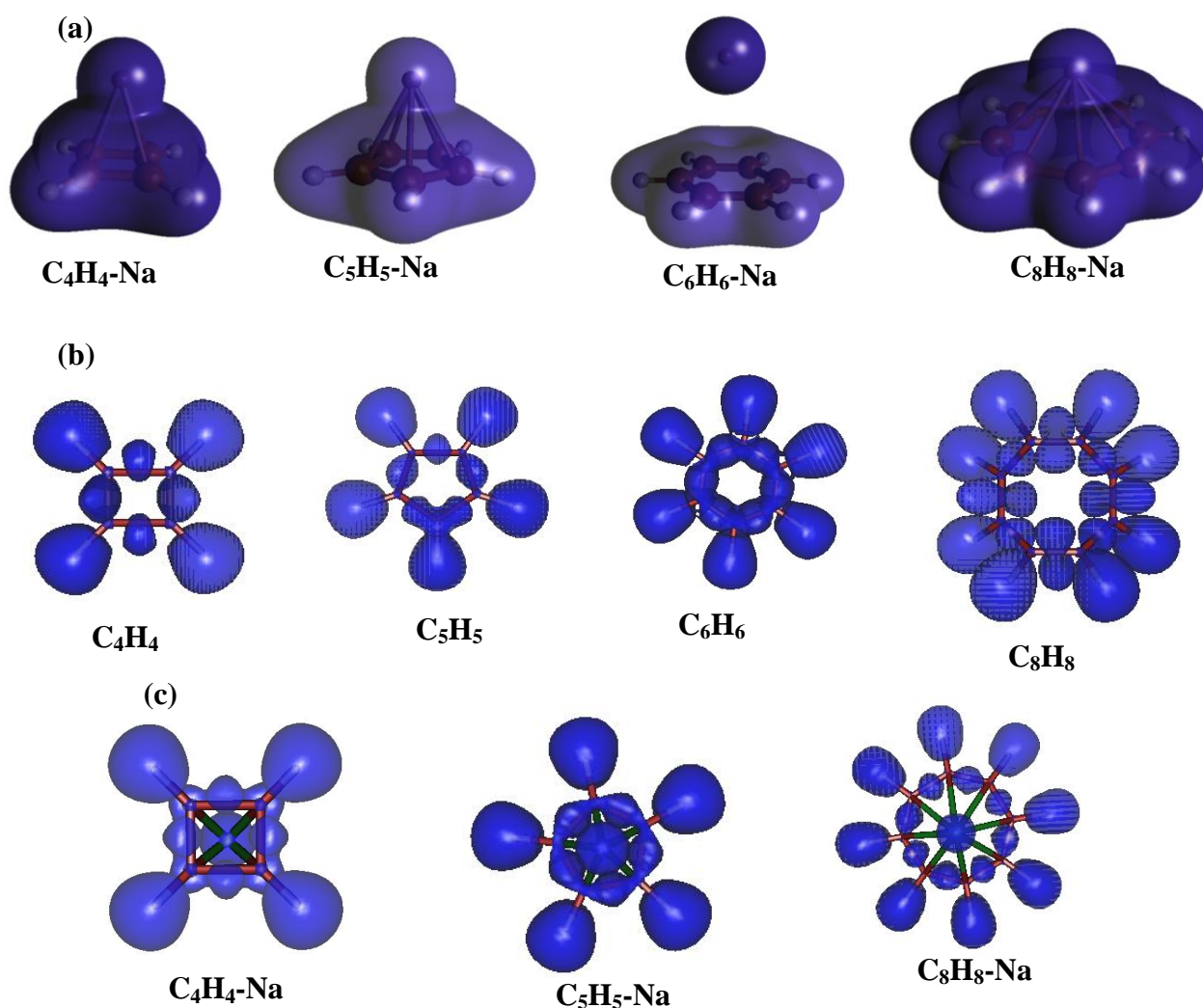


Figure 3.6 a) Charge density plots of the sodium-doped C_nH_n molecular complexes. b) ELF plots of the C_nH_n molecular system (contour value=0.7). c) ELF plots of the C_nH_n-Na molecular system (contour value=0.7).

In addition, the most striking result is for the interaction strength of sodium atom with C_5H_5 molecule, which is the highest among all the complexes considered. It is also interesting to note that the C_5H_5 -Na structure optimized using MP2/6-31G++ (2d,2p) is found to have a C_{5v} symmetry with identical C-C bond distances (1.42 Å) indicating the possibility of complete electron delocalization in the carbon ring. Similarly, in the case of C_8H_8 also, we observe that the minimum energy structure of the complex, C_8H_8 -Na, is the planar C_8H_8 capped with the sodium metal rather than the tub like carbon ring structure and the energy difference between these two structures is found to be ~ 19.42 kcal/mol. Although the structure of C_5H_5 and C_8H_8 in their complexes with sodium atom is planar, we observed that all the C-C bond distances in the C_8H_8 case are not equal and two sets of C-C bond lengths are found to exist. Another interesting aspect is the spontaneous ionization of the sodium atom upon binding with these organic molecular systems. The charge on the sodium atom adsorbed in benzene is negligible whereas in the case of all other systems, the charge on sodium is around 0.6 a.u. This is attributed to the high electron affinity of the molecular systems, which are π electron deficient and favor the electron transfer from the metal atom to the molecular system leaving positive charge on the metal for getting aromatic nature.

Let us now discuss the extent of electron delocalization and hence the aromaticity of these alkali metal atoms doped organic systems, through the nucleus-independent chemical shifts (NICS) and the harmonic oscillator model of aromaticity (HOMA) analysis. In general, the negative and positive values of the NICS, calculated at the ring centers, denote aromaticity and anti-aromaticity, respectively. In Table 3.2.2, we have tabulated the NICS as well as the HOMA for all the sodium metal atom doped and undoped systems. It is known that C_6H_6 is an aromatic sextet compound and the negative value of NICS, -9.7, indicates its aromaticity whereas the remaining systems, C_4H_4 , C_5H_5 and C_8H_8 are found to have a positive NICS value, indicating that they are anti-aromatic in nature. More interestingly, it

can be seen that there is a change in the sign of the NICS values of metal atom doped and undoped C_5H_5 system, which clearly indicates that the aromaticity can be induced upon doping the sodium metal atom to the C_5H_5 system. In addition, we also note that the NICS value of C_5H_5 at the center as well as above the center (up to 1.0 Å from the center of the ring), is much higher than that of C_6H_6 case and the NICS values calculated at 1.5 and 2.0 Å from the center of both C_5H_5 -Na as well as C_6H_6 become more comparable to each other. In contrast to the C_5H_5 -Na case, NICS value for the other systems, viz. C_4H_4 -Na and C_8H_8 -Na, is found to be positive, indicating that these complexes are anti-aromatic in nature.

Table 3.6 The nucleus-independent chemical shifts (NICS) and the harmonic oscillator model of aromaticity (HOMA) values of the sodium metal atom doped and undoped molecular systems, calculated by B3LYP/6-31+G(d,p) method.

System	NICS(0)	NICS(0.5)	NICS(1)	NICS(1.5)	NICS(2)	HOMA
C_4H_4	29.837	29.963	19.722	9.766	4.732	-2.97
C_5H_5	3.080	1.902	-0.429	-1.211	-1.072	0.43
C_6H_6	-9.739	-11.545	-11.528	-8.384	-5.333	0.98
C_8H_8	0.797	- 1.385	- 1.528	- 0.729	- 0.259	-0.40
C_4H_4 -Na	18.533	26.924	21.912	10.300	4.454	0.65
C_5H_5 -Na	-13.653	-13.316	-12.135	-8.739	-5.386	0.71
C_8H_8 -Na	12.499	12.129	9.930	6.985	4.489	0.65

In addition to the NICS criterion, we have also calculated the geometry based aromaticity index, HOMA for all the complexes. In general, if the HOMA value of the compound is close to unity, the compound is described to be aromatic. It is evident from Table 3.2.2 that the HOMA value of C_5H_5 -Na is closer to that of C_6H_6 than other complexes, C_4H_4 -Na and C_8H_8 -Na. Hence, it can be mentioned that C_5H_5 -Na can be considered as an aromatic compound based on the geometry as well as the magnetic criteria.

Let us now analyze the nature of chemical bonding or change in the bonding characteristics of the organic molecular systems and their complexes with sodium atom by the use of ELF at certain isosurface values. In general, the ELF is dependent on the gradient of the density parameter¹⁷⁶ and hence, it is possible to describe regions of space that are associated with different electron localization in a molecular system. The ELF's at different iso-surface values for all the organic molecules and their complexes with sodium atom as shown in Figures 3.6(b) and 3.6(c) have been calculated at the B3LYP level using the 6-31++G(2d,2p) basis set. From Figure 3.7(b), it can be seen that the plot corresponding to the benzene ring has the symmetric electron delocalization along all C-C bonds whereas the other systems show different ELF (at 0.7 contour value) at different C-C bonds, referring the localization of electrons at each carbon atoms. On the other hand, the nature of the contours for ELF equal to 0.7, shown in Figure 3.6(c), for the sodium atom doped organic molecular surface, viz., C_4H_4-Na , C_5H_5-Na and C_8H_8-Na is indicative of an ionic type of environment around sodium atom in the organic complex. In the case of C_5H_5-Na , it is found that ELF's are equal along all C-C bonds, which shows a complete electron delocalization like in C_6H_6 while in C_4H_4-Na and C_8H_8-Na , alternate bonds are having equal ELF indicating the electron localization nature of the C-C bonds. This can be attributed to the charge transfer from the sodium atom to the organic surface, causing a delocalization of the π electrons.

3.3.2.3 Molecular hydrogen adsorption in sodium metal doped organic molecular systems ($Na-C_nH_n$, $n=4, 5$ and 8)

Now discuss the results on the hydrogen adsorption in sodium doped organic molecular systems systematically. All the equilibrium geometries of $C_mH_m-Na(H_2)_n$ ($m = 4, 5$ and 8 ; $n = 1-6$) are given in Figures 3.7-3.9 obtained by the HLYP/6-31++G(2d,2p) method and the corresponding energy quantities are given in Tables 3.7-3.9

In the case of $\text{C}_4\text{H}_4\text{-Na}$, the first molecular hydrogen ($n=1$) is found to bind to the sodium metal with an interaction energy, -2.02 kcal/mol, the distance between the metal atom and H_2 being 2.4 \AA , as calculated by MP2 method. The H-H bond length is found to be 0.731 \AA which is slightly larger than the bond length of molecular hydrogen optimized by the same method (0.728 \AA) and the Mulliken charge on the sodium metal is found to decrease from 0.58 (charge on $\text{Na-C}_4\text{H}_4$) to 0.53 upon interaction with hydrogen. The next hydrogen ($n=2$) is found to bind with a binding energy of -2.48 kcal/mol per hydrogen and similarly the subsequent hydrogen molecules are found to interact with the interaction energies of -1.79 , -1.74 , -1.66 and -1.38 kcal/mol per H_2 for $n=3,4,5$ and 6 respectively. This decrease in the interaction energy of hydrogen molecules with the $\text{C}_4\text{H}_4\text{-Na}$ system is found to be in good correlation with the charge on the cation.

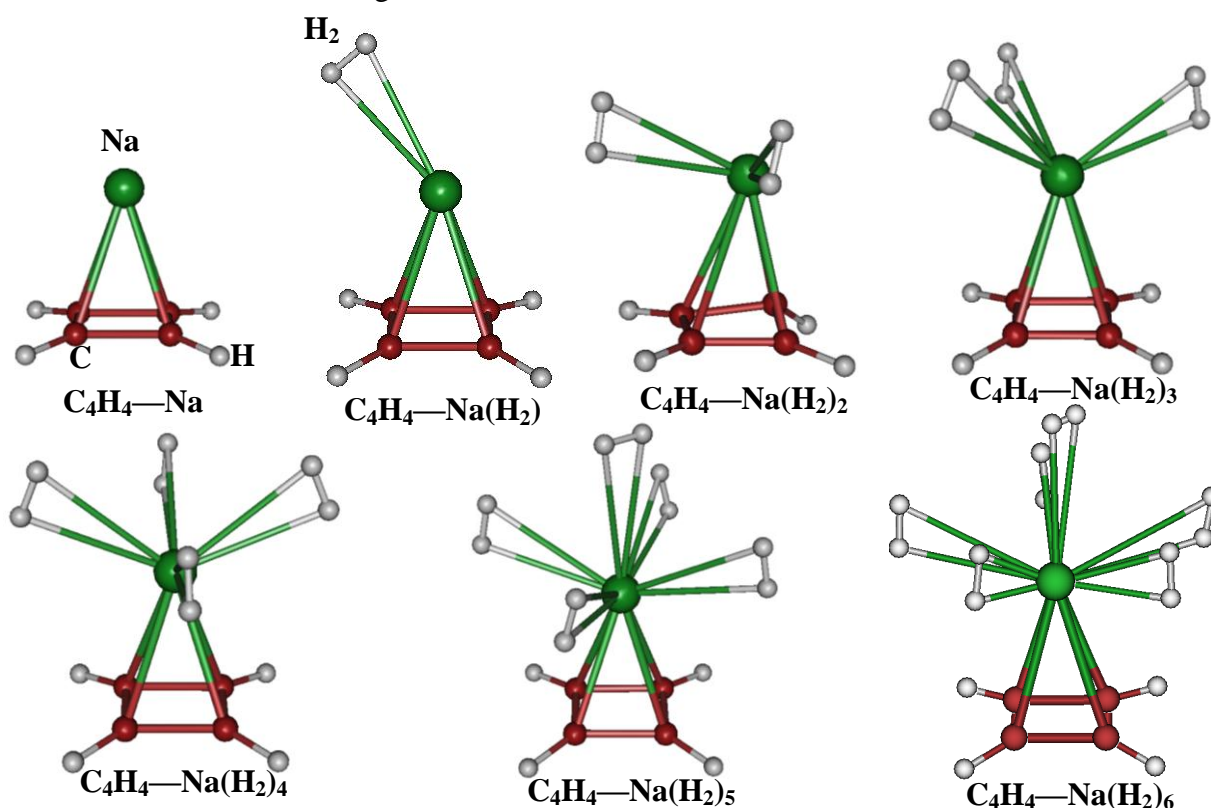


Figure 3.7 Equilibrium geometries of $\text{C}_4\text{H}_4\text{-Na}(\text{H}_2)_m$ ($m=0-6$).

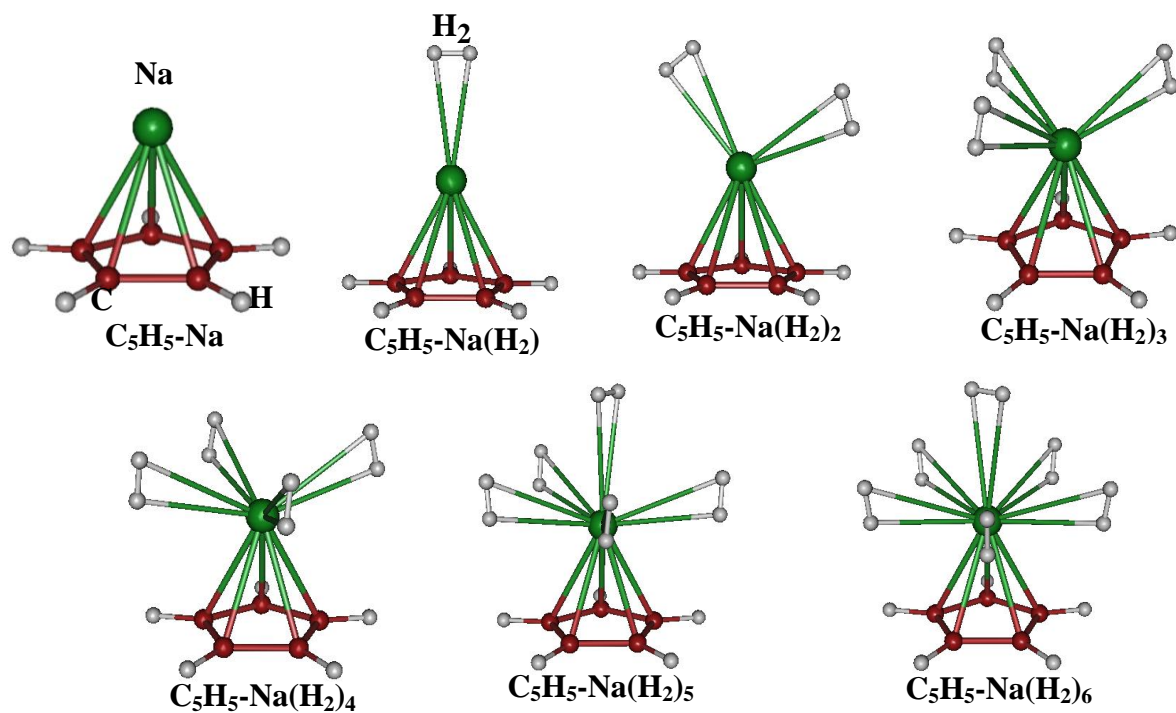


Figure 3.8 Equilibrium geometries of $\text{C}_5\text{H}_5\text{-Na}(\text{H}_2)_m$ ($m=0-6$).

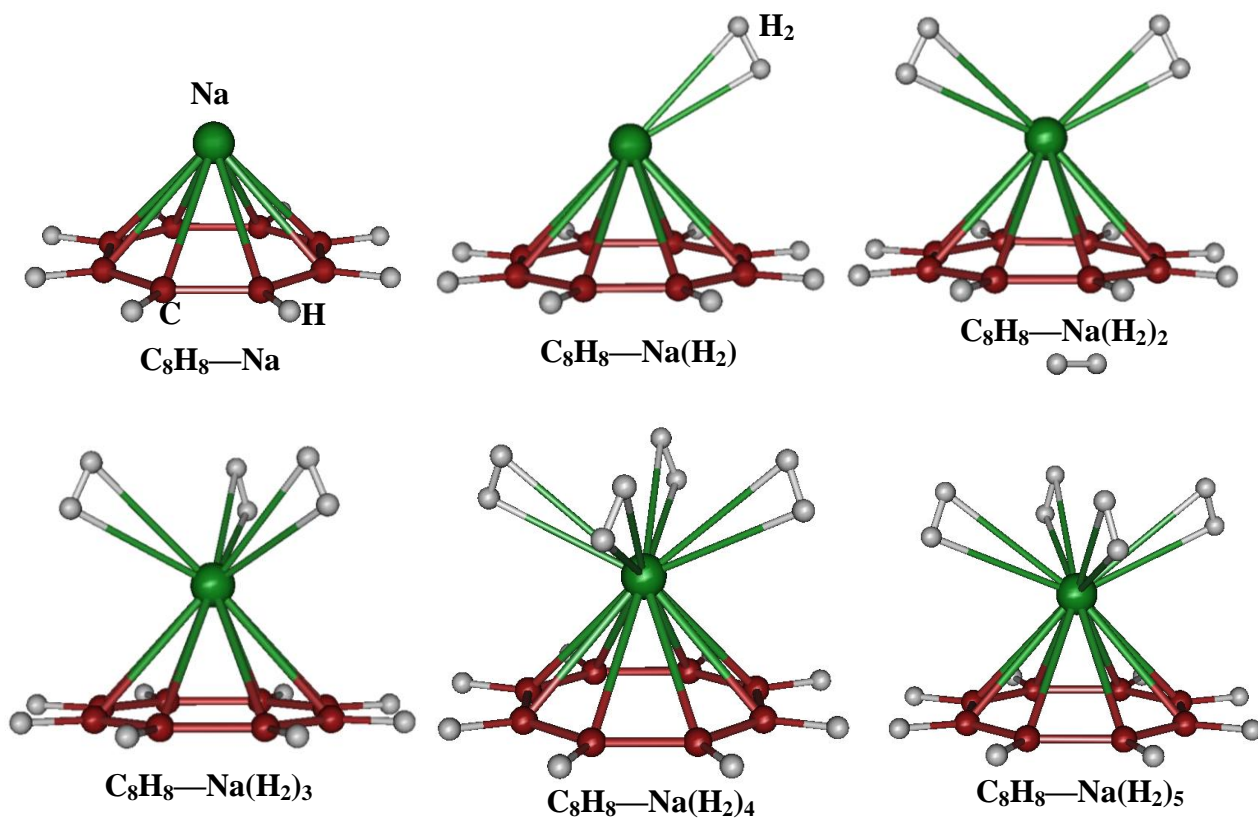


Figure 3.9 Equilibrium geometries of $\text{C}_8\text{H}_8\text{-Na}(\text{H}_2)_m$ ($m=0-5$).

We now discuss the molecular hydrogen adsorption in Na-C₅H₅. The first hydrogen molecule is found to interact with the sodium metal doped in C₅H₅ with interaction energy of -2.13 kcal/mol and the minimum Na-H₂ distance of 2.56 Å. The H-H bond length is found to be 0.738 Å which is slightly larger than the bond length of molecular hydrogen optimized by the same method (0.728 Å) and also it is found to be adsorbed at on-top position of the complex as shown in Figure 3.8. The Mulliken charge on the sodium metal is found to decrease from 0.61 a.u. to 0.55 a.u. The subsequent hydrogen molecules are found to interact with an average binding energy of -2.02, -2.05, -2.04, -1.90 and -1.92 kcal/mol for n=2, 3, 4, 5 and 6 respectively. The variation of binding energy with the number of H₂ molecules adsorbed is shown in Figure 3.10

Table 3.7 Interaction of molecular hydrogen with C₄H₄-Na complex

System	Interaction Energy (kcal/mol)						Charge on Na (a.u) (SV6) ^[a]			HOMO- LUMO gap (ev)
	HLYP		HOP		M06	MP2	HLYP	HOP	MP2	
	ACCT ^[a]	SV6 ^[a]	ACCT ^[a]	SV6 ^[a]	SV6 ^[b]	SV6 ^[a]				
C ₄ H ₄ -Na(H ₂)	-2.53	-1.77	-1.73	-1.60	-2.68	-2.02	0.51	0.55	0.53	1.90
C ₄ H ₄ -Na(H ₂) ₂	-5.19	-4.72	-2.80	-2.47	-5.55	-4.97	0.44	0.50	0.47	2.31
C ₄ H ₄ -Na(H ₂) ₃	-6.19	-5.01	-3.66	-3.40	-7.47	-5.38	0.36	0.41	0.39	1.97
C ₄ H ₄ -Na(H ₂) ₄	-8.02	-6.85	-4.58	-4.11	-9.35	-6.98	0.30	0.39	0.35	1.94
C ₄ H ₄ -Na(H ₂) ₅	-9.03	-7.77	-4.81	-4.49	-11.21	-8.28	0.33	0.43	0.39	1.99
C ₄ H ₄ -Na(H ₂) ₆	-9.96	-9.37	-4.71	-4.87	-14.26	-9.64	0.37	0.48	0.45	2.00

Table 3.8 Interaction of molecular hydrogen with C₅H₅-Na complex

System	Interaction Energy (kcal/mol)						Charge on Na (a.u) (SV6) ^[a]			HOMO- LUMO gap (ev)
	HLYP		HOP		M06	MP2	HLY	HOP	MP2	
	ACCT ^[a]	SV6 ^[a]	ACCT ^[a]	SV6 ^[a]	SV6 ^[b]	SV6 ^[a]	P			
C ₅ H ₅ -Na(H ₂)	-2.16	-1.98	-1.49	-1.16	-1.79	-2.13	0.55	0.59	0.55	7.78
C ₅ H ₅ -Na(H ₂) ₂	-4.36	-3.84	-2.55	-2.06	-4.06	-4.03	0.50	0.54	0.50	7.94
C ₅ H ₅ -Na(H ₂) ₃	-6.13	-5.48	-3.66	-3.11	-6.40	-6.16	0.42	0.51	0.45	7.99
C ₅ H ₅ -Na(H ₂) ₄	-7.75	-7.15	-4.36	-3.92	-8.74	-8.18	0.41	0.51	0.42	7.98
C ₅ H ₅ -Na(H ₂) ₅	-8.95	-8.36	-4.51	-4.25	-11.08	-9.519	0.46	0.58	0.41	8.03
C ₅ H ₅ -Na(H ₂) ₆	-10.15	-9.70	-4.77	-4.61	-14.37	-11.55	0.42	0.65	0.34	8.03

[a]SV6 and ACCT refer to 6-31++G(2d,2p) and aug-cc-pVTZ basis sets, respectively

[b]SV6 refer to 6-31++G(d, p)

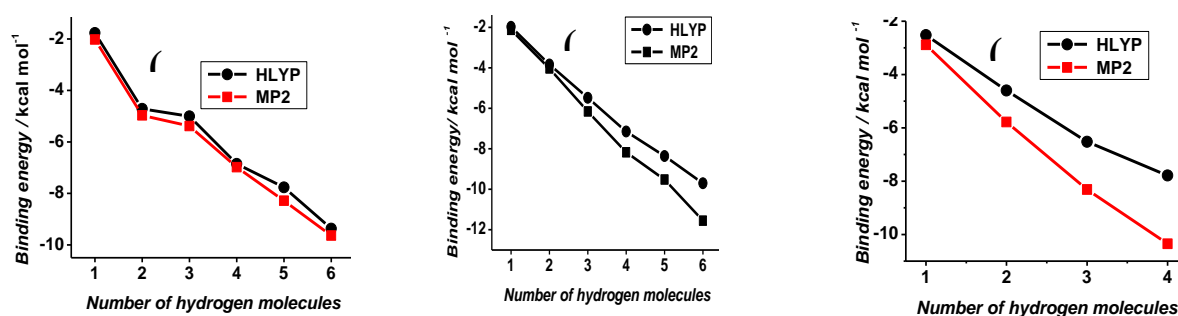
Table 3.9 Interaction of molecular hydrogen with C₈H₈-Na complex

System	Interaction Energy (kcal/mol)						Charge on Na (a.u) (SV6) ^[a]			HOMO- LUMO gap (ev)
	HLYP		HOP		M06	MP2	HLYP	HOP	MP2	
	ACCT ^[a]	SV6 ^[a]	ACCT ^[a]	SV6 ^[a]	SV6 ^[b]	SV6 ^[a]				
C ₈ H ₈ -Na(H ₂)	-2.66	-2.52	-1.28	-1.52	-1.70	-2.88	0.54	0.62	0.60	3.10
C ₈ H ₈ -Na(H ₂) ₂	-5.07	-4.60	-2.44	-2.83	-4.50	-5.78	0.43	0.54	0.50	3.21
C ₈ H ₈ -Na(H ₂) ₃	-7.10	-6.52	-3.60	-3.94	-7.58	-8.31	0.46	0.56	0.53	3.23
C ₈ H ₈ -Na(H ₂) ₄	-8.12	7.79	-4.01	-4.05	-10.84	-10.30	0.38	0.53	0.46	3.21

[a]SV6 and ACCT refer to 6-31++G(2d,2p) and aug-cc-pVTZ basis sets, respectively

[b]SV6 refer to 6-31++G(d, p)

Finally, in the case of Na-C₈H₈, the interaction energy of the first molecular hydrogen is -2.88 kcal/mol and the corresponding Na-H₂ distance and the H-H bond lengths are 2.35 and 0.733 Å, respectively. As observed in other cases, the charge on the sodium metal is found to decrease from 0.63 to 0.59 a.u. upon interaction with H₂. For subsequent hydrogen molecules the binding energy values are -2.89, -2.77 and -2.59 kcal/mol for n=2, 3 and 4, respectively. More interestingly, it is observed that the maximum number of hydrogen molecules which are adsorbed at the sodium ionic site is only four and the additional hydrogen molecules is found to depart from the on-top side as shown in Figure 3.9. This can be attributed to the

**Figure 3.10** Variation of binding energy with increase in number of hydrogen molecules in

a) C₄H₄-Na, b) C₅H₅-Na, and c) C₈H₈-Na complexes

shorter distance between the organic surface and the metal atom. As sodium atom is near to the surface, the additional hydrogen molecules will attempt to be away from the surface as well as the adsorbed hydrogen molecules in order to minimize the strong intermolecular repulsion. It can easily be understood from the values of the distance between the adjacent H_2 molecules in the complexes, which in $C_5H_5-Na(H_2)_4$ and $C_8H_8-Na(H_2)_4$ are 3.3 Å and 2.8 Å, respectively.

The variation of the interaction energy with number of hydrogen molecules adsorbed in all these three model systems is presented in Figure 3.10. It can be seen from this figure that the interaction energies obtained using the HLYP method are found to be always less than that obtained by MP2 method. It should be noted that the interaction energy as well as the structure of the $Na-(H_2)_n$ for the doped organic species are somewhat analogous to the same as that for the interaction hydrogen with bare sodium cation.¹³⁹ It can also be mentioned that the interactions of H_2 with metal-doped organic systems are mostly driven by electrostatic interactions due to the charged surface developed by the electron transfer from the metal atom to the organic systems. Some of the recent studies have also concluded that the interactions in alkali metal–dihydrogen complexes are electrostatic in nature and the predominant terms of the interaction are those due to the quadrupole and dipole polarizability terms.¹⁷⁷⁻¹⁷⁸

The hydrogen adsorption in C_4H_4-Na and C_5H_5-Na is ~13.8 and 12 wt%, respectively, with the six hydrogen molecules adsorbed per metal site whereas in C_8H_8-Na the maximum number is only four which is equivalent to 5.9 wt%. The complexes of C_5H_5 are quite common in many systems like ferrocenes and hence other types of systems can be explored.¹⁷⁹⁻¹⁸⁰ This would lead to the development of new materials for hydrogen storage purpose. In all the cases considered, the gradual increase in the HOMO-LUMO gap with the number of hydrogen molecules shows the stabilization of the complexes. The Hessian

calculations for all the systems have also been performed and we note that all the frequencies are positive, indicating that the systems are actually situated at one of the local minima in the potential energy surface.

To model materials with C_5H_5-Na as the main building block, we have connected the five membered carbon rings decorated with metal atom using the $-C\equiv C-$ as a linking agent. We have systematically connected these rings and found that after ten carbon rings, it forms a cyclic oligomer type structure as shown in Figure 3.11(a). The metal binding energy per metal atom is calculated to be around -40.0 kcal/mol. We have hydrogenated all the metal sites, as shown in Figure 3.11(b) and the calculated hydrogen adsorption energy is found to be 1.90 kcal/mol per hydrogen.

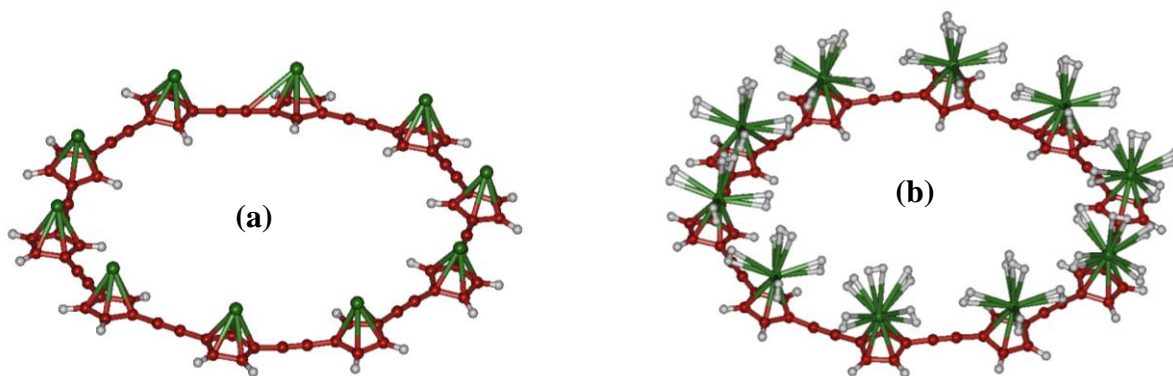


Figure 3.11 Optimized geometry of the (a) model oligomeric structure and (b) its hydrogenated form.

3.4 Conclusions

We have demonstrated that creating a charged surface on the model system by doping the alkali metal cations can improve the hydrogen adsorption energy significantly. Among the alkali metal cations (Na^+ and Li^+), it is observed that Na^+ can interact with more number of hydrogen molecules as compared to Li^+ . Introduction of a functional group in the model system also affects the binding of the alkali metal cation to the organic system and the hydrogen adsorption significantly due to the electronic induction effects. These effects can be used to tune the interaction strength of the alkali metal cation as well as the hydrogen adsorption energy such that the material can be stable towards recycling. It can be mentioned that the model studies considered in the present investigation can provide a detailed insight into the adsorption of hydrogen molecules in carbon nanomaterials, metal-organic frameworks and other materials where benzene derivatives are the building blocks. We have also shown that the binding of sodium atom, especially, with the π electron deficient systems like C_4H_4 , C_5H_5 and C_8H_8 is observed to be energetically feasible and there is a charge transfer from the sodium atom to the organic molecules. The hydrogen adsorption in $\text{C}_4\text{H}_4\text{-Na}$, $\text{C}_5\text{H}_5\text{-Na}$ and C_8H_8 is ~ 13.8 , 12.0 and 5.9 wt% respectively. Such interactions are not possible with benzene molecule due to its exceptional aromatic stability. Among all the alkali metal atom doped complexes, $\text{C}_5\text{H}_5\text{-Na}$ is found to be the most stable and the interaction of molecular hydrogen is also found to be very strong. The aromaticity in such molecular systems plays a very important role in stabilizing the ionized organometallic complex doped with alkali metal atoms.

CHAPTER 4

Hydrogen Adsorption Properties of Alkali Metal Decorated Boron Hydrides (B_mH_n-M)

4.1 Introduction

As already mentioned, the low molecular weight materials like carbon and boron based materials are promising materials for high gravimetric density hydrogen storage application. In the present chapter, we discuss the results of our studies on the hydrogen adsorption characteristics of alkali metal decorated small boron hydrides (boranes) and corresponding assembled materials designed by using these boranes as the building blocks.

Boron is well known for its hydrides, the so called boranes like B_2H_6 , B_4H_{10} , B_5H_9 , B_6H_{10} etc, which have been studied extensively after the characterization of diborane, the first member of the borane family, by Stock *et al.* in 1912.¹⁸¹ Boranes generated lot of interest in the field of chemistry as well as physics due to their non classical bonding and polyhedral structure which were explained using the concept of three-centre two-electron (3c-2e) bonding.¹⁸² Based on the number of electron pairs associated with the cage bonding in boranes, these are categorized into different groups viz. *closo*($B_nH_n^{2-}$), *nido*(B_nH_{n+4}) and *arachno* (B_nH_{n+4}) boranes with (n+1), (n+2) and (n+3) number of skeletal electron pairs respectively. Boranes with fewer than (n+1) electron pairs are known as hypercloso boranes. According to the Wade-Mingos (electron counting) rule, (n+1) pairs of skeletal electrons are required for the stable *closo*-boranes ($B_nH_n^{2-}$).¹⁸³ However, McKee *et al.*¹⁸⁴ had predicted that the loss of one electron from $B_nH_n^{2-}$ (n=5-13) is exothermic except for $B_{12}H_{12}^{2-}$ which shows high stability of dianionic form of the icosahedra $B_{12}H_{12}^{2-}$. These *closo*-borane dianions are known to be aromatic which was first discussed by Aihara who coined the term three dimensional aromaticity.¹⁸⁵ Each face of the deltahedra which involves 3c-2e bonding in boranes is aromatic because of association with a ring current and a negative (diatropic) NICS value. $B_6H_6^{2-}$ is the smallest unit among the *closo*-boranes which was found to have an octahedral symmetry.¹⁸⁴

In first part of the present study, we have explored the hydrogen adsorption in boron analogues of ethylene and acetylene decorated with lithium atoms ($B_2H_4Li_2$ and $B_2H_4Li_2$). B_2H_6 is the boron analogue of ethane which is a well known electron deficient molecule.¹⁸⁶ However, the boron analogues of ethylene and acetylene are not much studied. Vincent et al.¹⁸⁷ studied the structure and vibrational frequencies of neutral B_2H_4 using ab initio electronic structure theory. Kaufmann et al.¹⁸⁸ studied the structure of $B_2H_4Li_2$ and quoted it as an experimentally viable species with B=B bond. Very recently, Wang et al.¹⁸⁹ synthesised the stable neutral diborene. In the present study, we consider B_2H_4 as a dianion which is equivalent to the replacement of two CH units of C_2H_4 with two BH^- units. This dianion can bind with two lithium ions through ionic bonding and produce the stable neutral $B_2H_4Li_2$. Similarly in the case of acetylene also, replacement of both CH units with BH^- units gives a $B_2H_2^{2-}$ anion, which can bind with two lithium ions giving neutral $B_2H_2Li_2$. As these lithium sites are cationic in nature, they can hold hydrogen through ion-quadrupole and ion-induced dipole interactions. We have also modelled a one dimensional nanowire with $C_6H_4B_2Li_2$ as a repeating unit and studied hydrogen adsorption by this nanowire.

In the second part of the study, we have investigated the hydrogen adsorption in B_6H_6 doped with two lithium atoms ($Li_2B_6H_6$) which is equivalent to the hexaborane(6) di-anion doped (neutralized) with two lithium ions on the two opposite faces of the regular octahedron. Though the icosahedra $B_{12}H_{12}^{2-}$ is the most stable species in the *closo*-borane series, for computational simplicity we have considered the species $B_6H_6^{2-}$. Very recently Li et al.¹⁸⁹ showed that though $B_6H_6^-$ and $B_{10}H_{10}^-$ clusters are more stable than $B_6H_6^{2-}$ and $B_{10}H_{10}^{2-}$ clusters by 1.78 and 0.55 eV, respectively, the binding energy of $M_2B_nH_n$ ($M = Li, Na$, and $n = 6, 10$) clusters are higher than twice that of MB_nH_n ($M = Li, Na$, and $n = 6, 10$). This shows that even though small borane monoanions for $n = 6, 10$ are more stable than the corresponding dianions, they are less stable once they interact with metal atoms. Due to the

electron transfer from lithium to the borane framework, a positive charge is developed at the lithium site which can induce a dipole in the molecular hydrogen and can bind to hydrogen molecule through the ion-induced dipole interaction. To check the possibility of building the three dimensional molecular materials we design here a 3D solid with the octahedral six membered boron cluster doped with two lithium atoms as the building blocks which are connected three dimensionally with $\text{-C}\equiv\text{C-}$ as a bridging unit (glue), i.e, each unit cell consisting of $\text{B}_6\text{C}_6\text{Li}_2$. We have also studied the hydrogen adsorption in these 3D materials where three hydrogen molecules are adsorbed at each lithium site.

4.2. Computational details

All the energy calculations and geometry optimization for the molecular systems have been performed by using the electronic structure theory based GAMESS software.¹⁵⁵ We have employed the density functional theory (DFT) with pure Hartree-Fock exchange and Lee-Yang-Parr (HLYP)¹⁰⁶ correlation energy functionals as well as M06 functionals.¹⁰⁷⁻¹¹⁰ We have used the extensive split-valence basis sets with diffuse and polarization functions, 6-31++G(2d,2p), and also the Dunning type correlation-consistent basis set, aug-cc-pVTZ. In order to characterize the aromatic nature of all the complexes considered in the present study, we have calculated the NICS parameters. All the NICS calculations are carried out using the Amsterdam Density Functional (ADF) package 2007 at PW91/TZP level of theory.¹⁹⁰ The initial geometries, all the structures, and the charge density have been obtained using the graphical softwares GABEDIT¹⁶⁴ and MOLDEN.¹³⁵

Three dimensional (3D) solid of the alkali metal doped hexa-*closo* boranes linked with $\text{-C}\equiv\text{C-}$ were optimized using the periodic boundary condition (PBC) within DFT calculations implemented in the Vienna *ab initio* Simulation Package (VASP),¹³¹⁻¹³² using a plane wave basis set. Projector augmented wave (PAW)¹²⁹⁻¹³⁰ potentials were employed for

the elemental constituents. The exchange–correlation part ϵ_{xc} of the density functional was treated within the local density approximation (LDA) of Ceperley–Alder as parameterized by Perdew–Zunger¹⁰¹ and within the Generalized Gradient Approximation (GGA) of Perdew–Burke–Ernzerhof (PBE).¹⁰³ The convergence threshold was set as follows: energy change per atom less than 1×10^{-5} eV and the force components on each atom relaxed to less than $0.05 \text{ eV } \text{\AA}^{-1}$. A set of $6 \times 6 \times 6$ Monkhorst-Pack special k points were used for sampling the Brillouin zone.¹³³

4.3 Results and discussion

4.3.1 Hydrogen adsorption properties of lithium decorated diborene ($\text{B}_2\text{H}_4\text{Li}_2$) and diboryne ($\text{B}_2\text{H}_2\text{Li}_2$)

Dihydrodiborate dianion, $\text{B}_2\text{H}_2^{2-}$ and tetrahydrodiborate dianion, $\text{B}_2\text{H}_4^{2-}$ can be considered to be analogues and isoelectronic to acetylene (C_2H_2) and ethylene (C_2H_4) respectively as each CH unit is equivalent to BH^- unit. The optimized geometries of $\text{B}_2\text{H}_4^{2-}$ and its dilithium complex isomers as obtained by using MP2/6-311++(2d 2p) method are given in Figure 4.1(a). Out of the optimized geometries of two different isomers of $\text{B}_2\text{H}_4\text{Li}_2$ as shown in Figure 4.1(a), the planar structure having D_{2h} symmetry is found to be the stable one as compared to other non-planar structure with same symmetry and the energy difference is found to be around 22.26 kcal/mol. The B-B bond distance is found to be 1.61 \AA which is shorter as compared to that in diborane (1.72 \AA) and is comparable with the reported B-B double bond.¹⁸⁸ The HOMO is found to be the bonding π orbital between the two boron atoms which confirms the presence of B-B double bond as shown in Figure 4.1(b). The B-H and B-Li bond distances in $\text{B}_2\text{H}_4\text{Li}_2$ are found to be 1.22 and 2.04 \AA respectively. Unlike in diborane, where the bridging hydrogen atoms are in a plane perpendicular to the remaining

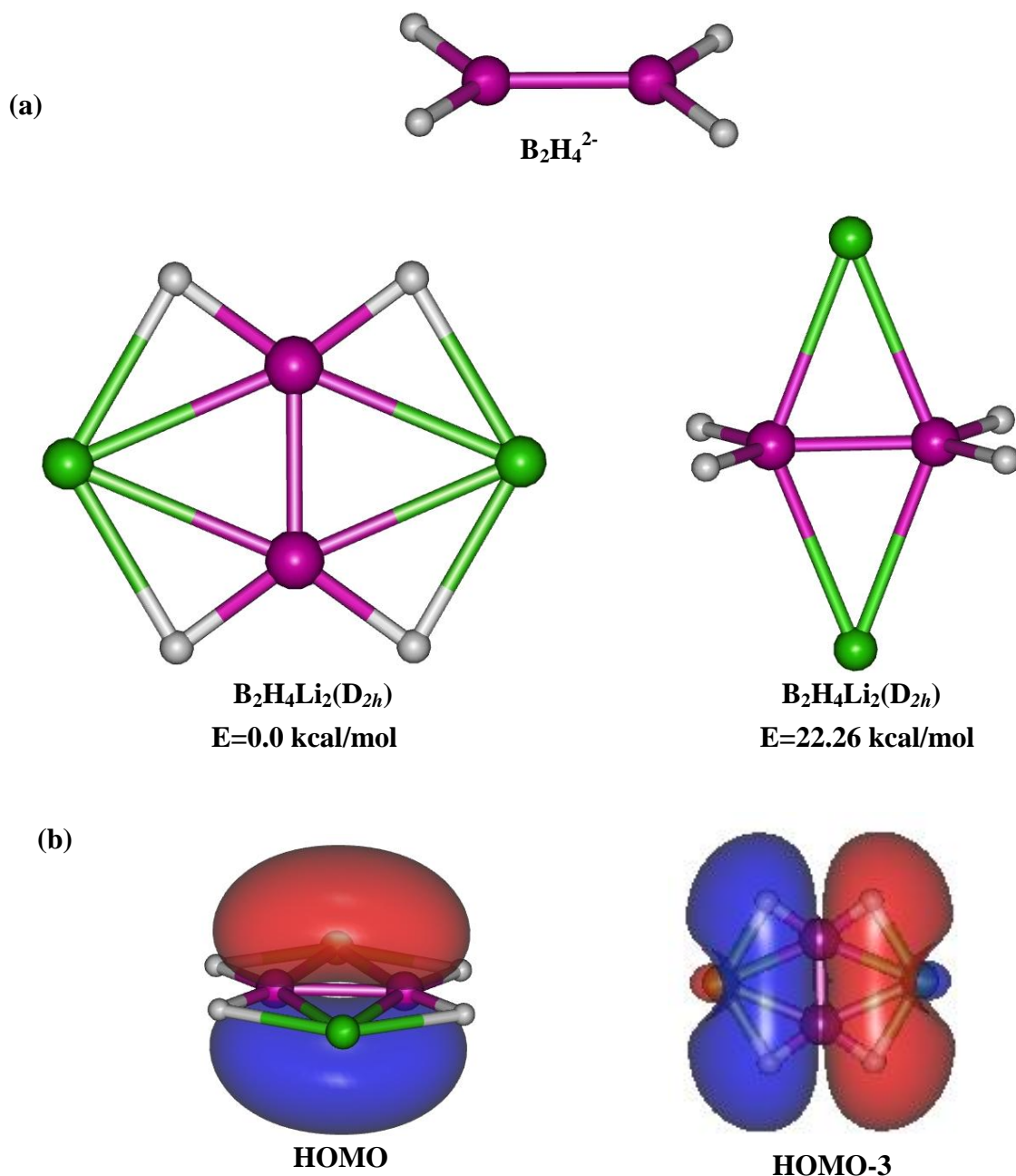


Figure 4.1: (a). Optimized geometries of $\text{B}_2\text{H}_4^{2-}$ and $\text{B}_2\text{H}_4\text{Li}_2$. (b).HOMO and HOMO-3 orbital pictures of $\text{B}_2\text{H}_4\text{Li}_2$.

B_2H_2 plane, here both the lithium atoms are in the same plane with B_2H_4 which is consistent with the previous report¹⁸⁸ where it was explained that the dominating Li ion hydrogen atom interaction leads to planar geometry. The HBH bond angle in diborane is 122° whereas in $\text{B}_2\text{H}_4\text{Li}_2$ planar structure the corresponding angle is compressed to 107.4° which can be compared with the reported value of 116.6° in neutral B_2H_4 species. This HBH bond angle in

$B_2H_4^{2-}$ is 112° which is reduced to 107.4° in $B_2H_4Li_2$ that can be attributed to the weak antibonding interaction between Li and BH_2 group orbitals as shown in the HOMO-3 orbital picture in Figure 4.1(b). Each lithium atom in $B_2H_4Li_2$ is found to carry a positive charge of around 0.76 and this charged site can adsorb molecular hydrogen through ion-quadrupole and ion-induced dipole interactions. To ascertain that a complex is a stable one, the complex should not only have no imaginary frequencies, but the smallest vibrational frequency calculated should also be reasonably large.¹⁹¹ From our calculated result on the Hessian, we find that the smallest vibrational frequency of $B_2H_4Li_2$ is 156.31 cm^{-1} which shows that the dilithium complex is stable. Similarly, the HOMO-LUMO separation in the complex should be appreciable in magnitude to indicate stability. The calculated HOMO-LUMO gap is also found to be large (6.62 eV), which is also an indication for its stability.

Another hydrocarbon analogue of boron hydride considered here is the species $B_2H_2^{2-}$ which is analogue of C_2H_2 and the corresponding optimized geometries of dihydrodiborate dianion and its lithiated isomers are given in Figure 4.2(a). Here also we have optimized two different isomers out of which, one with butterfly like structure having C_{2v} symmetry is found to be the minimum energy isomer as compared to the other planar structure with C_{2h} symmetry. In the case of $B_2H_2Li_2$, the B-B bond distance is found to be 1.47 \AA which is in consistency with the earlier results of Kaufmann et al.¹⁸⁸ This bond distance is shorter than that of B-B double bond (1.61 \AA) in $B_2H_4Li_2$ and can be considered as a B-B triple bond. The B-H and B-Li bond distances are found to be 1.19 and 2.17 \AA respectively. From the orbital pictures of HOMO and HOMO-1 shown in Figure 4.2(b) it is clear that they belong to bonding π orbitals and the presence of two π bonds between B-B confirms the presence of a B-B triple bond. From Hessian calculations, we find that there is no imaginary frequency and the minimum vibrational frequency is 59.74 cm^{-1} .

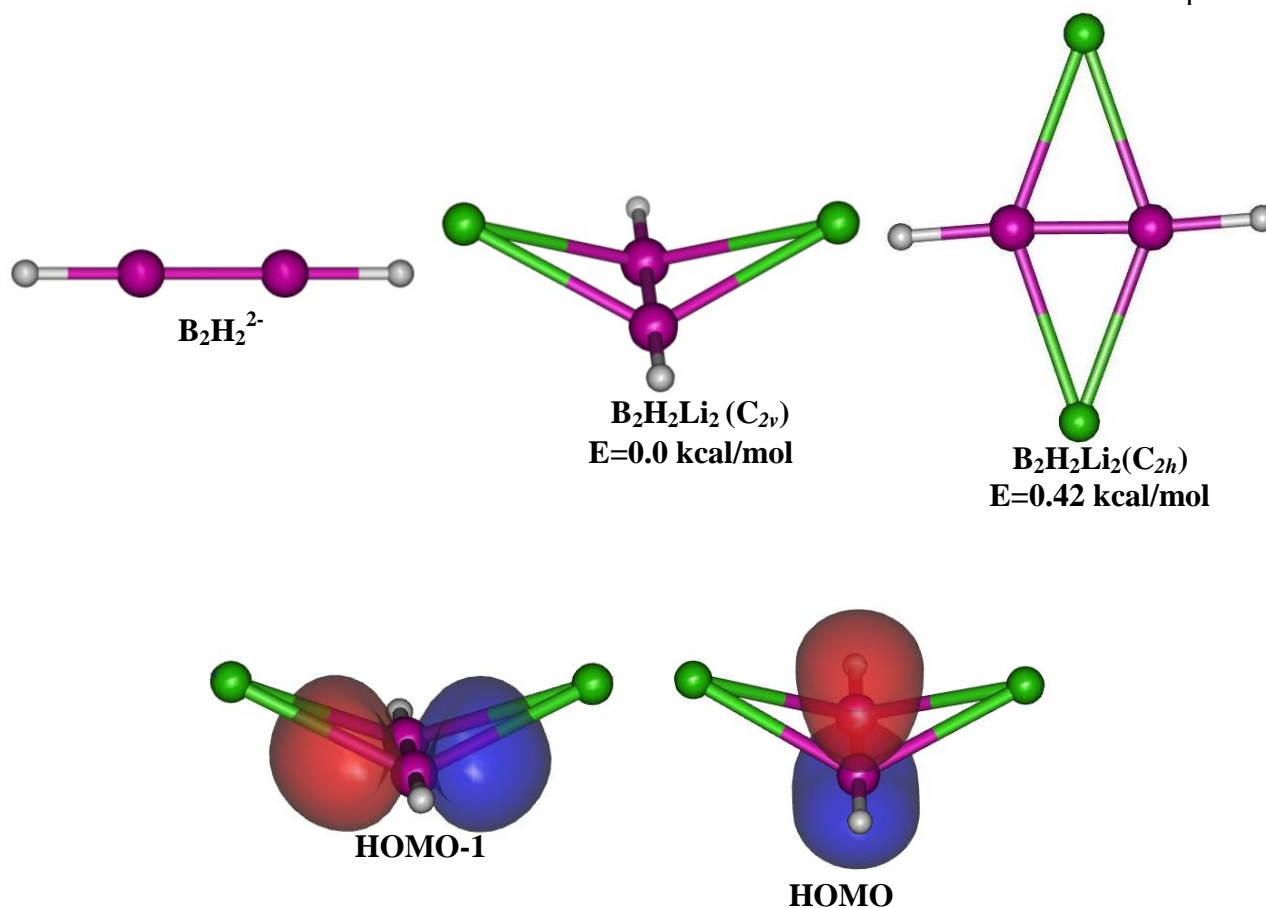


Figure 4.2: (a) Optimized geometries of $\text{B}_2\text{H}_2^{2-}$ and $\text{B}_2\text{H}_2\text{Li}_2$ (b). HOMO and HOMO-1 orbital pictures of $\text{B}_2\text{H}_2\text{Li}_2$

The calculated HOMO-LUMO gap is found to be 6.22 eV. These two results indicate the stability of the complex, $\text{B}_2\text{H}_2\text{Li}_2$. In this case also both the lithium sites carry a positive charge of 0.86 and can be utilized for trapping molecular hydrogen.

Hydrogen adsorption properties of these two lithium decorated unsaturated boron hydrides ($\text{B}_2\text{H}_2\text{Li}_2$ and $\text{B}_2\text{H}_4\text{Li}_2$) have been investigated systematically by gradually increasing the number of H_2 molecules adsorbed per metallic site. MP2/6-31++(2d 2p) optimized geometries of the hydrogenated complexes, $\text{B}_2\text{H}_4\text{Li}_2(\text{H}_2)_{2n}$ for $n=1-4$ are given in Figure 4.3, and the corresponding results at different levels of theory are reported in Table 4.1. Though we have performed calculations based on both DFT and MP2 methods, we will discuss mainly the MP2 results here. The first molecular hydrogen on each lithium site is adsorbed with adsorption energy of -2.62 kcal/mol per H_2 molecule. The optimized

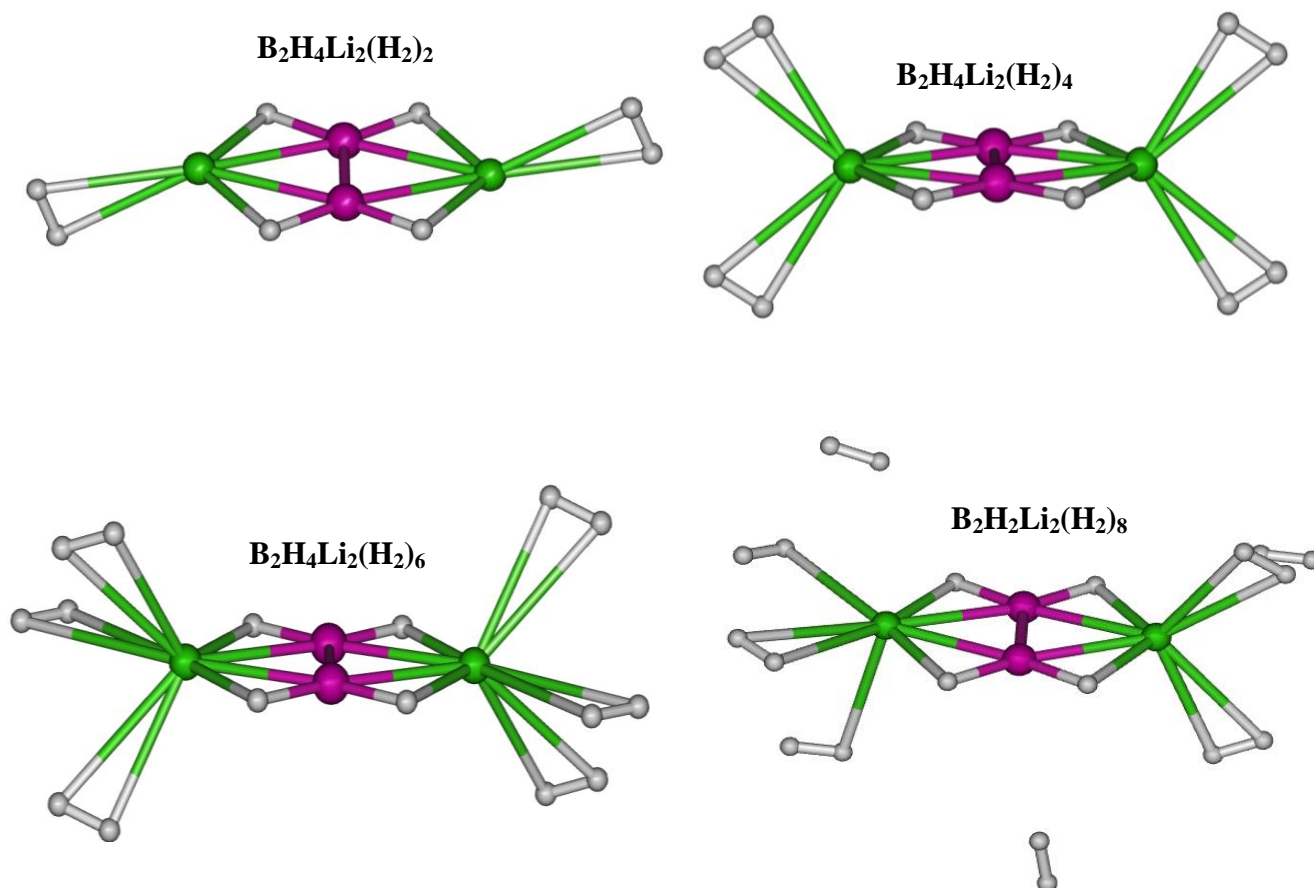


Figure 4.3: Optimized geometries of $B_2H_4Li_2(H_2)_{2n}$ ($n=1-4$)

geometry of $B_2H_4Li_2(H_2)_2$ is found to be of C_{2h} symmetry with Li- H_2 distance of around 2.1 Å as shown in Figure 3. The H-H bond distance is found to be 0.74 Å which is slightly longer than that of free molecular hydrogen (0.73 Å) optimized by using the same method. In the case of $B_2H_4Li_2(H_2)_4$ the adsorption energy per molecular hydrogen is found to be -2.01 kcal/mol. The optimized structure of $B_2H_4Li_2(H_2)_4$ is found to have D_{2h} symmetry where all the adsorbed molecular hydrogen are in a plane perpendicular to the $B_2H_4Li_2$ molecular plane and the Li- H_2 distances are around 2.2 Å. The third molecular hydrogen on each Li is found to bind with an interaction energy of -1.85 kcal/mol per H_2 molecule and the minimum energy structure is of C_{2h} symmetry. Out of the three H_2 molecules per Li, two are bonded with a Li- H_2 distance of 2.3 Å whereas the remaining H_2 is a bit away with a Li- H_2 distance

of 2.55 Å. From the geometry of $B_2H_4Li_2(H_2)_8$ given in Figure 4.3, it can be seen that once the fourth hydrogen molecule approaches the Li site, two of the four H_2 molecules move away from the metal site which can be attributed to the intermolecular repulsions between adsorbed hydrogen molecules. From these results, we can conclude that each Li can bind with a maximum of three hydrogen molecules to have $B_2H_4Li_2(H_2)_6$ which corresponds to a gravimetric density of ~23.0 wt%.

The optimized geometries of the hydrogenated complexes, $B_2H_2Li_2(H_2)_{2n}$ for $n=1-4$ are given in Figure 4.4. The hydrogen adsorption energy per H_2 molecule in the case of $B_2H_2Li_2(H_2)_2$ as calculated by the MP2 method is found to be -2.52 kcal/mol. The minimum energy structure of $B_2H_2Li_2(H_2)_2$ is found to have C_s symmetry with Li- H_2 distance of 2.15 Å.

Table 4.1 Interaction energies, charge on lithium atoms and HOMO-LUMO gaps of lithiated B_2H_2 , B_2H_4 and their hydrogen adsorbed complexes.

System	^a Interaction energy in kcal/mol			Charge on Li (a.u)			HOMO-LUMO gap (eV) HLYP
	HLYP	M06-2X	MP2	HLYP	M06	MP2	
$B_2H_4-Li_2$	-223.28	-220.52	-218.58	0.775	0.747	0.766	6.62
$B_2H_2-Li_2$	-218.04	-214.42	-211.30	0.887	0.859	0.862	6.22
$B_2H_4Li_2-(H_2)_2$	-3.19	-2.62	-2.62	0.577	0.622	0.615	6.73
$B_2H_4Li_2-(H_2)_4$	-2.50	-2.29	-2.01	0.509	0.512	0.545	6.63
$B_2H_4Li_2-(H_2)_6$	-2.02	-1.92	-1.85	0.452	0.457	0.514	6.58
$B_2H_2Li_2-(H_2)_2$	-3.17	-2.61	-2.52	0.453	0.436	0.605	6.27
$B_2H_2Li_2-(H_2)_4$	-3.31	-2.14	-2.16	0.594	0.425	0.578	6.14
$B_2H_2Li_2-(H_2)_6$	-2.85	-2.64	-2.55	0.567	0.360	0.686	6.08

The LiBBLi dihedral angle in this hydrogenated complex is found to be increased to 150° from 134° in $B_2H_2Li_2$. In the case of $B_2H_2Li_2(H_2)_4$ the optimized geometry is found to have C_{2v} symmetry where the adsorbed hydrogen molecules are in a plane perpendicular to the

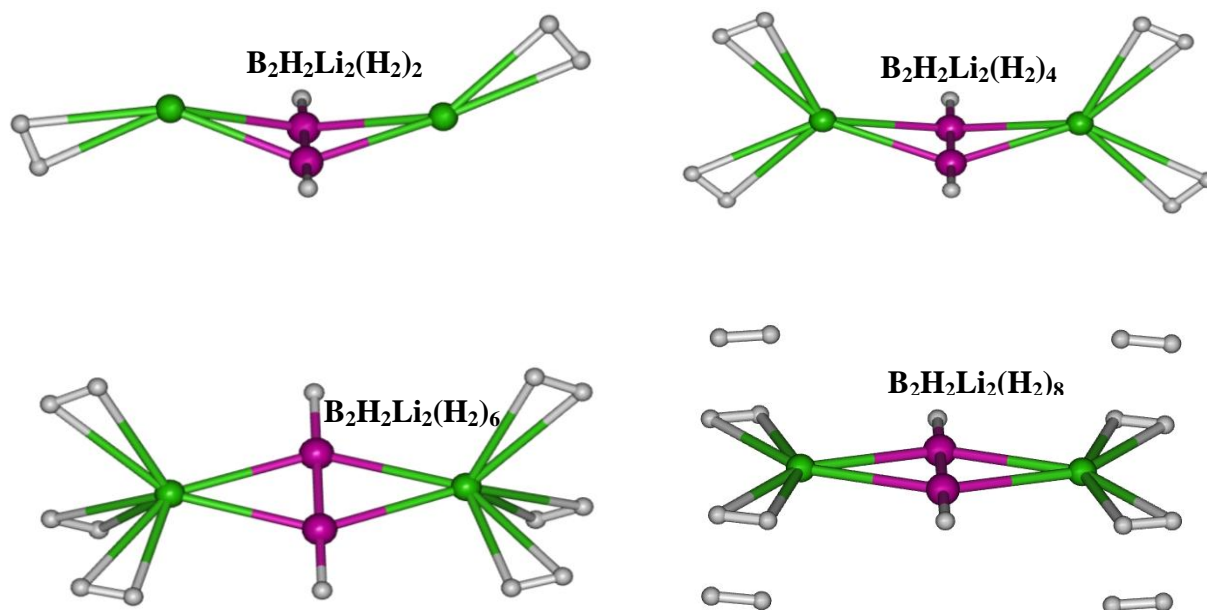


Figure 4.4: Optimized geometries of $B_2H_2Li_2(H_2)_{2n}$ ($n=1-4$)

B-B bond. The hydrogen adsorption energy per molecule is found to be -2.16 kcal/mol with a Li-H₂ distance of 2.2 Å. The dihedral angle is further increased to 153.3° which shows that on hydrogen adsorption, the complex $B_2H_2Li_2$ gradually transforms from non-planar towards planar geometry. On adsorption of the third molecular hydrogen on each lithium site, the geometry of $B_2H_2Li_2$ in the complex $B_2H_2Li_2(H_2)_6$ is found to be completely transformed to planar and the resulting hydrogenated complex is found to have C_{2v} symmetry. The Li-H₂ distance is found to be around 2.2 Å, and the hydrogen adsorption energy per H₂ molecule in this case is -2.55 kcal/mol. After adsorption of the fourth hydrogen molecule, as shown in the Figure 4.4, two of the four molecules are found to be nearer to Li with Li-H₂ distance of around 2.1 Å while the other two H₂ molecules are at a distance of around 2.35 Å from the Li site. Even with three molecular hydrogens per Li, the gravimetric density of hydrogen in $B_2H_2Li_2(H_2)_6$ will be ~24.0 wt% which is very high and the adsorption energies are also reasonably good. We have calculated the Hessian for all the hydrogenated complexes of both

$B_2H_2Li_2$ and $B_2H_4Li_2$ and found that none of them leads to imaginary frequencies which is an indication that all these structures belong to local minima on their potential energy surfaces. The calculated HOMO-LUMO gaps of the hydrogenated complexes are reported in Table 4.1, and are found to be very high which is also an indication for the stability of these complexes.

We have also modeled a one-dimensional nanowire with $C_6H_4B_2Li_2$ as the building unit as shown in Figure 4.5(a). For this calculation, we have considered a unit cell of 14 atoms and optimized the geometry using periodic boundary condition through GGA (PW91) based density functional method. From the optimized structure, the B-B bond distance is found to be 1.48 Å which is close to the B-B triple bond length calculated in the $B_2H_2Li_2$ complex. The calculated Bader¹⁹² charge on each lithium is found to be around +0.9 which shows the ionic nature of lithium sites. We then consider

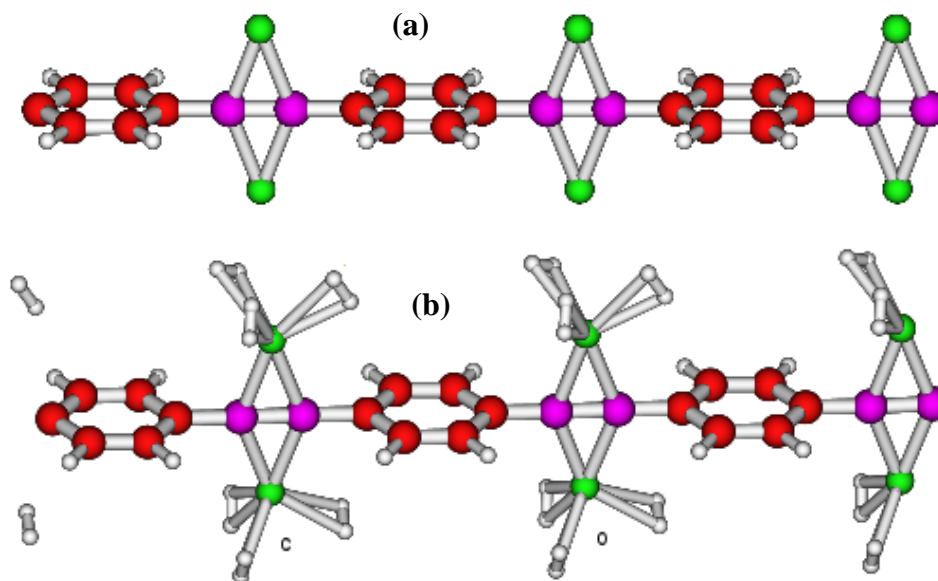


Figure 4.5: 1 x 1 x 3 supercell structures of optimized one dimensional nanowire with (a) $C_6H_4B_2Li_2$ as monomer and (b) its hydrogen adsorbed counterpart

hydrogen molecules interacting with these cationic sites and the 1 x 1 x 3 super cell of the hydrogenated nanowire optimized using PW91 method is shown in Figure 4.5(b). The Li- H_2

distance in this structure is found to be 2.2 Å and the hydrogen adsorption energy per molecular hydrogen is -2.34 kcal/mol. Each unit of $\text{C}_6\text{H}_4\text{B}_2\text{Li}_2$ is found to adsorb six hydrogen molecules, which corresponds to a hydrogen gravimetric density of 9.68 wt%.

4.3.2 Hydrogen adsorption in Li-doped *closo*-boranes

The equilibrium geometry of hexaborane (6) di anion, the smallest of the series of *closo*-boranes, which are known to be highly stable and aromatic in the di-anionic form, optimized at MP2/ aug-cc-pVTZ is given in Figure 4.6. The structure of $\text{B}_6\text{H}_6^{2-}$ is found to have a smaller octahedral B_6 unit with a B-B bond distance of 1.733 Å, surrounded by octahedrally arranged six hydrogens which are bonded to six borons exohedrally with a B-H bond distance of 1.207 Å. The nucleus-independent chemical shift value calculated at the centre of the $\text{B}_6\text{H}_6^{2-}$ unit (NICS(0)) is found to be -28.51 which is also in agreement with the earlier reported value,⁵⁴ this large negative value is an indication for its aromatic nature. $\text{B}_6\text{H}_6^{2-}$ can form salts with electropositive cations like lithium ($\text{Li}_2\text{B}_6\text{H}_6$) and sodium ($\text{Na}_2\text{B}_6\text{H}_6$) where the metal atoms can sit on any two opposite faces out of the eight faces of the octahedral B_6 unit.

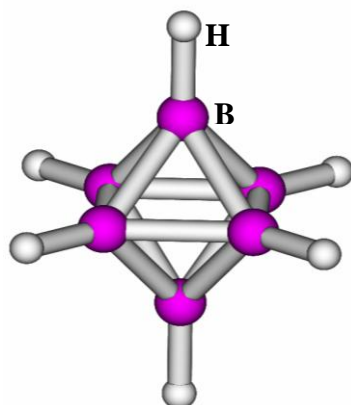


Figure 4.6 Equilibrium geometry of $\text{B}_6\text{H}_6^{2-}$

Two different structures of $\text{B}_6\text{H}_6\text{Li}_2$ which are optimized at MP2/aug-cc-pVTZ level of theory are shown in Figure 4.7. Among the two structures, one with the lithium atoms

bonded on opposite faces of the B_6H_6 octahedron having D_{3d} symmetry is found to be the minimum energy structure as compared to the other one where two lithium atoms are bonded

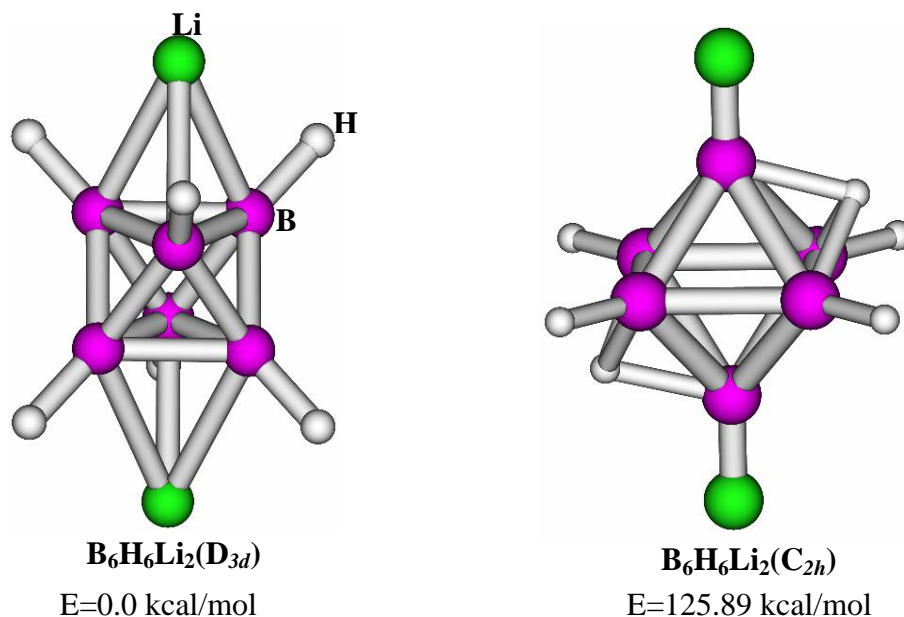


Figure 4.7 Equilibrium geometries for two different isomers of $B_6H_6Li_2$

exohedrally and two hydrogens are bonded to the two opposite faces with C_{2h} symmetry and the energy difference is found to be 125.89 kcal/mol. In both the cases, the facially bonded atoms can be considered as e bonded through 4c-2e bond which is not trivial and its study is very rare in the literature. Schleyer *et al.*¹⁹³ discussed the pseudo-tetrahedral B_3H motif in polyhedral borane and hydroborate, CB_5H_7 and $B_6H_7^-$, on the basis of Hartree-Fock (H-F) and DFT calculations. Very recently, Hofmann *et al.*¹⁹⁴ experimentally studied the structure of a salt ($N(C_4H_9)_4B_6H_7^-$) containing $B_6H_7^-$ and recognized the presence of 4c-2e bonding. The minimum energy structure of $B_6H_6Li_2$ is found to have two sets of B-B bond lengths, where out of the twelve B-B bonds, six B-B bonds which are not bonded to Li atom are having a bond length of 1.697 Å whereas the remaining six B-B bonds i.e three from each face of the Li bonded faces are having a bond length 1.742 Å and all the B-H bonds as well as all the B-Li bonds are found to be equivalent with bond lengths of 1.199 Å and 2.168 Å respectively. The binding energy of Li^+ to the $B_6H_6^{-2}$ framework calculated at MP2/aug-cc-pVTZ level of

theory is found to be -196.467 kcal/mol per lithium which is very high as compared to the cohesive energy of lithium¹⁹⁵ (37.7 kcal/mol at room temperature). This huge binding energy and large HOMO-LUMO gap (4.0 eV) shows the stability of the complex which is very important from the view point of recyclability of the material. The calculated NICS(0) value is found to be -25.16 which shows the aromatic stability of the complex. Each of the two lithium atoms is found to have a positive charge of 0.735 a.u which shows that there is considerable electron transfer from lithium to the B₆H₆ unit. Recently Zhang et. al.¹⁹⁶ studied the hydrogen adsorption in Ti substituted closo-boranes where Ti is substituted in place of one BH²⁻ and reported a hydrogen uptake of 8.6 wt% in B₅H₅Ti and 10.0 wt% in B₄H₄Ti₂H₂.

Table 4.2 Calculated parameters for Interaction of Li⁺ ions with B₆H₆²⁻ and molecular hydrogen with B₆H₆Li₂

System	Interaction Energy ^a (kcal/mol)			Charge on Li (a.u)			NICS(0)	HOMO-LUMO gap (eV)
	MP2	M06	HLYP	MP2	M06	HLYP		
B ₆ H ₆ ²⁻ -2Li ⁺	-196.47	-192.46	-197.24	0.7444	0.7351	0.7806	-25.16	4.000
B ₆ H ₆ Li ₂ -(H ₂) ₂	-3.353	-3.289	-3.287	0.6114	0.6683	0.6527	-24.50	4.272
B ₆ H ₆ Li ₂ -(H ₂) ₄	-3.198	-3.382	-3.188	0.6079	0.5720	0.5190	-23.84	4.435
B ₆ H ₆ Li ₂ -(H ₂) ₆	-3.082	-3.542	-3.067	0.5557	0.4835	0.5425	-23.76	4.544

We have carried out a systematic study of molecular hydrogen adsorption in B₆H₆Li₂. The optimized geometries of the resulting species B₆H₆Li₂(H₂)_n, where n=1-3, at MP2/ aug-cc-pVTZ level of theory are shown in Figure 4.8. The first molecular hydrogen on both the lithium sites is found to bind with interaction energy of -3.35 kcal/mol and the optimized structure of the hydrogenated species (B₆H₆Li₂H₂) is of C₂ symmetry. The Li-H bond length is found to be 2.06 Å and the molecular hydrogen is bound to lithium in a T shaped manner in contrast to the linear arrangement in case of anion-molecular hydrogen complex. The charge on lithium in B₆H₆Li₂(H₂) is reduced to 0.6683 from 0.7351 in B₆H₆Li₂. In B₆H₆Li₂, the distance between Li and the centre of the B₆ unit is found to be 2.604 Å which on adsorption

of the first hydrogen molecule increased marginally to 2.607 Å. In the adsorbed molecular hydrogen, one H atom is little closer to the Li atom (2.062 Å) as compared to the other hydrogen atom (2.106 Å) by 0.044 Å. This difference in the Li-H distance shows that the charge on Li induced a dipole in the molecular hydrogen and the negative end of the dipole is closer to the cationic site as compared to the other end of the dipole. The H-H bond length in the adsorbed molecular hydrogen is found to be 0.743 Å which is longer as compared to that in the free hydrogen molecule optimized at the same level of theory (0.737 Å).

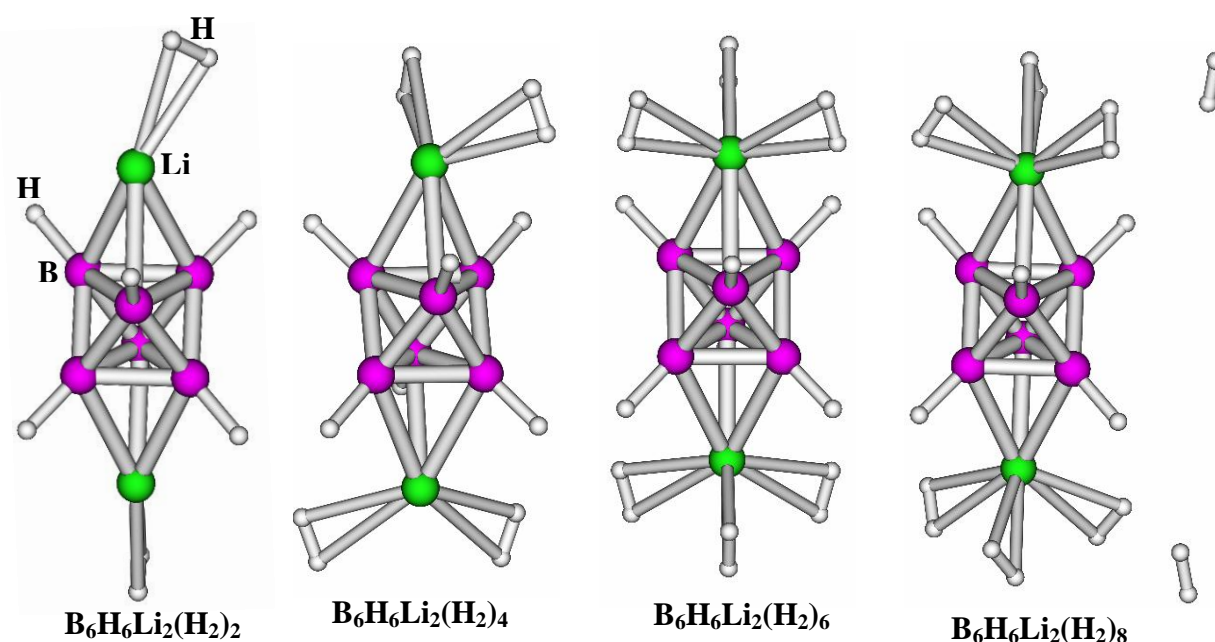


Figure 4.8 Equilibrium geometries of $B_6H_6Li_2(H_2)_n$ ($n=1-3$)

The MP2/aug-cc-pVTZ optimized structure of $B_6H_6Li_2(H_2)_2$ is found to have a C_2 symmetry as shown in Figure 4.8. The second molecular hydrogen on each metal site is found to bind with an interaction energy of -3.20 kcal/mol per molecular hydrogen. The Li-H as well as the H-H distances are similar to the earlier case whereas the distance between Li and the centre of the B_6 unit is found to be 2.633 Å as compared to 2.604 Å in $B_6H_6Li_2$. The charge on Li is found to be further diminished to 0.61 from 0.67 in $B_6H_6Li_2(H_2)$ indicating charge transfer between Li and the molecular hydrogen. In the case of $B_6H_6Li_2(H_2)_3$ the

binding energy of each molecular hydrogen is found to be -3.08 kcal/mol and the equilibrium geometry optimized at the MP2/aug-cc-pVTZ level of theory is found to possess the symmetry S_6 . The distance between Li and the centre of the B_6 unit is found to be 2.633 Å and the charge on each Li is found to be 0.56. From the optimized geometry of $B_6H_6Li_2(H_2)_8$ given in Figure 4.8, it can be seen that the fourth molecular hydrogen is not binding to the lithium site and is moving away from Li which shows that each lithium can adsorb a maximum of three molecular hydrogens which is equivalent to a gravimetric density of 12 wt% at 0 K. From the HOMO-LUMO gaps given in Table 4.2 as well as shown in Figure 4.9(a), it can be seen that there is an increase in the gap with increase in the number of hydrogens adsorbed which is an indication of stabilization of the complex on adsorption and the variation of charge on the lithium atom is shown in Figure 4.9(b). For all the hydrogen adsorbed systems, the NICS(0) values reported in Table 4.2 are highly negative which shows the aromatic nature of these complexes.

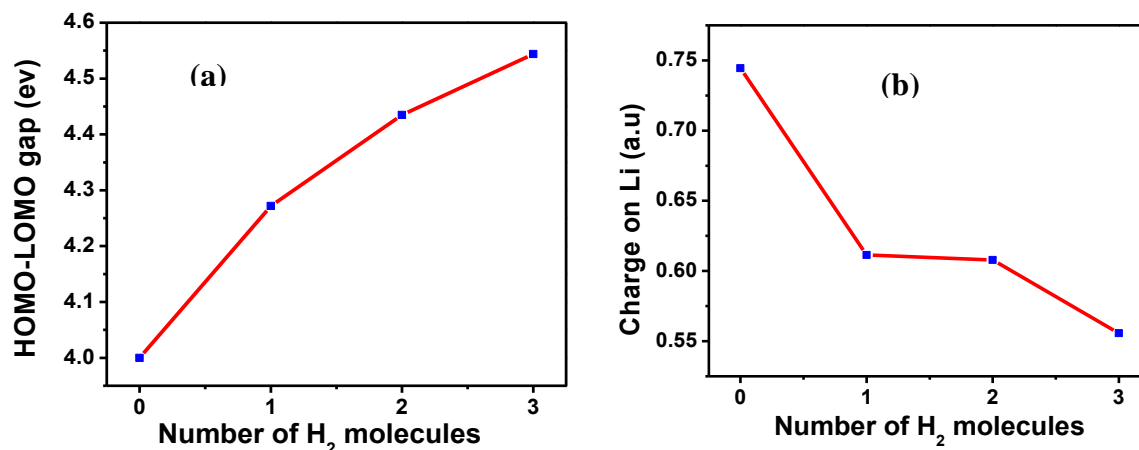


Figure 4.9 Variation of (a) HOMO-LUMO gap and (b) charge on lithium atom with number of hydrogen molecules in $B_6H_6Li_2(H_2)_n$ ($n=1-3$)

We have also verified the possibility of constructing a three dimensional solid using the di-lithium doped B_6 unit as a building block and $-C\equiv C-$ triple bonds as a linking agent. Each corner of the B_6 unit is connected to another B_6 unit through $-C\equiv C-$ three dimensionally

as shown in Figure 4.10. The positions of all the atoms in the cell as well as the lattice parameters have been fully relaxed without any constraint. The C-C bond distance in the structure optimized using LDA method is found to be 1.23 Å which is close to the C-C triple bond distance. Each B₆ octahedron is separated by a distance of around 4.2 Å and the Li-Li nearest neighbor distance is found to be 4.54 Å. Two lithium atoms are found to occupy the two mutually opposite faces of each B₆ unit with B-Li bond distance of 2.405 Å and the B-C bond distance is found to be 1.495 Å. As in the single unit case, here also the B₆ unit has two sets of bond lengths, viz. 1.69 Å in the edge not bonded to Li and 1.75 Å in the case of B-B edge bonded to the Li atom and each B₆Li₂ is found to possess D_{3d} symmetry.

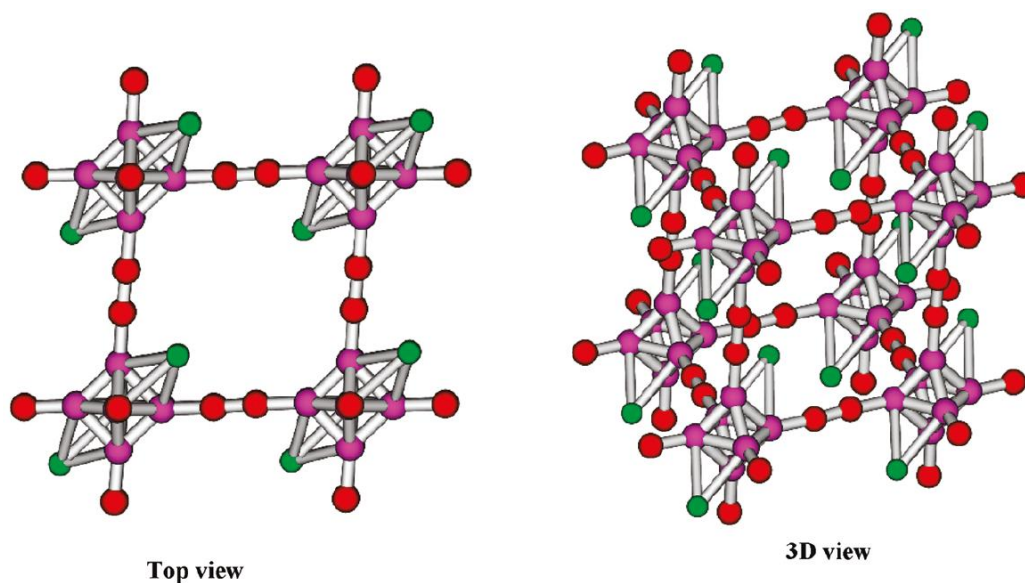


Figure 4.10 Three dimensional solid constructed by using B₆Li₂ units as building blocks and C≡C as linker.

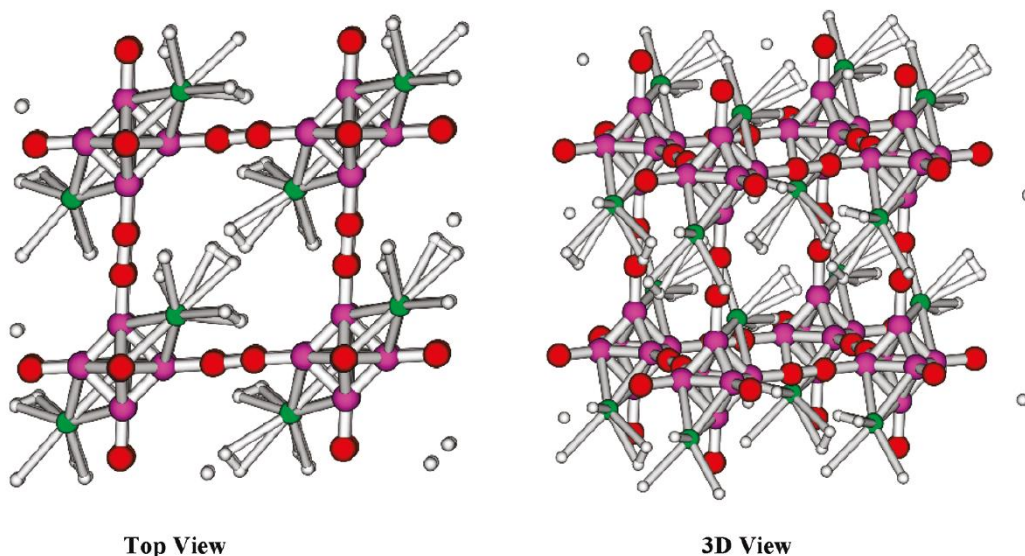


Figure 4.11 Three dimensional solid constructed by using $B_6Li_2(H_2)_3$ units as building blocks and $-C\equiv C-$ as linker.

The hydrogen adsorption properties of this designed structure are also studied using LDA as well as GGA (PBE) based DFT methods. The optimized structure of the above mentioned 3D material with three hydrogen molecules per lithium is shown in Figure 4.11. Each lithium atom in this periodic structure is found to bind a maximum of three hydrogen molecules. The binding energy per molecular hydrogen using LDA is found to be -2.32 kcal/mol whereas using GGA (PBE) it is found to be -1.944 kcal/mol. It is well known from the literature that GGA underestimates and LDA overestimates the weak interactions. Thus the interaction energy might be in between the two reported values. The minimum Li-H distance is found to be 2.04 Å. Each of the unit cells consists of $B_6C_6Li_2H_{12}$ which is equivalent to a gravimetric density of around 7.3 wt% at 0 K. Moreover, it is known from the literature that the alkyl and aryl derivatives of closo-borane dianions can be synthesized,¹⁹⁷ which supports the feasibility of the designed solids shown here.

4.4 Conclusions

In summary, we have examined the structure, stability and hydrogen adsorption properties of lithium decorated dihydrodiborate dianion, $B_2H_2^{2-}$ and tetrahydrodiborate dianion, $B_2H_4^{2-}$ which are isoelectronic with acetylene and ethylene respectively. In both these lithiated complexes, the Li sites are found to be cationic in nature, which can bind molecular hydrogen through ion-quadrupole and ion-induced dipole interactions. In both the complexes $B_2H_4Li_2$ and $B_2H_4Li_2(H_2)_6$, each lithium centre is found to adsorb three molecular hydrogen. We have also modeled a one dimensional nanowire with $C_6H_4B_2Li_2$ as the repeating unit and it is found that the B-B bond length is close to triple bond distance. The Bader charge analysis showed that each Li site carries nearly unit positive charge, and is found to adsorb three hydrogen molecules resulting into a gravimetric density of 9.68 wt% of hydrogen. We have also shown that hexaborane(6) di-anion ($B_6H_6^{2-}$) can form stable complex (salts) with highly electro-positive alkali metal cation, (Li^+). Each Li can adsorb a maximum of three hydrogen molecules which is equivalent to a gravimetric density of 12 wt%. We have also modeled a three-dimensional material with lithium doped borane as building block and $-C\equiv C-$ as a linking agent. The hydrogen adsorption studies in this designed material showed that it can adsorb molecular hydrogen with a gravimetric density of around 7.3 wt% and the binding energy per H_2 is found to be around -2.2 kcal/mol.

CHAPTER 5

Electronic Structure and Properties of Boron Hydride Analogues of Aluminum Hydrides

5.1. Introduction

Light metal hydrides and complex metal hydrides are the important classes of materials studied for hydrogen storage. AlH_3 can be a potential hydrogen storage material as it contains 10% hydrogen. Although aluminum and boron belong to the same group in the periodic table, there is a large difference in the chemistry of their hydrides.¹⁹⁸⁻²⁰⁰ Aluminum hydride chemistry is limited to very few systems like AlH_3 , its dimer Al_2H_6 , its polymeric form $(\text{AlH}_3)_n$, AlH_4^- and its alkali alanates like LiAlH_4 whereas boron is having a great history of its hydride chemistry.²⁰¹ Monomeric AlH_3 has been isolated at low temperature in a solid noble gas matrix and it is planar in structure.²⁰² Andrews *et al.*²⁰³ isolated the molecular Al_2H_6 in solid hydrogen by the reaction of laser-ablated aluminium atoms with pure hydrogen at 3.5 K followed by UV irradiation and annealing to 6.5 K. It has been characterized through infrared spectra and is found to have a structure similar to that of diborane. Polymeric aluminum hydride known as alane exists in seven different forms out of which, α -alane is known to be the most thermodynamically stable form with a hexagonal structure.²⁰⁴ Aluminum hydrides are known to be good reducing agent used for reducing functional groups in organic chemistry.²⁰⁵

Boron, in contrast, can form a large number of hydrides popularly known as boranes like B_2H_6 , B_4H_{10} , B_5H_9 , B_6H_{10} etc.²⁰⁶⁻²⁰⁷ which are well studied since the preparation and characterization of diborane, the first borane, by Stock *et al.*²⁰⁸ in 1912. The unusual composition and structures of boranes created great interest towards understanding their structure and bonding. Lipscomb and co-workers¹⁸² came up with the concept of three-centre two-electron (3c-2e) bonding to explain the structure and bonding in three dimensional boranes. In the cyclic 3c-2e bonding, three atomic orbitals, one from each atom interact to form one bonding and two anti-bonding molecular orbitals. This 3c-2e bonding is useful in explaining the bonding

in electron deficient compounds like diborane where the number of bonding electrons (12) is less than the number of atomic orbitals (14). Boranes are usually named by indicating the number of B atoms with a Greek prefix and the number of H atoms by an Arabic number in parentheses, e.g. B_5H_9 , pentaborane(9); B_5H_{11} , pentaborane(11), etc.²⁰⁹ All these boranes are found to have the deltahedral structures where each face is a triangle as suggested by Williams,²¹⁰ who also recognized that the loss of boron vertices from deltahedral *closo*-boranes generates the neutral boranes, *nido*-boranes (B_nH_{n+4}) and *arachno*-boranes (B_nH_{n+6}). Wade²¹¹ developed an important relationship between these structural relations and the number of valence electrons involved in the skeletal bonding in the boranes. Deprotonation of all the bridging hydrogens from the *nido* ($B_{(n-1)}H_{(n-1)+4}$) and *arachno* ($B_{(n-2)}H_{(n-2)+6}$) boranes leads to the ions $B_{(n-1)}H_{(n-1)}^{4-}$ and $B_{(n-2)}H_{(n-2)}^{6-}$ respectively which have the same number of skeletal (n+1) electron pairs, as the n-vertex *closo*-borane, $B_nH_n^{2-}$ is having. So the *closo*, *nido* and *arachno* boranes are related as shown by Williams because they share the same number bonding molecular orbitals (electrons) associated with the aluminum skeleton. Later, Mingos²¹² used these ideas to develop the “Polyhedral Skeletal Electron Pair Theory (PSEPT)” which provides a simple understanding of the structure of boranes. Later, this has been designated as Wade-Mingos electron counting rules and applied to the metal clusters. Recently, Balakrishnan and Jemmis²¹³ have extended the Wade-Mingos rule for the isolated deltahedra to the fused ones which requires $(n+m)$ skeletal electron pairs, where n is the total number of vertices and m is the number of individual deltahedra, which was further extended to include the single vertex sharing polyhedral structures as *mno* rule²¹⁴ which contains $(m+n+o)$ skeletal electron pairs and m=1, o=0 will reduce the Jemmis rule to the Wade-Mingos rule. The deltahedral borane anions $B_nH_n^{2-}$ are known to be highly stable and the resonance stabilization of these ions leads to three dimensional aromaticity which was explained

using the graph theory²¹⁵ as well as the six interstitial electron rules of Jemmis.²¹⁶ Each 3c-2e bond in boranes is aromatic because it involves a ring current which gives the diatropic chemical shift.

In recent times there has been a great interest in the study of chemistry of aluminium hydrides because of their low molecular weight which can make it useful as a rocket fuel and also as a prominent hydrogen storage material. McKee²¹⁷ predicted the structures and heats of formation of aluminum hydrides up to Al_6H_{10} by carrying out *ab initio* molecular orbital calculations. Bowen and coworkers²¹⁸ have demonstrated the high stability of Al_4H_6 using the anion photoelectron spectroscopy and the results were strongly supported by theoretical calculations. Later, the same group studied the homologue of the alanes series, such as Al_4H_4 , $\text{Al}_n\text{H}_{n+2}$, ($4 \leq n \leq 8$).²¹⁹ Very recently, Martínez *et al.*²²⁰ calculated the structures of a series of $\text{Al}_n\text{H}_{n+2}$ ($n=4-11$) clusters. Fu *et al.*²²¹ studied the structures and energetics of $\text{Al}_n\text{H}_n^{2-}$ ($n=5-12$) and $\text{Al}_n\text{H}_{n+2}$ ($n=4-12$) and discussed the analogy between alanes and boranes. In the present study, we have explored the possibility of existence of different classes of alanes like *closo*, *nido* and *arachno* alanes analogues to the boranes.

5.2. Computational details

All the energy calculations and geometry optimization have been performed using the GAMESS suite of programs.¹⁵⁵ We have employed the DFT approach B3LYP¹⁰⁴⁻¹⁰⁶ and the second order Møller-Plesset (MP2) perturbation method for all the systems. The extensive split-valence basis sets with diffuse and polarization functions, 6-31++G (2d, 2p), and also the Dunning type correlation-consistent basis set, aug-cc-pVTZ have been used. The initial geometries are generated using the graphical software MOLDEN¹³⁵ and all the reported figures are obtained using the graphical software Gabedit.¹⁶⁴

5.3. Results and Discussion.

All the aluminium hydride systems studied here are categorized into *closo*, *nido* and *arachno* alanes similar to the boranes. Geometries of all the systems are optimized at different levels of theory like DFT based B3LYP method as well as the MP2 method using the extensive basis sets and are discussed in the following four sections.

5.3.1 The *closo*-alanes ($\text{Al}_n\text{H}_{n+2}$): Equilibrium geometries of all the *closo*-alanes of the general formula $\text{Al}_n\text{H}_{n+2}$ ($n=5, 6, 8, 10$ and 12) optimized by MP2/6-31++G(2d,2p) method are shown in Figure 5.1 and the corresponding results are given in Table 5.1. The equilibrium geometry of Al_5H_7 is found to have a distorted trigonal bipyramidal Al_5H_5 structure with two bridging hydrogens on the opposite edges, such that there is minimum steric repulsion. This bridge bonding can be treated as 3c-2e bonding which is common in case of boranes. It also agrees with the Wade's rule with six pairs of skeletal bonding electrons (five pairs from five vertices and one pair from the two bridge bonded hydrogens). The adiabatic as well as vertical ionization potentials and electron affinities of all the systems studied are reported in the Table 5.1, but only the adiabatic values are discussed here. The calculated adiabatic electron affinity of Al_5H_7 is found to be 1.83 eV which is in agreement with the experimental value of 1.9 eV.²¹⁹ The HOMO-LUMO gap is found to be around 2.12 eV, and it is associated with a high IP (7.0 eV) indicating its high stability.

The minimum energy structure of Al_6H_8 belongs to the symmetry group D_{3d} with a distorted octahedral Al_6H_6 core and the two extra hydrogen atoms are bound to two of its faces instead of the edges. More interestingly, our analysis has shown that the facial bonding, which can be assumed as a 4c-2e bond, is more favorable as compared to the 3c-2e edge bonding. The

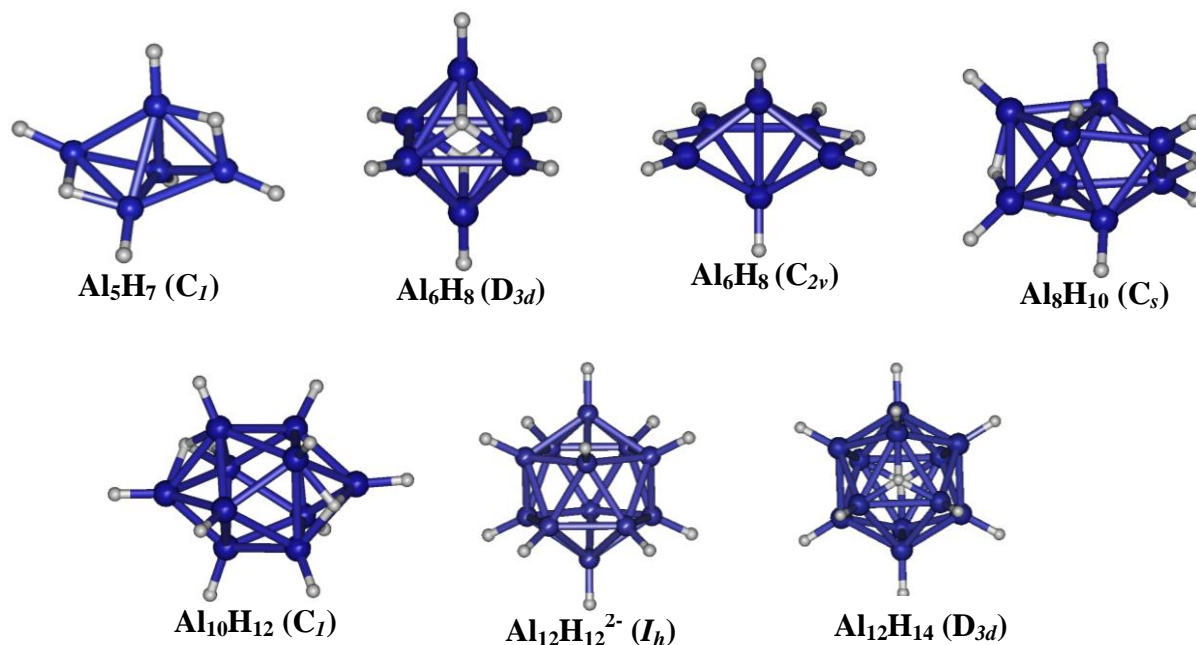


Figure 5.1: Optimized structures of *closo*-alanes, $\text{Al}_n\text{H}_{n+2}$ ($n=5, 6, 8, 10$ and 12) as obtained by MP2 method. The symmetries are given in parenthesis.

structure corresponding to the D_{3d} symmetry is found to be energetically more stable by 14.0 kcal/mol as compared to the C_{2v} geometry with a bi-capped tetrahedral Al_6H_6 core and the two extra hydrogens are bonding to the edges through the 3c-2e, as shown in Figure 5.1 which was reported to be the minimum energy structure in the earlier studies by Grubisic *et al.*²¹⁹ The 4c-2e type of bonding is not trivial and its study is very scarce in the literature. A few such type of 4c-2e bond has been predicted by Schleyer *et al.* as well as Olah *et al.*²²²⁻²²³ in adamantane type of organic molecular systems. Later Schleyer *et al.*¹⁹² discussed the pseudo-tetrahedral B_3H motif in polyhedral borane and hydroborate, CB_5H_7 and B_6H_7^- , on the basis of Hartree-Fock (H-F) and DFT calculations. Recently Hoffmann and Balakrishnarajan²²⁴ have studied a planar rhomboid of four boron atoms; Simon *et al.*²²⁵ observed triangles of metal atoms centered by a hydrogen

atom in the $\text{Th}_6\text{Br}_{12}\text{H}_7$ cluster. Very recently, Hofmann *et al.*²²⁶ experimentally studied the structure of a salt $(\text{N}(\text{C}_4\text{H}_9)_4\text{B}_6\text{H}_7^-)$ containing B_6H_7^- and recognized the presence of 4c-2e bonding. A 4c-2e bond will be favorable, when there is an effective overlap among the four atomic orbitals from four atoms which are forming the facial bond. There will be a deformation barrier to bring these four orbitals closer so that there will be an effective overlap. If the stabilization energy is less than the barrier, the system will prefer 3c-2e bonding which has been clearly demonstrated by Schleyer *et al.*¹⁹² for the borane case. The corresponding 3c-2e bonding system has also been reported to be the minimum energy structure in the earlier studies. The minimum energy structure is found to have a significant HOMO-LUMO gap of 1.38 eV, an electron affinity of 0.80 eV and ionization potential of 7.25 eV, revealing its high stability. It is also interesting to note that the *closo*-hexaalane(8) is having seven skeletal bonding electron pairs (6 from six vertices and 1 from two 4c-2e bonds), which is in accordance with the Wade's $(n+1)$ electron counting rule.

In the case of Al_8H_{10} , the minimum energy structure is the Al_8H_8 polyhedra with two bridging hydrogens on the two Al-Al edges with C_s geometry, as shown in Figure 5.1. Each of the bridging hydrogens is bonded to the edge connecting the aluminium atoms with lower connectivity (four). The observed HOMO-LUMO gap for this cluster is 2.23 eV, adiabatic EA is 1.78 eV and IP is 7.45 eV. The next higher homologue in this series, $\text{Al}_{10}\text{H}_{12}$, is having a ten vertex polyhedra with a distorted bicapped square antiprism structure and the two extra hydrogens are connected to two of its faces (as observed in Al_6H_8) instead of the edges, as shown in Figure 5.1. The aluminium atoms at the capping positions are having a skeletal connectivity of four whereas all others are having connectivity of five. $\text{Al}_{10}\text{H}_{12}$ follows the Wade's $(n+1)$ electron counting rule with eleven pairs of skeletal bonding electrons, ten pairs from the ten

vertices and one pair from the two facial hydrogen atoms. This structure is found to have the HOMO-LUMO gap, EA and IP, of 2.15, 2.24 and 7.31 eV, respectively.

In the case of 12 vertex system, the dianion $\text{Al}_{12}\text{H}_{12}^{2-}$ as well as its neutral counterpart $\text{Al}_{12}\text{H}_{14}$ have been studied and the corresponding equilibrium geometries are shown in Figure 5.1. The minimum energy structure of $\text{Al}_{12}\text{H}_{12}^{2-}$ is found to be an icosahedra analogues to the *closo*-dodecaborane(12) dianion, $\text{B}_{12}\text{H}_{12}^{2-}$ and the structure is having a very low ionization potential of 0.656 eV which can be due to the presence of two excess electrons. $\text{Al}_{12}\text{H}_{12}^{2-}$ is having large HOMO-LUMO gap of 1.84 eV. This *closo* alane, dodecaalane(12) dianion also follows the electron counting rule with 26 skeletal bonding electrons. The optimized geometry of neutral *closo*-dodecaalane(14), $\text{Al}_{12}\text{H}_{14}$ is found to have a $\text{Al}_{12}\text{H}_{12}$ icosahedra with the two hydrogens bonded to the two opposite faces with D_{3d} symmetry where the corresponding C_3 axis is passing through the two facially bound hydrogen atoms. The HOMO-LUMO gap of $\text{Al}_{12}\text{H}_{14}$ is found to be 2.3 eV which is larger than that of its dianion counterpart. The calculated IP and EA are 7.58 and 2.1 eV, respectively. These results conform to the higher stability of dodecaalane(14) over the dodecaalane(12) dianion system.

From the results discussed above it can be seen that all of the *closo* alanes $\text{Al}_n\text{H}_{n+2}$ are having polyhedral structure with n-vertex similar to the *closo* borane analogue ($\text{B}_n\text{H}_n^{2-}$) with the two extra hydrogens forming the bridge/facial bonding with the edge/face of the n-vertex polyhedron. Most of our *closo*-alane results are comparable with the existing results.^{219, 220} This indicates the applicability of the Wade's (n+1) electron counting rule for the *closo*-alane series.

5.3.2 The *nido*-alanes ($\text{Al}_n\text{H}_{n+4}$): The equilibrium geometries of all the *nido*-alanes of the general formula $\text{Al}_n\text{H}_{n+4}$ (n=5, 6, 8, 10 and 11) optimized by MP2/6-31++G(2d,2p) method are shown in Figure 5.2 and the corresponding results are given in Table 5.1. The five membered

nido-alane is found to have a structure with C_{4v} symmetry analogous to that of pentaborane(9) which can be considered as an octahedron, corresponding to hexaalane(8), with one vertex missing. The apical aluminium is connected to all other four Al atoms with a bond distance of 2.606 Å and the basal aluminium atoms are connected with each other with a bond distance of 2.658 Å. The four extra hydrogens are bonded to the four edges of the base through 3c-2e bonding with Al-H bond length of 1.74 Å and Al-H-Al angle of 99.63 degrees. Al_5H_9 is having 14 skeletal bonding electrons (10 from the five vertices and 4 from the four bridge hydrogens) which are in accordance with the Wade's $(n+2)$ rule for *nido*-boranes. The IP and EA of this cluster are 7.48 and 0.73 eV, respectively and the HOMO-LUMO gap is 2.76 eV.

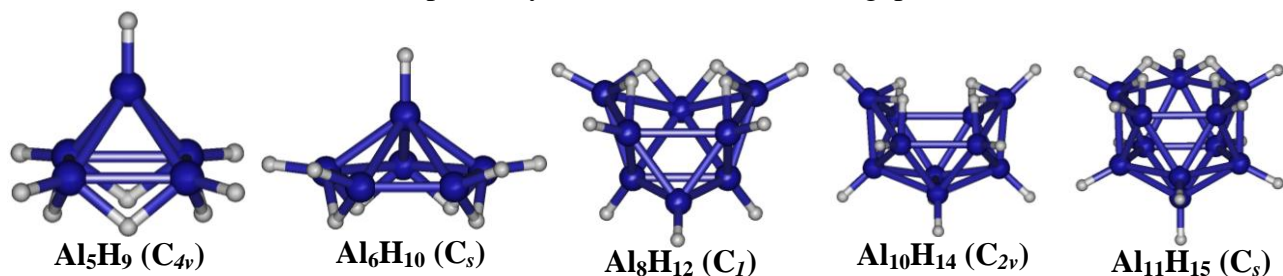


Figure 5.2: Optimized structures of *nido*-alanes, Al_nH_{n+4} ($n=5, 6, 8, 10$ and 11) as obtained by MP2 method. The symmetries are given in parenthesis.

The six vertex *nido*-alane, Al_6H_{10} having structure belonging to C_s symmetry, with a slightly distorted Al_6H_6 pentagonal pyramidal core and four hydrogens forming bridge bonding with four of the five edges of the five membered base ring, which is same as the structure of B_6H_{10} reported. All the four edges participating in bridge bonding are found to have equal Al-Al bond lengths (2.63 Å) which are different from the fifth one (2.45 Å). The number of skeletal bonding electrons in Al_6H_{10} is 16 (12+4), indicating the applicability of the Wade's electron counting rule. Hexaalane(10) is found to have an IP and EA of 7.13 and 1.00 eV respectively with a HOMO-LUMO gap of 2.24 eV. The equilibrium geometry of 8-vertex *nido*-alane, Al_8H_{12}

is having a Al_8H_8 core with six open edges out of which four are connected by the four bridging hydrogen atoms. As observed in earlier cases, Al_8H_{12} is also found to validate the electron counting rule with 20 skeletal electrons. The stability of the complex can be realized from the values of low EA (1.796 eV), high IP (7.318 eV) and the large HOMO-LUMO gap of 2.3 eV.

Table 5.1: Vertical ionization potential (IP_{vert}), adiabatic ionization potential (IP), vertical electron affinity (EA_{vert}) and adiabatic electron affinity (EA) (in eV) of *closo*, *nido*, *arachno* and *tetra* alanes.

Class	System	IP_{vert}		IP		EA_{vert}		EA	
		B3LYP		MP2	B3LYP	B3LYP		MP2	B3LYP
		SV6 ^a	ACCT ^a	SV6 ^a	SV6 ^a	SV6 ^a	ACCT ^a	SV6 ^a	SV6 ^a
<i>closo</i> - <i>alanes</i>	Al_5H_7	7.579	7.761	8.026	6.996	0.826	0.881	0.957	1.830
	Al_6H_8	7.362	7.334	7.504	7.251	0.268	0.518	0.022	0.799
	Al_8H_{10}	7.586	7.570	8.242	7.450	1.155	1.159	1.131	1.779
	$\text{Al}_{10}\text{H}_{12}$	7.493	7.466	7.619		1.259		1.207	2.241
					7.307		1.260		
	$\text{Al}_{12}\text{H}_{12}^{-2}$	0.784	0.780	0.898	0.656	--- ^b	--- ^b	--- ^b	--- ^b
	$\text{Al}_{12}\text{H}_{14}$	7.740	7.772	7.985	7.587	1.546	1.565	1.786	2.097
<i>nido</i> - <i>alanes</i>	Al_5H_9	7.978	7.946	8.096	7.478	0.247	0.293	0.281	0.731
	Al_6H_{10}	7.386	7.367	7.473	7.128	0.657	0.658	0.554	1.000
	Al_8H_{12}	7.617	7.610	7.778	7.318	1.124	1.105	0.989	1.796
	$\text{Al}_{10}\text{H}_{14}$	7.464	7.386	7.550	7.304	1.673	1.652	1.616	1.991
	$\text{Al}_{11}\text{H}_{15}$	7.395	7.312	7.574	7.230	1.933	1.954	2.104	2.373
<i>arachno</i> - <i>alanes</i>	Al_6H_{12}	7.575	7.560	7.714	7.245	1.292	1.293	1.012	1.748
	Al_8H_{14}	7.599	7.802	7.752	6.933	1.156	1.393	0.988	1.921
	$\text{Al}_{10}\text{H}_{16}$	7.758	7.761	8.002	7.295	1.749	1.762	1.853	1.879
<i>Tetra</i> - <i>alanes</i>	Al_4H_6	8.084	8.060	8.192	7.568	1.014	1.028	0.902	1.149
	Al_4H_8	8.377	8.354	8.599	7.697	0.086	0.176	0.022	1.055
	Al_4H_{10}	8.738	8.696	8.886	7.910	-0.281	-0.080	-0.077	0.951

^aSV6 and ACCT refer to 6-31++G(2d,2p) and aug-cc-pVTZ basis sets, respectively

^cThe calculation of EA for $\text{Al}_{12}\text{H}_{12}^{-2}$ by the finite difference method is very difficult due to the highly negative charge and the SCF for this system did not converge.

The ten vertex *nido*-alane $\text{Al}_{10}\text{H}_{14}$ is found to have a minimum energy structure of C_{2v} symmetry as shown in Figure 5.2 which is similar to that of its borane analogue, decaborane(14). The structure of decaalane(14) consists of two slightly distorted pentagonal pyramids of aluminium atoms which are joined through one edge of their bases, leading to a structure of C_{2v} symmetry. Herein, each Al atom is connected to one exo-hydrogen leading to an open structure with six open edges out of which four are connected to the four remaining hydrogen atoms through Al-H-Al bridging bonds. This cluster is also found to obey the electron counting rules with 24 skeletal bonding electrons. The calculated EA, IP and HOMO-LUMO gap are found to be 1.99, 7.30 and 1.81 eV respectively. The next higher member of the family, namely, eleven vertex *nido*-alane $\text{Al}_{11}\text{H}_{15}$ whose structure is found to have a C_s symmetry, can be seen as a regular icosahedral twelve vertex *closo*-alane, $\text{Al}_{12}\text{H}_{12}^{2-}$ structure with one vertex missing. In this case, the open edges are bonded through four Al-H-Al bridge bonds and this structure is similar to that of the borane analogue, *nido*-undecaborane(15), $\text{B}_{11}\text{H}_{15}$ which is also in agreement with Wade's rule with 13 skeletal electron pairs. As evident from the geometry closing rule, the reactivity of this cluster is expected to be more than that of the other members of this (*nido*-alane) family which can be realized from the high value of EA (2.37 eV) and relatively low value of HOMO-LUMO gap (1.60 eV).

In summary, it can be mentioned that all the *nido*-alanes discussed above are having open structures and the bonding in these complexes can be rationalized in a manner similar to the case of *closo*-alanes. The *nido*-alanes are having one electron pair more than is required to fill the (n+1) bonding orbitals in an n-vertex polyhedron. The structure in this particular case can, however, be considered as a (n+1) vertex polyhedron with one vertex missing and the unsaturation at the open site is compensated through the 3c-2e Al-H-Al bonding. In all the cases,

each vertex provides two electrons and each Al-H-Al bridge bond contributes one electron to the skeletal bonding. Hence, a total number of $(n+2)$ electron pairs which are participating in the skeletal bonding, exactly follows the Wade-Mingos rules according to which a *nido* structure generated from the *closo* structure by the removal of one vertex, should have $(n+2)$ skeletal electron pairs.

5.3.3 The *arachno*-alanes ($\text{Al}_n\text{H}_{n+6}$): All the geometries of *arachno*-alanes $\text{Al}_n\text{H}_{n+6}$ ($n=6, 8$ and 10) optimized through MP2/6-31++G(2d,2p) method are shown in Figure 5.3 and the corresponding results are given in Table 5.1. The six vertex *arachno*-alane, Al_6H_{12} is found to have a quite open structure having an Al_6 skeleton which looks like two butterflies with Al_4 skeletons joined through an edge sharing. It has four 3c-2e Al-H-Al bonds and two AlH_2 units. This structure is

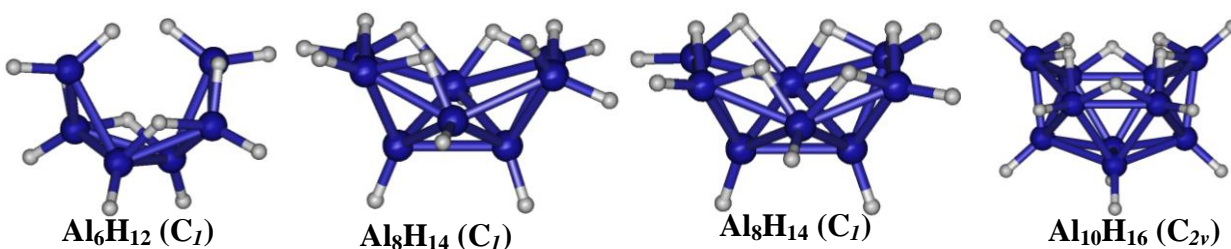


Figure 5.3: Optimized structures of *arachno*-alanes, $\text{Al}_n\text{H}_{n+6}$ ($n=6, 8$ and 10) as obtained by MP2 method. The symmetries are given in parenthesis.

also having 9 pairs of bonding electrons (6 from the six AlH vertices, 2 from four 3c-2e bonds and 1 from two extra hydrogens in two AlH_2 units) which is in accordance with the Wade's $(n+3)$ electron pair rule for the *arachno* boranes. The low EA (1.75 eV), high IP (7.24 eV) and large HOMO-LUMO gap (1.75 eV) conform to its stability. The second member of this series,

Table 5.2: Enthalpy of atomization (ΔH_a), free energy of atomization (ΔG_a) calculated at 298 K, and the HOMO-LUMO gap of *closo*, *nido*, *arachno* and *tetra* alanes.

Class	System	Enthalpy of atomization (ΔH_a) (kcal/mol)	Free energy of atomization (ΔG_a) (kcal/mol)	HOMO-LUMO gap (eV)					
				DFT (B3LYP)		TDDFT			
						B3LYP		PW91	
				SV6	ACCT	SV6	ACCT	SV6	ACCT
<i>closo-alanes</i>	Al_5H_7	549.09	466.31	2.785	2.890	2.148	2.243	2.047	2.117
	Al_6H_8	643.96	544.35	3.037	2.941	1.412	1.420	1.380	1.377
	Al_8H_{10}	856.25	723.27	2.840	2.825	2.355	2.331	2.262	2.234
	$Al_{10}H_{12}$	1060.13	892.97	2.568	2.551	2.364	2.349	2.177	2.154
	$Al_{12}H_{12}^{-2}$	1268.42	1081.40	2.749	2.512	2.567	2.512	2.284	1.844
	$Al_{12}H_{14}$	1274.56	1073.16	2.777	2.754	2.508	2.471	2.347	2.302
<i>Nido-alanes</i>	Al_5H_9	671.85	571.85	3.799	3.522	3.241	2.979	3.013	2.757
	Al_6H_{10}	766.93	650.96	3.160	3.120	2.435	2.410	2.268	2.242
	Al_8H_{12}	959.69	810.40	2.900	3.676	2.499	2.482	2.294	2.301
	$Al_{10}H_{14}$	1172.67	989.99	2.587	2.572	1.922	1.915	1.821	1.813
	$Al_{11}H_{15}$	1270.00	1070.90	2.142	2.081	1.755	1.717	1.657	1.605
<i>arachno-alanes</i>	Al_6H_{12}	854.87	723.63	2.883	2.876	1.844	1.802	1.786	1.748
	Al_8H_{14}	1058.10	893.08	3.051	3.080	2.390	2.362	2.239	2.219
	$Al_{10}H_{16}$	1260.48	1062.05	2.589	2.538	2.186	2.130	1.989	1.924
<i>Tetra-alanes</i>	Al_4H_6	462.99	394.47	3.028	3.007	2.045	2.010	1.957	1.918
	Al_4H_8	653.91	569.59	4.257	4.282	3.400	3.410	3.127	3.141
	Al_4H_{10}	676.13	577.94	4.842	4.805	3.837	3.762	3.552	3.478

the octaalane(14) is found to have two minimum energy structures with an energy difference of 1.3 kcal/mol. The most stable structure is identified with five bridging hydrogens and one AlH_2 unit. More interestingly, the other lower energy structure contains six bridging hydrogens without the AlH_2 unit. The lowest energy structure is having 22 skeletal electrons (16 from 8 AlH vertices, 5 from 3c-2e bonds and 1 from the extra hydrogen on the AlH_2 unit). The low EA (1.92 eV), high IP (6.93 eV) and large HOMO-LUMO gap (2.22 eV) are indications of its stability. Finally, in the case of ten vertex *arachno*-alane, decaalane(16), the structure is found to

be similar to that of decaborane(16) and it can be generated by the removal of two adjacent vertices from the icosahedral *closo*-alane. The structure is found to have C_{2v} symmetry with six open edges and all of them are bonded to hydrogen atoms through bridge bonding. This decaalane(16) is found to have 26 skeletal electrons (20 from 10 vertices and six from the six bridge hydrogen atoms), thus exactly following the Wade's $(n+3)$ electron pair rule for *arachno*-boranes. The low EA (1.88 eV), high IP (7.29 eV) and the presence of large HOMO-LUMO gap (1.92 eV) in this alane indicate its stability.

All the *arachno*-alanes discussed above are having quite open structures as compared to the *closo* and *nido* cases and bonding in these complexes also can be explained in a manner similar to that used in earlier sections. The *arachno*-alanes are having two extra electron pairs than required to fill the $(n+1)$ bonding orbitals in an n -vertex polyhedron. However, it can be considered as a $(n+2)$ vertex polyhedron with two vertices missing. According to the Wade's rule, for the case of *arachno*-alanes (Al_nH_{n+6}), each Al atom should be bonded to at most one hydrogen at the *exo*-position and the remaining six hydrogens should participate in the skeletal or bridge types of bonding. We, however, observe that the number of bridging hydrogens is not six in all the cases especially in lower members ($n=6$ and 8) and some of the cases are found to have AlH_2 units. The six bridging bonds are found to exist only in the ten-vertex case which is in accordance with the Wade's rules. For the lower members, it can be argued that in all the cases, each vertex, AlH_2 group and Al-H-Al bridge bond provides respectively two, one and one electrons to the skeletal bonding, which leads to a total of $(n+3)$ skeletal electron pairs. In this sense, it can be mentioned that the Wade-Mingos rules apply to the *arachno*-alanes. A similar argument has also been found to be suitable for the case of *arachno*-boranes.

5.3.4 The tetra-alanes (Al_4H_m) ($m=6, 8$ and 10): The tetra alanes, Al_4H_m (with $m=6, 8$ and 10) are discussed in this section separately because of the exception of the applicability of the PSEPT for the $n=4$ case²²⁷ and also because of the extreme stability observed for these alanes in comparison to the other members of all the above discussed classes, $\text{Al}_n\text{H}_{n+2}$, $\text{Al}_n\text{H}_{n+4}$ and $\text{Al}_n\text{H}_{n+6}$. The equilibrium structures of all the tetra alanes studied here are shown in Figure 5.4. The minimum energy structure of Al_4H_6 is found to have D_{2d} symmetry with four vertices and two bridging hydrogen atoms on two opposite edges. In the case of *clos*o-boranes ($\text{B}_n\text{H}_n^{2-}$), the applicability of PSEPT is an exception for $n=4$ ($\text{B}_4\text{H}_4^{2-}$) because of its tetrahedral symmetry which corresponds to six bonding orbitals, whereas in Al_4H_6 , which belongs to D_{2d} symmetry, the degeneracy of the orbitals is lifted and the energy of one of the degenerate highest occupied orbital will be lowered which will now have five bonding orbitals thereby obeying the Wade's $(n+1)$ rule as has been clearly explained by Li *et al.*²¹⁹ The HOMO-LUMO gap (1.92 eV) observed in Al_4H_6 is also an evidence for this. The low EA (1.15 eV) and high IP (7.57 eV) reported in Table 5.1 also reflects the stability of the system. The minimum energy structure of Al_4H_8 shown in Figure 5.4 has a slightly distorted tetrahedral Al_4H_4 core which can also be seen as one vertex missing from the trigonal bipyramidal Al_5H_5 with four extra hydrogens bonded through the 3c-2e Al-H-Al bonding and its symmetry is D_{2d} . The IP and EA are 7.7 and 1.05 eV respectively, and the HOMO-LUMO gap is found to be very high, viz. 3.14 eV. All these results show the high stability of the structure. The optimized geometry of Al_4H_{10} is found to have a quite open structure with butterfly-like aluminium skeleton corresponding to C_{2v} symmetry which can be viewed as the hexaalane(8) with two adjacent vertices missing as shown in the Figure 5.4 which is similar to the tetraborane(10). It is having four 3c-2e Al-H-Al bonds, one Al-Al 2c-2e bond and two AlH_2 units and is having seven skeletal bonding electron pairs (two

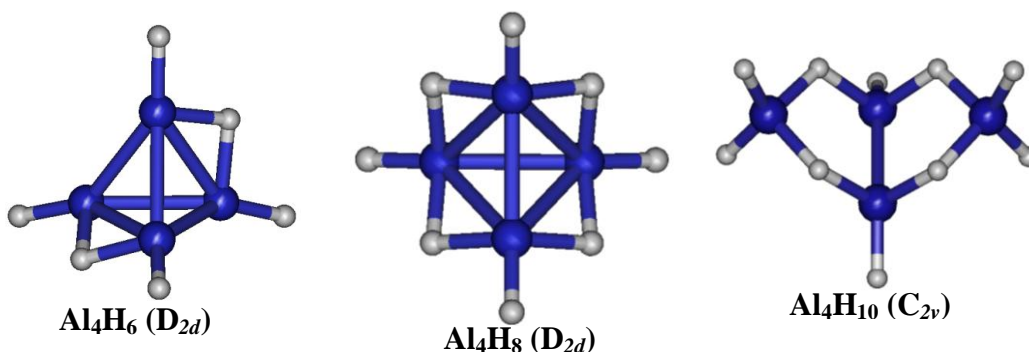


Figure 5.4: Optimized structures of *tetra*-alanes, Al_4H_n ($n= 6, 8$ and 10) as obtained by MP2 method. The symmetries are given in parenthesis.

from the four 3c-2e bonds, one from two extra hydrogens in AlH_2 and four from the four AlH units, then contributing 14 electrons). The electronic requirements for these open borane structures can also be evaluated using the Lipscomb "*styx*" rule which is applicable to the boranes. Here, s is the number of 3c-2e Al-H-Al bonds, t is the number of 3c-2e Al-Al-Al bonds, y is the number of 2c-2e Al-Al bonds and x is the number of AlH_2 groups present in the structure. According to the *styx* rule "the sum of *styx* value should be equivalent to the half of the total number of atoms ($N/2$) in the structure". In Al_4H_{10} , $N/2 = 7$ and $s+t+y+x=4+0+1+2 = 7$ and hence the written structure is expected to be stable. The large HOMO-LUMO gap (3.48 eV), very high IP (7.91 eV) and low EA (0.95 eV) also supports the above statement.

To prove the stability of all these aluminum hydrides further, we have calculated the enthalpy of atomization (ΔH_a) as well as the free energy of atomization (ΔG_a) at 298 K. All the classes of alanes are found to have large enthalpy and free energy of atomization as shown in Table 5.2. This shows the thermodynamic stability of the complexes which can be compared with that of the borane analogues reported earlier.²²⁸⁻²³⁰ For example, in the cases of Al_5H_9 , Al_6H_{10} , $\text{Al}_{10}\text{H}_{14}$ and Al_4H_{10} , the present calculated values of ΔH_a are found to be 671.85, 766.93, 1172.68 and 676.13 kcal/mol respectively, whereas the corresponding results for their boron

analogues B_5H_9 , B_6H_{10} , $B_{10}H_{14}$ and B_4H_{10} are 1129.91, 1312.62, 2078.66 and 1047.98 kcal/mol respectively. Similarly we can even compare the HOMO-LUMO gap of a few alane systems with the borane analogues reported earlier.²²⁸⁻²³⁰ For example, in the cases of Al_5H_9 , Al_6H_{10} , $Al_{10}H_{14}$ and Al_4H_{10} , the present calculated values of HOMO-LUMO gaps are found to be 2.76, 2.24, 1.81 and 3.48 eV respectively, whereas the corresponding results for their boron analogues B_5H_9 , B_6H_{10} , $B_{10}H_{14}$ and B_4H_{10} are 9.75, 7.23, 6.32 and 12.48 eV respectively. From this comparison, one can notice that in boron hydrides the enthalpies of atomization as well as the HOMO-LUMO gaps are very high (almost double and triple respectively) as compared to the corresponding aluminum hydrides, which can be a reason why the experimentally observed diversity of the alane structures is less in comparison to the boranes. We have optimized the geometries of the cations as well as the anions of all the systems studied to verify the effect of geometry relaxation on the energy and the corresponding results are reported in Table 5.1. From the results we can observe that in the case of cations, the relaxation effect is less compared to that in the anion. There is a decrease in the ionization potentials on relaxation as compared to the vertical values and the variations are within 10%, whereas in the case of electron affinity values there is an increase on relaxation and the variations are huge which are even more than double in some cases as shown in Table 5.1.

To verify the stability of the optimized clusters, we have carried out the Hessian calculation at the same level of theory as used for optimization. All the geometries are associated with all real frequencies which indicate that each one is a local minimum on its potential energy surface. We have also studied the vibrational spectra of all the hydrides and the frequencies are compared with the existing results. Strong peak around 1950 cm^{-1} corresponds to the terminal Al-H stretching mode, weak peaks around 1200 and 1400 cm^{-1} correspond to the

bridged Al-H-Al stretching mode and the broad peak around $400\text{-}800\text{ cm}^{-1}$ corresponds to the Al-H bending modes. The vibrational frequencies obtained from our study are nearly comparable to some of the existing results.^{203, 231}

5.4. Conclusions

In view of the recent interest in the study of aluminium hydrides, we have carried out a detailed study of the electronic structure of three different classes of hydrogenated aluminium clusters, $\text{Al}_n\text{H}_{n+2}$, $\text{Al}_n\text{H}_{n+4}$ and $\text{Al}_n\text{H}_{n+6}$ namely *closo*, *nido* and *arachno* alanes respectively. All the *closo* structures are found to have n -vertex Al polyhedron with n -number of Al-H bonds whereas the remaining two hydrogens form bridge bonding and all these structures are found to have $(n+1)$ pairs of skeletal bonding electrons which is in accordance with the Wade's electron counting rule. In the case of *nido* alanes also, each structure is having n -vertex Al core with n -number of Al-H terminal bonds. The remaining four hydrogens are forming bridge bonds and each one is having $(n+2)$ pairs of skeletal bonding electrons which are also in accordance with the Wade's electron counting rule. In the case of *arachno* alanes, which are having quite open structures, some are having more than one Al-H exo-bond. All these clusters are having considerably large HOMO-LUMO gaps, low electron affinities, large ionization potentials and also large enthalpy and free energy of atomization. These exceptional properties can be indicative of the pronounced stability and hence, it can be expected that these complexes can indeed be observed experimentally. Although some of the clusters mentioned in the present study have already been experimentally observed, the present study can give an impetus for further exploration in the area of aluminum hydrides.

CHAPTER 6

Hydrogen Adsorption in Light Metal Decorated Fullerenes Clusters

6.1 Introduction

As mentioned in the earlier discussions, carbon-based nanomaterials have become the subject of intense research for the purpose of storing hydrogen due to their low molecular weight and unique structural, mechanical, and electrical properties. Especially the metal decorated carbon nanomaterials are found to be more efficient as compared to their undoped counterparts. This chapter deals with two different studies, concerned with the (a) Effect of nanoscale curvature on the hydrogen adsorption in alkali metal doped carbon nanomaterials and (b) Hydrogen adsorption in transition metal decorated porphyrin like porous fullerene, $C_{24}N_{24}$.

In the first part of the work, our objective has been to explore systematically the effect of curvature of the different carbon nanomaterials on the adsorption of molecular hydrogen. The curvature of the carbon surface can, in fact, have an important role in determining the physical and chemical properties in a significant way. Hence, it is essential to understand to what extent the curvature of the systems affects their functional properties, in particular, the adsorption of hydrogen molecules. Despite the significance of the effect of the curvature being known, explicit studies on this subject are very scarce in the literature. Park et al. have shown that the mechanically bent carbon nanotubes are, in general, more reactive than the planar carbon sheets.²³² Lu and Chen have recently reviewed the curved π -conjugation and aromaticity, as well as the related chemistry of fullerenes and its larger homologues.²³³ Li et al. have studied the effect of bond curvature on the structure and reactivity of singlewalled carbon nanotubes, especially for the cycloaddition reactions.²³⁴ Force-field-based simulation studies carried out by Cheng et al. reveal that there is a strong dependence of hydrogen adsorption energies on the diameter but only a weak dependence on the chirality of the nanotubes.²³⁵ The main lacuna present in most of the calculations is that they generally employ model-potential-based molecular dynamics or Monte Carlo methods.

Since a six- or five-membered ring is one of the common units of the fullerenes or nanotubes, the benzene molecule is considered here as a prototype model system and deformed systematically by varying the dihedral angle. Then, the structurally deformed benzene molecule is allowed to interact with the hydrogen molecule to reveal the effect of the curvature. In order to represent the curvature effects in more realistic manner, we have considered different sizes of fullerenes, C_{20} , C_{28} , C_{32} , C_{36} , C_{60} , and C_{70} .

In another study, we have explored the transition metal decorated $C_{24}N_{24}$ fullerene as potential hydrogen storage materials. Transition metal decorated carbon nano-materials are found to have hydrogen adsorption energies that are suitable for ambient temperature hydrogen storage.⁷⁵⁻⁷⁷ On the other hand, the transition metal decoration has the drawback suffering from the problem of clustering of metals due to the very high metal cohesive energies associated with them.⁷⁸ In recent studies it was shown that this clustering problem can be avoided through substitutional doping of the base material with hetero atoms like boron.⁸⁰ Doping with hetero atoms like boron and nitrogen is well demonstrated in carbon materials to alter their properties.²³⁶⁻²³⁷ Recently, Lee et. al.²³⁸ reported the synthesis of porphyrine-like CNT through plasma-enhanced chemical vapour deposition, where four carbon atoms are substituted by truncation doping using four nitrogen atoms. Usachov et. al.²³⁹ also synthesized the nitrogen doped graphene from s-triazine molecules. Cao et. al.¹²⁷⁻¹²⁸ could synthesize the porous 1:1 graphitic carbon nitride and carbon nitride nanotubes consisting of all s-triazine (C_3N_3) rings. Inspired from these experimental studies, we attempt here to design a new porous fullerene, $C_{24}N_{24}$, consisting of eight s-triazine rings connected through C-C bonds. This modified fullerene is found to have six N_4 cavities which are similar to those present in porphyrine with a cavity diameter of 3.708 Å and can be expected to bind transition metal atoms effectively which also avoid the clustering problem. As each

cavity in $C_{24}N_{24}$ resembles the porphyrine N_4 cavity, here we have studied the hydrogen adsorption in transition metal (Sc, Ti and V) decorated $C_{24}N_{24}$.

6.2 Computational Details

In first part of the study, all the geometry optimization and the energy calculations have been performed at the level of density functional theory (DFT) with Becke's three-parameter exchange functional and Lee-Yang-Parr correlation functional⁹⁶ (B3LYP)¹⁰⁴⁻¹⁰⁶ using the electronic structure program GAMESS.¹⁵⁵ The split valence basis set along with diffuse and polarization functions, namely, 3-21G(d,p) and 6-31G(d,p) (hereafter these basis sets will be referred as SV3 and SV6, respectively), were employed for all the calculations involving the fullerene systems. The basis set superposition error (BSSE) has been corrected using the full counterpoise method, for all the complexes.

In the second part of the chapter, we have used the first-principles based Vienna *ab initio* Simulation Package (VASP)¹³¹⁻¹³² for all the electronic structure calculations. Projector augmented wave (PAW)¹²⁹⁻¹³⁰ potentials were used with a kinetic energy cut-off of 550 eV for all the elemental constituents (C, N, Ti, Sc, V and H). Density functional calculations were carried out using the generalized gradient approximation (GGA) of Perdew-Burke-Ernzerhof (PBE)¹⁰³ exchange–correlation potential. All the structures were fully optimized with an energy convergence for total energy in the self consistent field iteration as 1×10^{-6} eV and keeping the unit cell unchanged until the Hellmann-Feynman force components on each elemental constituent is less than $0.01 \text{ eV } \text{\AA}^{-1}$. A vacuum region of about 18 \AA between the neighbouring images was considered to avoid the image interactions. Bader¹⁹² charge density analysis has been performed to calculate the atomic charges. Graphical software, Molden¹³⁵ and Gabedit¹⁶⁴ were used in generating the initial geometries as well as the reported pictures.

6.3 Results and discussion

6.3.1: Nanoscale curvature-induced hydrogen adsorption in alkali metal doped carbon nanomaterials

In the present study, we will first focus on the effect of curvature within the ring, by considering the benzene molecule as a prototype system. The structural deformation is induced by changing the dihedral angle of the carbon atoms gradually to 35° in steps of 5° , and its effect on the interaction with hydrogen molecule and with sodium atom has been studied. It is evident from the results presented in Table 6.1 and Figure 6.1 that the binding strength increases drastically with the curvature introduced in the benzene molecule and the variation is almost linear. For instance, in the case of a H_2 molecule, the interaction energy with the planar benzene ring is only -0.05 kcal/mol and the energy changes linearly with the bending angle to -2.34 kcal/mol. In the case of interaction with a sodium atom, there is a significant effect of the bending angle of benzene on the binding energy as well as the charge on the sodium atom as reported in Table 6.1. We have also shown the relationship between the curvature and binding energy of the sodium atom in Figure 6.1(B).

Table 6.1: Effect of Intrabending on the Binding of a Sodium Atom with a Benzene Ring

Local curvature (in degree)	Shortest bond distance (Na-C) (Å)		Interaction Energy (kcal/mol)		Mulliken Charge on sodium (au)	
	Concave	Convex	Concave	Convex	Concave	Convex
0	3.755	-----	-0.508	-----	0.001	-----
10	3.317	3.359	-0.833	-0.724	0.014	0.024
15	2.845	3.043	-2.348	-1.953	0.055	0.039
20	2.610	2.768	-6.199	-4.335	0.250	0.192
25	2.576	2.601	-10.250	-8.516	0.376	0.339
30	2.493	2.521	-15.969	-11.805	0.469	0.433
35	2.406	2.467	-21.330	-16.273	0.597	0.516

Another interesting aspect is the spontaneous (gradual) ionization of the sodium atom upon binding with the curved benzene structure. The charge on the sodium atom changes from 0.00 to 0.516 au, corresponding to the bending angle variation from 0° to 35° , respectively.

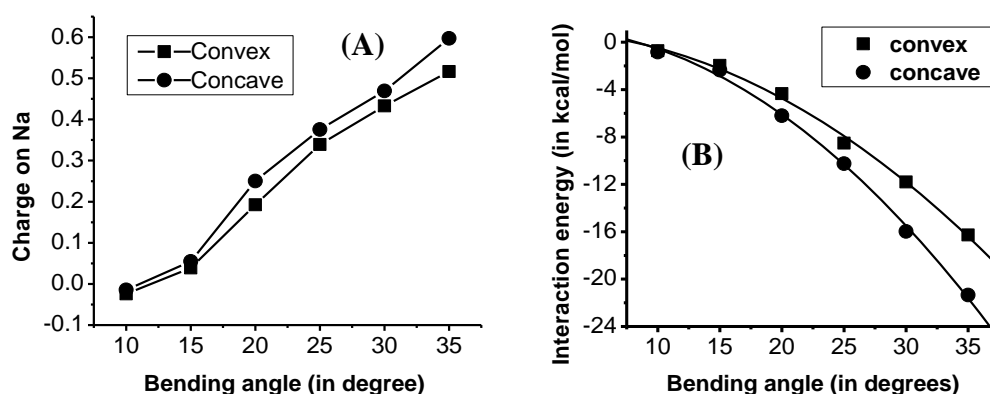


Figure 6.1. Effect of curvature on the (A) charge and (B) binding energy of a sodium atom interacting with intradeformed concave and convex benzene models.

It can indeed be observed from Figure 6.2 that the degree of overlap of the electron density of the sodium atom is amplified as the bending angle in benzene is increased linearly.

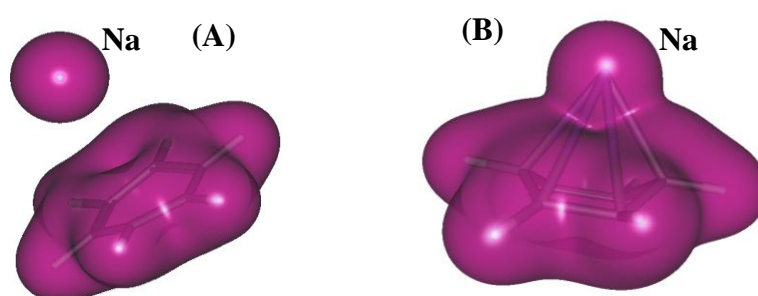


Figure 6.2 Electron Charge density distribution in Na-C₆H₆ with the bending angle: (A)10° (B)35°

It can be seen from the results presented in Tables 6.1 and 6.2 that the direction of approach of the interacting species to the curved surface (concave or convex) is also an important factor. The interaction of sodium as well as H₂ molecule with the concave side is stronger than that with the convex side. The reactivity of the convex and concave carbon ring surface increases with the value of the curvature and the observed difference between these two surfaces becomes very significant at the higher curvature values.

Table 6.2:Effect of intra-bending on the binding of hydrogen molecule with Benzene ring

Local Curvature (in degree)	Shortest bond Distance (H-C) (Å)		Interaction energy (kcal/mol)		Mulliken charge on H ₂ molecule (au)	
	Concave	Convex	Concave	Convex	Concave	Convex
0	2.970	---	-1.666	---	-0.010	---
10	2.880	2.950	-1.889	-1.852	-0.023	-0.023
15	2.828	2.903	-1.986	-1.914	-0.027	-0.027
20	2.797	2.849	-2.066	-1.955	-0.030	-0.028
25	2.677	2.805	-2.148	-1.972	-0.031	-0.028
30	2.598	2.761	-2.238	-1.979	-0.312	-0.025
35	2.509	2.724	-2.337	-1.980	-0.030	-0.020

The above results should be considered as a model study which shows the effect of the structural deformation within the ring (intra-bending) on the interaction with other molecules. In real systems, however, the bending or curvature is observed not only in the single ring but also between the rings, which is discussed in the next section. The local curvature induced by the intra and inter-bending can in general occur together in the nanotubes and fullerenes.

Let us now analyze the nature and the degree of curvature involved in different sized fullerenes, viz., C₂₀, C₂₈, C₃₂, C₃₆, C₆₀ and C₇₀ and their effect on the reactivity of these carbon nanomaterials. The systems, which are considered in the present study, can be representative for the degree of curvature normally encountered in other carbon nanomaterials as well. The approximate diameter and the inter- as well as the intra-curvature values at 5m and 6m-rings are presented in Table 6.3. On analyzing the results shown in Table 6.3 it is clear that the 6m-rings of C₂₈ and C₆₀ have the lowest curvature (intra-bending angle) whereas for the systems like C₃₂ and C₃₆, the curvature is found to be very large. It is also interesting to note that the type of curvature present in C₂₈ is concave while for the case of C₃₂, it is convex. Although the intra-bending angle present in C₂₀, C₂₈ and C₆₀ fullerenes is very small, the inter-bending angle (angle between the 6m-rings or 6m-5m-rings) is quite significant and it is maximum in C₂₀ making it highly unstable. From the results reported in

the earlier section, it can be inferred that the systems C_{32} and C_{36} should be more reactive than other systems due to the presence of large curvature. It should however be noted that the reactivity of these fullerenes is driven by the presence of not only the intra-curvature but also the inter-curvature. Hence, the net effect is the result of a combined act of these two curvatures present in these fullerenes and is expected to be more significant. In general, the different properties of these fullerenes can be related to the curved π -conjugation present in the intra and inter-deformed 6m-rings or 6m-5m rings of the carbon materials. Moreover, there is an enhanced steric strain as well as resonance destabilization in such highly curved surfaces. This effect is more pronounced in smaller fullerenes with 5m-rings than in the higher fullerenes and the stability of such systems is found to be much less than C_{60} .

Table 6.3: Approximate diameter (\AA units) and curvature (in degree) of the fullerenes

Fullerenes and their symmetry	Diameter	Intra-Curvature		Inter- Curvature
		5m-ring	6m-ring	
C_{20} (Ci)	4.200	1.5	0.0	65
C_{28} (Td)	4.811	7.2	4.3	52
C_{32} (Ci)	6.093	7.1	18.3	36
C_{36} (D6h)	5.225	1.9	14.5	57
C_{60} (Ih)	6.695	0.31	0.5	38
C_{70} (D5h)	7.319	0.55	4.17	48

The calculated HOMO-LUMO gaps, presented in **Table 6.4**, confirm the stability/reactivity of these fullerenes and it can be seen that the HOMO-LUMO gap for C_{60} is much higher than that of other fullerenes, including C_{70} . It is also interesting to note that the HOMO-LUMP gap of all the alkali metal doped fullerenes is almost 50% less than that of the undoped fullerenes, indicating their high reactivity. The Li-C bond distance in the 6m-ring of C_{32} is 2.154\AA , which increases to 2.401\AA and 2.863\AA in the C_{32} fullerene doped with Na and K atoms, respectively. We also find that the carbon-alkali metal atom distance in the 5m-ring is found to be higher than that of 6m-ring. The effect of alkali metal atom binding on the fullerene C-C bond distance is not very significant and the effect is more pronounced in the case of lithium atom than with sodium or potassium.

Table 6.4: HOMO-LUMO gap of the pristine and alkali metal doped fullerenes C_nX ($n=20, 28, 32, 36, 60, 70$ and $X=Li, Na$ and K) (in atomic units)

System	C_{20}	C_{28}		C_{32}		C_{36}	
	5m	5m	6m	5m	6m	5m	6m
SV3	0.0686	0.0499	---	0.0545	---	0.0376	---
SV6	0.0719	0.0527	---	0.0587	---	0.0403	---
Li							
SV3	0.037	0.0186	0.0209	0.0265	0.0237	0.0386	0.0407
SV6	0.0386	0.0193	0.021	0.0271	0.0241	0.0358	0.037
Na							
SV3	0.0362	0.0187	0.02	0.0293	0.0239	0.0391	0.039
SV6	0.0359	0.0194	0.0209	0.0272	0.0242	0.0356	0.0352
K							
SV3	0.0371	0.0182	0.0208	0.0244	0.024	0.0397	0.0397
SV6	0.0362	0.0189	0.0201	0.0269	0.0244	0.0361	0.0363

Let us now discuss the trend in the binding energy of the alkali metal atoms with fullerenes that has been reported in Table 6.5. It is observed that the binding energy of Li atom with all the fullerenes considered here, is higher than that of Na and K atoms and although, the binding energy of Na and K is found to differ only marginally. It may be noted that the binding energy of the alkali metal atoms is observed to be very high particularly for smaller fullerenes and the respective binding energy in the cases of C_{60} and C_{70} is ~20% less than for other smaller fullerenes. Most interestingly, the trend rather correlated the intra- and inter-bending angle, in other words, the curvature present in the interacting region of 6m or 5m-ring. Let us first consider the reactivity at the 6m- and 5m-rings of each fullerene. Considering the 5m-ring, maximum intra-bending angle is present in C_{28} fullerene while the 5m-ring in C_{60} has a minimum intra-bending angle. The measured intra-curvature is in fact in the following order: $C_{28} > C_{32} > C_{36} > C_{20} > C_{70} > C_{60}$ and its value is in the range of 7° to 0.3° . Based on these values, one can expect that the binding energy of an alkali metal atom interacting at the 5m-ring should be stronger with C_{28} than with other fullerenes. It can be seen from Table 6.5 that the binding energy of lithium atom with C_{28} (-73.69 kcal/mol) is

indeed highest among all other fullerenes and the minimum value is found for C_{60} (-30.0 kcal/mol). The trend in the binding energy of the alkali metal atom interacting with the 5m-ring of fullerene is in the order: $C_{28} > C_{36} > C_{32} > C_{20} > C_{70} > C_{60}$. It is pertinent to note that the variation of curvature as well as binding energy follows a similar trend except for the case of C_{36} and C_{32} . Although the degree of curvature in C_{32} is more than that in C_{36} , the alkali metal atom binding energy is higher for the case of C_{36} than C_{32} . The reason for their reactivity difference may be the difference in the nature of the curvature present in these two systems. The nature of the curvature in C_{32} and C_{36} , is convex and concave, respectively. Another possible explanation for this particular trend may involve the inter-bending angle (the curvature induced by any two rings) present in these fullerenes, the values of which follow the order: $C_{20} > C_{36} > C_{28} > C_{32} > C_{70} > C_{60}$. The combined effect of inter- and intra-bending angle of C_{36} makes it more reactive than C_{32} . The influence of inter-bending angle effect can explicitly be seen in the case of C_{20} for which the intra-bending angle is only 1.53° , but the binding energy of the alkali metal atom is quite significant. One of the important reasons for the high reactivity of C_{20} is attributed to the presence of highest inter-curvature among other fullerenes. Similarly, one can explain the reactivity of C_{60} and C_{70} for which the intra-curvature is almost zero and inter-curvature is quite significant. The high binding energy of alkali metal atoms with C_{28} is also due to the combined effect of intra- and inter-curvatures. The reactivity of alkali metal atoms with the 6m-ring of each fullerene follows a trend similar to that for 5m-ring and the combined intra- and inter-curvature effects can explain the observed reactivity trend as discussed above.

Let us now discuss another important effect of the binding of alkali metal atom with the carbon nanosurfaces. The net charge acquired by each alkali metal atom as calculated by the Mulliken population analysis is reported in Table 6.5. The charge transfer occurs from the singly occupied atomic orbital of the alkali metal atom to the lowest unoccupied

molecular orbital of the fullerenes. The molecular hydrogen binds with the alkali metal ions more effectively through the charge-induced dipole mechanism. The ionization of the alkali metal atoms due to other smaller fullerenes is also very significant and is in the range of 0.60 – 0.81au. In the next section, the hydrogen adsorption ability of the alkali metal doped fullerenes has been discussed in detail.

The optimized geometries and binding energies of hydrogen molecules adsorbed at the cationic site of doped carbon nanomaterials are given in Figure 6.3 and Table 6.6, respectively. Here, two comments are pertinent. Firstly, the number of hydrogen molecules attached to the alkali metal atoms and their binding energy are observed to be strongly dependent on the size of the alkali metal atoms. In all the cases considered here, Li atom is found to interact with less number (2 to 4) of hydrogen molecules, whereas both sodium and potassium are found to interact with six hydrogen molecules. The bond distance between the alkali metal atom and hydrogen is also found to depend on the size of the alkali metal atoms and follows the order, $K > Na > Li$. Although both sodium and potassium interacts with six hydrogen molecules, the total binding energy is always more in the case of sodium than for potassium. It is also interesting to note that the binding energy per hydrogen molecule attached to lithium is more than that for the case of other alkali metal atoms. In general, for materials to be efficient storage media, the essential criteria are the weak and non-dissociative adsorption of molecular hydrogen along with fast kinetics at ambient conditions. Hence, the alkali metal doped carbon materials can have several advantages over the transition metal-doped materials.

Table 6.5: Geometrical parameters (Å), binding energy (kcal/mol) and Mulliken charge (atomic units) of the alkali atoms with different fullerene molecules.^a

C – X ^a	C ₂₀	C ₂₈		C ₃₂		C ₃₆		C ₆₀		C ₇₀	
	5m	5m	6m	5m	6m	5m	6m	5m	6m	5m	6m
Bond Length^b											
Li											
SV3	2.179	2.136	2.243	2.154	2.243	2.104	2.150	2.188	2.268	2.152	2.194
SV6	1.973	2.127	2.190	2.102	2.190	2.127	2.141				
Na											
SV3	2.379	2.326	2.380	2.361	2.401	2.330	2.357	2.395	2.478	2.393	2.426
SV6	2.450	2.438	2.479	2.458	2.486	2.424	2.514				
K											
SV3	2.903	2.794	2.860	2.823	2.863	2.793	2.777	2.857	2.971	2.844	2.890
SV6	2.820	2.844	2.899	2.848	2.906	2.845	2.830				
Binding Energy											
Li											
SV3	-46.58	-73.69	-64.42	-59.00	-57.64	-66.28	-59.08	-35.46	-35.02	-	-33.58
SV6	-46.02	-62.42	-54.97	-47.69	-45.32	-52.78	-47.19			36.80	
Na											
SV3	-41.65	-68.54	-61.54	-54.54	-54.57	-59.55	-59.21	-29.98	-32.61		-30.47
SV6	-24.99	-49.27	-44.11	-35.04	-33.99	-39.06	-37.44			-	
K											
SV3	-41.87	-67.09	-62.74	-54.11	-54.34	-60.09	-58.10	-30.20	-32.75		-32.18
SV6	-34.54	-52.61	-50.06	-39.82	-38.69	-44.59	-40.70				
Charge											
Li											
SV3	0.600	0.624	0.673	0.650	0.674	0.656	0.674	0.732	0.754		0.746
SV6	0.290	0.289	0.322	0.299	0.339	0.312	0.366				
Na											
SV3	0.695	0.767	0.824	0.794	0.829	0.810	0.824	0.901	0.899	0.739	0.903
SV6	0.456	0.485	0.519	0.494	0.517	0.520	0.494				
K											
SV3	0.718	0.764	0.802	0.760	0.807	0.799	0.803	0.873	0.680	0.907	0.889
SV6	0.502	0.673	0.704	0.681	0.704	0.703	0.703			0.881	

^a shortest alkali-Carbon bond length as observed in alkali doped C₆₀.^b In case of C₆₀ and C₇₀, only the B3LYP/3-21G(d,p) results are given here.

The second important point is that there is a strong effect of curvature on the number and binding energy of the hydrogen molecules attached to the alkali metal atoms. Let us consider the case of lithium doped carbon nanosurfaces wherein stronger binding of hydrogen molecule is observed with C₂₀ and C₃₆. In both the cases, the intra-curvature at the 5m-ring is

Table 6.6: Binding energy (in kcal/mol) of the hydrogen molecules interacting with alkali metal doped fullerene molecules C_nX ($n=20, 28, 32, 36, 60, 70$ and $X=Li, Na$ and K)^a

$C - X^a$	C_{20}	C_{28}		C_{32}		C_{36}		C_{60}		C_{70}	
	5m	5m	6m	5m	6m	5m	6m	5m	6m	5m	6m
Binding Energy											
Li											
SV3	-15.04	-8.66	-10.72	-7.98	-9.57	-10.10	-11.89	-6.65	-5.33	-10.23	-8.57
SV6	-6.30	-6.35	-6.33	-4.89	-6.26	-7.65	-6.83				
Na											
SV3	-13.38	-13.61	-14.39	-14.00	-13.90	-16.42	-12.79	-12.98	-10.33	-14.89	-16.55
SV6	-9.38	-6.17	-5.68	-4.98	-6.14	-7.44	-5.27				
K											
SV3	-10.83	-6.73	-10.99	-9.57	-10.66	-10.11	-10.77	-9.07	-7.24	-12.69	-11.25
SV6	-5.390	-11.12	-3.15	-5.12	-5.61	-10.67	-10.88				

^aIn case of C_{60} and C_{70} , only the B3LYP/3-21G(d,p) results are given here.

almost zero and hence, the binding of hydrogen molecules is fully controlled by inter-curvature. In other cases, such as, C_{28} and C_{32} , the intra curvature at 5m and 6m-rings is quite significant. The presence of intra-curvature brings the alkali metal atoms closer to the carbon rings of the fullerenes which causes a difficulty to the incoming hydrogen molecules for accessing the alkali metal atoms. This could be the reason why the binding energy of hydrogen molecules with Li-doped C_{20} and C_{36} are in general higher than that of C_{28} and C_{32} . This effect is more prominent in the case of fullerene doped with Li than with Na and K atoms due to the larger size of these ions. In the case of Na and K atoms, a similar argument can be employed for the energetics of hydrogen molecules. Although the number of hydrogen molecules adsorbed is less in lithium doped fullerenes, it is interesting to note that the interaction strength is higher than other alkali metal atoms. The sodium-doped materials can act as a better hydrogen storage material at lower temperature with better hydrogen adsorption efficiency. Further, the adsorption can even be tuned by functionalizing with other suitably chosen organic functional groups.

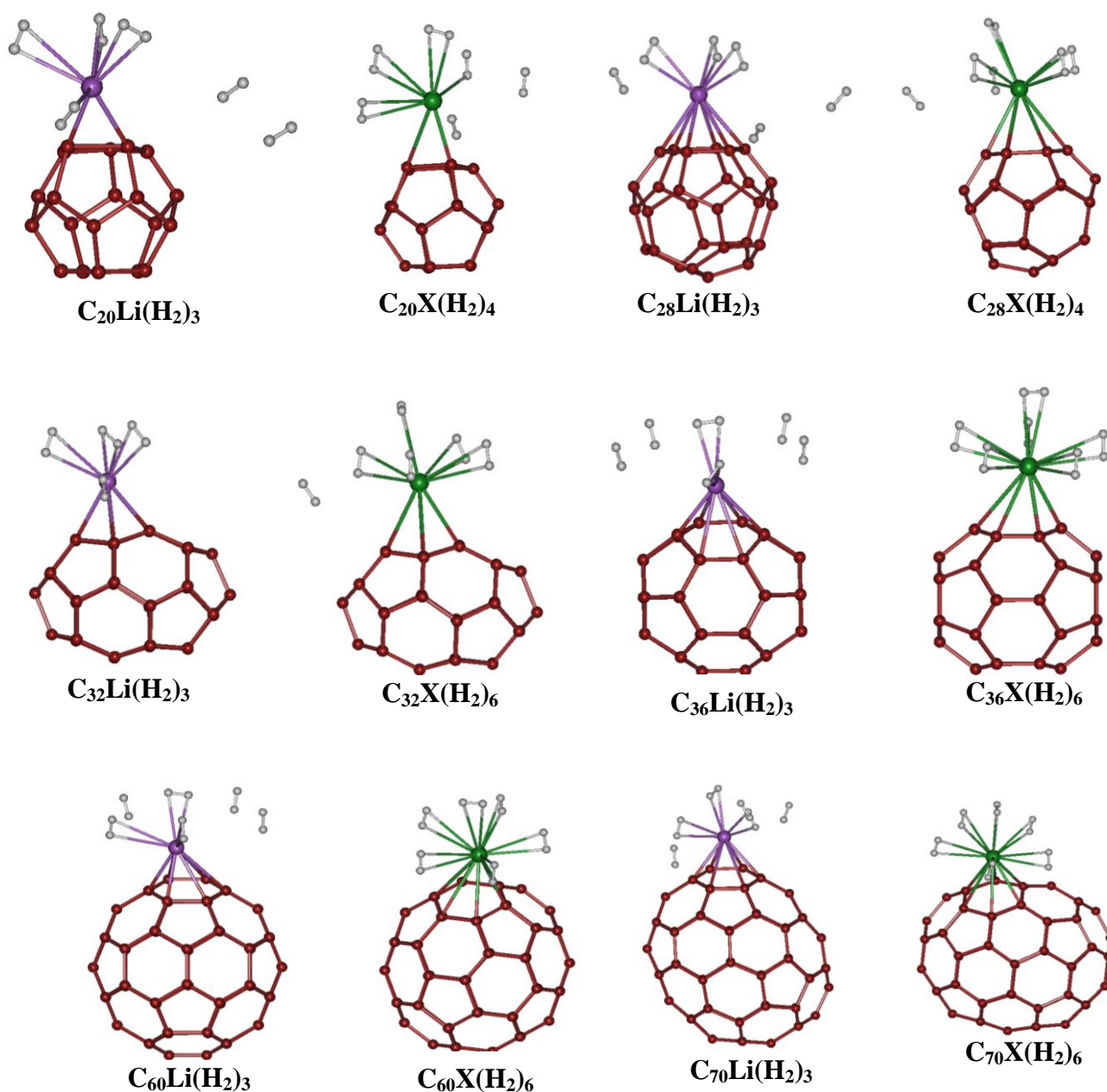


Figure 6.3 Molecular hydrogen adsorption in alkali metal atom doped fullerenes (only at the 6m-ring). X refers to the Na and K atoms.

In general, the results obtained from the present study demonstrate that (1) the system with the minimum intra-curvature but with significant inter-curvature, makes the interaction of hydrogen molecules stronger with the alkali metal atoms. (2) binding of alkali metal atoms with the systems having intra-curvature is much stronger than that with inter-curvature. (3) the interaction strength of hydrogen molecules with the metal atom can be tuned with respect to the small change in the value of the inter- or intra-curvature of the carbon materials.

6.3.2 Transition metal decorated porphyrin like porous fullerene: Promising materials for molecular hydrogen adsorption

First we discuss the electronic structure of the porous fullerene considered for the present study. The carbon nitride fullerene $C_{24}N_{24}$ is generated through truncated doping of 24 carbon atoms by 24 nitrogen atoms. How the truncated doping is carried out is shown in Figure 6.4, where two carbons connecting the five membered rings (indicated using a green ellipse) are removed and the four carbons (marked by blue circles) connecting these two carbons are replaced with nitrogen atoms. As there are six such equivalent C-C bonds, a total of 12 carbons are removed and 24 carbons are replaced by nitrogens which generates $C_{24}N_{24}$ with six N_4 cavities that resemble the porphyrine cavities. This modified fullerene is found to be composed of eight equivalent s-triazine rings connected through C-C bonding. The optimized geometry of $C_{24}N_{24}$ is found to have C-C and C-N bond length of 1.555 Å and 1.341 Å respectively. The Hessian calculated analytically for this fullerene shows that there are no imaginary frequencies and the minimum vibrational frequency is 61.35 cm^{-1} which indicates that the structure is stable and is at one of the minima on the potential energy surface. The calculated formation energy per atom in $C_{24}N_{24}$ is found to be -7.40 eV which is less than that of C_{60} (-8.66 eV) calculated at the same level of theory and this could be because of the more open structure of $C_{24}N_{24}$ with six cavities. From the band decomposed charge density pictures reported in Figure 6.5, it can be seen that the major contribution to highest valence band is coming from nitrogen orbitals and the lowest conduction band is composed of both carbon and nitrogen orbitals. The calculated vertical ionization potential, electron affinity and HOMO-LUMO gap of $C_{24}N_{24}$ are found to be 8.31, 3.17 and 2.48 eV respectively, which are comparable to those of C_{60} (7.39, 2.06 and 2.87 eV) indicating the stability of the fullerene considered.

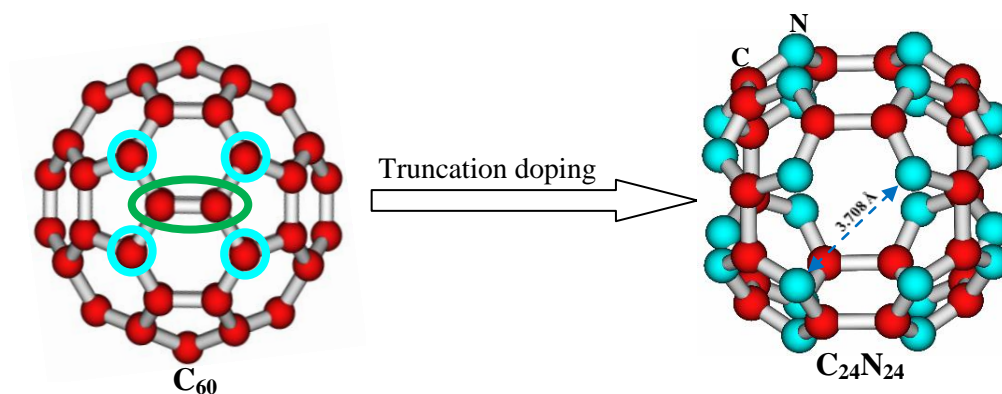


Figure 6.4. Schematic presentation of truncation substitutional doping of C_{60} to generate $C_{24}N_{24}$.

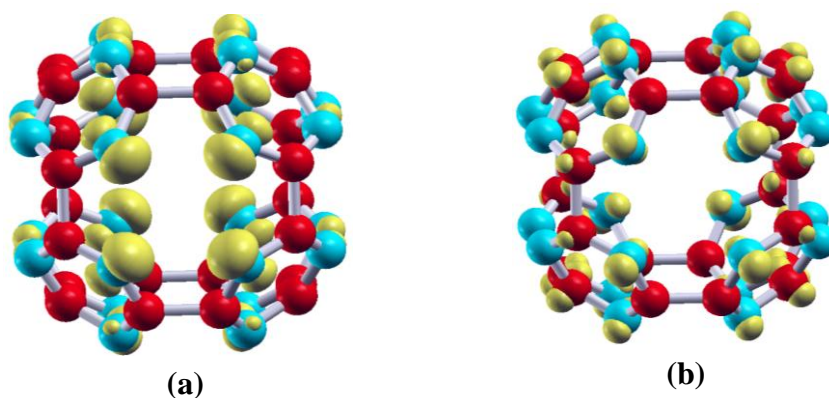


Figure 6.5. Band decomposed charge density iso-surfaces of (a) highest valence band and (b) lowest conduction band of $C_{24}N_{24}$.

From the structure of $C_{24}N_{24}$, one can see that there are six porphyrine like N_4 cavities which can be decorated with transition metals (TM) similar to the porphyrine-TM complexes. We considered three different metals viz. scandium (Sc), titanium (Ti) and vanadium (V) for decorating the N_4 sites. All the optimized geometries of the metal decorated $C_{24}N_{24}$ are shown in Figure 6.6. The TM-N bond lengths for Sc, Ti and V are found to be 2.117, 2.044 and 1.989 Å respectively. The metal binding energies calculated using PBE method are found to be -188.0, -187.6 and -172.8 kcal/mol per metal atom for Sc, Ti and V respectively. As all these metal binding energies are considerably large (nearly double) as compared to the corresponding metal cohesive energies,^{75, 240} the problem of metal aggregation to form cluster

is expected to be overcome and the material will be stable for designing a recyclable hydrogen storage material. The atomic charges on each metal site, calculated through Bader charge density analysis are reported in Table 6.7. The positive charge accumulated on all the transition metals shows that there is a charge transfer from metal to $C_{24}N_{24}$ which could also be observed from the overlap of metal orbitals with the nitrogen orbitals shown in Figure 6.7.

The magnetic moments calculated on each metal atom in the metal complexes $C_{24}N_{24}-M_6$

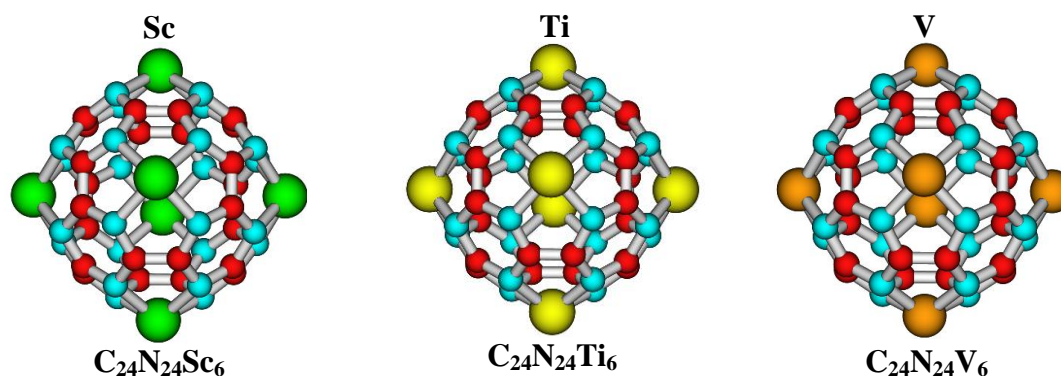


Figure 6.6 Optimized geometries of $C_{24}N_{24}TM_6$ (TM=Sc, Ti and V)

Table 6.7 Calculated metal binding energies (per metal atom) in kcal/mol, bond lengths in Å and charge on metal atoms in a.u

System	Metal binding energy ^a (kcal/mol)	bond lengths (Å)			Charge on metal atoms	Magnetic moment per metal atom (μ_B)
		TM-N	C-C	C-N		
$C_{24}N_{24}$			1.555	1.341		
$C_{24}N_{24}-Sc_6$	188.01	2.117	1.410	1.396	+1.78	0.04
$C_{24}N_{24}-Ti_6$	187.65	2.044	1.397	1.394	+1.41	1.11
$C_{24}N_{24}-V_6$	172.80	1.989	1.398	1.390	+1.31	2.21

^a The metal binding energy is calculated as $BE(M) = (1/6)(E(C_{24}N_{24}-M_6) - 6E(M) - E(C_{24}N_{24}))$

are found to be 0.04, 1.11 and 2.21 Bohr magnetons for Sc, Ti and V respectively which are also reported in Table 6.7. From the variation in C-N bond lengths reported in Table 6.7, it can be observed that there is an elongation in the C-N bond lengths from 1.34 Å to 1.39 Å on metal complexation which could be because of loss of π bonding interaction between the carbon and nitrogen. At the same time, the C-C bond length is shortened from 1.55 Å to 1.4 Å after the metal decoration.

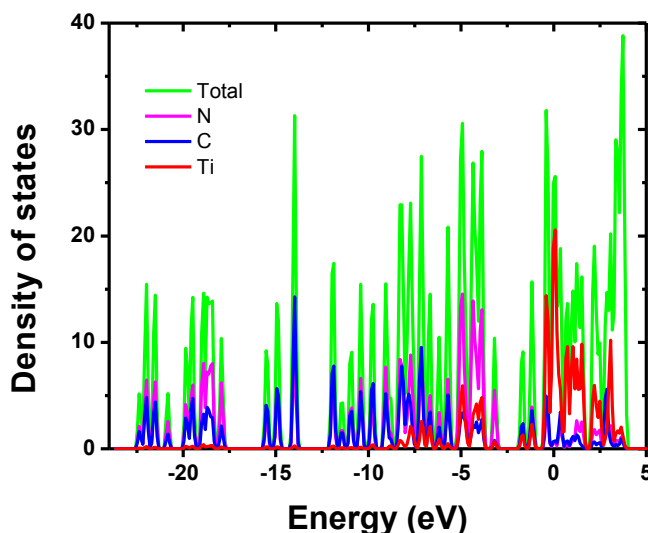


Figure 6.7 Calculated total density of states (Total) and projected density of states on nitrogen (N), carbon (C) and titanium (Ti) atoms of $C_{24}N_{24}Ti_6$

As the transition metals decorated on suitable host materials are known to trap hydrogen with suitable adsorption enthalpies for room temperature hydrogen storage applications, we have studied the hydrogen adsorption properties of all the three different metal decorated porous fullerenes ($C_{24}N_{24}-Sc_6$, $C_{24}N_{24}-Ti_6$ and $C_{24}N_{24}-V_6$) considered here. The optimized structures of systematically hydrogenated $C_{24}N_{24}-Sc_6$ using PBE method are given in Figure 6.8. The interaction energy per molecular hydrogen in $C_{24}N_{24}-Sc_6(H_2)_6$, where each metal site adsorbs one molecular hydrogen, is found to be -5.4 kcal/mol. The H-H bond length in the adsorbed molecular hydrogen is found to be 0.771 Å which is slightly elongated as compared to the free H_2 molecule (0.750 Å) calculated at the same level of theory. The molecular hydrogen adsorption mechanism on transition metal systems has been well explored and is explained through Kubas type of interaction. According to this mechanism, there will be electron transfer from occupied σ orbitals of hydrogen to the metal d orbitals and back electron transfer from metal d orbitals to hydrogen σ^* orbital. To check this, we have plotted the density of states as shown in Figure 6.9 where one can see the overlap of hydrogen σ orbitals with metal d orbitals (at ~ 9.0 eV) and also σ^* hydrogen

orbitals with metal d orbitals near the Fermi level. The second and third hydrogen molecules per metal site are found to be adsorbed with interaction energy of -3.6 and -3.1 kcal/mol per hydrogen molecule respectively. In the case of $C_{24}N_{24}Sc_6(H_2)_{24}$, where each metal is allowed to interact with four H_2 molecules, the fourth one is found to move away from the metal site as shown in the Figure 6.8. Though the fourth H_2 is far from the metal site (~ 3.0 Å), the interaction energy per molecular hydrogen in $C_{24}N_{24}Sc_6(H_2)_{24}$ is found to be -2.5 kcal/mol which shows that the fullerene surface also plays a role in holding the molecular hydrogens. With a total of 24 molecular hydrogens adsorbed around the $C_{24}N_{24}Sc_6$ fullerene, one has a hydrogen gravimetric density of ~ 5.1 wt% at 0 K which is very close to the target of 5.5 wt% set by DOE for the year 2015.

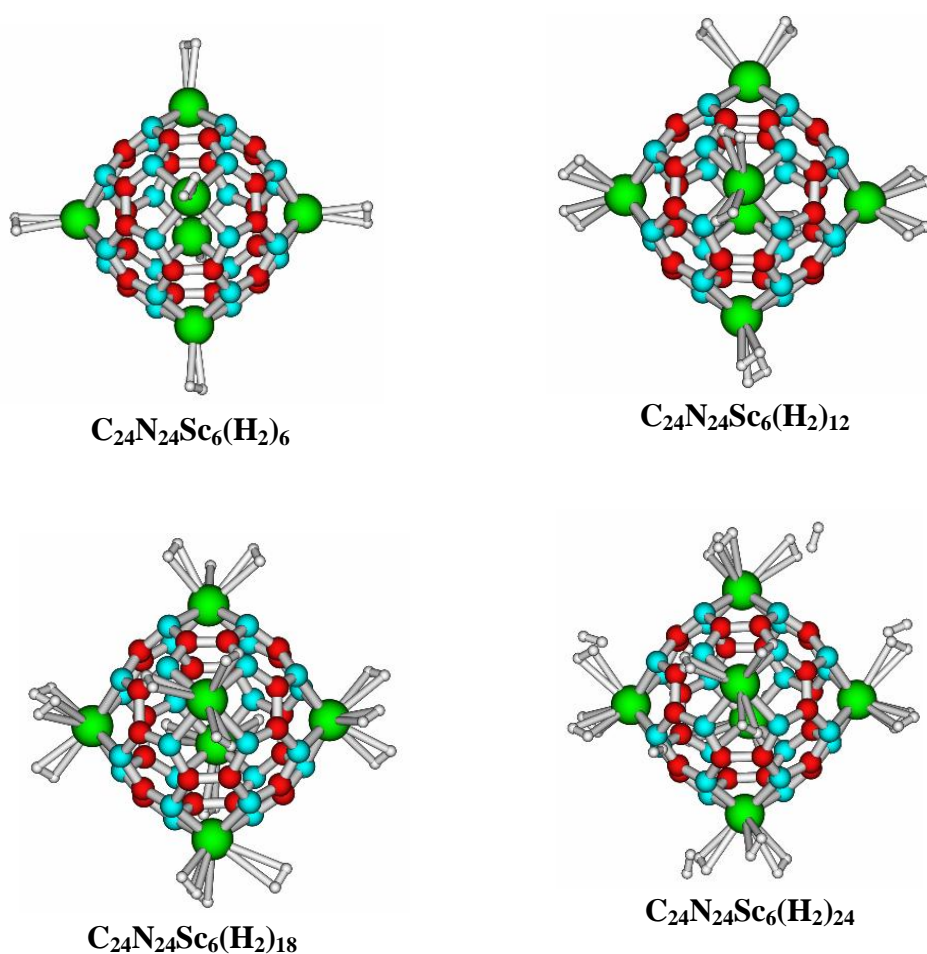


Figure 6.8. Optimized geometries of $C_{24}N_{24}Sc_6(H_2)_{6n}$ ($n=1-4$)

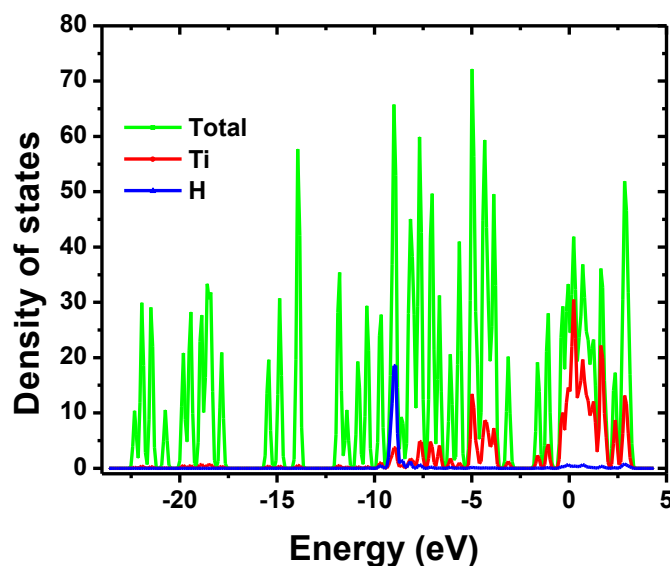


Figure 6.9 Calculated total density of states (Total) and projected density of states on titanium (Ti) and hydrogen (H) atoms of $C_{24}N_{24}Ti_6(H_2)_6$

Table 6.8. Calculated hydrogen interaction energies (per hydrogen molecule) in kcal/mol and metal-hydrogen bond lengths in Å

System	Interaction energy per H_2 (kcal/mol)		Shortest M-H bond length (Å)
$C_{24}N_{24}-Sc_6(H_2)_6$	-5.38 ^a	-5.38 ^b	2.32
$C_{24}N_{24}-Sc_6(H_2)_{12}$	-3.64 ^a	-1.90 ^b	2.34
$C_{24}N_{24}-Sc_6(H_2)_{18}$	-3.13 ^a	-2.11 ^b	2.36
$C_{24}N_{24}-Sc_6(H_2)_{24}$	-2.49 ^a	-0.57 ^b	2.36
$C_{24}N_{24}-Ti_6(H_2)_6$	-7.35 ^a	-7.35 ^b	2.00
$C_{24}N_{24}-Ti_6(H_2)_{12}$	-5.81 ^a	-4.27 ^b	2.07
$C_{24}N_{24}-Ti_6(H_2)_{18}$	-4.06 ^a	-0.56 ^b	2.1
$C_{24}N_{24}-V_6(H_2)_6$	-8.90 ^a	-8.90 ^b	1.85
$C_{24}N_{24}-V_6(H_2)_{12}$	-5.44 ^a	-1.98 ^b	1.86
$C_{24}N_{24}-V_6(H_2)_{18}$	-5.08 ^a	-4.36 ^b	1.86

^ainteraction energy is calculated as $\Delta E(H_2) = (1/6n)(E(C_{24}N_{24}Ti_6(H_2)_{6n}) - E(C_{24}N_{24}Ti_6) - 6n E(H_2))$

^binteraction energy is calculated as $\Delta E(H_2) = (1/6)(E(C_{24}N_{24}Ti_6(H_2)_{6n}) - E(C_{24}N_{24}Ti_6(H_2)_{6(n-1)}) - 6E(H_2))$

In the case of Ti decorated fullerene, $C_{24}N_{24}Ti_6$, the first molecule of hydrogen per metal is found to get adsorbed with an interaction energy of -7.3 kcal/mol which is quite higher as compared to the Sc decorated fullerene case. The Ti-H bond length is also found to be shorter (2.00 Å) as compared to the Sc-H distance (2.32 Å). The H-H bond length in the adsorbed hydrogen is found to be elongated to 0.809 Å from 0.750 Å in the free H_2 molecule.

This larger elongation as compared to that observed in the Sc case is due to the strong interaction between Ti and molecular hydrogen which may be attributed to the availability of more number of d electrons in Ti as compared to Sc. The second molecular hydrogen is adsorbed with an interaction energy of -5.8 kcal/mol per molecular hydrogen. On introducing the third molecular hydrogen per metal site, one of the three hydrogen molecules is found to move far (~ 3.5 Å) away which shows that Ti can adsorb only two molecules of hydrogen which is consistent with the earlier reports on Ti-porphyrine complexes.²⁴¹ The adsorption energy per molecular hydrogen in $C_{24}N_{24}Ti_6(H_2)_{18}$ is found to be -4.06 kcal/mol and the corresponding gravimetric density is calculated to be 3.8 wt% at 0 K.

In the case of $C_{24}N_{24}V_6$ also, we have hydrogenated the vanadium centers systematically and the calculated hydrogen adsorption energy per molecular hydrogen in $C_{24}N_{24}V_6(H_2)_6$ is found to be -8.9 kcal/mol. This adsorption energy is still higher as compared to both Sc and Ti metal decorated cases which might be attributed to the higher d orbital population in vanadium as compared to the other two metals. The V-H distance is found to be 1.85 Å which is the shortest among all the M-H distances studied here and the variation is also consistent with the calculated adsorption energies. The adsorption energy per H_2 in the case of $C_{24}N_{24}V_6(H_2)_{12}$ is calculated to be -5.4 kcal/mol. On introducing the third molecular hydrogen per metal site, one of the molecules is found to move far away from the metal site quite similar to the Ti case. However, the hydrogen adsorption energy per H_2 is calculated to be -5.08 kcal/mol which could be because of the contribution from the fullerene surface in binding the molecular hydrogen. With a total of eighteen molecular hydrogen adsorbed around the metal doped fullerene, the hydrogen gravimetric density is 3.7 wt% at 0 K for this species.

Although the Scandium decorated fullerene is found to adsorb hydrogen with higher gravimetric capacity, the adsorption energies are less as compared to the other two metal

decorated systems. In the case of titanium and vanadium decorated $C_{24}N_{24}$, the hydrogen adsorption energies are quite good and are also near to the required adsorption energies proposed for ambient temperature hydrogen storage. Hence, though the gravimetric capacity is little less (3.8 wt%) as compared to the scandium decorated system (5.1 wt%), titanium and vanadium decorated porous fullerenes appear to be better candidates as constituents of hydrogen storage materials. More interestingly, as the one dimensional nanotubes and two dimensional graphitic carbon nitride sheets consisting of s-triazine rings are already synthesized,¹²⁷⁻¹²⁸ it could be possible to synthesize the model fullerene considered in this study as well.

6.4 Conclusions

In summary we have demonstrated the important role of the curvature exhibited by different carbon nanomaterials on the molecular hydrogen adsorption. The high reactivity of the surface with the maximum curvature has been attributed to the weakening of the pi-conjugation due to the bending of the carbon surface which makes the system have quasi- sp^2 - sp^3 hybridization with substantial s-orbital character. Based on the present results, it can be mentioned that the metal doped nanotubes with smaller radius and concave surface will be a better candidate for hydrogen adsorption. We have also shown that the truncated doping of carbon with nitrogen in C_{60} can generate porphyrin-like porous fullerene, $C_{24}N_{24}$ that can bind with transition metal atoms with high interaction energies which are nearly double the cohesive energies of the corresponding metals. Hence the clustering problem associated with the transition metals can be avoided. These transition metal sites are found to trap molecular hydrogen through Kubas type of interaction, and the hydrogen adsorption energies are also found to be suitable for ambient temperature hydrogen storage.

CHAPTER 7

Alkali Metal Decorated Two-dimensional Materials as Promising Hydrogen Storage Materials

7.1 Introduction:

In this chapter, we discuss the energy storage applications of the two-dimensional carbon materials. The first part of the chapter consists of the studies on the newly emerging carbon allotropes graphyne and graphdiyne. In the latter part we will discuss the hydrogen adsorption properties of the conjugated microporous polymers (CMPs).

As it has already been shown, the light metals, like alkali and alkaline earth metal decorated carbon nanomaterials are found to be good candidates for hydrogen adsorption.⁶⁹⁻⁷² In this view, a large number of materials mainly carbon nanomaterials, decorated with light alkali and alkaline earth metals have been studied for hydrogen storage applications. Du et al.²⁴² proposed lithium dispersed porous graphene as a good hydrogen storage material. Later, Reunchan et al.²⁴³ studied the hydrogen adsorption in metal dispersed porous graphene using PBE method and found that in most of the cases, the metal binding energies are less than the cohesive energies of the corresponding metals.

Graphyne and graphdiyne are the two-dimensional carbon allotropes with one atom thick layer of carbon sheet having two different types of carbon atoms with sp and sp^2 hybridization both having the same symmetry as graphene.²⁴⁴⁻²⁴⁶ Graphdiyne has been recently synthesized and found to be a semiconductor.²⁴⁷⁻²⁴⁹ In the present study, we report the investigation of these two novel two-dimensional conjugated carbon materials as possible anode material for lithium batteries as well as effective hydrogen storage materials based on our first principles based calculations.

In the second part of the study, we have considered two different porous two-dimensional CMPs based on benzene, 1,3,5-triethynyl and benzene and 1,3,5-tributadiyne (HCMP-1) with larger pore sizes. Conjugated Microporous Polymers or CMPs are new class of porous materials which can be synthesized through the Pd-catalyzed Sonogashira-Hagihara cross-coupling

reaction between aryethynyls and aryl halides.²⁵⁰⁻²⁵² In 2007, Jiang et al.²⁵³ synthesized a series of three networks, CMP-1, CMP-2, and CMP-3, each possessing two ethynyl modules and the number of phenylene moieties in each linker increasing from one (CMP-1) to three (CMP-3). Jiang et al.²⁵⁴ synthesized another network, homocoupled conjugated microporous polymer (HCMP-1) through palladium-catalyzed homocoupling of 1,3,5-triethynylbenzene. It is experimentally shown that lithium decorated CMPs can store hydrogen with a gravimetric density of ~6.1 wt% at 1 bar and 77 K.²⁵⁵

7.2 Computational Details

All the electronic structure calculations are performed using the VASP software.¹³¹⁻¹³² (PAW)¹²⁹⁻¹³⁰ potentials with a kinetic energy cutoff of 550 eV were employed. LDA¹⁰¹ as well as the GGA of Perdew-Burke-Ernzerhof (PBE)¹⁰³ has been used to treat the exchange–correlation part ϵ_{xc} of the density functional which was shown to give interaction energies comparable to MP2 method.²⁵⁶ In all these calculations, the convergence criteria for total energy in the self consistent field iteration was set to 1×10^{-6} eV and the optimizations have been carried out by keeping the volume of the unit cell as constant until the Hellmann-Feynman force components on each atom is less than $0.01 \text{ eV } \text{\AA}^{-1}$. The Brillouin zone has been sampled using the automatically generated 6x6x1 Monkhorst-Pack set of k -points.¹³³ We have also used the hybrid functional B3LYP¹⁰⁴⁻¹⁰⁶ as implemented in Crystal06²⁵⁷ to calculate the band structure. The initial geometries and all the reported structures have been obtained by using the graphical software MOLDEN.¹³⁵ Bader¹⁹² charge analysis has been performed to calculate the atomic charges.

The lithiation potential, V , is calculated using the following relation.²⁵⁸

$$V = -\Delta G/z.F$$

where z denotes the number of lithium atoms exchanged and

$$\Delta G = \Delta E + P\Delta V - T\Delta S .$$

The quantity ΔG can be approximated to ΔE as the remaining terms are negligible as compared to the energy term. If the energies are given in electron volts, the lithiation potential vs. Li/Li^+ can be evaluated by

$$V = - \Delta E/n$$

where n is the number of lithium atoms dispersed. The specific capacity of the anode is calculated using the formula²⁵⁹

$$C_p = F/W$$

F = Faraday constant (taken as 96500 C/mol) and W is the molecular weight of the Li_xC_x (x varies from 12 to 3 in graphyne and 18 to 2.25 in graphdiyne) formula unit.

7.3 Results and discussion:

7.3.1 Graphyne and graphdiyne: Promising materials for nanoelectronics and energy storage applications

In this part of the study, we are mainly interested in studying the (1) electronic band structure of the conjugated carbon materials and effect of the length of the linking chain on the band structure, (2) potential of the lithium dispersed graphyne and graphdiyne as anode material for lithium batteries and (3) hydrogen adsorption properties of these lithium dispersed graphyne and graphdiyne materials.

First, we look at the electronic structure of pristine graphyne and graphdiyne, calculated by using the first principles based density functional (DFT) based approach as implemented in VASP code. Figures 7.1(a) and 7.1(b) present the optimized structure of graphyne and graphdiyne with 12 and 18 atoms per unit cell respectively as obtained by using the Generalized

Gradient Approximation of Perdew-Burke-Ernzerhof (PBE). The optimized cell parameters of graphyne and graphdiyne are calculated to be 6.889 Å and 9.464 Å respectively which are in good agreement with previous reported results.²⁴⁹

From the band structure plots of graphyne and graphdiyne, as calculated through PBE functional and shown in Figures 7.1(c) and 7.1(d), we can see that both the species are associated with direct band gaps. The band gaps calculated through PBE method in graphyne and graphdiyne are found to be 0.47 eV and 0.52 eV respectively which are in good agreement with earlier reported results.²⁶⁰⁻²⁶¹ Graphyne is found to have the CB_{\min} and VB_{\max} along the k -point M whereas the corresponding minimum and maximum in graphdiyne are along the Γ point.

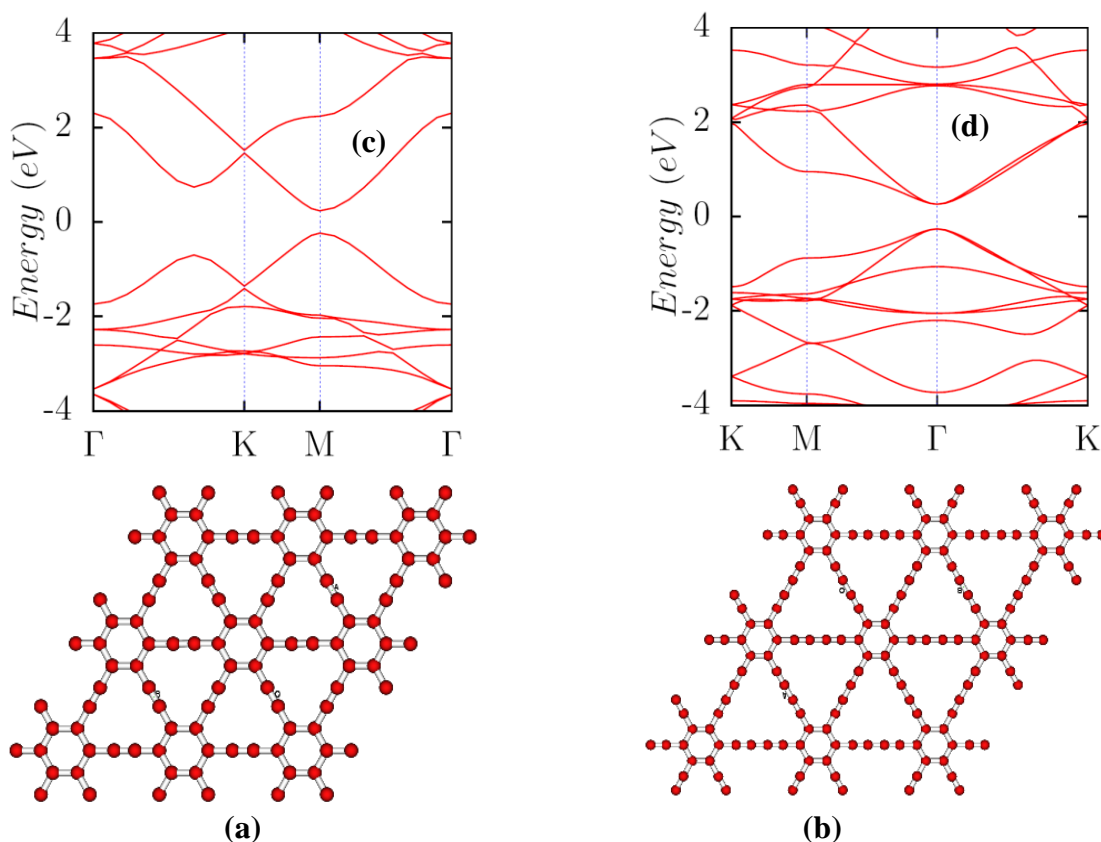


Figure 7.1: 3x3x1 super cell of the optimized geometries of (a) graphyne (b) graphdiyne and the calculated band structure of (c) graphyne and (d) graphdiyne

However, as it is known from the literature that the band gaps from pure DFT functionals are underestimated, we have also calculated the corresponding band structures using the B3LYP functional as implemented in the Crystal06 code. From the B3LYP results, we find that even though the CB_{\min} and VB_{\max} lie along the k -points which are same as the ones predicted by PBE method, the band gaps change considerably. The band gap in graphyne as calculated by using B3LYP is found to be 2.23 eV while the corresponding result for graphdiyne is 1.18 eV. The calculated band gap of graphdiyne through B3LYP functional is very close to the corresponding band gap reported by Jiao et al. (1.22 eV) using the hybrid exchange-correlation functional HSE06.²⁴⁹ From the PBE results on band gaps, the effect of length of the acetylenic linking chain in these materials cannot be inferred properly.²⁶⁰⁻²⁶¹ However, from the B3LYP results, one can see that there is nearly 50% decrease in the band gap on increasing the length of the linking carbon chain by one acetylenic unit. These results show that the band gap in these materials can be tuned by altering the chain length which might have lot of applications in semiconductor industry and nanoelectronics.

Charges on the atoms are calculated through Bader charge density analysis. In both the cases of graphyne and graphdiyne, we find that there is an electron transfer from ring carbon to nearby sp carbon and a total of 0.9 a.u of charge is transferred from C_6 ring to the sp carbons. This charge density analysis shows that the C_6 rings are electron deficient and will favor the alkali metal binding through charge transfer from the metal atom to the carbon surface. We have considered different possible sites in graphyne and graphdiyne for lithium metal attack and found that in both the cases, lithium located within the carbon surface occupying the cavity is most preferred. This preference over other sites can be because the metal within the cavity can interact with three acetylenic units in graphyne and two such units in graphdiyne as shown in Figure 7.2. The next preference for lithium is found to be above the C_6 ring.

We have systematically decorated both graphyne and graphdiyne with lithium metals. For both graphyne and graphdiyne, we find that the first two lithium atoms preferably occupy the cavity positions and are within the carbon surface. After the occupancy of two metal atoms per unit cell, the third and fourth metal atoms are found to bind above and below the C_6 ring. The results of metal binding energies as well as the cell parameters are given in Table 7.1. The binding energy of the first lithium atom to graphyne as calculated by the PBE method is found to be -64.5 kcal/mol which is higher than the corresponding energy in the case of graphdiyne (-61.9 kcal/mol). This difference can be attributed to the suitable size of the cavity in graphyne where lithium can exactly sit at the centre of cavity and interact with three acetylenic units placed at equal distances, whereas, in the case of graphdiyne, the cavity size is larger and lithium can interact with only two acetylenic units which are closer to the metal site which can also be seen from Figure 7.2. Although the first metal binding energy is higher in the case of graphyne,

Table 7.1 Calculated cell parameter and lithium interaction energy with graphyne (C_{12}) and graphdiyne (C_{18})

System	Cell parameter		Li binding energy	
	LDA	PBE	LDA	PBE
C_{12} -Li	6.863	6.926	-75.9	-64.5
C_{12} -Li ₂	6.909	6.975	-64.7	-54.1
C_{12} -Li ₃	6.950	7.015	-54.2	-44.3
C_{12} -Li ₄	6.983	7.052	-48.9	-39.2
C_{18} -Li	9.397	9.473	-69.4	-61.9
C_{18} -Li ₂	9.398	9.479	-63.8	-55.4
C_{18} -Li ₃	9.377	9.458	-59.8	-51.0
C_{18} -Li ₄	9.406	9.486	-56.5	-47.7

subsequent lithium binding energies are larger in graphdiyne due to the presence of more acetylenic units. From Table 7.1, it is clear that the lithium adsorption energy in these materials

is higher than the cohesive energy of lithium and this binding is much stronger than the corresponding adsorption in the case of graphene and porous graphene.²⁴²⁻²⁴³ If we see the variation in the cell parameter with lithium loading, it is clear that the variation is very less (at the most 2.3% in the case of graphyne and just 0.2% in graphdiyne). The calculated Bader charge on the lithium occupying the cavity of graphyne is found to be +0.89 a.u and the corresponding charge on the lithium atoms bound to the C_6 ring is found to be +0.78 a.u. However, in the case of graphdiyne, both types of lithium atoms are having nearly same positive charge of +0.89 a.u.

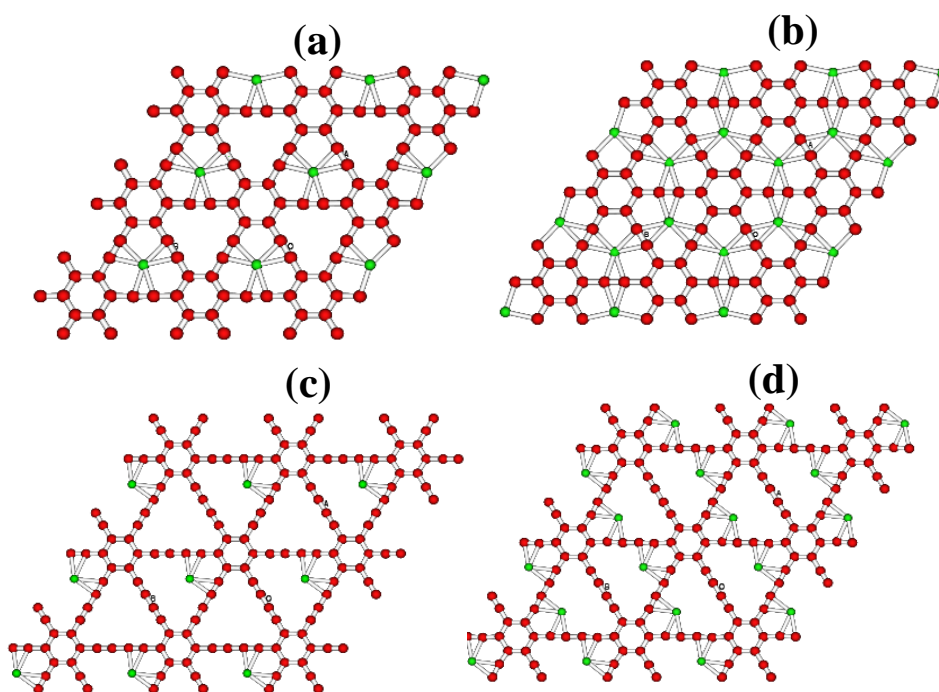


Figure 7.2. 3x3x1 super cell structures of the optimized geometries of (a) graphyne-Li (b) graphyne-Li₂ (c) graphdiyne-Li and (d) graphdiyne-Li₂

To designate these carbon allotropes as anode materials for lithium batteries, we have calculated the lithiation potentials (vs. Li/Li^+) as well as the specific capacities for all the above studied structures and reported in Table 7.2. In the case of graphyne, where each unit cell of 12 carbon atoms can host four lithium atoms with C_3Li as the overall composition, the specific capacity will be nearly double (623.4 mAh/gm) in comparison to the case of graphite. The

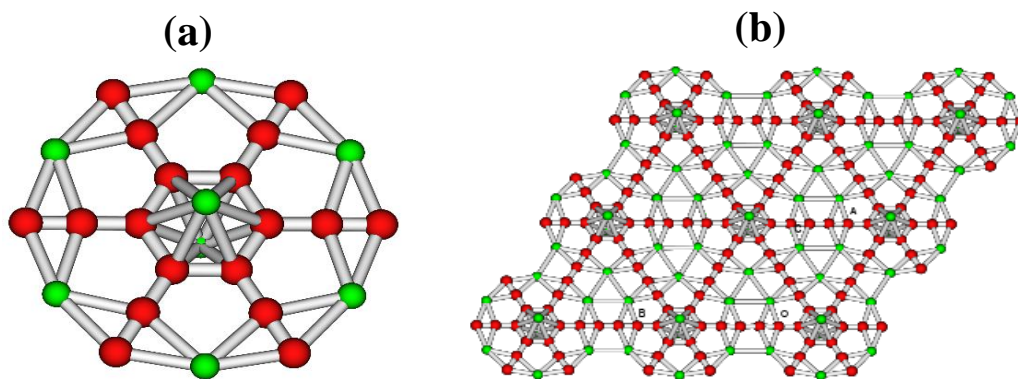


Figure 7.3 Optimized (a) primitive cell and (b) 3x3x1 super cell structures of graphdiyne-Li₈.

lithiation potentials (vs. Li/Li⁺) are also enhanced considerably to the range of 2.8 V to 1.7 V. In the case of graphdiyne, the lithiation potentials are further improved and found to be in the range of 2.7 V to 2.1 V. To check the maximum lithium loading capacity in graphdiyne, we optimized the structure with eight lithium atoms per unit cell of 18 carbons where each cavity can hold three lithium atoms and the remaining two lithium atoms are above and below the C₆ ring which

Table 7.2. Calculated lithiation potential vs. Li/Li⁺ for lithium dispersed graphyne and graphdiyne in Volts

System	Lithiation potential vs. Li/Li ⁺ (V)		Specific capacity (mAh/gm)
	PBE	LDA	
Graphyne-Li	2.8	3.3	177.5
Graphyne-Li ₂	2.3	2.8	339.3
Graphyne-Li ₃	1.9	2.4	487.4
Graphyne-Li ₄	1.7	2.1	623.4
Graphdiyne-Li	2.7	3.0	120.2
Graphdiyne-Li ₂	2.4	2.8	233.1
Graphdiyne-Li ₃	2.2	2.6	339.3
Graphdiyne-Li ₄	2.1	2.5	439.4
Graphdiyne-Li ₈	1.9	2.3	788.4

is shown in Figure 7.3. This composition C_{2.25}Li has still higher specific capacity of 788.4 mAh/gm and the calculated lithiation potential (vs. Li/Li⁺) is found to be 1.9 V. These results

show that graphyne and graphdiyne can be used to design an efficient anode material for lithium batteries.

Now we explore the adsorption of molecular hydrogen around these exposed metal centres mediated through ion-quadrupole as well as ion-induced dipole interactions. Figure 7.4 shows the optimized primitive cell geometries of the systematically hydrogenated species of the lithium decorated graphyne. We have optimized two different structures for the species with one H_2 per lithium. The structure with the hydrogen on top of the metal is found to have less adsorption energy as compared to the second isomer where the hydrogen is tilted towards the carbon surface as shown in Figure 7.4 and the difference in adsorption energy is found to be ~ 0.6 kcal/mol per molecular hydrogen. This energy difference shows that the carbon surface also

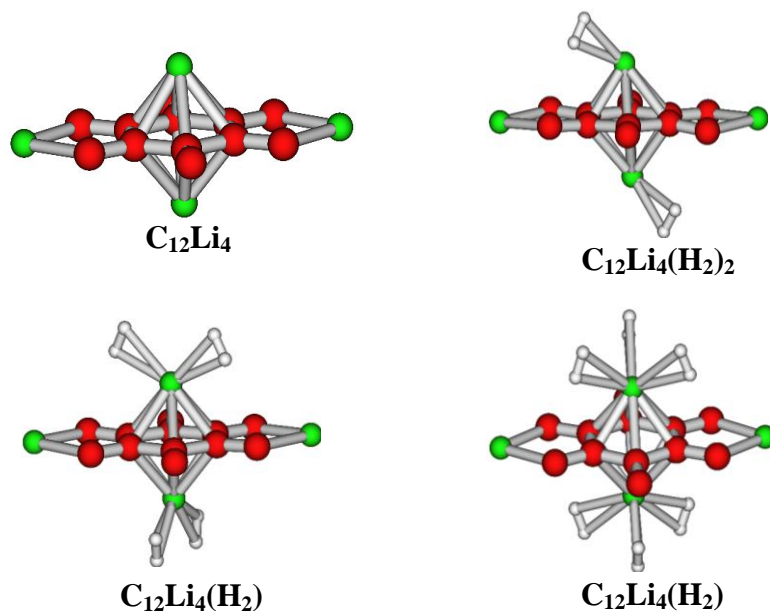


Figure 7.4 Optimized primitive cell structures of hydrogenated lithium decorated graphyne.

plays a direct role in promoting the hydrogen adsorption. In the case of the minimum energy isomer, the hydrogen adsorption energy is calculated to be -3.4 kcal/mol which is very close to the predicted required interaction energy for ambient hydrogen storage.²⁶² The minimum Li-H

distance is calculated to be 1.973 Å and the H-H bond in the adsorbed H₂ is found to be elongated to 0.770 Å from 0.750 Å in free H₂. The second hydrogen molecule at each lithium is found to interact with an average interaction energy of -2.8 kcal/mol per H₂ and the corresponding structure is also shown in Figure 7.4. The Li-H and H-H bond distances are found to be 2.031 Å and 0.765 Å respectively. In the case of the species hydrogenated with three H₂ molecules per Li, the H₂ molecules are found to be arranged in such a way that the three H₂ adsorbed on one Li are in staggered position with respect to the other three H₂ adsorbed on the other Li site so that there will be minimum repulsion between the adsorbed molecules. The hydrogen adsorption energy in this structure is found to be -2.4 kcal/mol per H₂. We also attempted to introduce the fourth molecular hydrogen per metal atom from the top of each metal atom and found that this molecule does not get adsorbed and is moved far (~3.7 Å) from the metal site. This shows that each Li can adsorb a maximum of three molecular hydrogens which in the case of lithium decorated graphyne corresponds to a gravimetric density of ~6.5 wt% of hydrogen.

In the case of lithium decorated graphdiyne also, we have carried out a similar systematic study. The first, second and third molecular hydrogen adsorption energies on each lithium site are calculated to be -3.5, -3.2 and -2.8 kcal/mol per H₂ molecule. Here also the maximum number of H₂ adsorbed per lithium is found to be three and the fourth one is found to move far away from the Li site. This relatively large hydrogen adsorption energies as compared to that in the case of lithiated graphyne can be expected as the lithium atoms in graphdiyne acquire higher positive charge than that in the case of graphyne. Although the number of H₂ adsorbed per Li is same in both graphyne and graphdiyne, the adsorption capacity is found to be lower (~4.7 wt%) in lithium decorated graphdiyne, as the number of carbons per unit cell is more (18) here as compared to that in graphyne case (12). However, as there are still possible sites for lithium

decoration in graphdiyne such as the C-C triple bonds, and also the C₆-C₆ ring distance is large (9.54 Å) as compared to graphyne (6.97 Å), it might be possible to increase the lithium loading in graphdiyne which can further increase the hydrogen adsorption capacity as well.

7.3.2 Hydrogen adsorption in lithium decorated conjugated microporous polymers.

In this part of the study, we have considered two planar expanded hydrocarbons namely, CMP-1 and HCMP-1 based networks. We have systematically studied the (1) electronic band structure (2) Lithium metal binding and (3) hydrogen adsorption properties of these two-dimensional networks as follows.

The optimized structures of the unit cell considered and 2 x 2 x 1 supercell of both the networks are shown in Figure 7.5. The unit cell of CMP-1 consists of 18 carbon and six hydrogen atoms whereas the HCMP-1 network consists of 24 carbon and six hydrogen atoms, as shown in Figure 7.5. The optimized cell parameters of CMP-1 and HCMP-1 as calculated by using DFT with PBE functional are found to be 11.923 Å and 16.366 Å respectively. All the different kinds of the C-C bond lengths observed are reported in Table 7.3. The calculated Bader charges show that the *sp* carbons are carrying a partial negative charge which is expected due to the high electronegativity of these carbons as compared to the *sp*² carbons. Because of this electron transfer from the ring carbons to the chain carbons, the C₆ ring will be somewhat electron deficient and thus can bind alkali metals like lithium more efficiently as compared to the simple graphene.

Table 7.3: Calculated cell parameters, different C-C bond lengths and the band gaps of **CMP-1** and **HCMP-1** using DFT with both PBE and B3LYP functionals.

System	Cell parameter (Å)	Bond lengths (Å)			Band gap (eV)	
		C _{sp} -C _{sp}	C _{sp2} -C _{sp2}	C _{sp} -C _{sp2}	PBE	B3LYP
CMP-1	11.923	1.220	1.408	1.419	2.66	3.96
HCMP-1	16.366	1.227	1.409	1.414	2.36	3.51

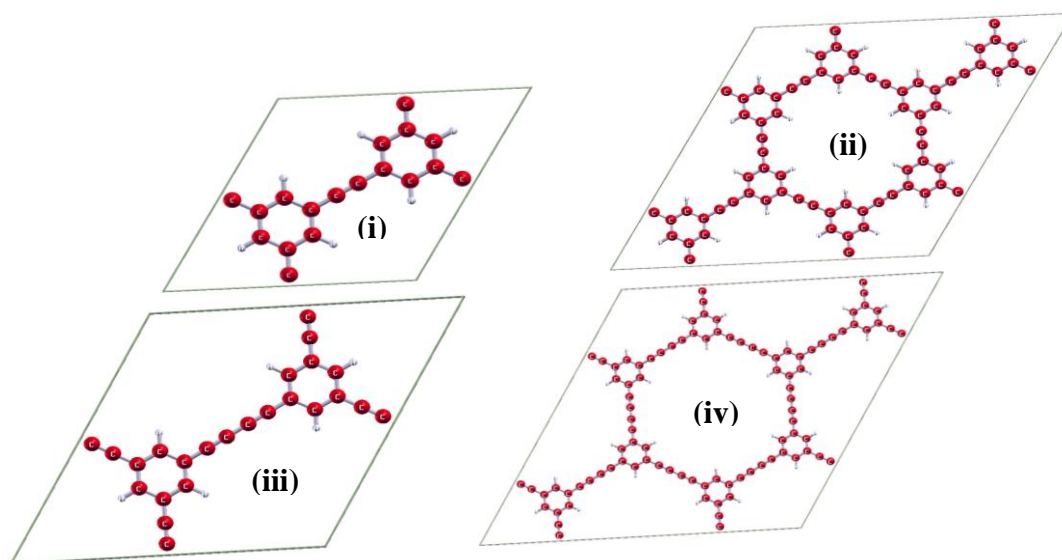


Figure 7.5 Optimized structures of the unit cell and the 2 x 2 x 1 super cell of (i & ii) CMP-1 and (iii & iv) HCMP-1 respectively.

The electronic band structure plots of both CMP-1 and HCMP-1 networks as calculated by using DFT with PBE functional are given in Figure 7.6. Both CMP-1 and HCMP-1 are found to have nearly flat conduction and valence bands with band gaps of 2.66 eV and 2.36 eV respectively. Since the pure DFT functionals are known to underestimate the band gap values, we have also calculated these gaps by using the hybrid functional B3LYP which is known to give reasonably good estimate of band gaps.²⁶³⁻²⁶⁴ The band gaps of CMP-1 and HCMP-1 as calculated through B3LYP functional are found to be 3.96 eV and 3.51 eV respectively. Though there is a little decrease in the band gap on increasing the length of the carbon chain, it is not as significant as it is observed in the graphyne to graphdiyne case. The calculated partial density of states show that the top of the valence band and bottom of the conduction band are mainly contributed by the carbon p_z orbitals.

To study the lithium metal binding, we have considered three different possible sites for the metal atoms to bind, viz. above the six membered carbon ring, above the C-C triple bond and

within the cavity where metal exists in the same plane as that of the hydrocarbon. The optimized results show that the most preferred site is above the C_6 ring as compared to the other two sites

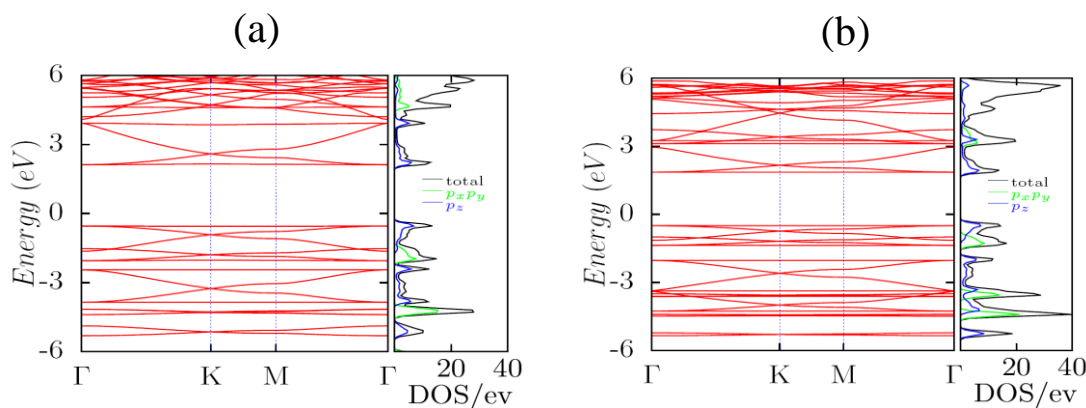


Figure 7.6 Band structure plots along with the partial density of states of (a) CMP-1 and (b) HCMP-1 as calculated from the DFT-PBE method.

considered. As each unit cell of both CMP-1 and HCMP-1 consists of two C_6 rings, we could decorate them with four lithium atoms with one above and one below each of the C_6 rings. The interaction energy per lithium atom in CMP-1 and HCMP-1 as obtained through dispersion corrected PBE functional is found respectively to be -40.9 kcal/mol and -44.9 kcal/mol which are more than the cohesive energy of the metallic lithium. The higher value of interaction energy of Li with HCMP-1 as compared to CMP-1 can be expected due to the presence of more number of sp-carbon atoms in HCMP-1 as compared to HCMP-1. The C-Li bond length is found to be 2.23 Å and the Li-Li distance on the same side is 6.96 Å whereas the corresponding distance between the Li atoms adsorbed on the same ring (opposite sides) is found to be 3.38 Å. The optimized cell parameter of lithiated CMP-1 and HCMP-1 are found to be 12.05 Å and 16.47 Å respectively which shows that there is slight expansion in the cell on lithiation. The calculated Bader charges on lithium atoms show that the Li sites in lithiated CMP-1 and HCMP-1 are found to be carrying a positive charge of 0.88 and 0.89 respectively indicating a charge transfer from the metal to the carbon ring.

Hydrogen Adsorption

The optimized geometries of the unit cells of lithiated CMP-1 and its systematically hydrogenated species are shown in Figure 7.7. We have reported hydrogen adsorption energies calculated using both PBE and PBE-D2 methods in Table 7.4. At first, we optimized the system with one H_2 per lithium site by keeping the hydrogen on top of the metal site. In the optimized structure, the molecular hydrogen is found to move towards the carbon surface from the on top position which indicates that the carbon surface also interacts with the adsorbed hydrogen. The shortest Li-H distance is calculated to be 1.889 Å and the H-H bond distance is 0.773 Å which is little elongated from the corresponding distance in the free H_2 calculated at the same level of theory (0.750 Å). The calculated binding energy per molecular hydrogen using PBE-D2 method is found to be -7.5 kcal/mol. This adsorption energy value is quite higher (nearly double) as compared to the corresponding adsorption energies calculated using simple PBE method (-3.6 kcal/mol) and also higher as compared to the bare Li^+-H_2 binding energies reported (\sim -5.3 kcal/mol).⁶⁸ This can be an artefact of DFT-D2 method which is known to show over bound nature in presence of partial ionic charges.²⁶⁵ However, as the PBE

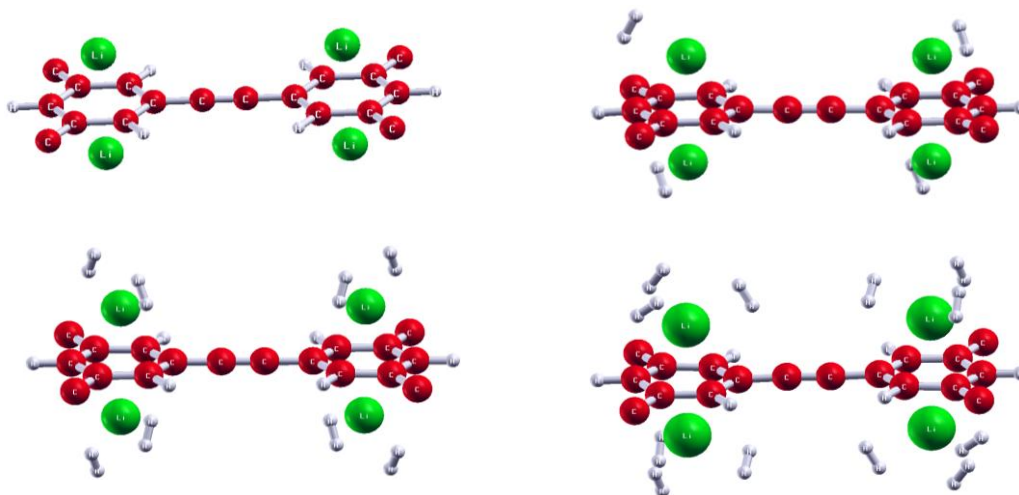


Figure 7.7. Optimized unit cell of CMP-1- Li_4 and its hydrogenated species CMP-1- $Li_4(H_2)_{4n}$

functional is known to underestimate the weak interactions, the actual binding energy can be expected to be in-between PBE and PBE-D2 values. Thus, both PBE and PBE-D2 binding energies are reported for all the systems in Table 7.4. However, only the PBE based binding energies are discussed below in details.

Table 7.4 The calculated hydrogen adsorption energies per H_2 , shortest Li-H and H-H bond lengths of the hydrogenated species of lithiated **CMP-1** and **HCMP-1**.

System	Adsorption energy per H_2 (kcal/mol)		Shortest Li-H distance (Å)	H-H bond distance (Å)
	PBE	PBE-D		
CMP-1-Li ₄ (H ₂) ₄	-3.6	-7.5	1.889	0.773
CMP-1-Li ₄ (H ₂) ₈	-3.4	-7.3	1.909	0.769
CMP-1-Li ₄ (H ₂) ₁₂	-2.8	-6.5	1.956	0.759
HCMP-1-Li ₄ (H ₂) ₄	-3.4	-7.0	1.906	0.765
HCMP-1-Li ₄ (H ₂) ₈	-3.2	-6.8	1.919	0.764
HCMP-1-Li ₄ (H ₂) ₁₂	-2.7	-6.3	1.995	0.758

In the next species, two molecules of hydrogen are allowed to be adsorbed on each metal site with a total of eight H_2 per unit cell and the corresponding optimized cell structure is shown in Figure 7.7. The adsorption energy per molecular hydrogen is found to be -3.6 kcal/mol. The shortest Li-H bond distance is found to be 1.909 Å with the H-H distance equal to 0.769 Å. In case of the species where three H_2 are adsorbed on each lithium site, all three H_2 are found to be symmetrically situated around the Li site such that each H_2 is pointing to one $-C\equiv C-$ unit as shown in Figure 7.7. Three H_2 molecules adsorbed on one side of the C_6 ring are in eclipsed configuration with respect to the other three adsorbed on opposite side of the surface. The adsorption energy calculated per molecular hydrogen is found to be -2.8 kcal/mol. The shortest Li-H and H-H distances are found to be 1.956 Å and 0.759 Å respectively. We have also tried to

introduce fourth hydrogen on top of each Li site, but found the hydrogen molecules to move away from the metal site. This can be attributed to the intermolecular repulsions between the adsorbed hydrogens. With three H_2 per metal site, the hydrogen gravimetric density is calculated to be 8.76 wt% at 0 K.

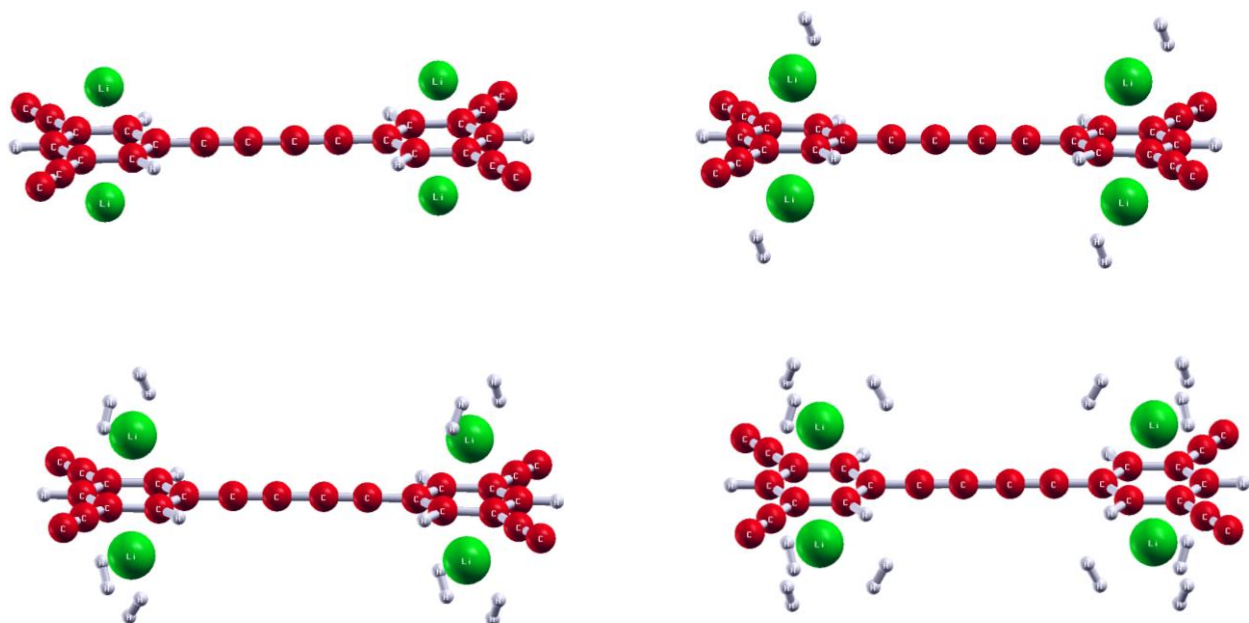


Figure 7.8 Optimized unit cell structures of HCMP-1- Li_4 and its hydrogenated species HCMP-1- $Li_4(H_2)_{4n}$ ($n=1-3$)

Similar systematic study has been carried out in the case of lithiated HCMP-1 as well. The optimized unit cell structures of lithiated HCMP-1 and its hydrogenated species with the general formula HCMP-1- $Li_4(H_2)_{4n}$ are shown in Figure 7.8. The first hydrogen on each Li in HCMP-1- $Li_4(H_2)_4$ is found to be adsorbed with an interaction energy of -3.4 kcal/mol per hydrogen molecule which is little less as compared to that observed in CMP-1- $Li_4(H_2)_4$. This difference in adsorption energy might be because of the difference in the nature of carbon surface since the Li sites are almost of similar charge (0.88 and 0.89). In CMP-1, the *sp*-carbons are more electronegative as compared to those in HCMP-1 which can be observed from the

difference in $C_{sp}-C_{sp}$ carbon bond lengths as shown in Table 7.3.2.1. This minor difference in the negative charge on the sp -carbons bonded to C_6 ring of CMP-1 and HCMP-1 is contributing to the higher hydrogen adsorption energy in lithiated CMP-1 observed. The second and third molecules of hydrogen per Li site are found to be adsorbed with interaction energies of -3.2 and -2.7 kcal/mol per hydrogen respectively. The Li-H and H-H bond distances are reported in Table 7.3.2.2, which are found to vary according to the variation in adsorption energy with increasing number of hydrogen molecules adsorbed per metal site. With a total of twelve H_2 molecules adsorbed per unit cell as shown in Figure 7.8, the theoretical gravimetric density will be 7.06 wt% at 0 K. As both these two-dimensional polymeric materials are already synthesized and similar kind of COF materials are also lithiated experimentally, it should also be possible experimentally to make the considered model structures to design a proper hydrogen storage material.

7.4 Conclusions:

In summary, we conclude that the band gap of the conjugated carbon materials considered here can be tuned by changing the length of the acetylenic linking chain. We could show that both graphyne and graphdiyne can host large amount of lithium with considerably higher lithiation potentials (vs. Li/Li^+) and specific capacities which indicates that these materials can be used to design efficient anode material for lithium batteries. Due to the electron transfer from lithium metal to the carbon surface in these materials, the lithium sites are found to be cationic and thus can adsorb molecular hydrogen with desired adsorption energies. Lithium decorated graphyne is found to adsorb hydrogen with a gravimetric density of 6.5 wt% whereas the corresponding figure in graphdiyne is found to be 4.7 wt%.

CHAPTER 8

Hydrogen Adsorption in Three-dimensional Porous Materials

8.1. Introduction

The present chapter deals with hydrogen adsorption in three dimensional (3D) porous materials. It consists of two parts, one on tuning the metal binding energy and hydrogen adsorption in metal organic frameworks, and the other on design of new 3D carbon allotropes based on supercubane.

During the past decade, lot of interest has grown in the design of new porous materials with large surface area.²⁶⁶⁻²⁶⁸ Among such materials, notable ones are the metal-organic frameworks (MOF), which form a new class of ordered organic-inorganic hybrid solids, composed of metal or metal oxide clusters as building blocks and organic bridges as linkers.⁶²⁻⁶⁴ One of the most important areas of application which holds high promise is the storage of hydrogen gas in molecular form.⁶⁶⁻⁶⁷

Li decoration was shown to improve hydrogen adsorption in MOFs and in most of the Li doped framework materials studied above, the Li atom is positioned on top of the six membered carbon rings (benzene) which is aromatic in nature. Because of the aromatic nature of the ring, the binding energy of the metal atom is poor leading to aggregation of adsorbed metal atoms to form clusters and is therefore not suitable for reversible hydrogen adsorption. Venkataramanan et al.²⁶⁹ have studied hydrogen adsorption in lithium decorated MOF-5 and reported the lithium binding energy to be around -35.9 kcal/mol. However, the lithium binding energy is found to be less than the cohesive energy of metallic lithium (-39 kcal/mol) which shows that at higher concentrations, lithium atoms would tend to form clusters, resulting into inefficient hydrogen storage capacity. In the present study, our objective is to explore the possibility of improving the adsorption energy of the lithium to the MOF-5. We propose to improve this binding strength of Li by substituting two of the carbon atoms of the carbon ring with two boron atoms which

contain one less electron as compared to carbon. These types of systems are also feasible experimentally since the synthesis of boron-substituted heterocycles has been already reported.²⁷⁰ Very recently, Zou et al.²⁷¹ showed that boron doping in transition metal doped COF can prevent the clustering problem through ab initio calculations.

Another class of materials that can be used for hydrogen storage are the porous carbon materials. Carbon is known to form a very large number of compounds due to its ability to bond with itself as well as most of the other atoms in the periodic table. Carbon mainly exists as two natural allotropes, namely graphite and diamond, where graphite is composed of all sp^2 carbons and diamond with all sp^3 carbons. The remarkable discovery of fullerene by Kroto et al.²⁷² in 1985 started the era of synthetic carbon allotropes. The next family of carbon allotrope is the carbon nanotube synthesized in 1991 followed by graphene in 2004 which consists of all sp^2 carbon atoms.²⁷³⁻²⁷⁴ In 1978, a unique allotrope of carbon, the body centered cubic (bcc) carbon was reported by Strel'nitskii et al.²⁷⁵ which is also designated as supercubane. Later, Johnston et al.²⁷⁶ carried out detailed theoretical calculations on the proposed super dense C_8 through tight-binding approach. In 2008, Liu et al.²⁷⁷ could synthesise the same bcc carbon through a pulsed-laser induced liquid–solid interface reaction. There are quite a good number of reports on designing new carbon allotropes which are composed of both sp^2 and sp , or sp^3 and sp hybridized carbons.²⁷⁸⁻²⁷⁹ Hence the exploration of new possible carbon allotropes with desired structure and property is an important area of research and still there might be a good number of unexplored forms of carbon yet to be discovered.

We have modeled different three-dimensional bcc carbon allotropes through the expansion of the supercubane by inserting acetylinic and diacetylinic units between both inter-

and intra-cubane C-C bonds. The C-C triple bond, where the carbons are in *sp* hybridized form, is found to be an important linking group in many of the carbon scaffold and conjugated hydrocarbons. We have considered here different supercubane based systems generated through the insertion of $\text{-C}\equiv\text{C-}$ units between both intra- and inter-cubane C-C bond. A detailed study on the electronic structure and hydrogen adsorption characteristics has been carried out.

8.2. Computational details

All the energy calculations and geometry optimization for the molecular systems have been performed by using the GAMESS software.¹⁵⁵ We have employed the density functional theory (DFT) with HLYP¹⁰⁶ as well as the Perdew-Wang (PW91) exchange correlation energy functionals.¹⁰² We have used the extensive split-valence basis sets with diffuse and polarization functions, 6-31++G(2d,2p). All the nucleus-independent chemical shift (NICS) parameter calculations are carried out at HLYP/6-31++G(d, p) level of theory. The initial geometries and all the reported structures have been obtained using the graphical softwares GABEDIT¹⁶³ and MOLDEN.¹³⁵

All the periodic systems were optimized using the periodic boundary condition (PBC) within DFT calculations implemented in the VASP,¹³¹⁻¹³² using plane wave basis set. Projector augmented wave (PAW)¹²⁹⁻¹³⁰ potentials with an energy cutoff of 800 eV were employed for the elemental constituents. The exchange–correlation part ϵ_{xc} of the density functional was treated using the GGA of PW91.¹⁰² In all these calculations, the convergence threshold was set with the energy change per atom less than 1×10^{-6} eV and the force components on each atom relaxed to less than $0.01 \text{ eV } \text{\AA}^{-1}$. As we are dealing with very large primitive cell, we used only Γ point for sampling the Brillouin zone. Bader¹⁹² charge analysis has been performed to evaluate the charges on lithium atoms.

8.3. Results and discussions

8.3.1: Tuning the Metal Binding Energy and Hydrogen Storage in Alkali Metal Decorated MOF-5 Through Boron Doping

The interaction between an alkali metal atom and benzene is found to be very poor in conformity with the earlier studies. However, making the carbon ring electron deficient towards the aromatic sextet can improve the interaction towards the alkali metal atoms. One such approach followed here is the substitution of a carbon atom of the ring with the electron deficient boron atom. Two of the CH units of benzene are replaced with two BH units which leads to $C_4B_2H_6^{2-}$, which can now bind with two alkali metal cations and form a neutral structure $C_4B_2H_6Li_2$. The optimized structures of $C_4B_2H_6$ and $C_4B_2H_6^{2-}$ are shown in Figures 8.1(a) and 8.1(b) respectively. Both the structures are found to have D_{2h} symmetry with a C-C bond length of 1.36 Å and C-B bond lengths of 1.56 Å in the case of $C_4B_2H_6$ while the corresponding bond lengths in $C_4B_2H_6^{2-}$ are found to be 1.42 and 1.52 Å.

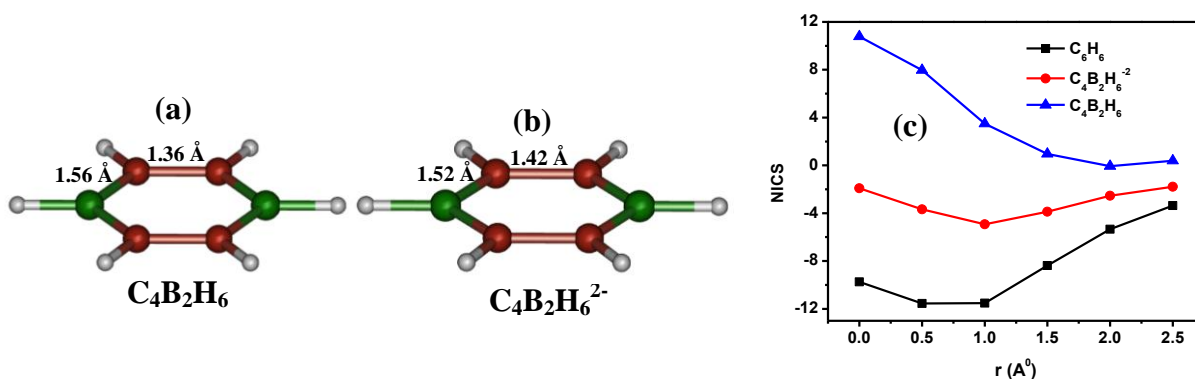


Figure 8.1(a). Optimized structure of $C_4B_2H_6$ (b) Optimized structure of $C_4B_2H_6^{2-}$ and (c) Variation of NICS value along the perpendicular direction from the centre of the rings of $C_4B_2H_6$, $C_4B_2H_6^{2-}$ and C_6H_6

To verify the aromatic nature of $C_4B_2H_6^{2-}$, we have carried out a NICS scan from the centre of the molecule to 2.5 Å above the ring centre and the variation of NICS value is found to follow the same trend as benzene which is shown in Fig. 1(c). However, from the NICS scan of the neutral $C_4B_2H_6$ shown in Figure 8.1(c) one can see the anti aromatic nature of $C_4B_2H_6$ as it is having highly positive NICS values.

The optimized geometries of all the metal decorated systems ($C_4B_2H_6$ -Li₂, $C_4B_2H_6$ -Na₂, $C_4B_2H_6$ -Mg and $C_4B_2H_6$ -Mg₂) at MP2/6-31++G(2d,2p) level of theory are shown in Figure 8.2. The minimum energy structure of $C_4B_2H_6$ -Li₂, is found to have a D_{2h} symmetry with

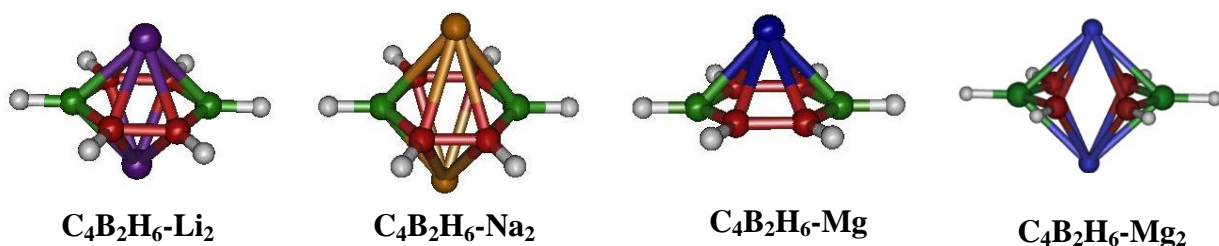


Figure 8.2 Optimized structures of $C_4B_2H_6M_2$ (M=Li, Na and Mg) and $C_4B_2H_6$ -Mg

C-Li and B-Li distances of 2.15 and 2.20 Å respectively, and the Li-Li distance is found to be around 3.14 Å. The lithium binding energy to the ring system is found to be -225.61 kcal/mol per lithium, which is extremely high and can thus ensure the stability towards recyclability. $C_4B_2H_6$ -Na₂ is also found to have a D_{2h} symmetry with C-Na and B-Na distances of 2.54 and 2.57 Å respectively, and a Na-Na distance of 4.13 Å. Each sodium is found to be bound with an interaction energy of -194.96 kcal/mol, which is also very high. The optimized geometry of $C_4B_2H_6$ -Mg has a C_{2v} symmetry with C-Mg and B-Mg distances of 2.21 and 2.29 Å respectively and the ring surface is found to be little distorted from the planar structure. The interaction energy between Mg^{2+} and $C_4B_2H_6^{2-}$ is found to be -595.59 kcal/mol which is extremely high

even compared to the earlier complexes. We have also calculated the interaction energy of metal atoms Li, Na and Mg with the neutral $C_4B_2H_6$ as well and found it to be -84.59, -61.37 and -51.72 kcal/mol per metal atom respectively. This strong interaction of the metal ions (or metal atoms) with $C_4B_2H_6^{2-}$ (or $C_4B_2H_6$) is an indication for the high stability of the complexes which conforms to the requirement of a stable and reversible hydrogen storage material. In all the above neutral complexes, the metal sites are found to be carrying a positive charge as shown in Table 8.1. The ESP charges calculated on Li, Na and Mg in the complexes $C_4B_2H_6-Li_2$, $C_4B_2H_6-Na_2$ and $C_4B_2H_6-Mg$ are found to be 0.79, 0.87 and 0.80 respectively.

To verify whether the complexes are stable or not, we have also carried out the Hessian calculation analytically for all the complexes mentioned above and found that none of the complexes is having imaginary frequencies. From our results we observe that the smallest vibrational frequencies in the complexes, $C_4B_2H_6-Li_2$, $C_4B_2H_6-Na_2$ and $C_4B_2H_6-Mg$ are 393.34, 166.52 and 336.15 cm^{-1} respectively which indicate the stability of these complexes.

Table 8.1: The calculated interaction energy, charge on metal, HOMO-LUMO gap and NICS(0) values in $C_4B_2H_6-M_n$ (M=Li, Na and Mg)

System	Interaction energy per metal ion (kcal/mol)			Charge on metal (a.u)		HOMO-LUMO gap (eV)		NICS(0)
	MP2 ^a	MP2 ^b	HLYP ^a	MP2	HLYP	MP2	HLYP	
$C_4B_2H_6-Li_2$	-225.61	-84.59	-226.61	0.79	0.80	7.32	8.00	-11.55
$C_4B_2H_6-Na_2$	-194.96	-61.37	-195.43	0.87	0.89	5.85	6.58	-4.74
$C_4B_2H_6-Mg$	-595.59	-51.72	-605.75	0.80	0.81	5.90	6.06	+4.07

^aThe interaction energy per metal ion is calculated as
 $1/n [E(C_4B_2H_6-M_n) - E(C_4B_2H_6^{2-}) - n \times E(M^{+1 \text{ or } 2})]$

^bThe interaction energy per metal is calculated as
 $1/n [E(C_4B_2H_6-M_n) - E(C_4B_2H_6) - n \times E(M)]$

The calculated HOMO-LUMO gaps of $C_4B_2H_6-Li_2$, $C_4B_2H_6-Na_2$ and $C_4B_2H_6-Mg$ are reported in Table 8.1 and are found to be 7.32, 5.85 and 5.90 eV respectively which also provide support to the high stability of the complexes. In order to characterize the aromatic nature of all these complexes considered, we have calculated the nucleus-independent chemical shifts (NICS) parameter. The NICS(0) values, calculated at the center of the complexes $C_4B_2H_6-Li_2$, $C_4B_2H_6-Na_2$ and $C_4B_2H_6-Mg$ are found to be -11.55, -4.74 and +4.07. The negative NICS(0) values indicate the aromatic nature of the lithium and sodium complexes, while for the Mg doped complex in which the base ($C_4B_2H_6$) is also distorted from planarity, the positive NICS value indicates that the base ring is not aromatic. We also tried to adsorb two Mg ions on both sides of the ring but the geometry was found to get distorted as shown in Figure 8.2.

We have carried out a systematic study on hydrogen adsorption in these metal doped systems ($C_4B_2H_6-M_2$, $M = Li$ and Na). In all these complexes, the metal atom interaction with the hexagonal ring can be considered as ionic and the charge accumulated on metal site can induce a dipole in the incoming hydrogen molecule and thereby the H_2 molecule gets adsorbed through ion-induced dipole interaction as well as ion-quadrupole interactions. In all these systems, hydrogen is found to be adsorbed in molecular form and $M-H_2$ geometry is T shaped.

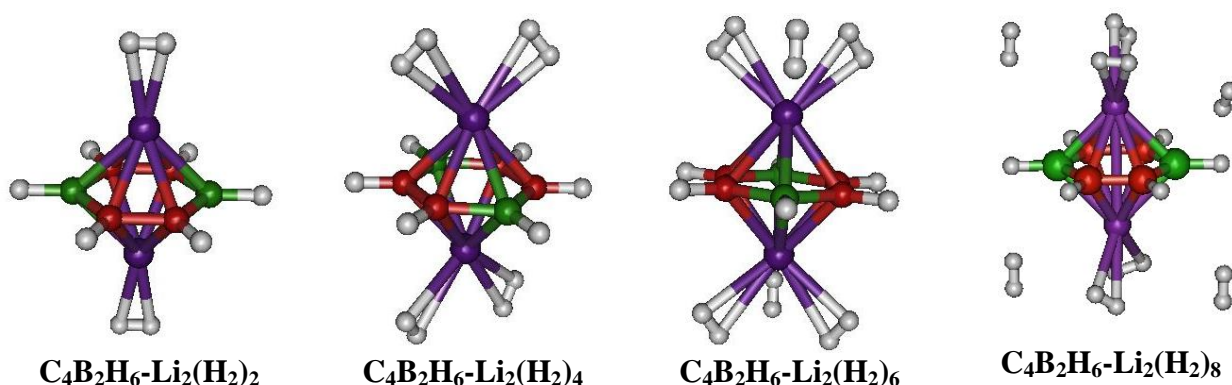


Figure 8.3 Optimized structures of $C_4B_2H_6Li_2(H_2)_{2n}$ ($n=1-4$)

First, we will discuss the hydrogen adsorption in lithium decorated system, resulting into the species $C_4B_2H_6Li_2(H_2)_n$. All the minimum energy structures of $C_4B_2H_6Li_2(H_2)_{2n}$ for $n = 1-4$, optimized at MP2/6-31++(2d, 2p) level of theory, are shown in Fig. 8.3. The first molecular hydrogen on each lithium site is found to bind in a symmetric manner with a binding energy -4.29 kcal/mol. The H-H distance in the adsorbed H_2 molecule is found to be 0.74 Å which is larger than that observed in a free H_2 molecule optimized at the same level (0.736 Å). In the case of $C_4B_2H_6Li_2(H_2)_4$, the interaction energy per molecular hydrogen is found to be -3.06 kcal/mol and the H-H bond distance is found to be 0.74 Å. From the optimized structure of $C_4B_2H_6Li_2(H_2)_6$ given in Figure 8.3, one can see that the third hydrogen molecule is little away from the metal site as compared to the other two H_2 molecules. However, the interaction energy per molecular hydrogen is found to be -2.50 kcal/mole.

Table 8.2: The calculated interaction energy, charge on metal and HOMO-LUMO gap of $C_4B_2H_6M_2(H_2)_n$ (M=Li and Na).

System	Interaction energy ^a per H_2 molecule (kcal/mol)			Charge on metal (a.u)		HOMO-LUMO gap (eV)	
	MP2	HLYP	PW91	MP2	HLYP	MP2	HLYP
$C_4B_2H_6-Li_2(H_2)_2$	-4.287	-3.405	-3.677	0.595	0.635	7.36	8.081
$C_4B_2H_6-Li_2(H_2)_4$	-3.057	-2.290	-2.510	0.453	0.570	7.28	8.00
$C_4B_2H_6-Li_2(H_2)_6$	-2.504	-1.787	-1.914	0.362	0.573	7.28	8.00
$C_4B_2H_6-Na_2(H_2)_2$	-2.197	-2.114	-2.185	0.795	0.819	6.02	6.56
$C_4B_2H_6-Na_2(H_2)_4$	-2.395	-1.993	-1.904	0.736	0.719	6.00	6.64
$C_4B_2H_6-Na_2(H_2)_6$	-2.334	-1.843	-1.942	0.701	0.719	5.99	6.63
$C_4B_2H_6-Na_2(H_2)_8$	-2.335	-1.754	-1.797	0.679	0.667	5.99	6.63
$C_4B_2H_6-Na_2(H_2)_{10}$	-2.176	-1.524	-1.622	0.657	0.445	6.03	6.66
$C_4B_2H_6-Na_2(H_2)_{12}$	-2.147	-1.509	-1.536	0.630	0.603	6.06	6.68

^aThe interaction energy per molecular hydrogen is calculated as

$$1/n[E(C_4B_2H_6M_2(H_2)_n)-E(C_4B_2H_6M_2)-nxE(H_2)]$$

We tried to incorporate the fourth molecular hydrogen also, but as shown in the optimized geometry in Figure 8.3, it is observed that the fourth H_2 does not get adsorbed and instead it goes away from the metal site. In all these hydrogen adsorbed systems, the minimum Li- H_2 distance is found to be around 2.20 Å and the calculated HOMO-LUMO gap is found to be considerably large as shown in Table 8.2 which is an indication of the stability of these complexes. We have also performed the Hessian calculation on all these complexes and no imaginary frequencies were found which again shows that all these structures correspond to the local minima on the potential energy surface.

Now, we discuss the hydrogen adsorption in $C_4B_2H_6Na_2$ and all the optimized geometries of $C_4B_2H_6Na_2(H_2)_{2n}$ at MP2/6-31++(2d, 2p) level of theory for $n = 1-6$ are given in Figure 8.4. The adsorption energy per molecular hydrogen in $C_4B_2H_6Na_2(H_2)_{2n}$ is found to be -2.20, -2.39, -2.33, -2.33, -2.18 and -2.15 kcal/mol for $n = 1, 2, 3, 4, 5$ and 6 respectively and the minimum M- H_2 distances are found to be around 2.5 Å. From the values of these interaction energies, it can be observed that the interaction energy of molecular hydrogen with $C_4B_2H_6Na_2$ is relatively low as compared to that observed in $C_4B_2H_6Li_2$. This difference in the interaction energy can be attributed to the difference in the polarizing power of the two metal ions lithium and sodium. Being small in size, lithium ion can polarize the molecular hydrogen more efficiently as compared to sodium ion and also can bind with hydrogen more effectively. In all these hydrogen adsorbed complexes of $C_4B_2H_6Na_2$, we have also calculated the Hessian and found all the frequencies to be positive. The calculated HOMO-LUMO gaps are given in Table 8.2 and all the complexes are found to have considerably large gaps which provide indication

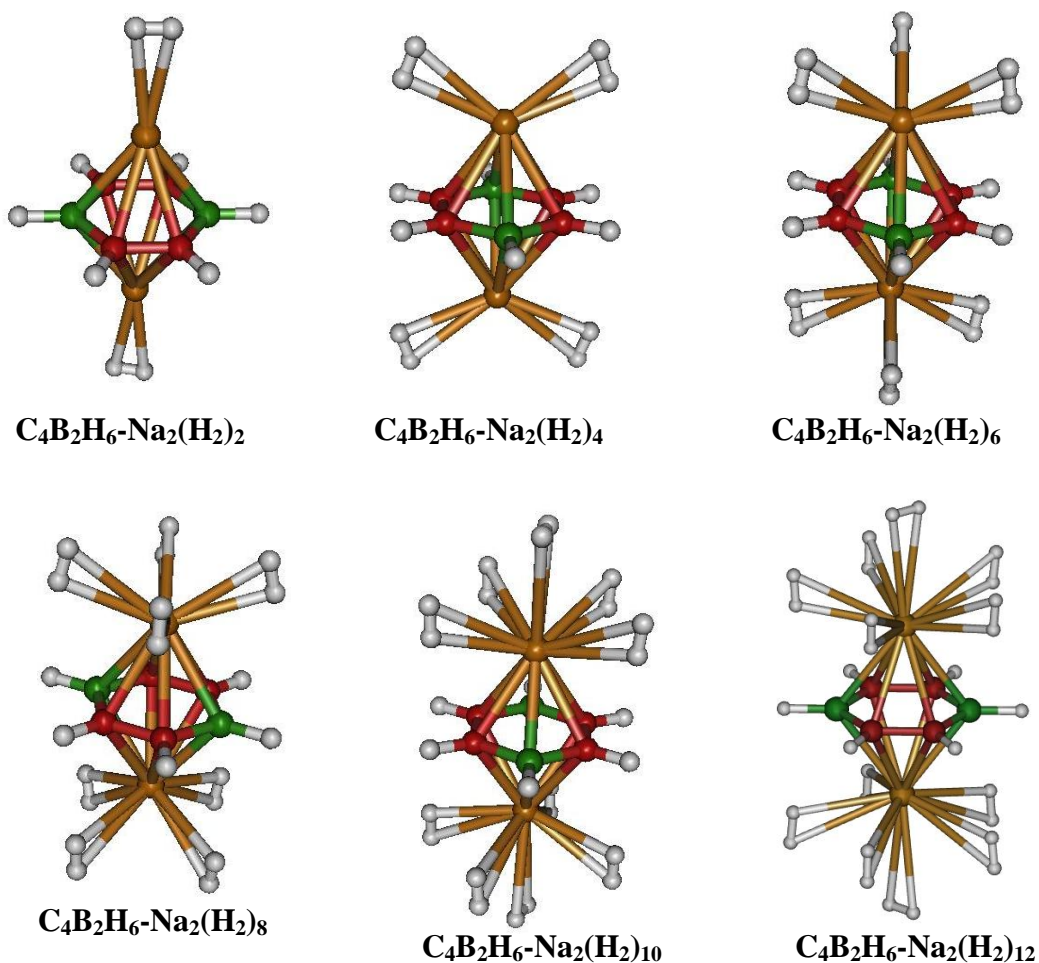


Figure 8.4 Optimized structures of $\text{C}_4\text{B}_2\text{H}_6\text{Na}_2(\text{H}_2)_{2n}$ ($n=1-6$)

of the stability of these hydrogenated complexes. In the case of the lithium doped system ($\text{C}_4\text{B}_2\text{H}_6\text{Li}_2$), where a total of six H_2 molecules are adsorbed, the gravimetric density is 11.6 wt%. In sodium doped system, where a total of twelve H_2 molecules are adsorbed, the corresponding density is 16.4 wt%. Though the gravimetric density is more in sodium doped systems, the adsorption energy is more in the case of lithium doped systems. In addition to the simple boron doped benzene, we have also optimized the boron doped benzene di-carboxylic acid decorated with two lithium ions ($\text{C}_4\text{B}_2\text{H}_4(\text{COOH})_2\text{Li}_2$). We have optimized the geometries

of two different isomers and found that the isomer where the two carboxylic acids are attached to two boron atoms which are in para position is found to be more stable by an energy of 11.3 kcal/mol as compared to other one with carboxylic acids attached to two carbons as shown in the Figure 8.5.

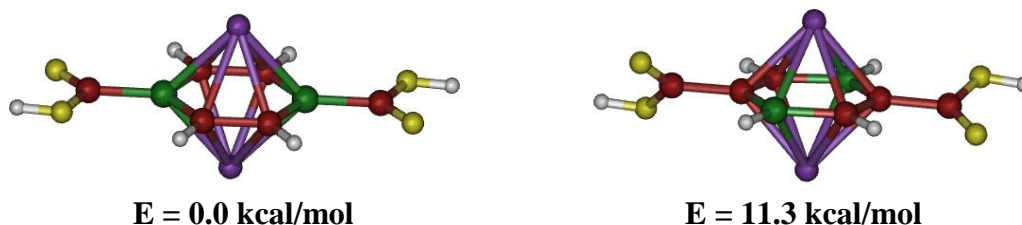


Figure 8.5 Optimized structures of two isomers of $C_4B_2H_6(COOH)_2$

In the present study, we have also extended our idea of doping with boron to three dimensional periodic systems of MOF-5 and its lithium decorated counterpart. For comparison, first we have optimized the structure of MOF-5 and its lithium decorated counterpart using a minimal primitive cell of 106 and 118 atoms respectively using GGA (PW91) based DFT method. The calculated cell parameter of MOF-5 is found to be 25.9 Å which is close to the experimental value of 25.83 Å,⁶²⁻⁶⁷ and the corresponding cell parameter of Li decorated MOF-5 is found to be 26.06 Å which exactly matches with the previous results of Blomqvist et al.⁸⁸ The calculated interaction energy of Li with MOF-5 using PW91 method is found to be around -35.5 kcal/mol per Li atom which is less than the cohesive energy of Li (39 kcal/mol). Although the Li sites are cationic and can adsorb molecular hydrogen, there is a chance for aggregation of Li atoms to form cluster which can diminish the wt% of adsorbed hydrogen. Hence the lithium decorated MOF-5 may not be a proper recyclable hydrogen storage material.

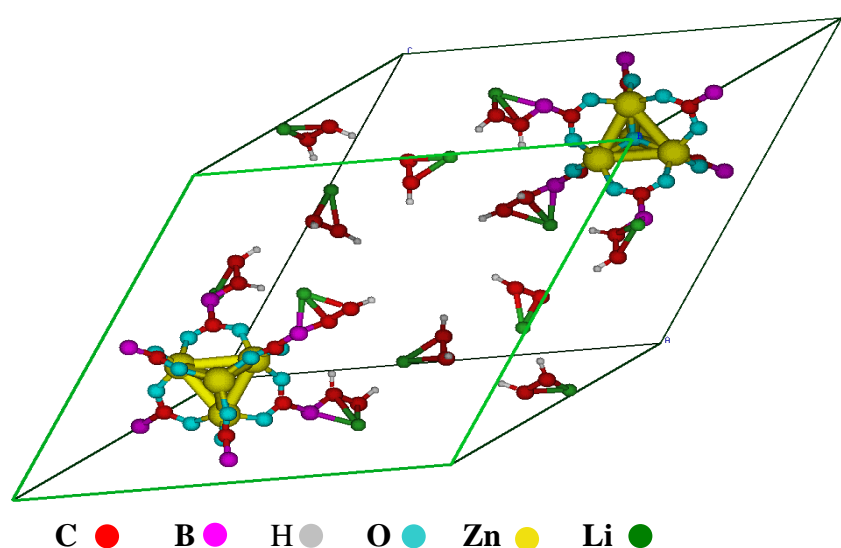


Figure 8.6 Optimized primitive cell structure of lithium decorated boron substituted MOF-5 with the formula unit $\text{Zn}_4\text{O}(\text{C}_4\text{B}_2\text{H}_4\text{Li}_2(\text{COO})_2)_3$

Now, we have optimized the periodic structures of modified MOF-5 (mMOF-5) where the original linking group $\text{C}_6\text{H}_4\text{Li}_2(\text{COO})_2$ is replaced by $\text{C}_4\text{B}_2\text{H}_4\text{Li}_2(\text{COO})_2$. The conventional cell of the optimized structure of lithium decorated boron doped MOF-5 is given in Figure 8.7 which consists of two lithium atoms per linking agent. The cell parameter of this optimized Li decorated modified MOF-5 is found to be 27.13 Å which is little longer than that reported for Li

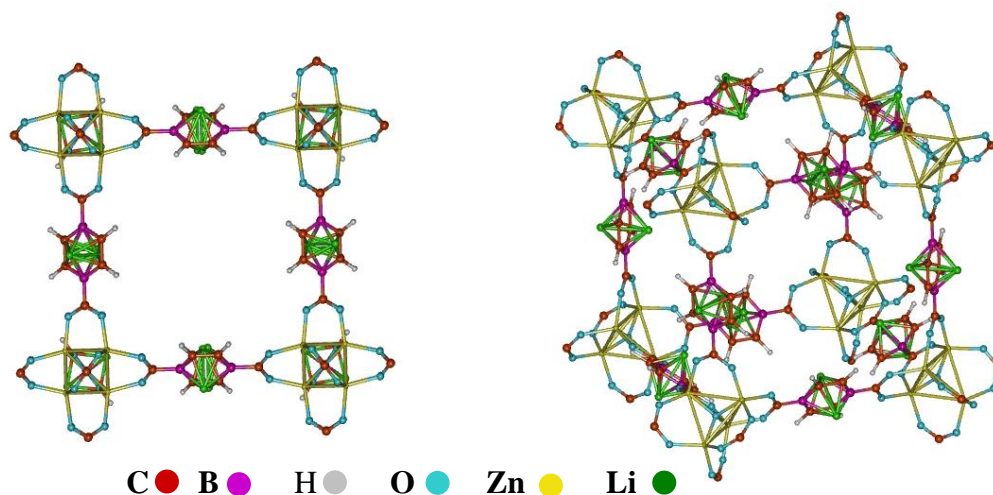


Figure 8.7 conventional cell structure of lithium decorated boron substituted MOF-5. For clarity, some of the peripheral linking groups are omitted.

decorated MOF-5 (26.06 \AA) and mMOF-5 (26.82 \AA).⁸⁸ The interaction energy of lithium with mMOF-5 is calculated to be -85.84 kcal/mol per lithium which is more than the cohesive energy of lithium (39.0 kcal/mol). Similar to the lithium decorated case, we have optimized the periodic structure of sodium decorated mMOF-5 as well and the optimized cell parameter is found to be 27.16 \AA . The calculated interaction energy of sodium with mMOF-5 is found to be -61.37 kcal/mol which is also more than the cohesive energy of sodium (26.0 kcal/mol). The calculated Bader charges show that all these lithium atoms carry a charge of $+0.86$ which demonstrates that there is a charge transfer from Li atoms to the framework.

Molecular hydrogen adsorption in this lithium decorated mMOF-5 has been studied using the same methods mentioned above. For this study, we have considered a similar type of primitive unit cell consisting of 190 atoms with three H_2 molecules per Li site having the formula unit of $\text{Zn}_4\text{O}(\text{C}_4\text{B}_2\text{H}_4\text{Li}_2(\text{H}_2)_6(\text{COO})_2)_3$. The conventional super cell of the optimized geometry using the PW91 method is given in Figure 8.8 and the corresponding cell parameter is found to be 26.88 \AA . The binding energy per molecular hydrogen as calculated through GGA (PW91)

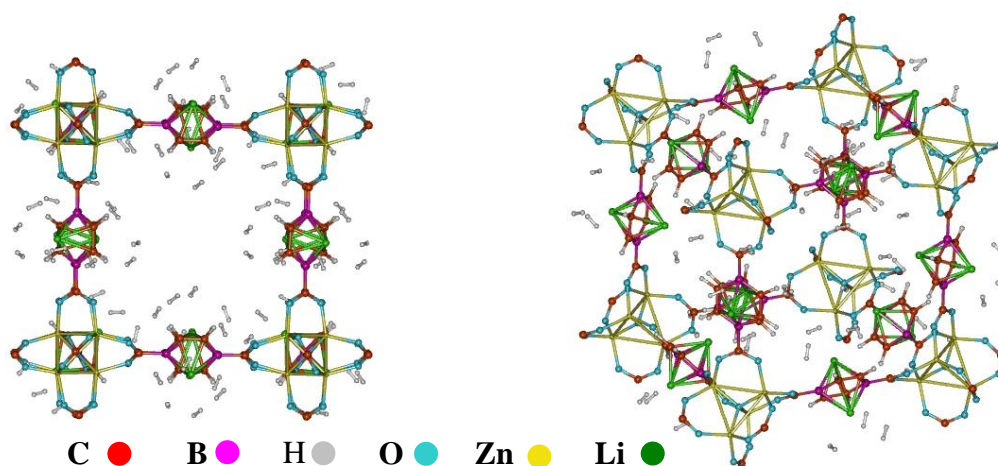


Figure 8.8 Conventional cell structure of hydrogen adsorbed lithium decorated modified MOF-5. For clarity, some of the peripheral linking groups are omitted.

method is found to be around -2.13 kcal/mol. There are 18 hydrogen molecules per formula unit and each primitive cell contains two formula units which correspond to a gravimetric density of around 4.3 wt%, at zero temperature. In the case of sodium decorated mMOF-5, we have studied the hydrogen adsorption at two different concentrations of hydrogenation, viz. one with three H_2 per metal site and other with six H_2 per metal site. With three H_2 per Na, the hydrogen adsorption energy per molecular hydrogen is calculated to be -2.01 kcal/mol. We have optimized the periodic system of the sodium decorated mMOF-5 also with six H_2 per meal site with a primitive cell of 262 atoms and the optimized cell parameter is found to be 27.10 Å. The hydrogen adsorption energy per molecular hydrogen is calculated to be -1.92 kcal/mol and there are 36 molecular hydrogen per formula unit which corresponds to a gravimetric density of around 7.4 wt%

8.3.2. Electronic structure and Hydrogen Adsorption Characteristics of Supercubane based Three-dimensional Porous Carbon.

We have considered different possible three-dimensional carbon allotropes ranging from 16 to 144 carbon atoms per unit cell and all with bcc lattice. In the present study, we have mainly studied the (i) electronic structure and stability and (ii) hydrogen adsorption properties of these carbon allotropes. As a starting member for this study, we considered the bcc C_8 cubane which is also known as supercubane with 16 carbon atoms per unit cell as shown in Figure 8.3.2.1(a). The calculated cell parameter using the PBE method is found to be 4.877 Å corresponding to a density of 2.75 gm/cm³ which is in good agreement with the earlier report.²⁷⁶ The C-C bond lengths of the intra-cubane bonds are found to be 1.586 Å and that of the inter-cubane bonds are found to be 1.476 Å. Similar to the graphyne structure, where each C_6 ring is connected to six C_6 rings through $C\equiv C$ linking groups, we connected each C_8 cube with other

eight such cubes by inserting one $\text{C}\equiv\text{C}$ between each inter-cubane C-C bond of the supercubane as shown in Figure 8.9(b) and this structure can be called as supercubyne. We have also modeled a supercubdiyne similar to graphdiyne with diacetylinic unit as linking groups as shown in Figure 8.9(c). The optimized cell parameters for supercubyne and supercubdiyne with 32 and 48 carbon atoms per unit cell are found to be 7.860 and 10.835 Å and the corresponding densities are calculated to be 1.31 and 0.75 gm/cm^3 respectively.

In the case of next member of the series considered, we have inserted acetylinic units between all the C-C (both inter- and intra-cubane) bonds of the supercubane structure as shown in Figure 8.9(d) and this can be considered as the complete carbomerization of the supercubane. The optimized cell parameter of this structure is found to be 10.026 Å with a density of 0.72 gm/cc . The C-C bond length of the acetylinic unit is found to be 1.21 Å which is

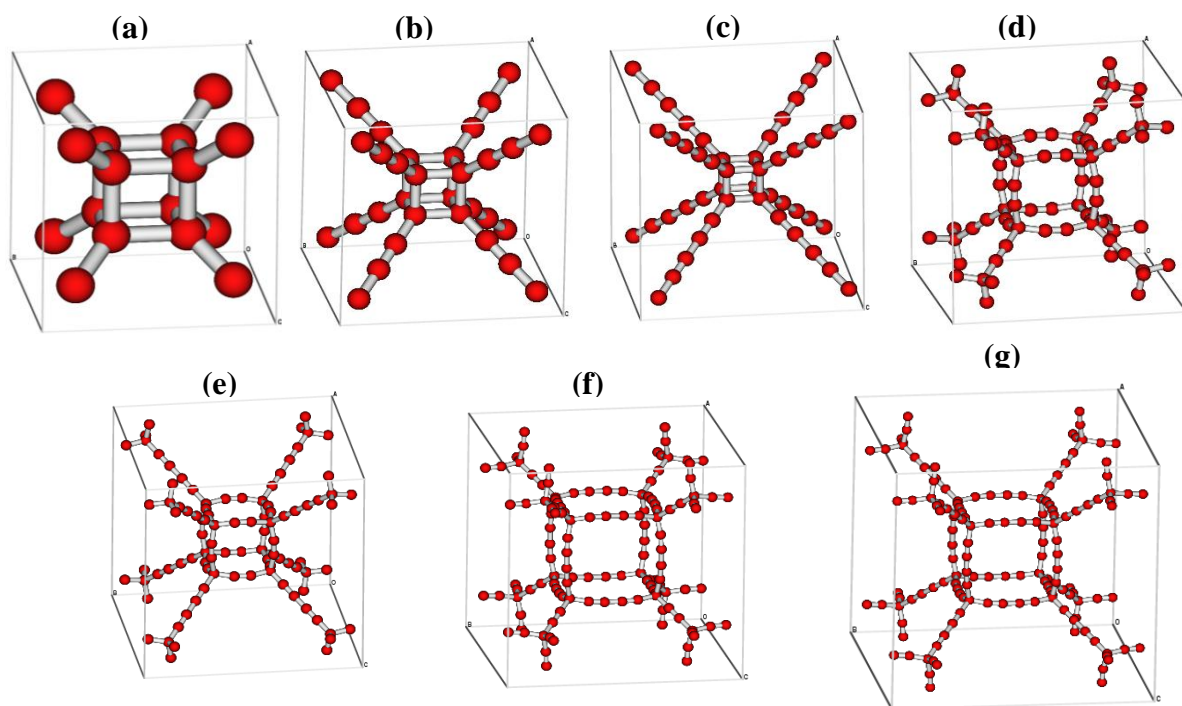


Figure 8.9: Optimized unit cell structures of (a) C_{12} , (b) C_{32} , (c) C_{48} , (d) C_{80} , (e) C_{96} , (f) C_{128} , and (g) C_{144} .

very close to the carbon-carbon triple bond length while the C(sp³)-C(sp) inter- and intra-cubane bond lengths are 1.475 and 1.486 Å respectively. More interestingly, the CCC bond angle at the corner of the cubane is found to expand to 105.93° from 90° in the supercubane. This expansion indicates a relaxation in the strain associated with the supercubane due to the highly compressed 90° angle instead of the sp³ bond angle of 109.5°.

Table 8.3: Calculated formation energies per atom, cell parameters, densities and CCC cubane corner bond angles of the different supercubane based carbon materials.

Number of carbon atoms per unit cell	Formation energy /atom (eV)	Cell parameter (Å)	Density (gm/cm ³)	CCC corner bond angle (Deg)
16	-8.46	4.877	2.75	90
32	-8.28	7.860	1.31	90
48	-8.25	10.835	0.75	90
80	-8.03	13.026	0.72	105.93
96	-8.05	16.004	0.47	105.95
128	-8.09	18.145	0.43	107.26
144	-8.09	21.129	0.30	107.26

The next structure considered consists of 96 carbon atoms per unit cell where diacetylinic units are inserted between the inter cubane C-C bonds as shown in Figure 8.9(e). The optimized cell parameter is found to be 16.004 Å and the corresponding density is calculated to be 0.47 gm/cm³. In the next structure studied, diacetylinic unit is inserted into the intra-cuabne C-C bonds resulting into a C₅₆ cubane unit and the acetylinic unit is inserted into the inter-cubane C-C bonds. The optimized cell parameter of this structure with 128 carbon atoms per unit cell is found to be 18.145 Å and the calculated density is 0.43 gm/cm³. The CCC cubane corner bond angle is found to get expanded further to 107.3° leading to the strain relaxation. In the case of the final structure considered, both inter- and intra-cubane C-C bonds are sandwiched by

diacetylinic units as shown in Figure 8.9(f) with a total of 144 carbon atoms per unit cell. The optimized cell parameter is found to be 21.129 Å and its density is calculated to be 0.3 gm/cm³.

The electronic band structure calculations are carried out for all the bcc structures considered along the symmetric k-path of the first Brillouin zone,²⁸⁰ P- Γ -H using PBE as well as B3LYP functionals and the corresponding results are reported in Table 8.4. The calculated band structures along with the density of states (DOS) plotted for the first three systems with 16, 32 and 48 carbon atoms per unit cell are shown in Figure 8.10. In the case of C₁₆, the indirect band gap calculated through the PBE functional is found to be 3.01 eV which is considerably less as compared to the earlier reported value.²⁷⁶ However, the band gap calculated for the same structure using the hybrid functional, B3LYP is found to be 5.26 eV which is in good agreement with the earlier reported band gap of 5.5 eV.²⁷⁶

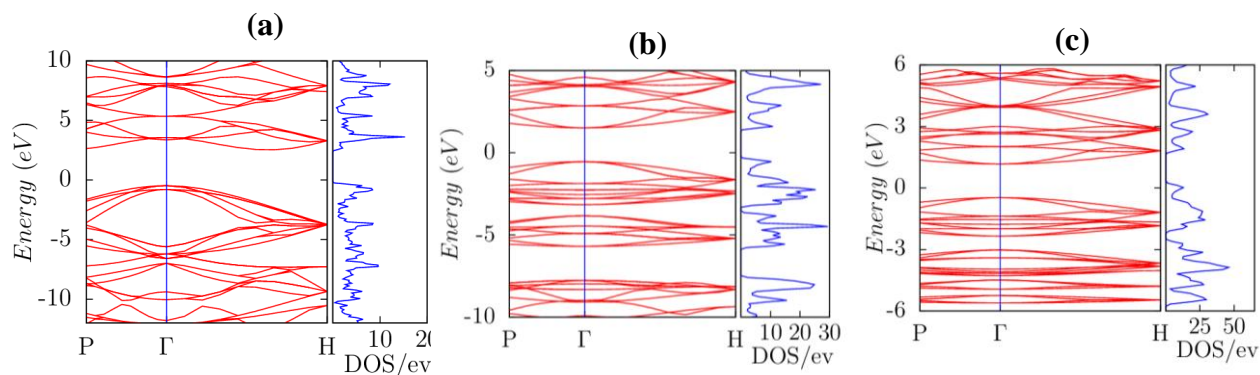


Figure 8.10: Calculated band structure along with the density of states (DOS) through PBE functional (a) C₁₆, (b) C₃₂ and (c) C₄₈ respectively.

The structure supercubyne and supercubdiyne are found to have direct band gaps of 3.56 eV and 2.95 eV respectively along the Gamma point as calculated through B3LYP functional. This shows that the insertion of acetylinic groups in-between the inter-cubane C-C bonds decreases the band gap of the supercubane. Completely carbomerized supercubane is again found to be an insulator with a direct band gap of 5.41 eV along the gamma point as calculated

through B3LYP method. On introduction of one more acetylinic unit in-between the inter-cubane C-C bonds, the band gap is found to decrease slightly, i.e. from 5.41 eV to 5.30 eV. In case of the system with diacetylinic unit between the intra-cubane C-C bonds and acetylinic unit between the inter-cubane C-C units, the band gap is 4.35 eV whereas the structure with diacetylinic units inserted between all C-C bonds of cubane shows a band gap of 4.44 eV.

Table 8.4: Energy of valence band maxima (VBM), conduction band minima (CBM) and the band gap values calculated using PBE and B3LYP functionals for all the modeled 3D-carbon materials. All energy values are reported in eV.

Number of C	Energy of VBM		Energy of CBM		Band gap	
	PBE	B3LYP	PBE	B3LYP	PBE	B3LYP
16	-2.54	-3.03	1.11	2.23	3.65	5.26
32	-3.70	-4.19	-1.51	-0.63	2.19	3.56
48	-3.85	-4.30	-2.12	-1.35	1.73	2.95
80	-5.01	-5.73	-1.27	-0.32	3.74	5.41
96	-4.92	-5.58	-1.16	-0.28	3.76	5.30
128	-4.60	-5.18	-1.64	-0.83	2.96	4.35
144	-4.60	-5.18	-1.56	-0.74	3.04	4.44

It is required to check the stability of the materials modeled here, by calculating the phonon dispersion because of the high porosity and low density associated with these materials. Except for the C₁₄₄ unit cell, we calculated the phonon frequencies for all the systems using the density functional perturbation theory as implemented in VASP. The calculated phonon dispersion plots along the high symmetry *k*-path of the first Brillouin zone are shown in Figure 8.11. These phonon dispersion plots indicate the stability of the expanded supercubane structures.

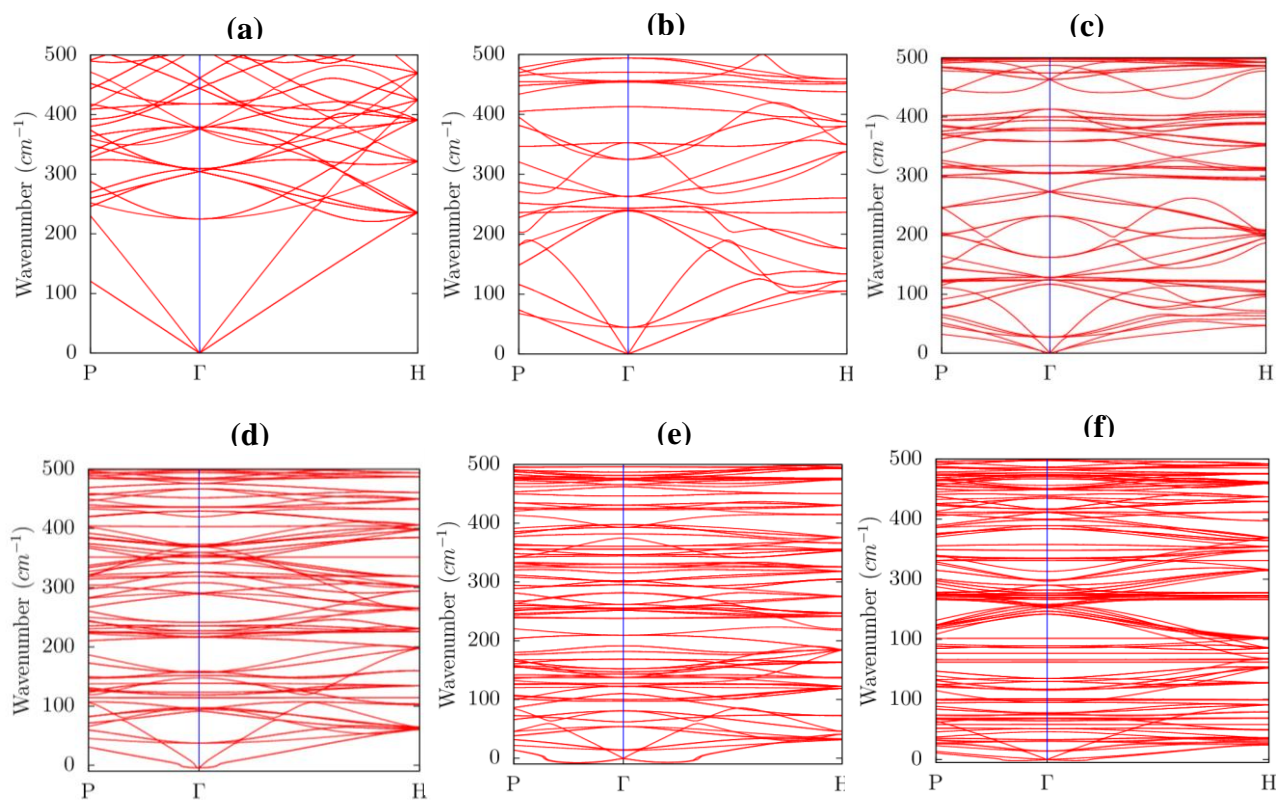


Figure 8.11 Phonon dispersion plot along the high symmetry k -path of the first Brillouin zone of the unit cell (a) C_{16} (b) C_{32} , (c) C_{48} , (d) C_{80} , (e) C_{96} and (f) C_{128} .

We have also calculated the formation energy per carbon atom to verify the thermodynamic stability of the proposed systems and results are reported in Table 8.3. Though the calculated formation energies per carbon are less as compared to that of graphene (-9.26 eV), diamond (-9.10 eV), and graphite (-9.25 eV), these are comparable to the formation energies of the recently explored carbon allotropes, viz. graphdiyne (-8.49 eV), planar T graphene (-8.78 eV), buckled T graphene²⁸¹ (-8.41 eV) and even higher than that of T carbon²⁸² (-7.95). These formation energies further indicate the possible thermodynamic stability of the proposed porous carbon allotropes. In addition, we have also calculated the variation of free energy with temperature and compared it with the previously explored two-dimensional carbon systems, viz. graphene, graphyne and graphdiyne in Figure 8.12. From the free energy plot one can observe that though the thermodynamic stability of these systems is less than that of graphene, at least for

the less porous systems like C_{16} , C_{32} and C_{48} , it is comparable with that of the recently synthesized carbon allotrope graphdiyne.

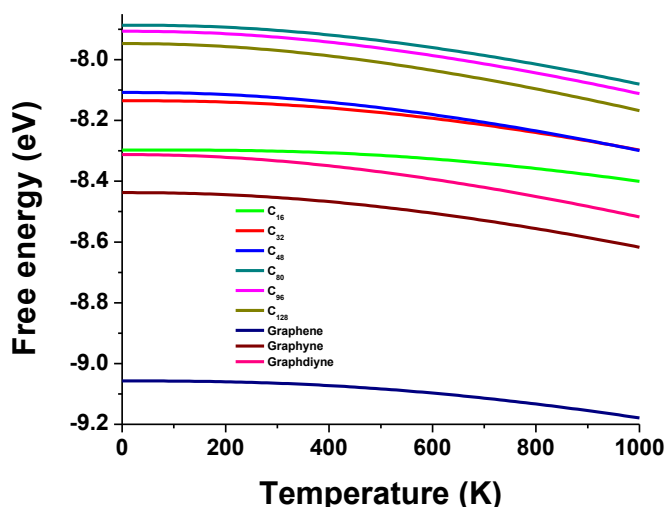


Figure 8.12 Variation of free energy of different carbon allotropes as a function of temperature.

These supercubane based materials modelled here can be expected to adsorb molecular hydrogen because of their highly porous nature and the presence of more electronegative *sp* carbon atoms. To explore the hydrogen storage properties, we have studied the molecular hydrogen adsorption in two of the seven model systems. In the first case, we have considered C_{32} unit cell and four molecules of hydrogen are allowed to interact near the acetylinic groups as shown in Figure 8.13(a) and the corresponding gravimetric density based on adsorbed hydrogen is calculated to be 2.04 wt%. The hydrogen adsorption energy per H_2 molecule, as calculated through the dispersion corrected PBE method is found to be -2.5 kcal/mol. In the same C_{32} unit cell, we have then allowed six H_2 molecules to be adsorbed as shown in Figure 8.13(b) and the calculated binding energy is found to be just -1.4 kcal/mol per H_2 which shows a large drop in the adsorption energy at higher hydrogen loading. The next member studied for hydrogen adsorption is the largest one considered, with 144 carbon atoms per unit cell. In this

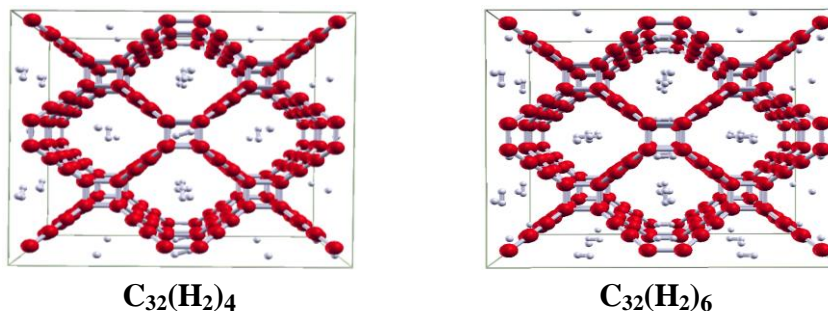


Figure 8.13 Optimized 2 x 2 x 2 super cell structures of hydrogenated C_{32} with four and six molecular hydrogens per unit cell.

case, initially we have studied the adsorption of eighteen H_2 molecules per unit cell as shown in Figure 8.14(a) with a gravimetric density of 2.1 wt% and the interaction energy per H_2 is calculated to be just -0.9 kcal/mol. The number of hydrogen molecules is then increased from 18 to 24 to check the hydrogen adsorption capacity of the material and the optimized structure is shown in Figure 8.14(b). The calculated hydrogen adsorption energy is found to be -0.7 kcal/mol with a gravimetric density of 2.7 wt%. These results indicate that the materials with medium porosity can hold hydrogen more effectively as compared to the highly porous materials like C_{144} systems

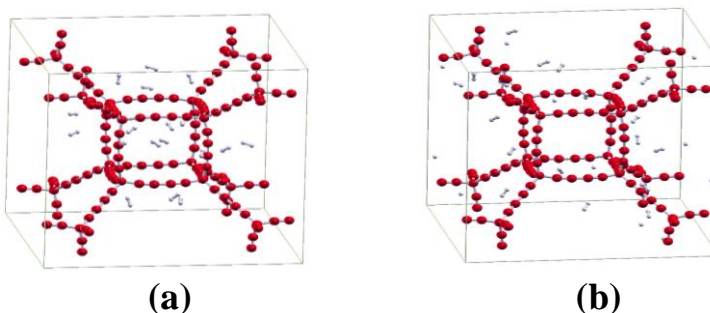


Figure 8.14 Optimized unit cell structures of C_{144} with (a) 18 and (b) 24 hydrogen molecules per unit cell.

considered here. However, as these results are based on one possible structure considered and the system can have complicated potential energy surface, there can be another minima which can give still higher adsorption energies. Because of the high surface areas and availability of

acetylinic groups, it may be further possible to modify the systems, for example through metal doping which is shown to be effective in improving the hydrogen adsorption in many of the carbon materials studied earlier.

8.4. Conclusions

In the present chapter, we have explored the possibility of hydrogen adsorption in light metal decorated boron substituted MOF-5. From our calculated results, it is observed that the binding energy of metal with MOF-5 can be improved by disturbing the aromatic nature of the linker group through the substitution of its two carbon atoms with two boron atoms. Each lithium site of the periodic system is found to adsorb three molecular hydrogens which correspond to a gravimetric density of around 4.3 wt% and in the case of Na decorated mMOF-5, as each Na can adsorb six molecular hydrogen, the corresponding gravimetric density is found to be 7.4 wt%. We have also modeled different three-dimensional supercubane based porous carbon materials with varying number of carbon atoms starting from C_8 cubane unit to an expanded C_{56} cubic unit and also with different inter-cubane C-C linking units. The expanded supercubane, C_{32} is found to adsorb hydrogen with a gravimetric density of 2 wt% and adsorption energy of -2.5 kcal/mol. However, at higher hydrogen densities and in the case of highly porous systems like C_{144} , the hydrogen adsorption energies are very low indicating that porous materials with medium size pores are preferred for better hydrogen storage.

CHAPTER 9

First Principles Modelling of New Catalyst for Oxygen Reduction Reaction

9.1. Introduction:

As already discussed earlier, slow kinetics of the oxygen reduction reaction (ORR) at the cathode is found to be one of the limiting factors for better performance of the fuel cells and the conventional platinum based catalysts make the fuel cell very expensive. Hence, there is a need to find an alternate non-platinum based catalyst for large scale commercialization of fuel cells.⁹⁸⁻¹⁰⁰

There are a large number of non-precious metal based catalysts viz. transition metals (Fe, Co, etc.), metal oxides, metal carbides, as well as metal free catalysts like carbon materials, boron and nitrogen doped carbon nanomaterials, graphitic carbon nitride, etc.²⁸³⁻²⁸⁶ One of the metal free catalysts which is extensively studied is the graphitic carbon nitride (g-C₃N₄). However, the catalytic activity of simple g-C₃N₄ is found to be poor, which is attributed to the poor electrical conductivity of g-C₃N₄.²⁸⁷ To improve the activity, different kinds of carbon materials have been mixed with g-C₃N₄ and it has been shown that as compared to pristine g-C₃N₄, the carbon composites are more active towards ORR.²⁸⁷⁻²⁸⁹ Zheng et al.²⁸⁹ have shown that g-C₃N₄@carbon can catalyze the ORR reaction with better activity which is explained by considering the enhanced electron transfer efficiency. Transition metal (TM) complexes of macrocyclic systems like phthalocyanines and porphyrines, especially the N₄-TM complexes of cobalt (Co) and iron (Fe) are another class of materials extensively studied for ORR catalysis.²⁸⁹⁻²⁹² It has been shown that the transition metal complexes of porphyrine-like carbon nanotubes and graphitic materials can exhibit excellent activity towards ORR.²⁹³⁻²⁹⁴

In the present study, we have carried out a detailed investigation on the ORR catalytic activity of transition metal decorated graphyne. In a recent study, Kong et al.²⁹⁵ have shown that, on boron doping, graphyne can be made active for ORR whereas the pristine graphyne is inactive. He et al.²⁹⁶ studied the adsorption of different 3d-transition metals on graphyne and

showed that TM doping not only modulates the electronic structure, but can also incorporate excellent magnetic properties. Earlier studies have shown that the ferromagnetic nature present in the platinum group metal electro catalysts improves the ORR catalytic activity.²⁹⁷ Inspired from these earlier studies, we have doped graphyne with three different TMs, viz. Fe, Co and Ni to study the adsorption of possible ORR intermediates on these metal decorated graphyne systems.

We have also explored another important material, silicene²⁹⁸⁻³⁰⁰, the silicon counterpart of the well known graphene as a metal free catalyst for ORR. The possible existence of silicene with puckered atomic arrangement in honeycomb fashion had been proposed some time back and its synthesis has also been reported recently.³⁰¹⁻³⁰⁴ After the synthesis of silicene on a substrate like Ag (111) surface, the number of studies on this interesting material has increased drastically and it is shown to have applications in different fields of science and technology.³⁰⁵⁻³⁰⁶ The presence of small puckering in the silicene indicates that it can be more reactive as compared to the graphene and therefore we are interested in studying the ORR catalytic activity of free standing silicene single layer as well as the double layers. Recently, Padova et al.³⁰⁷ investigated the room temperature oxidation of silicene nanoribbons through photo emission spectroscopy and they have shown that the oxidation starts at very high oxygen exposures indicating the stability of silicene towards oxidation. Later, Molle et al.³⁰⁸ have also shown that silicene is stable upon exposure up to 1000 L of ultrapure O₂, but it undergoes progressive oxidation in air and they have demonstrated different ways of encapsulating it to hinder the oxidation. In view of this, we are also interested to study the ORR mechanism on both single and bilayers and find the differences.

9.2. Computational details

All the electronic structure calculations have been carried out through the spin-polarized periodic DFT as implemented in the VASP.¹³¹⁻¹³² PAW¹²⁹⁻¹³⁰ based potentials were used with a plane-wave basis cutoff energy of 550 eV. GGA of PBE¹⁰³ has been used to treat the exchange-correlation energy density functional, $E_{xc}[\rho]$. Throughout the calculations, an energy cutoff of 1×10^{-6} eV is set as the convergence criteria for the electronic self-consistent field iterations. Geometry optimizations have been carried out at constant volume until the Hellmann–Feynman force component on each atom is less than $0.01 \text{ eV } \text{\AA}^{-1}$. The Brillouin zone has been sampled using the automatically generated Gamma centered $9 \times 9 \times 1$ Monkhorst–Pack set of k points.¹³³ The atomic charges have been calculated through the Bader¹⁹² charge density analysis. The initial geometries and all reported structures have been obtained using the graphic software MOLDEN.¹³⁵

9.3. Results and Discussion.

9.3.1 Transition Metal Decorated Graphyne: An Efficient Catalyst for Oxygen Reduction Reaction

Before studying the adsorption of TMs on graphyne, we have optimized the graphyne structure with a unit cell of 12 carbon atoms. To study the adsorption of TMs on this structure, we have considered different possible sites, like above the C_6 ring, above the C-C bond, above the C atom and above the cavity. Most preferred site for metal binding is found to be above the cavity as shown in Figure 9.1 where the metal can bind with six sp carbon atoms. We have considered three TMs viz. Fe, Co and Ni for adsorption and the optimized geometries are given in Figure 1 with the corresponding results reported in Table 9.1. In TM decorated graphyne systems, the cell parameters are found to increase as compared to pristine graphyne as reported in Table 1 and the variation is maximum in Fe-graphyne system. The adsorption energy per metal atom of Fe is calculated to be -4.52 eV whereas it is -5.26 eV in Co and Ni decorated

systems. In all the systems, the metal binding energies are found to be higher than the cohesive energies of the corresponding metals. The calculated magnetic moments show that the Fe and Co decorated systems are magnetic in nature whereas the Ni-graphyne system is diamagnetic in nature, which is in consistency with the earlier report.²³ In the case of Fe-graphyne system, the metal atom is found to be slightly above (~ 0.15 Å) the carbon plane and in cases of Co and Ni decorated systems, the metal atoms are almost in the plane of carbon atoms.

Table 9.1: Graphyne-TM binding energy, O₂ adsorption energy, metal-carbon distance, metal-oxygen distance and O-O bond length as calculated through the PBE method.

System	Cell parameter (Å)	ΔE_M (eV)	ΔE_{O_2} (eV)	L_{M-C} (Å)	L_{M-O} (Å)	L_{O-O} (Å)
C ₁₂ -Fe	6.981	-4.52	-0.91	1.963	1.744	1.286
C ₁₂ -Co	6.963	-5.26	-0.58	1.947	1.858	1.278
C ₁₂ -Ni	6.950	-5.26	-0.01	1.956	2.824	1.242

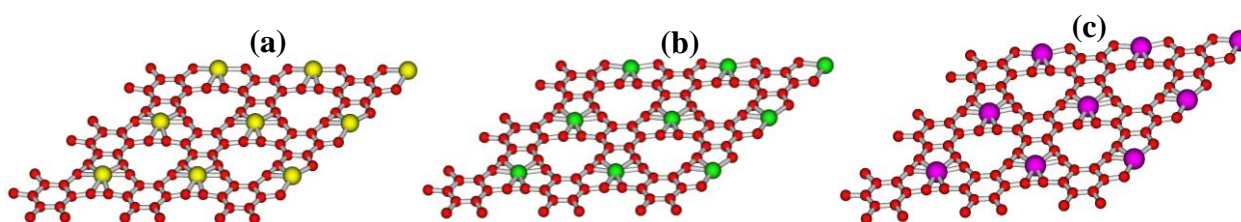


Figure 9.1. Optimized geometries of 3 x 3 x 1 super cell structures of (a) GY-Fe (b) GY-Co and (c) GY-Ni

3.2 Adsorption of molecular oxygen on graphyne-TM complex

One of the rate limiting steps of ORR observed in most of the catalysts is the adsorption of O₂ molecule on the catalyst surface. Here, we have studied the adsorption of O₂ on all three metal decorated graphyne systems. We have considered different possible sites for O₂ adsorption and found that adsorption above the metal site is the most preferred site as shown in Figure 9.2. In the case of Fe decorated system, the O₂ adsorption energy is found to be -0.91 eV and the O-O bond distance is found to be stretched to 1.286 Å from the value 1.233 Å in

free O_2 . The corresponding binding energies in Co and Ni decorated systems are found to be -0.58 eV and -0.01 eV with the O-O distance of 1.278 and 1.242 Å respectively. The calculated atomic charges through Bader charge density analysis show that there is a charge transfer from the GY-TM system to the adsorbed oxygen which is relatively high (0.4) in Fe systems as compared to the Co system (0.35). This charge density analysis

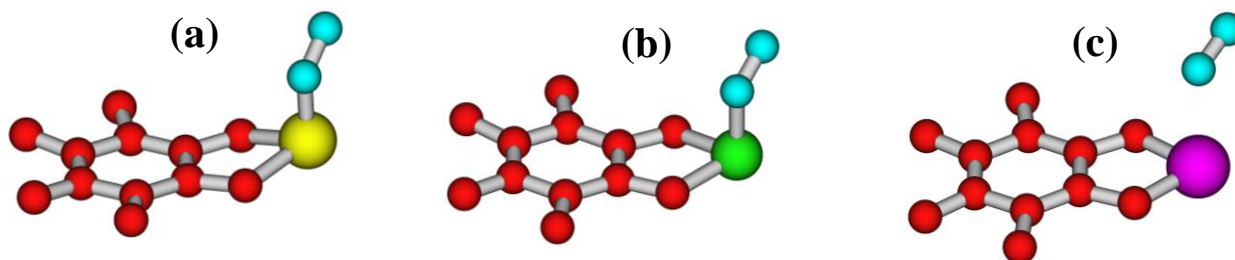


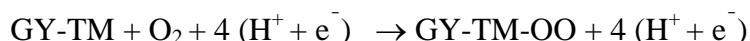
Figure 9.2 Optimized unit cell structures of oxygen adsorbed on (a) GY-Fe (b) GY-Co and (c) GY-Ni

shows that electron transfer is taking place from metal d orbital to the anti-bonding oxygen orbitals. From the calculated magnetic moments on oxygen it is found that in the case of O_2 adsorbed on Ni-graphyne, the O_2 is having the same magnetic moment as that of the free molecule whereas for Co and Fe decorated systems, there is a drop in magnetic moment on oxygen. The observed order of reactivity $Fe > Co > Ni$ is the same as that of their magnetic moments or available unpaired d -electron present in the system. These results show that graphyne-Ni system is not suitable for ORR catalyst and Fe-graphyne is better as compared to Co-graphyne system.

3.3 Oxygen reduction path on TM-graphyne in acid medium

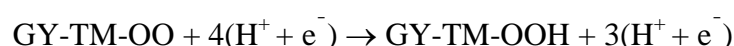
A systematic study of the possible ORR paths is carried out on both Fe and Co decorated graphyne system. The Ni-graphyne system is omitted as the oxygen adsorption energy is very less in this case. As discussed in the previous section the O-O elongation in Fe

system is high as compared to the Co system and the stretching is comparable to that observed in TM-N_x (X= 2 or 4) chelates observed earlier. This reaction can be written as



and the calculated free energy changes (ΔG_1) are found to be -0.92 eV and -0.65 eV for Fe and Co decorated systems respectively.

In the next reaction step, the adsorbed oxygen accepts hydrogen and forms OOH adsorbed on the metal site as shown below.



The associated free energy change (ΔG_2) is found to be -0.53 eV and -0.25 eV for Fe and Co decorated systems respectively. In these optimized structures, the O-O bond lengths are found to be 1.449 Å and 1.425 Å in Fe and Co decorated systems respectively. The observed TM-O

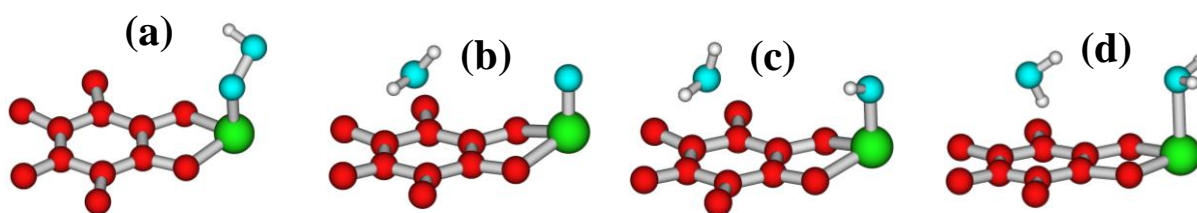
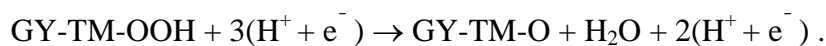


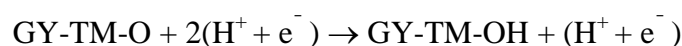
Figure 9.3. Optimized unit cell structures of (a) GY-Co-OOH (b) GY-Co-O-OH₂ (c) GY-Co-OH-OH₂ and (d) GY-Co-OH₂-OH₂

distances in Fe and Co decorated systems are found to be 1.812 Å and 1.859 Å respectively. Once the OOH species is formed, the adsorption of next hydrogen is possible on two oxygen sites. From the energies of the optimized structures, we have found that in both Fe and Co systems, the most favourable oxygen site is the one which is already bound to hydrogen and not the oxygen bonded to metal. This shows that in both the systems considered here, the ORR process proceeds through a more efficient four electron process and not through a two electron process where hydrogen peroxide intermediate is formed. This step can be represented as

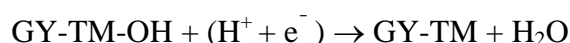


The free energy change (ΔG_3) for this reaction is calculated to be -2.24 eV and -1.95 eV on Fe and Co decorated systems respectively. The optimized geometry for this step on Co decorated system is given in Figure 9.3. After adsorption of two hydrogen atoms on oxygen site the O-O bond distances are found to be 2.829 Å and 2.836 Å on Fe and Co decorated systems respectively. This bond lengths show that in both the cases, the O-O bond is completely cleaved and one water molecule is generated. The TM-O bond distances are found to be 1.636 Å (Fe-O) and 1.671 Å (Co-O).

The adsorbed oxygen atom is found to react with another hydrogen to form OH adsorbed on the TM site as



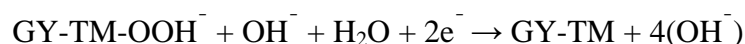
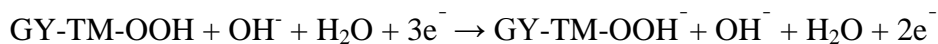
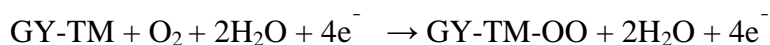
and the free energy change (ΔG_4) for this step is found to be -0.78 eV and -0.99 eV on Fe and Co decorated systems respectively. The TM-O bond lengths are found to increase from the same in the previous intermediate and are found to be 1.814 Å (Fe-O) and 1.846 Å (Co-O). In the final step, the adsorbed OH species picks up one hydrogen and forms H₂O adsorbed as shown in Figure 9.3 which has to get desorbed ultimately and this can be shown as



For this reaction, the free energy changes (ΔG_5) are calculated to be -0.44 eV and -1.08 eV on Fe and Co systems respectively. The TM-O distance in H₂O adsorbed on GY-TM system are found to be 2.239 Å (Fe-O) and 2.334 Å (Co-O) which are considerably higher than that observed in the previous intermediate. The free energies of all the five intermediate steps discussed above are given in Table 9.2 for both Fe and Co systems.

3.4 Oxygen reduction path on TM-graphyne in alkaline medium

In alkaline medium, the proposed ORR mechanism can be given as



and the corresponding free energy changes for these four reaction steps can be assigned as ΔG_1 to ΔG_4 .

The intermediate OOH^- , the peroxide ion adsorbed on both Fe and Co decorated systems are shown in Fig-6. From the optimized geometry, it is found that in the case of GY-Fe, the O-O bond distance in the adsorbed OOH^- ion is elongated to 1.946 Å from 1.449 Å in OOH adsorbed. This O-O bond distance shows that the peroxide formation is not

Table 9.2: Calculated free energy changes (in eV) for different intermediate steps of ORR on GY-Fe and GY-Co in both acid and alkaline medium.

	In acid medium		In alkaline medium	
	GY-Fe	GY-Co	GY-Fe	GY-Co
ΔG_1 (eV)	-0.92	-0.65	-0.92	-0.65
ΔG_2 (eV)	-0.53	-0.25	+0.24	+0.51
ΔG_3 (eV)	-2.24	-1.95	-1.96	-1.68
ΔG_4 (eV)	-0.78	-0.99	+0.83	+0.01
ΔG_5 (eV)	-0.44	-1.08		

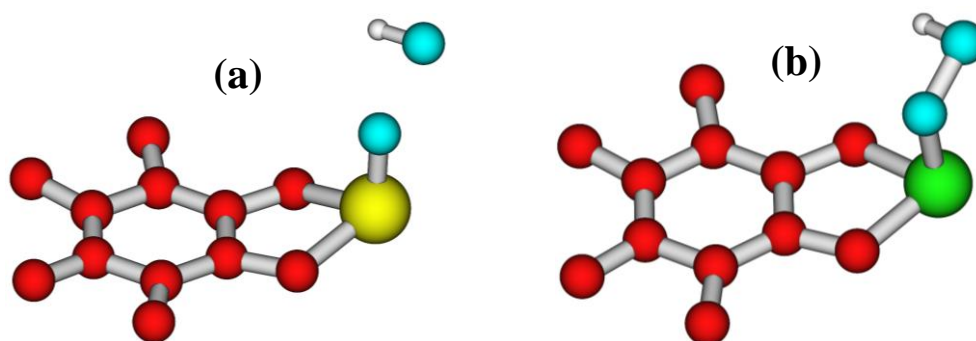


Figure 9.4 Optimized unit cell structures of (a) GY-Fe- OOH^- and (b) GY-Co- OOH^-

energetically favourable and the O-O bond is almost dissociated indicating that the ORR is proceeding through a more efficient four electron reduction. In the case of the GY-Co system, the corresponding O-O bond distance in the adsorbed OOH^- ion is calculated to be 1.459 Å which is very close to the O-O bond distance in hydrogen peroxide. This result shows that the ORR on GY-Co proceeds through two electron mechanism by the formation of hydrogen peroxide. Free energies for all the four proposed intermediate steps for both the systems are reported in Table 9.2. From the results discussed above, one can understand that the GY-Fe system is more efficient catalyst for ORR as compared to GY-Co in both acid and alkaline mediums.

9.3.2 Silicene: a metal-free catalyst for ORR

In this study, we have mainly studied the electronic structure of single and bilayer silicene and their electro catalytic activity towards the ORR. We have optimized the basic hexagonal unit cell of silicene containing two silicon atoms whose $3 \times 3 \times 1$ supercell is shown in Figure 9.7(a). The optimized cell parameter is found to be 3.868 Å and the Si-Si bond length is calculated to be 2.278 Å. The optimized structure of silicene is found to have a puckered structure with a puckering constant (distortion along z-direction) of 0.45 Å and the puckering angle is found to be 37.81° . The calculated electronic band

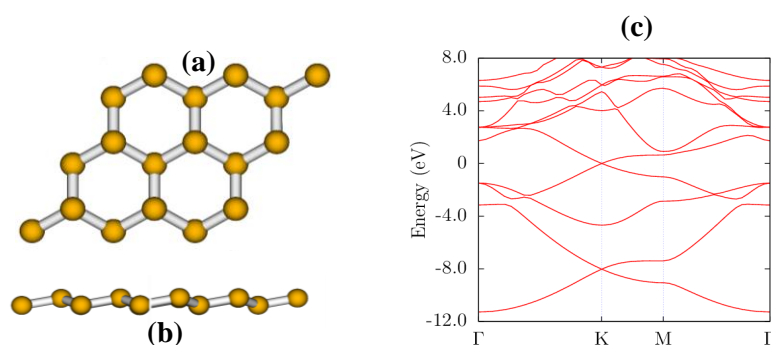


Figure 9.5 Optimized geometries of the $3 \times 3 \times 1$ super cell in (a) top view and (b) side view along with the band dispersion plot of the silicene

structure as obtained through the PBE method is shown in Fig 9.7(c), which shows a zero band gap along the k -point 'K' similar to graphene. The buckling nature present in silicene has been earlier explained by Jose et al. through pseudo-Jahn-Teller effect due to the strong coupling between the unoccupied and occupied molecular orbitals and also it is attributed to the weak interaction between the π orbitals because of the large Si-Si distance. To model the bilayer silicene, we have considered two different modes of stacking, viz. AA and AB modes. The optimized structures of both the conformations are shown in Figure 9.8. From the energy values calculated through PBE method, the AA mode is found to be energetically more favourable as compared to the AB mode. Interestingly, the AA double layer contains two perfectly planar silicene sheets stacked one above the other with an inter-planar distance is of 2.412 Å showing a strong bonding, which is in accordance with the earlier report. The in plane Si-Si bond length of double layer is found to get increased to 2.386 Å from 2.278 Å in a single layer. In the case of AB conformer, the puckering angle is found to increase to 53.06° from 37.81° in single layer with the inter- and intra-planar Si-Si bond distances of 2.524 Å and 2.322 Å respectively. As the system changes from non-planar buckled structure to a perfectly planar, as one goes from single layer to double layer, the two cases are expected to show different reactivity.

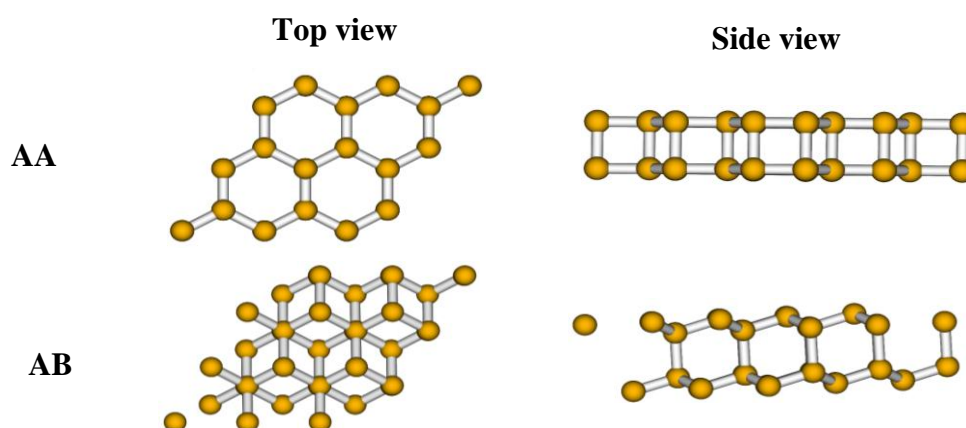


Figure 9.6: Optimized super cell structures of silicene double layer in AA and AB stacking mode.

O₂ adsorption

We have considered different possible sites for O₂ adsorption on silicene viz. above a Si atom and perpendicular to the plane, above the center of the Si₆ ring, above the Si-Si bond and perpendicular to plane, above the Si-Si bond and parallel to the plane. Among all these sites, O₂ adsorption on Si-Si bond and parallel to the plane is found to be energetically more favourable. The optimized minimum energy structure of O₂ adsorbed on silicene for single layer and bilayer, are shown in Figure 9.9. The O-O distance in O₂ adsorbed on single and bilayer silicene are found to be 1.513 Å and 1.511 Å respectively which is considerably elongated from 1.233 Å in free O₂. The Si-O bond distance in single and bilayer cases are found to be 1.727 Å and 1.742 Å respectively. The corresponding binding energy of oxygen on silicene single and double layers, as calculated through the PBE method is found to be -1.82 eV and -2.68 eV respectively. As shown in Figure 9.9, upon adsorption of O₂ on single layer silicene, one of the Si atoms is found to move down and in the case of double layer, two of the Si atoms to which the oxygen atoms are bonded are lifted up and the two corresponding Si atoms in the lower layer are pressed down.

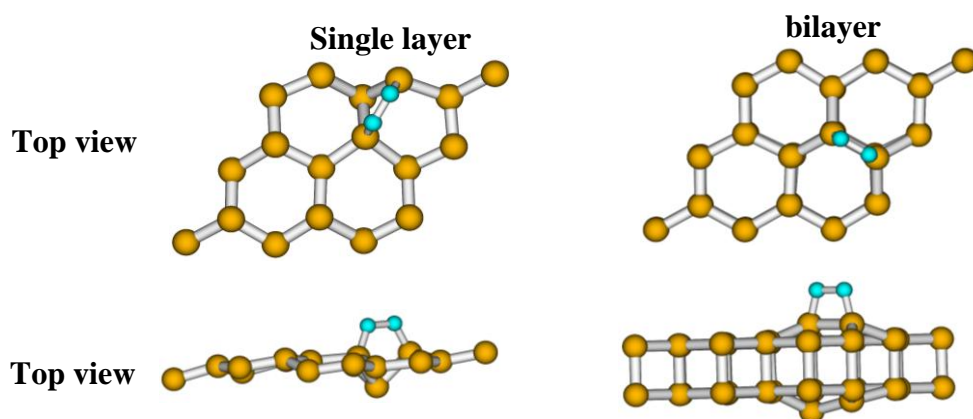
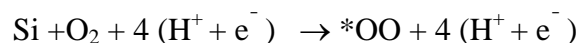


Figure 9.7: Optimized cell structures of O₂ adsorbed on single layer and bilayer silicene

Now, we discuss the different possible intermediate steps of ORR in acid medium. A systematic study of the ORR process on both single and bilayer silicene has been carried out and the corresponding geometries are reported in Figures 9.10 and 9.11 respectively. The first step in ORR is the O₂ adsorption as already discussed in earlier and it can be written as



where, the * indicates adsorbed (on silicene) and the calculated free energy change of this reaction on single and bilayer is found to be -1.92 eV and -2.71 eV respectively. Once the O₂ is adsorbed, it picks up a proton and electron to form OOH adsorbed on the surface. The optimized geometries of the OOH adsorbed on single and bilayer show that the O-O bond is completely broken. On the single layer, one of the oxygen atom is found to move to bridging position on one of the Si-Si bonds with the OH adsorbed on one Si atom site and the measured O-O bond distance is found to be 4.773 Å. However, on the bilayer, the oxygen does not move to the bridging position but stays on one Si atom with OH adsorbed on another Si atom as shown in Figure 9.11. The measured O-O distance is found to be 2.717 Å and the hydrogen of OH is found to form hydrogen bonding with the adsorbed oxygen atom with a H--O distance of 1.807 Å. In both the cases, it is observed that the O-O bond is completely broken indicating that there is no way for the formation of H₂O₂ intermediate observed in the two electron path and the ORR will follow a more efficient four electron reduction path. This reaction can be represented as

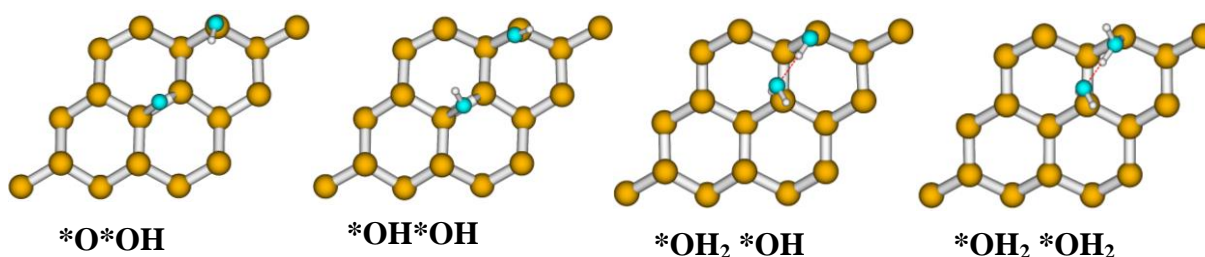
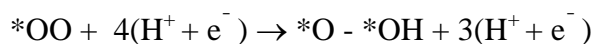
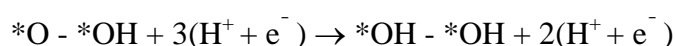


Figure 9.8: Possible intermediates in ORR on silicene single layer

and the corresponding free energy of this reaction on single and bilayer are calculated to be -3.53 and -3.00 eV respectively.

As a next step of the reaction we have considered two possible sites for the next hydrogen attack, i.e on the *O and *OH sites. In both the cases, hydrogen is found to prefer to bind on *O site as shown in Figures 9.10 and Figure 9.11. In case of single layer, as it is shown in Fig 9.10, one of the *OH is bridge bonded to Si-Si bond with Si-O bond distance of 1.904 Å whereas the other *OH is bonded to one Si atom with Si-O bond distance of 1.679 Å. In the case of bilayer, both the *OH are bonded to adjacent Si atoms and the shortest Si-O bond distance is found to be 1.679 Å. This reaction can be given as



and the change in free energy of this reaction on single and bilayer silicene are calculated to be +0.43 eV and -0.87 eV respectively. In the next reaction step, one of the *OH get converted to water by capturing a proton and electron which can be represented as

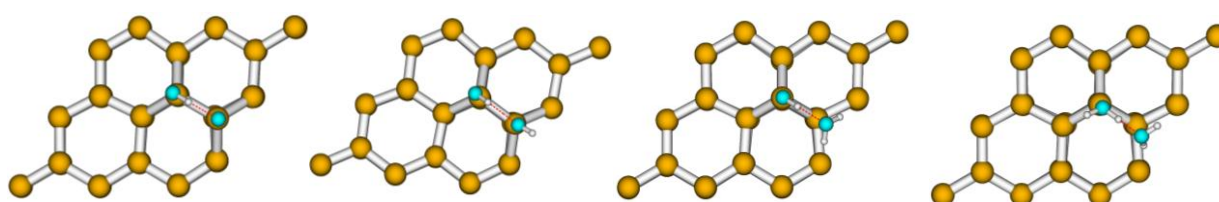
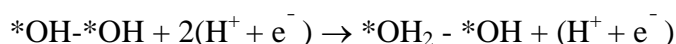
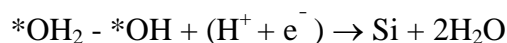


Figure 9.9: Possible intermediates in ORR on bilayer silicene

In the case of single layer silicene, it is seen that the *OH on Si-Si bridge is the preferred site for hydrogen and the water molecule formed moves away from the surface, forming hydrogen bonding with the other *OH group as shown in Figure 9.10. In the case of bilayer also, the water molecule formed is found to move away from the silicene surface, forming a hydrogen

bond with the adsorbed OH group. The free energy change for this reaction step on single and double layer are found to be -0.14 and +0.75 eV respectively. In the final step of the reaction, the remaining *OH reacts with a proton and electron to form the second water molecule which can be written as



The free energy change for this step on single and double layers is calculated to be +0.24 and +0.91 eV respectively. This positive free energy changes indicate that the desorption of the water molecule from the surface is energetically uphill.

9.4 Conclusions

In summary, we have shown here that the binding energies of all the three transition metals to graphyne are higher than the corresponding metal cohesive energies. Fe and Co decorated systems are found to adsorb molecular oxygen whereas Ni decorated system is inactive. In acid medium, the ORR on both GY-Fe and GY-Co systems is found to proceed through the more efficient four electron reduction mechanism. In alkaline medium, ORR on GY-Fe system is shown to follow a four electron reduction path whereas on GY-Co system ORR proceeds by two electron reduction path through the formation of hydrogen peroxide. In the case of silicene system, we have shown that the ORR on both single layer and double layer will be through the four electron path.

CHAPTER 10

Outlook and Future Explorations

In this final concluding chapter, we present brief conclusions to all the works elaborated throughout the thesis and also discuss the possible future extensions of these studies. From chapters 2-9, three different important problems associated with hydrogen energy have been addressed and the studies definitely provide a basic understanding for the future studies. The simple and important chemical concepts like electron induction effect and aromaticity are shown to play important role in stabilising the complexes which can be used in designing new materials.

As hydrogen is an energy carrier but not a source, it is important to generate hydrogen and the generation through solar water splitting is shown to be ideal as it does not evolve any harmful gases. In chapter 2, we have explored the g-CN based materials as an important class of materials for use in photocatalytic water splitting to generate hydrogen. These kinds of polymeric materials are shown to have more advantages over the conventional metal oxide based semiconductors. Designing a metal free photocatalyst for hydrogen generation is extremely important and the results from our studies can be useful in experimentally exploring these materials. The modelled g-CN materials are found to be wide band gap semiconductor materials and we have tried to engineer the band gap through doping of different metals as well as non-metals. It can be further possible to tune the band gap using other methods like creating defects, adsorption of molecular species, etc. which were shown to be effective in other materials like g-C₃N₄. As the synthesis of these materials has already been reported in literature, it will be interesting and also possible to make the photocatalyst based on these materials.

As hydrogen is the lightest element, it is extremely challenging to store hydrogen with high volumetric and gravimetric densities. Hence, we have designed different molecular systems and nanomaterials for molecular hydrogen storage. In chapter 3, we have explained the importance of the presence of ionic site on the hydrogen adsorption energies in carbon

materials. We have also shown that the metal ion binding energy as well as the hydrogen adsorption energy can be tuned through the substitution of different functional groups using the well known concept of electron induction effect. These studies can be helpful in designing the new framework materials like MOFs, where the metal ion binding energy on the linking chain can be tuned through the functionalization of the linking group. We have also shown that the aromaticity plays an important role in designing a stable metal decorated system. All these studies are helpful in designing new carbon materials containing the ionic metal site with improved metal binding energies required to make a stable system.

To achieve high gravimetric densities, light element based materials like carbon and boron based systems are more advantageous. In chapter 4, we explored the metal decorated boron hydrides as an important class of hydrogen adsorption materials. With one electron less than carbon, the tendency of boron to bind with electropositive metal atoms will be higher as compared to the carbon materials. Though we have considered small size boron hydrides, the studies can be extended to the more stable boranes which are stable at normal conditions. We have also attempted to design one-dimensional nanowires and three-dimensional frameworks based on these borane building blocks. In recent studies, boranes and carboranes based MOFs are being developed and are shown to have superior hydrogen adsorption properties as compared to the carbon based MOFs. It may be further possible to build new functional materials based on these borane and metal decorated boranes.

Aluminium hydrides and complex metal alanates are found to be promising materials for hydrogen storage. In chapter 5, we have studied the electronic structure and stability on different classes of aluminium hydrides similar to the well known boron hydrides. These results reveal that similar to boranes, alanes also follow the famous electron counting rules and are found to have considerably large HOMO-LUMO gaps and ionization potentials. As the aluminium hydride chemistry was not much explored like borane chemistry, it could be

interesting to further explore their physical and chemical properties as well as their applications in different fields.

It has been shown that the light metal decorated carbon nanomaterials can be used for hydrogen storage application. In chapter 6, we discussed the hydrogen adsorption properties of different light metal atom decorated fullerenes. It has been shown that the extent of curvature as well as the nature of curvature plays a vital role in binding with metal atoms. These conclusions can be useful in designing carbon nanomaterials with desired radius. Transition metal decorated carbon nanomaterials are found to be promising hydrogen storage materials with adsorption energies in the range desirable for ambient hydrogen adsorption. However, the weak metal binding energies to the carbon surface leads to the well known problem of metal aggregation to form clusters. Here, we have designed a new porous fullerene through the truncation doping of C_{60} which leads to a $C_{24}N_{24}$ fullerene with six N_4 cavities. These N_4 cavities can strongly hold the transition metals, thereby overcoming the clustering problem. In recent experiments, it has been shown that it is possible to generate these kinds of nitrogen doped cavities in single walled carbon nanotubes and hence the hydrogen storage studies can be carried out in those materials.

In chapter 7, we have explored the electronic structure and energy storage properties of two-dimensional carbon materials. It has been shown that the graphyne and graphdiyne are having direct band gaps which can be tuned by changing the length of the linking chain. More interestingly, the band gap of graphdiyne is close to the silicon bandgap and hence this material can have applications in nanoelectronics. These 2D carbons are found to be capable of holding large amounts of lithium due to the presence of more electronegative *sp*-carbon atoms and hence these materials can be used as anode materials in lithium materials. The lithium decorated graphyne and graphdiyne are shown to have improved hydrogen adsorption properties as compared to the earlier studied 2D carbons. We have also studied the hydrogen

adsorption in conjugated microporous materials which were also shown to have better adsorption properties. It can be possible to design more new form of carbons with carbon atoms in different hybridised states to get materials with versatile applications.

In recent years, there is a growing interest in designing new porous materials with high surface area for different applications like gas storage and catalysis. In chapter 8, the hydrogen adsorption properties of three-dimensional porous materials are discussed. Lithium decorated metal organic frameworks are shown to be more efficient hydrogen storage materials as compared to their undoped counterparts. However, these materials are unstable and are not recyclable due to the lack of strong binding force between the metal and the framework. In our study, it has been suggested that if two carbon atoms of the linking group can be substituted with boron atoms, the metal binding strength increases significantly so that the materials will be stable towards recycling. This kind of doping can be used in other carbon nanomaterials to enhance the metal binding energies. We have also designed super-cubane based 3D porous carbon by inserting the $\text{-C}\equiv\text{C-}$ units in-between inter and intra cubane C-C bonds. These materials, being porous in nature, are shown to adsorb hydrogen in molecular form. A similar technique can be used to generate different porous materials with varying porosity.

Another important problem related to the hydrogen energy is the design of a new catalyst for the oxygen reduction reaction, an important and rate limiting step in the fuel cell operation which has been addressed in chapter 9. The conventional platinum based catalysts are not suitable because of the low abundance and high cost of platinum and developing non-noble metal based catalyst is very important. We have proposed the transition metal decorated graphyne as an efficient catalyst for ORR. The Fe and Co decorated graphyne materials are shown to have better activity as compared to the Ni decorated graphyne. We have also studied the newly emerging 2D materials, silicene, the graphene counterpart of

silicon as a metal free catalyst for ORR. We have considered both single layer and double layer silicene for the study. Being a new member of the family of 2D materials, further studies on silicene will have more importance and especially its applications in nanoelectronics are more interesting because it is easy to interface with the existing silicon technology. It might be interesting to study the ORR activity of the substrate supported silicene as the free standing silicene is not yet experimentally reported. It will be interesting to study the effect of water environment on the stability of the intermediates of ORR to mimic the real fuel cell reaction.

REFERENCES:

- (1) Hoffert, M. I.; Caldeira, K.; Jain, A. K.; Haites, E. F.; Harvey, L. D. D.; Potter, S. D.; Schlesinger, M. E.; Schneider, S. H.; Watts, R. G.; Wigley, T. M. L. Wuebbles, D. J. *Nature* **1998**, 395, 891.
- (2) *Energy Information Administration's International Energy Outlook 2011* available at <http://www.eia.gov/forecasts/ieo/>
- (3) (a) Raupach, M. R.; Marland, G.; Ciais, P.; Quéré, C.; Canadell, J. G.; Klepper, G.; Field, C. B. *Proc. Natl Acad. Sci. USA* **2007**, 104, 10288.
- (4) Armaroli, N.; Balzani, V. *Chem. Asian J.* **2011**, 6, 768.
- (5) Conway, T. & Tans, P. Trends in atmospheric carbon dioxide. <http://www.esrl.noaa.gov/gmd/ccgg/trends> (2011).
- (6) (a) Züttel, A.; Remhof, A.; Borgschulte, A.; Friedrichs, O. *Phil. Trans. R. Soc. A* **2010**, 368, 3329.
- (7) Coontz, R.; Hanson, B. *Science* **2004**, 305, 957.
- (8) Crabtree, G. W.; Dresselhaus, M. S.; Buchanan, M. V. *Phys. Today* **2004**, 57, 39.
- (9) Lewis, N. S.; Nocera, D. G. *Proc. Natl. Acad. Sci. U.S.A.* **2006**, 103, 15729.
- (10) Midilli, A.; Dincer, I. *Int. J. Hydrogen Energy* **2008**, 33, 4209
- (11) Lubitz, W.; Tumas, W. *Chem. Rev.* **2007**, 107, 3900.
- (12) Ibrahim, H.; Ilinca, A.; Perron, J. *Renewable Sustainable Energy Rev.* **2008**, 12, 1221.
- (13) Schlapbach, L.; Züttel, A. *Nature* **2001**, 414, 353.
- (14) <http://www.cleanenergystates.org/>
- (15) Dodds, P.; McDowall, W. A review of hydrogen production technologies for energy system models, UKSHEC social science working paper 7 UCL Energy Institute (**2012**).
- (16) Bilgen, E. *Solar Energy* **2004**, 77, 47

- (17) Dincer, I. *Int. J. Hydrogen Energy* **2012**, *37*, 1954.
- (18) Turner, J.; Sverdrup, G.; Mann, M. K.; Maness, P.; Kroposki, B.; Ghirardi, M.; Evans, R. J.; Blake, D. *Int. J. Energy Res.* **2008**, *32*, 379
- (19) Funk, J. E. *Int. J. Hydrogen Energy* **2001**, *26*, 185.
- (20) Rosen, M. A. *Energy* **2010**, *35*, 1068.
- (21) Abanades, S.; Charvin, P.; Flamant, G.; Neveu, P. *Energy* **2006**, *31*, 2805.
- (22) Onuki, K.; Kubo, S.; Terada, A.; Sakaba, N.; Hino, R. *Energy Environ. Sci.*, **2009**, *2*, 491.
- (23) Barbarossa, V.; Brutti, S.; Diamanti, M.; Sau, S.; Maria, G. D. *Int. J. Hydrogen Energy* **2006**, *31*, 883.
- (24) Maeda, K.; Domen, K. *J. Phys. Chem. Lett.* **2010**, *1*, 2655.
- (25) Navarro, R. M.; Sánchez-Sánchez, M. C.; Alvarez-Galvan, M. C.; del Valle, F.; Fierro, J. L. G. *Energy Environ. Sci.*, **2009**, *2*, 35.
- (26) Fujishima, A.; Honda, K. *Nature* **1972**, *238*, 37.
- (27) Yerga, R. M. N.; Galván, M. C. A.; del Valle, F.; de la Mano, J. A. V.; Fierro, J. L. G. *ChemSusChem* **2009**, *2*, 471.
- (28) Chen, X.; Shen, S.; Guo, L.; Mao, S. S. *Chem. Rev.* **2010**, *110*, 6503.
- (29) Wang, X.; Maeda, K.; Thomas, A.; Takanabe, K.; Xin, G.; Carlsson, J. M.; Domen, K.; Antonietti, M. *Nat. Mater.* **2008**, *8*, 76.
- (30) Ducat, D. C.; Sachdeva, G.; Silver, P. A. *Proc. Natl Acad. Sci. USA* **2011**, *108*, 3941.
- (31) Eberle, U.; Felderhoff, M.; Schüth, F. *Angew. Chem. Int. Ed.* **2009**, *48*, 6608.
- (32) Reardon, H.; Hanlon, J. M.; Hughes, R. W.; Godula-Jopek, A.; Mandal, T. K.; Gregory, D. H. *Energy Environ. Sci.*, **2012**, *5*, 5951.
- (33) Graetz, J. *Chem. Soc. Rev.*, **2009**, *38*, 73.
- (34) van den Berg, A. W. C.; Areán, C. O. *Chem. Commun.*, **2008**, 668.

- (35) Yang, J.; Sudik, A.; Wolverton, C.; Siegel, D. J. *Chem. Soc. Rev.*, **2010**, 39, 656.
- (36) Pukazhselvan, D.; Kumar, V.; Singh, S. K. *Nano Energy* **2012**, 1, 566.
- (37) Grochala, W.; Edward, P. P. *Chem. Rev.* **2004**, 104, 1283.
- (38) Reilly, J. J. *Metal Hydrides as Hydrogen Storage and their Applications*, CRC Press, Cleveland, OH, **1977**.
- (39) Fukai, Y. *The Metal–Hydrogen System*, 2nd ed., Springer, Berlin, **2005**.
- (40) Chandra, D.; Reilly, J. J.; Chellappa, R. Chandra, D., Reilly, J. J., and Chellappa, R. J. *Metals* **2006**, 58, 26.
- (41) Schüth, F. *Nature* **2005**, 434, 712.
- (42) Ivey, D. G.; Northwood, D. O. *J. Mater. Sci.*, **1983**, 18, 321.
- (43) Schüth, F. Bogdanović, B. Felderhoff, M. *Chem. Commun.* , **2004**, 2249.
- (44) Sakintuna, B. Lamari-Darkrim, F.; Hirscher, M. *Int. J. Hydrogen Energy* **2007**, 32, 1121.
- (45) Larsson, P.; Araújo, C. M.; Larsson, J. A.; Jena, P.; Ahuja, R. *Proc. Natl Acad. Sci. USA* **2008**, 105, 8227.
- (46) Jain, I. P.; Lal. C.; Jain, A. *Int. J. Hydrogen Energy* **2010**, 35, 5133.
- (47) Hanada, N.; Ichikawa, T.; Fujii, H. *J. Phys. Chem. B* **2005**, 109, 7188.
- (48) Orimo, S.; Nakamori, Y.; Eliseo, J. R.; Züttel, A.; Jensen, C. M. *Chem. Rev.* **2007**, 107, 4111.
- (49) Xiong, Z.; Yong, C. K.; Wu, G.; Chen, P.; Shaw, W.; Karkamkar, A.; Autrey, T.; Jones, M. O.; Johnson, S. R.; Edwards, P. P.; David, W. I. F. *Nat. Mater.* **2008**, 7, 138.
- (50) Staubitz, A.; Robertson, A. P. M.; Manners, I. *Chem. Rev.* **2010**, 110, 4079.
- (51) Israelachvili, J. *Intermolecular and Surface Forces*, Academic Press, New York, **1992**.
- (52) Darkrim, F. L.; Malbrunot, P.; Tartaglia, G. P. *Int. J. Hydrogen Energy* **2002**, 27, 193.

- (53) Mpourmpakis, G.; Tylianakis, E.; Froudakis, G. E. *Nano Lett.* **2007**, *7*, 1893.
- (54) Züttel, A.; Sudan, P.; Maunon, Ph.; Kiyobayashi, T.; Emmenegger, Ch.; Schlapbach, L. *Int. J. Hydrogen Energy* **2002**, *27*, 203.
- (55) Yürüm, Y.; Taralp, A.; Veziroglu, T. N. *Int. J. Hydrogen Energy* **2009**, *34*, 3784.
- (56) Meregalli, V.; Parrinello, M. *Appl. Phys. A* **2001**, *72*, 143.
- (57) Gundiah, G.; Govindaraj, A.; Rajalakshmi, N.; Dhathathreyan, K. S.; Rao, C. N. R. *J. Mater. Chem.*, **2003**, *13*, 209.
- (58) Dillon, A. C.; Jones, K. M.; Bekkedahl, T. A.; Kiang, C. H.; Bethune, D. S.; Heben, M. J. *Nature*, **1997**, *386*, 377.
- (59) Liu, C.; Fan, Y. Y.; Liu, M.; Cong, H. T.; Cheng, H. M.; Dresselhaus, M. S. *Science* **1999**, *286*, 1127.
- (60) Patchkovskii, S.; Tse, J. S.; Yurchenko, S. N.; Zhechkov, L.; Heine, T.; Seifert, G. *Proc. Natl. Acad. Sci. U.S.A.* **2005**, *102*, 10439.
- (61) Chae, H. K.; Siberio-Pérez, D. Y.; Kim, J.; Go, Y.; Eddaoudi, M.; Matzger, A. J.; O’Keeffe, M.; Yaghi, O. M. *Nature* **2004**, *427*, 523.
- (62) Yaghi, O. M.; Li, G.; Li, H. *Nature*, **1995**, *378*, 703.
- (63) Rowsell, J. L. C.; Yaghi, O. M. *Microporous and Mesoporous Materials* **2004**, *73*, 3.
- (64) James, S. L. *Chem. Soc. Rev.*, **2003**, *32*, 276.
- (65) Rowsel, J. L. C.; Millward, A. R.; Park, K. S.; Yaghi, O. M. *J. Am. Chem. Soc.*, **2004**, *126*, 5666.
- (66) Rosi, N. L.; Eckert, J.; Eddaoudi, M.; Vodak, D. T.; Kim, J.; O’keeffe, M.; Yaghi, O. M. *Science*. **2003**, *300*, 1127.
- (67) Rowsel, J. L. C.; Yaghi, O. M. *Angew. Chem., Int. Ed.* **2005**, *44*, 4670. (c) Muller, T.; Ceder, G. *J. Phys. Chem. B* **2005**, *109*, 17974.
- (68) Lochan, R. C.; Head-Gordon, M. *Phys. Chem. Chem. Phys.* **2006**, *8*, 1357.

- (69) Dimitrakakis, G. K.; E.; Froudakis, G. E. *Nano Lett.*, **2008**, 8, 3166.
- (70) Deng, W.; Xu, X.; Goddard, W. A.; *Phys. Rev. Lett.* **2004**, 92, 166103.
- (71) Chandrakumar, K. R. S.; Ghosh, S. K. *Nano Lett.*, **2008**, 8, 13.
- (72) Sun, Q.; Jena, P.; Wang, Q.; Marquez, M. *J. Am. Chem. Soc.* **2006**, 128, 9741.
- (73) Chen, P.; Wu, X.; Lin, J.; Tan, K. L. *Science*, **1999**, 285, 91.
- (74) Yang, R. T. *Carbon*, **2000**, 38, 623.
- (75) Zhao, Y.; Kim, Y.-H.; Dillon, A. C.; Heben, J. M.; Zhang, S. B. *Phys. Rev. Lett.* **2005**, 94, 155504.
- (76) Yildirim, T.; Ciraci, S. *Phys. Rev. Lett.* **2005**, 94, 175501.
- (77) Phillips, A. B.; Shivaram, B. S. *Phys. Rev. Lett.* **2008**, 100, 105505.
- (78) Sun, Q.; Wang, Q.; Jena, P.; Kawazoe, Y. *J. Am. Chem. Soc.* **2005**, 127, 14582.
- (79) Sun, Q.; Wang, Q.; Jena, P.; Reddy, B. V.; Marquez, M. *Chem. Mater.* **2007**, 19, 3074.
- (80) Singh, A. K.; Sadrzadeh, A.; Yakobson, B. I. *J. Am. Chem. Soc.* **2010**, 132, 14126.
- (81) Kaye, S. S.; Long, J. R. *J. Am. Chem. Soc.* **2008**, 130, 806.
- (82) Maark, T. A.; Pal, S. *Int J Hydrogen Energy* **2010**, 35, 12846.
- (83) Klontzas, E.; Mavrandonakis, A.; Tylianakis, E.; Froudakis, G. E. *Nano Lett.*, **2008**, 8, 1572.
- (84) Dalach, P.; Frost, H.; Snur, R. Q.; Ellis, D. E. *J. Phys. Chem. C*, **2008**, 112, 9278.
- (85) Froudakis, G. E. *Nano Lett.*, **2001**, 1, 531.
- (86) Mulfort, K. L.; Hupp, J. T. *Inorg. Chem.*, **2008**, 47, 7936
- (87) Han, S. S.; Goddard III, W. A. *J. Am. Chem. Soc.* **2007**, 129, 8422.
- (88) Blomqvist, A.; Araújo, C. M.; Srepusharawoot, P.; Ahuja, R. *Proc. Natl. Acad. Sci.* **2007**, 104, 20173.
- (89) Lan, J.; Cao, D.; Wang, W. *J. Phys. Chem. C* **2010**, 114, 3108.
- (90) Cao, D.; Lan, J.; Wang, W.; Smit, B. *Angew. Chem. Int. Ed.* **2009**, 48, 4730.

- (91) Mulfort, K. L.; Hupp, J. T. *J. Am. Chem. Soc.* **2007**, *129*, 9604.
- (92) White, C. M.; Steeper, R. R.; Lutz, A. E. *Int. J. Hydrogen Energy* **2006**, *31*, 1292.
- (93) Trimm, D. L.; Onsan, Z. I. *Catal. Rev.* **2001**, *43*, 31
- (94) Carrette, L.; Friedrich, K. A.; Stimming, U. *ChemPhysChem*, **2000**, *1*, 162, *Fuel Cells*, **2001**, *1*, 5.
- (95) Borup, R. et al. *Chem. Rev.* **2007**, *107*, 3904.
- (96) Steele, B. C. H.; Heinzl, A. *Nature*, **2001**, *414*, 345.
- (97) Debe, M. K. *Nature* **2012**, *486*, 43.
- (98) Greeley, J.; Greeley, J.; Stephens, I. E. L.; Bondarenko, A. S.; Johansson, T. P.; Hansen, H. A.; Jaramillo, T. F.; Rossmeisl, J.; Chorkendorff, I.; Nørskov, J. K. *Nat. Chem.* **2009**, *1*, 552–556.
- (99) Yang, H. *Angew. Chem. Int. Ed.* **2011**, *50*, 2674 – 2676.
- (100) Sha, Y.; Yu, T. H.; Merinov, B. V.; Shirvanian, P.; Goddard, W. A. *J. Phys. Chem. C* **2012**, *116*, 21334.
- (101) Ceperley, D. M.; Alder, B. J. *Phys. Rev. Lett.* **1980**, *45*, 566.
- (102) Perdew, J. P.; Wang, Y. *Phys. Rev. B* **1992**, *45*, 13244.
- (103) Perdew, J. P.; Burke, K.; Ernzerhof, M. *Phys. Rev. Lett.* **1996**, *77*, 3865. (b) Perdew, J. P.; Burke, K.; Ernzerhof, M. *Phys. Rev. Lett.* **1997**, *78*, 1396.
- (104) Becke, A. D. *J. Chem. Phys.* **1988**, *88*, 2547.
- (105) Becke, A. D. *Phys. Rev. A* **1988**, *38*, 3098.
- (106) Lee, C.; Yang, W.; Parr, R. G. *Phys. Rev. B* **1988**, *37*, 785.
- (107) Zhao, Y.; Truhlar, D. G. *Theor. Chem. Acc.* **2008**, *120*, 215.
- (108) Zhao, Y.; Truhlar, D. G. *Acc. Chem. Res.* **2008**, *41*, 157.
- (109) Zhao, Y.; Truhlar, D. G. *J. Phys. Chem. C* **2008**, *112*, 4061.
- (110) Zhao, Y.; Truhlar, D. G. *Phys. Chem. Chem. Phys.* **2005**, *7*, 2701.

- (111) Levine, I. *Quantum Chemistry*, Prentice Hall of India Pvt. Ltd. **2001**.
- (112) Szabo, A.; Ostlund, N. S. *Modern Quantum Chemistry: Introduction to Advanced Electronic Structure Theory* McGraw-Hill, INC. New York, **1989**.
- (113) Parr, R. G.; Yang, W. *Density-Functional Theory of Atoms and Molecules*, Oxford University Press, New York, **1989**.
- (114) Hohenburg, P.; Kohn, W. *Physical Review*, **1964**, *136*, B864.
- (115) Kohn, W.; Sham, L. J. *Physical Review*, **1965**, *140*, A1133.
- (116) Ashcroft, N. W.; Mermim, N. D. *Solid State Physics*, Saunders College Publishing, **1976**.
- (117) Liu, G.; Niu, P.; Sun, C.; Smith, S. C.; Chen, Z.; Lu, G. Q.; Cheng, H. *J. Am. Chem. Soc.* **2010**, *132*, 11642.
- (118) Zhang, J.; Zhang, G.; Chen, X.; Lin, S.; Möhlmann, L.; Dołęga, G.; Lipner, G.; Antonietti, M.; Blechert, S.; Wang, X. *Angew. Chem., Int. Ed.* **2012**, *51*, 3183.
- (119) Wang, X.; Maeda, K.; Chen, X.; Takanabe, K.; Domen, K.; Hou, Y.; Fu, X.; Antonietti, M. *J. Am. Chem. Soc.* **2009**, *131*, 1680.
- (120) Lin, Z.; Wang, X. *Angew. Chem. Int. Ed.* **2013**, *52*, 1735.
- (121) Shalom, M.; Inal, S.; Fettkenhauer, C.; Neher, D.; Antonietti, M. *J. Am. Chem. Soc.* **2013**, *135*, 7118.
- (122) Ma, X.; Lv, Y.; Xu, J.; Liu, Y.; Zhang, R.; Zhu, Y. *J. Phys. Chem. C*, **2012**, *116*, 23485.
- (123) Hong, J.; Xia, X.; Wang, Y.; Xu, R. *J. Mater. Chem.*, **2012**, *22*, 15006.
- (124) Zheng, Y.; Liu, J.; Liang, J.; Jaroniec, M.; Qiao, S. Z. *Energy Environ. Sci.* **2012**, *5*, 6717.
- (125) Xiang, Q.; Yu, J.; Jaroniec, M. *J. Phys. Chem. C*, **2011**, *115*, 7355.
- (126) Pan, H.; Zhang, Y.; Shenoy, V. B.; Gao, H. *ACS Catal.* **2011**, *1*, 99.

- (127) Cao, C.; Huang, F.; Cao, C.; Li, J.; Zhu, H. *Chem. Mater.*, **2004**, *16*, 5213.
- (128) Li, J.; Cao, C.; Hao, J.; Qiu, H.; Xu, Y.; Zhu, H. *Diamond Relat. Mater.* **2006**, *15*, 1593.
- (129) Blöchl, P. E. *Phys. Rev. B.* **1994**, *50*, 17953.
- (130) Kresse, G.; Joubert, D. *Phys. Rev. B.* **1999**, *59*, 1758.
- (131) Kresse, G.; Furthmüller, J. *Comput. Mat. Sci.* **1996**, *6*, 15.
- (132) Kresse, G.; Furthmüller, J. *Phys. Rev. B.* **1996**, *54*, 11169.
- (133) Monkhorst, H. J.; Pack, J. D. *Phys. Rev. B* **1976**, *13*, 5188.
- (134) Heyd, J.; Scuseria, G. E.; Ernzerhof, M. *J. Chem. Phys.* **2003**, *118*, 8207; **2006**, *124*, 219906(E).
- (135) Schaftenaar, G.; Noordik, J. H. *J. Comput.-Aided Mol. Design* **2000**, *14*, 123.
- (136) Wu, F.; Liu, Y.; Yu, G.; Shen, D.; Wang, Y.; Kan, E. *J. Phys. Chem. Lett.* **2012**, *3*, 3330.
- (137) Kiran, B.; Kandalam, A. K.; Jena, P. *J. Chem. Phys.*, **2006**, *124*, 224703.
- (138) Weck, P. F.; Kumar, T. J. D.; Kim, E.; Balakrishnan, N. *J. Chem. Phys.*, **2007**, *126*, 094703.
- (139) Chandrakumar, K. R. S.; Ghosh, S. K. *Chem. Phys. Lett.*, **2007**, *447*, 208.
- (140) Special edition on aromaticity (Ed.: P. v. R. Schleyer), *Chem. Rev.* **2001**, *101*, 1115.
- (141) Chen, Z.; Wannere, C. S.; Corminboeuf, C.; Puchta, R.; Schleyer, P. v. R. *Chem. Rev.* **2005**, *105*, 3842.
- (142) Villaume, S.; Fogarty, H. A.; Ottosson, H. *ChemPhysChem* **2008**, *9*, 257.
- (143) Carey, A.; Sundberg, R. J. *Advanced Organic Chemistry: Structure and Mechanisms (Part A)*, Springer, New York, **2000**.
- (144) Pauling, L.; Sherman, J.; *J. Chem. Phys.* **1933**, *1*, 606.
- (145) Wheland, G. W.; Pauling, L. *J. Am. Chem. Soc.* **1935**, *57*, 2028.

- (146) Pauling, L. *The Nature of the Chemical Bond*, 3rd ed., Cornell University Press, New York, **1960**.
- (147) Smith, M. B.; March, J. *Advanced Organic Chemistry*, 5th ed., Wiley-Interscience, New York, **2001**.
- (148) Pierrefixe, S. C. A. H.; Bickelhaupt, F. M. *Chem. Eur. J.* **2007**, *13*, 6321.
- (149) Pierrefixe, S. C. A. H.; Bickelhaupt, F. M. *J. Phys. Chem. A* **2008**, *112*, 12816.
- (150) Li, X.; Kuznetsov, A. E.; Zhang, H. F.; Boldyrev, A. I.; Wang, L. S. *Science* **2001**, *291*, 859.
- (151) Kuznetsov, A. E.; Birch, K.; Boldyrev, A. I.; Li, X.; Zhai, H.; Wang, L. S. *Science* **2003**, *300*, 622.
- (152) Datta, A.; Mallajosyula, S. S.; Pati, S. K. *Acc. Chem. Res.* **2007**, *40*, 213.
- (153) M. Yoon, S. Yang, E. Wang, Z. Zhang, *Nano Lett.* **2007**, *7*, 2578.
- (154) Kubas, G. J. *Metal Dihydrogen and σ -Bond Complexes: Structure, Theory, and Reactivity*, Kluwer Academic, New York, **1999**.
- (155) Schmidt, M. W.; Baldrige, K. K.; Boatz, J. A.; Elbert, S. T.; Gordon, M. S.; Jensen, J. H.; Koseki, S.; Matsunga, N.; Nguyen, K. A.; Su, S. J.; Dupuis, M.; Montgomery, J. A. *J. Comput. Chem.* **1993**, *14*, 1347.
- (156) Tsuneda, T.; Hirao, K. *Chem. Phys. Lett.* **1997**, *268*, 510.
- (157) Tsuneda, T.; Suzumura, T.; Hirao, K. *J. Chem. Phys.* **1999**, *110*, 10664.
- (158) Kamiya, M.; Tsuneda, T.; Hirao, K. *J. Chem. Phys.* **2002**, *117*, 6010.
- (159) Schleyer, P. v. R.; Maerker, C.; Dransfeld, A.; Jiao, H.; Hommes, N. J. R. v. E. *J. Am. Chem. Soc.* **1996**, *118*, 6317.
- (160) Krygowski, T. M.; Cyranski, M. K. *Chem. Rev.* **2001**, *101*, 1385.
- (161) Kruszewski, T. M.; Krygowski, T. M. *Tetrahedron Lett.* **1972**, 3839.
- (162) Krygowski, T. M. *J. Chem. Inf. Comput. Sci.* **1993**, *33*, 70.

- (163) Savin, A.; Becke, A. D.; Flad, J.; Nesper, R.; Preuss, H.; von Schnering, H. G. *Angew. Chem. Int. Ed.* **1991**, *30*, 409.
- (164) Allouche, A. R. Gabedit-2.0.11, 2007, <http://gabedit.sourceforge.net/>.
- (165) Hammett, L. P. *Chem. Rev.*, **1935**, *17*, 125.
- (166) Hammett, L. P. *J. Am. Chem. Soc.*, **1937**, *59*, 96.
- (167) Hübner, O.; Glöss, A.; Fichtner, M.; Klopper, W. *J. Phys. Chem. A*, **2004**, *108*, 3019.
- (168) Hübner, O.; Klopper, W. *J. Phys. Chem. A*, **2007**, *111*, 2426.
- (169) Schwabe, T.; Grimme, S. *Phys. Chem. Chem. Phys.*, **2007**, *9*, 3397.
- (170) Neese, F.; Schwabe, T.; Grimme, S. *J. Chem. Phys.*, **2006**, *126*, 124115.
- (171) Schneider, H.; Vogelhuber, K. M.; Schinle, F.; Weber, J. M. *J. Am. Chem. Soc.*, **2007**, *129*, 13022.
- (172) Amunugama, R.; Rodgers, M. T. *J. Phys. Chem. A*, **2002**, *106*, 5529.
- (173) Ma, J. C.; Dougherty, D. A. *Chem. Rev.*, **1997**, *97*, 1303.
- (174) Dunsch, L.; Yang, S. *Phys. Chem. Chem. Phys.*, **2007**, *9*, 3067.
- (175) CRC Handbook of Chemistry and Physics, 84th ed. (Ed.: D. R. Lide), CRC Press, **2003–2004**, pp. 10–147.
- (176) Becke, A. D.; Edgecombe, K. E. *J. Chem. Phys.* **1990**, *92*, 5397.
- (177) Vitillo, J. G.; Damin, A.; Zecchina, A.; Ricchiardi, G. *J. Chem. Phys.* **2005**, *122*, 114311.
- (178) Vitillo, J. G.; Damin, A.; Zecchina, A.; Ricchiardi, G. *J. Chem. Phys.* **2006**, *124*, 224308.
- (179) E. W. Neuse, H. Rosenberg, *Metallocene Polymers*, Marcel Dekker, New York, **1970**.
- (180) Werner, H. *Angew. Chem. Int. Ed.* **1977**, *16*, 1.
- (181) Stock, A.; Massenez, C. *Ber. Dtsch. Chem. Ges.* **1912**, *45*, 3539.
- (182) Eberhardt, W. H.; Crawford, B.; Lipscomb, W. N. *J. Chem. Phys.* **1954**, *22*, 989.

- (183) Wade, K. *Chem. Commun.* **1971**, 792.
- (184) McKee, M. L.; Wang, Z -X.; Schleyer, P.v.R. *J. Am. Chem. Soc.* **2000**, *122*, 4781.
- (185) Aihara, J. *J. Am. Chem. Soc.* **1978**, *100*, 3339.
- (186) Nöth, H. *Homonuclear boron clusters*. In: Driess, M.; Nöth, H. editors. *Molecular clusters of the main group elements* 2004. WILEY-VCH, Weinheim, p. 34-94.
- (187) Vincent, M. A.; Schaefer III HF. *J. Am. Chem. Soc.* **1981**, *103*, 5677.
- (188) Kaufmann, E.; Schleyer, P. V. R. *Inorg. Chem.* **1988**, *27*, 3987.
- (189) Li, S.; Willis, M.; Jena, P. *J. Phys. Chem. C* **2010**, *114*, 16849.
- (190) Schreckenbach, G. Ziegler, T. *J. Phys. Chem.* **1995**, *99*, 606.
- (191) Hoffmann, R.; Schleyer, P. V. R.; Schaefer, H. F. *Angew. Chem. Int. Ed.* **2008**, *47*, 7164.
- (192) Henkelman, G.; Arnaldsson, A.; Jónsson, H. *Comput. Mater. Sci.* **2006**, *36*, 254.
- (193) McKee, M. L.; Bühl, M.; Charkin, O. P.; Schleyer, P. v. R. *Inorg. Chem.* **1993**, *32*, 4549.
- (194) Hofmann, K.; Prosencb, M. H.; Albert, B. R. *Chem. Commun.* **2007**, 3097.
- (195) Kittel, C. *Introduction to solid state physics*, 5th ed. Wiley: New York, **1976**
- (196) Zhang, C.-G.; Zhang, R.; Wang, Z. -X.; Zhou, Z.; Zhang, S. B.; Chen, Z. *Chem. Eur. J.* **2009**, *15*, 5910.
- (197) Finze, M. *Inorg. Chem.* **2008**, *47*, 11857.
- (198) Aldridge, S.; Downs, A. J. *Chem. Rev.* **2001**, *101*, 3305
- (199) Rao, B. K.; Jena, P. *Phys. Rev. Lett.* **2001**, *86*, 692
- (200) King, R. B.; Schleyer, P. v. R.; Nöth, H. in *Molecular Clusters of the main group elements* (Eds: M. Driess, H. Nöth.) **2004**. WILEY-VCH, Weinheim, pp. 1-94.
- (201) Greenwood, N. N. *Chem. Soc. Rev.* **1992**, *21*, 49.

- (202) Kurth, F. A.; Eberlein, R. A.; Schnöckel, H.; Downs, A. J.; Pulham, C. R. *J. Chem. Soc., Chem. Commun.* **1993**, 1302.
- (203) Andrews, L.; Wang, X. *Science* **2003**, 299, 2049.
- (204) Brower, F. M.; Matzek, N. E.; Reigler, P. F.; Rinn, H. W.; Roberts, C. B.; Schmidt, D. L.; Snover, J. A.; Terada, K. *J. Am. Chem. Soc.* **1976**, 98, 2450.
- (205) Carey, A.; Sundberg, R. J. *Advanced Organic Chemistry: Structure and Mechanisms (Part B)*, Springer, New York, **2000**.
- (206) Lipscomb, W. N. *Boron Hydrides*. W. A. Benjamin: New York, 1963.
- (207) Greenwood, N. N.; Earnshaw, A. *Chemistry of the Elements*, 2nd ed.; Elsevier Science: Amsterdam, The Netherlands, **1997**.
- (208) Stock, A.; Massenez, C. *Ber. Dtsch. Chem. Ges.* **1912**, 45, 3539.
- (209) Cotton, F. A.; Wilkinson, G.; Murillo, C. A.; Bochmann, M. *Advanced Inorganic Chemistry*, 6th ed. Wiley: New York, **1999**.
- (210) Williams, R. E. *Chem. Rev.* **1992**, 92, 177.
- (211) Wade, K. *Chem. Commun.* **1971**, 792.
- (212) Mingos, D. M. P. *Nature Phys. Sci.* **1972**, 236, 99.
- (213) Balakrishnarajan, M. M.; Jemmis, E. D. *J. Am. Chem. Soc.* **2000**, 122, 4516.
- (214) Jemmis, E. D.; Balakrishnarajan, M. M.; Pancharatna, P. D. *J. Am. Chem. Soc.* **2001**, 123, 4313.
- (215) King, R. B. *Chem. Rev.* **2001**, 101, 1119.
- (216) Jemmis, E. D.; Schleyer, P. v. R. *J. Am. Chem. Soc.* **1982**, 104, 4781.
- (217) McKee, M. L. *J. Phys. Chem.* **1991**, 95, 6519.
- (218) Li, X.; Grubisic, A.; Stokes, S. T.; Cordes, J.; Ganteför, G. F.; Bowen, K. H.; Kiran, B.; Willis, M.; Jena, P.; Burgert, R.; Schnöckel, H. *Science* **2007**, 315, 356.

- (219) Grubisic, A.; Li, X.; Stokes, S. T.; Cordes, J.; Ganteför, G. F.; Bowen, K. H.; Kiran, B.; Jena, P.; Burgert, R.; Schnöckel, H. *J. Am. Chem. Soc.* **2007**, *129*, 5969.
- (220) Martínez, J. I.; Alonso, J. A. *J. Chem. Phys.* **2008**, *129*, 074306.
- (221) Fu, L.-J.; Xie, H.-B.; Ding, Y.-H. *Inorg. Chem.* **2009**, *48*, 5370.
- (222) Bremer, M.; Schleyer, P. v. R.; Schotz, K.; Kausch, M.; Schindler, M. *Angew. Chem. Int. Ed.*, **1987**, *26*, 761.
- (223) Olah, G. A.; Rasul, G.; Prakash, G. K. S. *J. Org. Chem.* **2000**, *65*, 5956.
- (224) Balakrishnarajan, M. M.; Hoffmann, R. *J. Am. Chem. Soc.* **2004**, *126*, 13119.
- (225) Simon, A.; Böttcher, F.; Cockcroft, J. K. *Angew. Chem. Int. Ed.* **1991**, *30*, 101.
- (226) Hofmann, K.; Prosencb, M. H.; Albert, B. R. *Chem. Commun.* **2007**, 3097.
- (227) Stone, A. J.; Alderton, M. J. *Inorg. Chem.* **1982**, *21*, 2297.
- (228) Gunn, S. R.; Green, L. G. *J. Phys. Chem.* **1961**, *65*, 2173.
- (229) Hoffmann, R.; Lipscomb, W. N. *J. Chem. Phys.* **1962**, *37*, 2872.
- (230) Tian, S. X. *J. Phys. Chem. A* **2005**, *109*, 5471.
- (231) Lee, M. H.; Sankey, O. F.; Björling, T.; Moser, D.; Noréus, D.; Parker, S. F.; Häussermann, U. *Inorg. Chem.* **2007**, *46*, 6987.
- (232) Park, S.; Srivastava, D.; Cho, K. *Nano Lett.* **2003**, *3*, 1273.
- (233) Lu, X.; Chen, Z. *Chem. ReV.* **2005**, *105*, 3643.
- (234) Li, J.; Jia, G.; Zhang, Y.; Chen, Y. *Chem. Mater.* **2006**, *18*, 3579.
- (235) Cheng, H.; Cooper, A. C.; Pez, G. P.; Kostov, M. K.; Piotrowski, P.; Stuart, S. J. *J. Phys. Chem. B* **2005**, *109*, 3780.
- (236) Karfunkel, H. R.; Dressler, T.; Hirsch, A. *J. Comput.-Aided Mol. Des.* **1992**, *6*, 521.
- (237) Hirsch, A.; Nuber, B. *Acc. Chem. Res.* **1999**, *32*, 795.
- (238) Lee, D. H.; Lee, W. J.; Lee, W. J.; Kim, S. O.; Kim, Y.-H. *Phys. Rev. Lett.* **2011**, *106*, 175502.

- (239) Usachov, D.; Vilkov, O.; Grüneis, A.; Haberer, D.; Fedorov, A.; Adamchuk, V. K.; Preobrajenski, A. B.; Dudin, P.; Barinov, A.; Oehzelt, M.; Laubschat, C.; Vyalikh, D. V. *Nano Lett.* **2011**, *11*, 5401.
- (240) Miwa, K.; Fukumoto, A. *Phys. Rev. B* **2002**, *65*, 155114.
- (241) Ryou, J.; Kim, G.; Hong, S. *J. Chem. Phys.* **2011**, *134*, 234701.
- (242) Du, A.; Zhu, Z.; Smith, S. C. *J. Am. Chem. Soc.*, **2010**, *132*, 2876.
- (243) Reunchan, P.; Jhi, S—H. *Appl. Phys. Lett.* **2011**, *98*, 093103.
- (244) Baughman, R. H.; Eckhardt, H.; Kertesz, M. *J. Chern. Phys.* **1987**, *87*, 6687.
- (245) Diederich, F. *Nature*, **1994**, *369*, 199.
- (246) Haley, M. M.; Brand, S. C.; Pak, J. J. *Angew. Chem. Int. Ed. Engl.* **1997**, *36*, 835.
- (247) Li, G.; Li, Y.; Liu, H.; Guo, Y.; Li, Y.; Zhu, D. *Chem. Commun.*, **2010**, *46*, 3256.
- (248) Long, M.; Tang, L.; Wang, D.; Li, Y.; Shuai, Z. *ACS Nano*, **2011**, *5*, 2593.
- (249) Jiao, Y.; Du, A.; Hankel, M.; Zhu, Z.; Rudolph, V.; Smith, S. C. *Chem. Commun.*, **2011**, *47*, 11843.
- (250) Cooper, A. I. *Adv. Mater.* **2009**, *21*, 1291.
- (251) Thomas, A. *Angew. Chem. Int. Ed.* **2010**, *49*, 8328.
- (252) Jiang, J. X.; Su, F.; Trewin, A.; Wood, C. D.; Niu, H.; James, J. T. A.; Khimyak, Y. Z.; Cooper, A. I. *J. Am. Chem. Soc.*, **2008**, *130*, 7710.
- (253) Jiang, J. X.; Su, F.; Trewin, A.; Wood, C. D.; Campbell, N. L.; Niu, H.; Dickinson, C.; Ganin, A. Y.; Rosseinsky, M. J.; Khimyak, Y. Z.; Cooper, A. I. *Angew. Chem. Int. Ed.* **2007**, *46*, 8574.
- (254) Jiang, J. X.; Su, F.; Niu, H.; Wood, C. D.; Campbell, N. L.; Khimyak, Y. Z.; Cooper, A. I. *Chem. Commun.*, **2008**, 486.
- (255) Li, A.; Lu, R. F.; Wang, Y.; Wang, X.; Han, K. L.; Deng, W. Q. *Angew. Chem. Int. Ed.* **2010**, *49*, 3330.

- (256) Sun, Y. Y.; Lee, K.; Kim, Y.-H.; Zhang, S. B. *Appl. Phys. Lett.* **2008**, *92*, 013106.
- (257) Dovesi, R.; Saunders, V. R.; Roetti, C.; Orlando, R.; Zicovich-Wilson, C. M.; Pascale, F.; Civalleri, B.; Doll, K.; Harrison, N. M.; Bush, I. J.; D'Arco, P.; Llunell, M.; CRYSTAL06 User's Manual. University of Torino: Torino, 2006.
- (258) Aydinol, M. K.; Kohan, A. F.; Ceder, G.; Cho, K.; Joannopoulos, J. *Phys. Rev. B* **1997**, *56*, 1354.
- (259) Zheng, J. P.; Liang, R. Y.; Hendrickson, M.; Plichta, E. *J. Electrochem. Soc.* **2008**, *155*, A432.
- (260) Narita, N.; Nagai, S.; Suzuki, S.; Nakao, K. *Phys. Rev. B.* **1998**, *58*, 11009.
- (261) Zhou, J.; Lv, K.; Wang, Q.; Chen, X. S.; Sun, Q.; Jena, P. *J. Chem. Phys.* **2011**, *134*, 174701.
- (262) Bhatia, S. K.; Myers, A. L. *Langmuir* **2006**, *22*, 1688.
- (263) Muscat, J.; Wander, A.; Harrison, N. M. *Chem. Phys. Lett.* **2003**, *342*, 397.
- (264) Matsuda, Y.; Tahir-Kheli, J.; Goddard, W. A. *J. Phys. Chem. Lett.* **2010**, *1*, 2946.
- (265) Grimme, S.; Antony, J.; Ehrlich, S.; Krieg, H. *J. Chem. Phys.* **2010**, *132*, 154104.
- (266) Corma, A. *Chem. Rev.* **1997**, *97*, 2373.
- (267) Davis, M. E. *Nature* **2002**, *417*, 813.
- (268) Feréy, G. *Chem. Soc. Rev.*, **2008**, *37*, 191.
- (269) Venkataramanan, N. S.; Sahara, R.; Mizuseki, H.; Kawazoe, Y. *Int. J. Mol. Sci.* **2009**, *10*, 1601.
- (270) Nöth, H.; Schmidt, M. *Angew. Chem. Int. Ed. Engl.* **1996**, *35*, 292.
- (271) Zou, X.; Zhou, G.; Duan, W.; Choi, K.; Ihm, J. *J. Phys. Chem. C* **2010**, *114*, 13402.
- (272) Kroto, H. W.; Heath, J. R.; O'Brien, S. C.; Curl, R. F. Smalley, R. E. *Nature* **1985**, *318*, 162.
- (273) Iijima, S. *Nature* **1991**, *354*, 56

- (274) Novoselov, K. S.; Geim, A. K.; Morozov, S. V.; Jiang, D.; Zhang, Y.; Dubonos, S. V.; Grigorieva, I. V.; Firsov, A. A. *Science*, **2004**, *306*, 666.
- (275) Strel'nitskii, V. E.; Padalka, V. G.; Vakula, S. I. *Zh. Tekh. Fiz.* **1978**, *48*, 377. *Sov. Phys. Tech. Phys.* **1978**, *23*, 222.
- (276) Johnston, R. L.; Hoffmann, R. *J. Am. Chem. Soc.* **1989**, *111*, 810.
- (277) Liu, P.; Cui, H.; Yang, G. W.; *Cryst. Growth Des.*, **2008**, *8*, 581.
- (278) Hirsch, A. *Nature materials* **2010**, *9*, 868.
- (279) Gleiter, R.; Kratz, D. *Angew. Chem. Int. Ed. Engl.* **1993**, *32*, 842.
- (280) Bradley, C. J.; Cracknell, A. P. *The Mathematical Theory of Symmetry in Solids*; Clarendon Press: Oxford, England, **1972**.
- (281) Liu, Y.; Wang, G.; Huang, Q.; Guo, L.; Chen, X. *Phys. Rev. Lett.* **2012**, *108*, 225505.
- (282) Sheng, X. L.; Yan, Q. B.; Ye, F. Zheng, Q. R. Su, G. *Phys. Rev. Lett.* **2011**, *106*, 155703.
- (283) Viswanathan, V.; Hansen, H. A.; Rossmeisl, J.; Nørskov, J. K. *J. Phys. Chem. Lett.* **2012**, *3*, 2948.
- (284) Suntivich, J.; Gasteiger, H. A.; Yabuuchi, N.; Nakanishi, H.; Goodenough, J. B.; Shao-Horn, Y. *Nature Chem*, **2011**, *3*, 546.
- (285) Ham, D. J.; Lee, J. S. *Energies* **2009**, *2*, 873.
- (286) Yu, D.; Nagelli, E.; Du, F.; Dai, L. *J. Phys. Chem. Lett.* **2010**, *1*, 2165.
- (287) Liang, J.; Zheng, Y.; Chen, J.; Liu, J.; Hulicova-Jurcakova, D.; Jaroniec, M.; Qiao, S. *Z. Angew. Chem. Int. Ed.* **2012**, *51*, 3892.
- (288) Zheng, Y.; Jiao, Y.; Chen, J.; Liu, J.; Liang, J.; Du, A.; Zhang, W.; Zhu, Z.; Smith, S. C.; Jaroniec, M.; Lu, G. Q.; Quia, S. Z. *J. Am. Chem. Soc.* **2011**, *133*, 20116.
- (289) Bezerra, C. W. B.; Zhang, L.; Lee, K.; Liu, H.; Marques, A. L. B.; Marques, E. P.; Wang, H.; Zhang, J. *Electrochimica Acta* **2008**, *53*, 4937.

- (290) Kattel, S.; Atanassov, P.; Kiefer, B. *J. Phys. Chem. C* **2012**, *116*, 17378.
- (291) Yang, J.; Liu, D. J.; Kariuki, N. N.; Chen, L. X. *Chem. Commun.*, **2008**, 329.
- (292) Sun, S.; Jiang, N.; Xia, D. *J. Phys. Chem. C* **2011**, *115*, 9511.
- (293) Lee, D. H.; Lee, W. J.; Lee, W. J.; Kim, S. O.; Kim, Y. H. *Phys. Rev. Lett.* **2011**, *106*, 175502.
- (294) Parvez, K.; Yang, S.; Hernandez, Y.; Winter, A.; Turchanin, A.; Feng, X.; Müllen, K. *ACS Nano*, **2012**, *6*, 9541.
- (295) Kong, X. K.; Chen, Q. W.; Sun, Z. *RSC Adv.*, **2013**, *3*, 4074.
- (296) He, J.; Ma, S. Y.; Zhou, P.; Zhang, C. X.; He, C.; Sun, L. Z. *J. Phys. Chem. C* **2012**, *116*, 26313.
- (297) Chaure, N.B.; Rhen, F. M. F.; Hilton, J.; Coey, J. M. D. *Electrochem. Commun.* **2007**, *9*, 155.
- (298) Takeda, K.; Shiraishi, K. *Phys. Rev. B* **1994**, *50*, 14916.
- (299) Durgun, E.; Tongay, S.; Ciraci, S. *Phys. Rev. B* **2005**, *72*, 075420.
- (300) Kara, A.; Enriquez, H.; Seitsonen, A. P.; Voon, L. C. L. Y.; Vizzini, S.; Aufray, B.; Oughaddou, H.; *Surf. Sci. Rep.* **2012**, *67*, 1.
- (301) Cahangirov, S.; Topsakal, M.; Aktürk, E.; Sahin, H.; Ciraci, S.; *Phys. Rev. Lett.* **2009**, *102*, 236804.
- (302) Lalmi, B.; Oughaddou, H.; Enriquez, H.; Kara, A.; Vizzini, S.; Ealet, B.; Aufray, B. *Appl. Phys. Lett.* **2010**, *97*, 223109.
- (303) Fleurence, A.; Friedlein, R.; Ozaki, T.; Kawai, H.; Wang, Y.; Yamada-Takamura, Y. *Phys. Rev. Lett.* **2012**, *108*, 245501.
- (304) Feng, B.; Ding, Z.; Meng, S.; Yao, Y.; He, X.; Cheng, P.; Chen, L.; Wu, K. *Nano Lett.* **2012**, *12*, 3507.
- (305) Wang, J.; Li, J.; Li, S. S.; Liu, Y. *J. Appl. Phys.* **2013**, *114*, 124309.

- (306) Trtsaris, G. A.; Kaxiras, E.; Meng, S.; Wang, E. *Nano Lett.* **2013**, *13*, 2258
- (307) Padova, P. D. Quaresima, C.; Olivieri, B.; Perfetti, P.; Lay, G. L. *J. Phys. D: Appl. Phys.* **2011**, *44*, 312001.
- (308) Molle, A.; Grazianetti, C.; Chiappe, D.; Cinquanta, E.; Cianci, E.; Tallarida, G.; Fanciulli, M. *Adv. Funct. Mater.* **2013**, *23*, 4340.